TECHNISCHE UNIVERSITÄT MÜNCHEN
Lehrstuhl für Leichtbau

Aircraft engine noise footprint reduction via a non-uniform inlet liner concept

Dominik Broszat

Vollständiger Abdruck der von der Fakultät für Maschinenwesen der Technischen Universität München zur Erlangung des akademischen Grades eines

Doktor-Ingenieurs

genehmigten Dissertation.

Vorsitzender: Univ.-Prof. Dr.-Ing. H.-P. Kau

Prüfer der Dissertation:

1. Univ.-Prof. Dr.-Ing. H. Baier
2. Hon.-Prof. Dr.-Ing. Dr. h. c. D. Schmitt

Die Dissertation wurde am 01.07.2008 bei der Technischen Universität München eingereicht und durch die Fakultät für Maschinenwesen am 01.12.2008 angenommen.

Abstract

Aircraft noise is one of the limiting factors in the growth of future air traffic. Of the various components contributing to the overall aircraft noise, the engine is among the most important ones during operations in the vicinity to the ground, i. e. at takeoff and approach. Even if engine noise has been reduced drastically since the first generation of jet powered aircraft in the 1960s, these achievements have to be attributed mainly to the increase in the Bypass Ratio (BPR) in modern turbofan engines. However, as a consequence, fan noise has become more and more important dominating the tonal components of both forward and rearward radiated noise.

Within this thesis, a specific non-uniform liner distribution called the Virtual Scarf Inlet (VSI) to be applied to the inlet of a commercial aircraft engine is being investigated. It aims at achieving a redirection of the radiation directivity by influencing the acoustic boundary conditions. By this concept, the sound pressure levels recorded within specific sectors, e. g. the most relevant ones for community noise at an airport, can be reduced significantly. In contrast to competing novel concepts involving modifications of the inlet geometry to achieve a shielding effect, the VSI avoids the drawbacks of aerodynamic or weight penalties while achieving a similar effect.

After an explanation of the corresponding physical phenomenon, the results of a systematic parametric study to analyze the main influencing quantities of the VSI effect by means of the Boundary Element Method (BEM) are being presented. Following, the VSI liner concept is being compared to a conventional uniform acoustic liner and their individual advantages and disadvantages are being highlighted. Concluding, several advanced lining concepts for an engine inlet involving the VSI are discussed and assessed with respect to their individual technological complexity and expected performance.

As a result of the preceding analysis, the VSI liner seems to offer a promising potential in the application to an aircraft engine inlet as a complement to existing absorptive liners. It requires only minor changes to the structure and avoids several penalties related to competing approaches. In contrast to most other lining concepts, the VSI influences the overall modal pressure distribution within the duct and is most effective for well cut-on nearly axially propagating modes which are difficult to affect by conventional designs. This fact motivates its application to the approach condition where it is able to achieve up to 9.0 dB of attenuation in the most favorable condition. Moreover, it is demonstrated that even in a worst case scenario, the VSI liner does not cause noticeable negative results compared to a conventional design.

Acknowledgments

This thesis originates from my time as a Ph. D. student at the EADS Corporate Research Centre/ Innovation Works (IW) in Ottobrunn, Germany. At first, I would like to thank my research advisor Dr.-Ing. Richard Maier for the chance to work on this fascinating subject and the continuous support and guidance throughout the years. Additionally, I would like to thank all colleagues at EADS IW who contributed to this work, especially Dipl.-Ing. Reinhard Pongratz for the numerous hours of fruitful discussion and the support in the experimental part of this thesis and Dr.-Ing. Alexander Peiffer for the introduction to the Boundary Element Method and valuable suggestions in the numerical field. My special thanks go to all other (former and current) Ph. D. students at EADS IW who contributed both on the technical level and by creating an encouraging working atmosphere.

Furthermore, I am indebted to my professors at the Technical University of Munich (TUM), Prof. Dr.-Ing. Horst Baier and Prof. Dr.-Ing. Dr. h. c. Dieter Schmitt for their support and valuable technical recommendations. In addition, I would like to thank Prof. Dr.-Ing. Hans-Peter Kau for chairing the committee.

For the provision of and their cooperative and kind support in the usage of the BEM code ACTIPOLE, I wish to thank the team of Isabelle Terrasse at EADS IW in Suresnes and Toulouse, France, in particular Vassili Srithammavanh, Guillaume Sylvand, and Fanny Darbas. As well, I am grateful to Hervé Batard, Head of Nacelle Acoustics Engineering at Airbus France for the cooperation concerning the use of this code.

In addition, my parents deserve all my gratitude for their continuous support. And finally, my wife Barbara has been of substantial importance for the outcome of this thesis thanks to her unconditional support and encouragement.

Contents

Nomenclature

Upper case roman letters

A	amplitude
A, B	coefficients
$\boldsymbol{A}, \boldsymbol{B}$	matrices in Direct BEM formulation
A_a	acoustic admittance
A_s	surface area
B	susceptance (imaginary part of acoustic admittance)
D	duct diameter
F	tone correction (in EPNL calculation)
G	Green's function
G	conductance (real part of acoustic admittance)
He	Helmholtz number
$\boldsymbol{I}$	intensity
J_m	Bessel function of order m
L	duct length
M	Mach number
N	quantity, number of
P	acoustic power
R	duct radius
R	resistance (real part of acoustic impedance)
T	transformation matrix
V	volume
X	reactance (imaginary part of acoustic impedance)
Y_m	Neumann function of order m
Z	acoustic impedance

Lower case roman letters

$\bar{p}$	DL potential (jump of pressure)
$\bar{q}$	SL potential (jump of pressure gradient)
a	width of rectangular duct
b	height of rectangular duct
c	speed of sound
d	throat diameter (of resonator)
dL	attenuation per length [dB]
f	frequency
f	mathematical function
f, g	excitation vectors
h	height
i	imaginary unit
k	wave number

l ..... length
l ..... throat length (of resonator)
m ..... azimuthal mode order (circ. duct)
m ..... mode number in x-direction (rect. duct)
n ..... mode number in y-direction (rect. duct)
n ..... radial mode order (circ. duct)
p ..... sound pressure
r ..... distance (of two points in space)
r ..... ratio
r ..... reflection coefficient
r, θ, z ..... coordinate directions (cylindrical coordinate system)
t ..... time
t_{10} ..... duration of noise level within 10 dB of peak level [s] (in EPNL calculation)
u ..... velocity (of piston)
$\boldsymbol{v}$ ..... sound particle velocity
$\boldsymbol{x}, \boldsymbol{y}$ ..... position vector in space
x, y, z ..... coordinate directions (cartesian coordinate system)

Upper case greek letters

Δ ..... difference
Γ ..... Gamma function
Ω ..... shaft angular velocity
Φ ..... potential

Lower case greek letters

α ..... absorption coefficient
α ..... tilt angle (directivity curve)
δ ..... particle displacement
η ..... dimensionless frequency parameter [Rice]
γ ..... ratio of specific heats
κ ..... imaginary part of complex distribution coefficient [Rice]
κ_{mn} ..... eigenvalue of Bessel function, order m, n
λ ..... acoustic wavelength
μ ..... dynamic viscosity
μ ..... real part of complex distribution coefficient [Rice]
ω ..... angular velocity
ϕ ..... circumference angle
ψ ..... group velocity angle
ρ ..... density of medium
σ ..... damping coefficient [Rice]
τ ..... propagation coefficient [Rice]
θ ..... azimuthal angle of radiation
ε ..... mechanical strain
φ ..... phase angle
φ ..... propagation angle
ϑ ..... rotation angle (of VSI configuration)
ξ ..... cut-off ratio
ζ ..... specific impedance

Subscripts

0	steady state, ambient
φ	phase
ax	axial
azi	azimuthal
B	number of rotor blades (Tyler-Sofrin)
BM	Bellmouth
c	cut-off limit
cav	cavity
$circumf$	circumferential
$crit$	critical
ext	exterior
f	fluid
g	group
int	interior
l	limit
max	maximum
mic	microphone
n	normal component
opt	optimum
p	peak
r	reflective
rad	radiated
ref	reference value
res	resonance
rms	root mean square, effective
sp	speakers
t	total (sum)
tip	(rotor) tip
V	number of stator vanes (Tyler-Sofrin)
w	wall

Superscripts

$*$	complex conjugate
$*$	normalized value
$+/-$	spinning or propagation direction (of mode)
T	transpose (of matrix)

Symbols / operators

Δ	Laplace operator
$\forall$	for all
$\mathcal{O}$	order (of magnitude)
∇	Nabla operator
$\partial/\partial t$	partial derivative
d/dt	substantial derivative

Abbreviations

$2DOF$	Double Degree of Freedom
$ACARE$	Advisory Council for Aeronautical Research in Europe
$ActiPRO$	ACTIPOLE Pre- and Postprocessing
$AIAA$	American Institute of Aeronautics and Astronautics
ANC	Active Noise Control
AOA	Angle of Attack
APS	Auto Power Spectrum
BB	Broadband
BC	Boundary Condition
BEM	Boundary Element Method
BPF	Blade Passage Frequency
BPR	Bypass Ratio
BSN	Buzz Saw Noise
$CEAS$	Confederation of European Aerospace Societies
CFD	Computational Fluid Dynamics
$CHIEF$	Combined Helmholtz Integral Equation Formulation
$D-BEM$	Direct BEM
dB	Decibel
DL	Double Layer
DLR	Deutsches Zentrum für Luft- und Raumfahrt
DOF	Degree of Freedom
DSP	Digital Signal Processor
$EADS$	European Aeronautic Defence and Space Company
ECL	Ecole Centrale de Lyon
$EPNL$	Effective Perceived Noise Level
EVF	Eigenvalue Function
EXP	Experiment
FAA	Federal Aviation Administration
FEM	Finite Element Method
FFT	Fast Fourier Transform
FMM	Fast Multipole Method
FOD	Foreign Object Damage
FP	Field Point
GTF	Geared Turbofan
GUI	Graphical User Interface
HP	High Pass (filter)
$I-BEM$	Indirect BEM
$ICAO$	International Civil Aviation Organization
IE	Infinite Element
Im	Imaginary part (of complex number)
JAA	Joint Aviation Authorities
LMS	Least Mean Square (algorithm)
LP	Low Pass (filter)
MAL	Mechanically Adaptive Liner
$MALTA$	Mechanically Adaptive Liner Test Assembly
MDF	Medium Density Fiberboard
$ML-FMM$	Multi Level FMM
$NASA$	National Aeronautics and Space Administration
$NDOF$	Multi Degree of Freedom

NLR	National Aerospace Laboratory - The Netherlands
NSI	Negatively Scarfed Intake
PNL	Perceived Noise Level
PWL	Sound Power Level
QC	Quota Count
QTD	Quiet Technology Demonstrator
$RANNTAC$	Reduction of Aircraft Noise by Nacelle Treatment and Active Control
Re	Real part (of complex number)
rms	Root Mean Square
$ROSTI$	Rotor-Stator Interaction Test Rig
RPM	Revolutions Per Minute
$SDOF$	Single Degree of Freedom
SEA	Statistical Energy Analysis
sgn	Signum (function)
SHR	Semi-Active Helmholtz Resonator
$SILENCER$	Significantly Lower Community Exposure to Aircraft Noise
SIM	Simulation
SL	Single Layer
$SL-FMM$	Single Level FMM
SPL	Sound Pressure Level
SVD	Singular Value Decomposition
SWR	Standing Wave Ratio
TS	Test Section
$TURNEX$	Turbomachinery Noise Radiation through the Engine Exhaust
$UHBR$	Ultra High Bypass Ratio
VL	Virtual Lab (LMS)
VSE	Virtual Scarf Exhaust
VSI	Virtual Scarf Inlet
ZSI	Zero Splice Intake

Chapter 1

Introduction / objectives

Aircraft noise is one of the limiting factors in the growth of future air traffic. Accordingly, more and more stringent noise regulations have been imposed by the ICAO (International Civil Aviation Organization) and the national authorities, i. e. the FAA (Federal Aviation Administration) in the United States and the JAA (Joint Aviation Authorities) in Europe. These specify the maximum allowable noise levels and allow for a categorization of aircraft types. Dependent on these, several airports, particularly the London city airports, define the landing fees and limit the number of night-time aircraft movements. Therefore, all aircraft are assigned a specific Quota Count (QC) rating characterizing the aircraft's noise impact based on certification data. To achieve longterm noise reductions, the corresponding quota are gradually reduced.

For the midterm future, the ACARE (Advisory Council for Aeronautical Research in Europe) set in its 'Vision 2020' very challenging targets of reducing the Effective Perceived Noise Level (EPNL) by 50% by the year 2020. These goals can only be met by a concerted effort of the aircraft and engine manufacturers, airlines, airport operators, and air traffic control.

Of the various components contributing to the overall aircraft noise, the engine is among the most important ones during operations in the vicinity to the ground, i. e. at takeoff and approach. Even if engine noise has been reduced drastically since the first generation of jet powered aircraft in the 1960s, these achievements have to be attributed mainly to the increase in the Bypass Ratio (BPR) in modern turbofan engines. The increasing amount of air flowing through the bypass duct reduces the specific thrust of the engine and the resulting jet exhaust velocity, which is strongly correlated with the broadband noise generation mechanisms.[1] However, as a consequence, fan noise has become more and more important dominating the tonal components of both forward and rearward radiated noise.

To counteract these clearly audible tones, the engine duct interior has been lined with acoustically absorbing materials since the first generation of jet engines. Due to several reasons (weight, contamination, erosion, drainage), the most commonly used lining type is the $\lambda/4$ absorber or resistive resonator consisting of a flow resistance sheet at the front side and a partitioned back cavity adjusted to the quarter wavelength resonance of the dominant tones. This concept is quite efficient at the resonance frequency and able to provide a certain bandwidth if properly designed. However, the potential for improvement is fairly limited as the design is already very well optimized.

Throughout the years, a variety of advanced concepts have been tested and analyzed: on the one hand adaptive or active concepts enabling the tuning of the liner to varying flight conditions and frequencies, and on the other hand non-uniform lining distributions to

[1] The radiated intensity of a turbulent jet is proportional to the eighth power of the jet exhaust velocity ($I \propto v_e^8$).

enhance noise reduction by a variety of strategies. Though the adaptability of the tuning frequency in general seems very interesting, most concepts suffered from a weak performance or a considerably increased technical complexity of the system.

The non-uniform solutions were related both to the inlet geometry and the layout of the lining material. With respect to the latter, only few concepts followed a pronounced strategy essentially dealing with mode scattering by an axial and/or circumferential segmentation of the lining material to enhance the resulting noise reduction. Even if theoretically quite effective, these concepts bear the risk of strong negative effects in case of unpredictable variations in the sound field. On the contrary, non-uniform inlet geometries as e. g. the Negatively Scarfed Intake (NSI) make use of a shielding effect of the prolonged lower inlet lip, and thus are able to reduce the radiated power into this sector. However, the modifications of the inlet geometry involve aerodynamic and weight penalties which have to be balanced with the acoustic advantages.

An attempt to achieve an effect comparable to the NSI, i. e. a redirection of the radiation directivity avoiding the above mentioned drawbacks, will be presented within this thesis. Since in this concept the acoustic effect is being achieved by the use of a specific non-uniform inlet liner distribution instead of an asymmetric shape of the inlet lip, it will be called the *Virtual Scarf Inlet (VSI)*.

To provide a basis for the discussions in the subsequent chapters, the relevant theory and state of the art concerning duct acoustics lining concepts and the associated methods of computation will be recapitulated in chapter 2.

In chapter 3, a specific adaptive liner concept (the Mechanically Adaptive Liner) will be analyzed both experimentally and numerically. This may serve, on the one hand, to validate the Boundary Element Method (BEM) for duct acoustic problems involving non-uniform impedance distributions, and, on the other hand, verify the means of an impedance adaption by discrete adaptive elements.

The first of the two main parts of this thesis (chapter 4) presents the physical concept of the Virtual Scarf Inlet and an analysis of its basic characteristics by means of a comprehensive parametric study comprising its geometric degrees of freedom. Finally, for a generalization of the VSI effect, the main influencing parameters will be extracted from the results.

In the second main part of this thesis, chapter 5, a VSI liner configuration will be compared to a conventional uniform absorptive liner, and the individual strengths, weaknesses, and favorable areas of application will be discussed.

In the concluding part of the thesis (chapter 6), several concepts of possible implementations of a VSI liner in an engine inlet will be compared with respect to their individual technological complexity and expected performance. This analysis will propose advanced lining concepts of differing complexity and capability depending on the characteristics of the input sound field and the objectives of the system.

Finally, chapter 7 summarizes the results and findings of the thesis and provides ideas for subsequent research work.

Chapter 2

Background / state of the art of duct acoustics

In this chapter, both the theoretical background and a comprehensive overview of the state of the art concerning duct acoustic concepts, applications, and numerical methods will be presented.

At first, the fundamental equation of linear acoustics - the wave equation - will be derived and applied to the duct acoustics problem involving propagation, diffraction, and radiation in the presence of a number of boundary conditions including flow and acoustic linings. In the second part, a short introduction will be given into the primary sources of forward radiated noise of a modern turbofan engine. The third part deals with the application of the theoretical results to different duct lining concepts - ranging from passive over adaptive or hybrid solutions to various kinds of non-uniform configurations. In the last part of the chapter, analytical and numerical means of solving duct acoustic problems will be named and described, with emphasis on the Boundary Element Method (BEM) used for the numerical studies presented within this thesis.

2.1 Duct acoustic theory

As sketched in figure 2.1, the duct acoustic theory comprises three basic steps: the in-duct propagation of acoustic waves, the reflection and diffraction at the finite duct termination, and the radiation of sound to a remote observer.

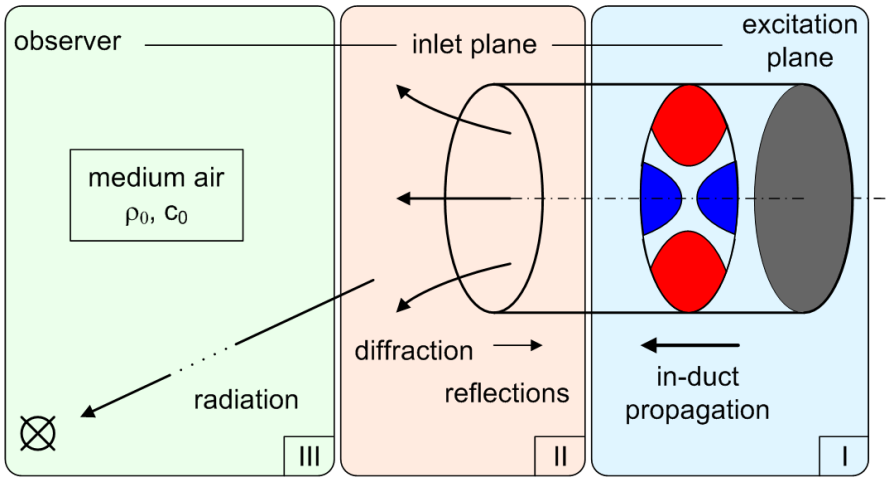

Figure 2.1: Schematic sketch of acoustic duct propagation and radiation problem

In the first step, solutions to the wave equation (time domain) or Helmholtz equation (frequency domain) have to be determined for the respective duct geometry (in this case a circular duct) including the effects of acoustic linings and flow. They are conveniently formulated in terms of a superposition of acoustic modes. Following, the influence of the duct termination is accounted for in terms of reflections back into the duct and a diffraction of the acoustic field. Finally, the radiation problem within the medium air has to be solved to obtain the sound pressure detected by an observer.

In the following, these three main subjects will be treated step by step to provide the theory necessary for the understanding of the subsequent chapters.

2.1.1 In-duct acoustic wave propagation

This first part comprises the derivation of the fundamental equation for acoustic problems and its solution for cylindrical ducts including a uniform mean flow and acoustic boundary conditions.

2.1.1.1 Derivation of convected wave / Helmholtz equation

The three equations governing the characteristics of an inviscid, isentropic, non heat conducting perfect gas are the equations of continuity, momentum, and state, respectively (derivation according to Hubbard [1] and Ehrenfried [2])

$$\frac{\partial \rho^*}{\partial t} + \nabla \cdot (\rho^* \cdot \boldsymbol{v}^*) = 0 \,, \tag{2.1}$$

$$\frac{\partial \boldsymbol{v^*}}{\partial t} + (\boldsymbol{v}^* \cdot \nabla) \cdot \boldsymbol{v^*} = -\frac{1}{\rho^*} \nabla p^* \,, \tag{2.2}$$

$$p^* = \frac{1}{\gamma} \rho^{*\gamma} \,, \tag{2.3}$$

in which the pressure p^*, density ρ^*, and velocity $\boldsymbol{v^*}$ have been normalized by corresponding reference values

$$p^* = \frac{\tilde{p}}{c_{ref}^2 \cdot \rho_{ref}} \,; \qquad \rho^* = \frac{\tilde{\rho}}{\rho_{ref}} \,; \qquad \boldsymbol{v^*} = \frac{\tilde{\boldsymbol{v}}}{c_{ref}} \,. \tag{2.4}$$

Considering only the small perturbations of a steady state (p_0, ρ_0, $\boldsymbol{v_0}$), which are the quantities of interest in acoustic problems,

$$p^* = p_0 + p \,; \qquad \rho^* = \rho_0 + \rho \,; \qquad \boldsymbol{v^*} = \boldsymbol{v_0} + \boldsymbol{v} \tag{2.5}$$

and an irrotational (potential) flow ($\boldsymbol{v^*} = \nabla \cdot \Phi$; $\nabla \times \boldsymbol{v^*} = 0$), a combination of the three equations above yields the *convected wave equation*,

$$\boxed{\frac{1}{c^2} \left(\frac{\partial}{\partial t} + \boldsymbol{v} \frac{\partial}{\partial z} \right)^3 p = \left(\frac{\partial}{\partial t} + \boldsymbol{v} \frac{\partial}{\partial z} \right) \nabla^2 p - 2 \frac{dM}{dr} \frac{\partial^2 p}{\partial z \partial r}} \tag{2.6}$$

in which M stands for the Mach number ($M = v/c$). Moreover, in the case of a uniform flow in the z-direction ($dM/dr = 0$), the equation simplifies to a more commonly used version

$$\frac{1}{c^2}\left(\frac{\partial}{\partial t} + \boldsymbol{v}\frac{\partial}{\partial z}\right)^2 p - \Delta p = 0 \tag{2.7}$$

using $\nabla^2 = \Delta$. The expression in the brackets is the convective, or substantial, derivative of the pressure due to the presence of the flow

$$\frac{d^2p}{dt^2} = \Big(\underbrace{\frac{\partial}{\partial t}}_{\text{local derivative}} + \underbrace{\boldsymbol{v}\frac{\partial}{\partial z}}_{\text{convective derivative}} \Big)^2 p \, . \tag{2.8}$$

After expanding the expression in the brackets, equation (2.7) yields

$$\frac{1}{c^2}\frac{\partial^2 p}{\partial t^2} + 2\frac{v_z}{c^2}\cdot\frac{\partial^2 p}{\partial t\,\partial z} + \left(\frac{v_z}{c}\right)^2 \cdot \frac{\partial^2 p}{\partial z^2} - \Delta p = 0 \, , \tag{2.9}$$

which can be simplified by introducing a time-harmonic source of frequency $\omega = 2\pi f$ and amplitude p_0

$$p(r, \theta, z, t) = p_0(r, \theta, z) \cdot e^{i\omega t} \tag{2.10}$$

and the definition of the *acoustic wave number*

$$k = \frac{\omega}{c} \tag{2.11}$$

to the following expression

$$\Delta p - M^2 \frac{\partial^2 p}{\partial z^2} - 2iMk\frac{\partial p}{\partial z} + k^2 p = 0 \, . \tag{2.12}$$

For a cylindrical geometry (as sketched in figure 2.2), the Laplace operator (Δ) is defined by

$$\Delta = \frac{1}{r}\frac{\partial}{\partial r}\left(r\frac{\partial}{\partial r}\right) + \frac{1}{r^2}\frac{\partial^2}{\partial \theta^2} + \frac{\partial^2}{\partial z^2} \, , \tag{2.13}$$

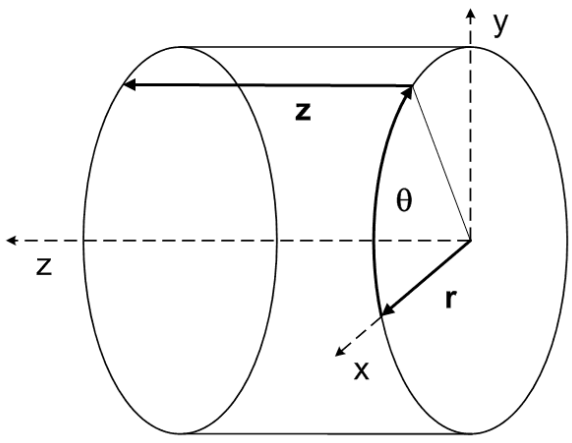

Figure 2.2: Cylindrical coordinate system

which yields in this case for the pressure

$$\Delta p = \frac{\partial^2 p}{\partial r^2} + \frac{1}{r}\frac{\partial p}{\partial r} + \frac{1}{r^2}\frac{\partial^2 p}{\partial \theta^2} + \frac{\partial^2 p}{\partial z^2} \ . \tag{2.14}$$

Inserting this into equation (2.12) yields the *convected Helmholtz equation*.

$$\boxed{\frac{\partial^2 p}{\partial r^2} + \frac{1}{r}\frac{\partial p}{\partial r} + \frac{1}{r^2}\frac{\partial^2 p}{\partial \theta^2} + \left(1 - M^2\right)\frac{\partial^2 p}{\partial z^2} - 2iMk\frac{\partial p}{\partial z} + k^2 p = 0} \tag{2.15}$$

This equation cannot be resolved directly by a separation of the variables, as the radial distance from the duct center line r does not only appear in the $\partial/\partial r$ terms, but also in the $\partial^2/\partial\theta^2$ term. Thus, the solution for the radial variation depends on the specification of a solution for the azimuthal variation.

2.1.1.2 Solution for hardwalled cylindrical duct

To obtain a formulation better reflecting the type of this differential equation, and to separate the individual constituents, the pressure variable is further decomposed into its radial, circumferential, and axial components

$$p_0(r, \theta, z) = \hat{p}(r) \cdot e^{\pm im\theta} \cdot e^{\pm ik_z z} \ , \tag{2.16}$$

in which $\hat{p}(r)$ stands for the radial variation of the pressure (its exact characteristic will be determined in the following), m defines the circumferential periodicity, and k_z is the axial wave number determining the propagation into the axial (z-) direction. Its interpretation will be given later on in this section in figure 2.7.

Combining equation (2.15) and (2.16) with a periodic boundary condition in the circumferential direction ($h(\theta) = h(\theta + 2\pi)$) because of the rotational symmetry of the geometry, constitutes a second order *Bessel equation* for the sound pressure p

$$\frac{d^2\hat{p}}{dr^2} + \frac{1}{r}\frac{d\hat{p}}{dr} + \left\{k^2\left[\left(1 - M\frac{k_z}{k}\right)^2 - \left(\frac{k_z}{k}\right)^2\right] \mp \frac{m^2}{r^2}\right\}\hat{p} = 0 \ , \tag{2.17}$$

the general formulation of which is the following

$$s^2\frac{d^2 a(s)}{ds^2} + s\frac{da(s)}{ds} + \left(s^2 - \nu^2\right)a(s) = 0 \ . \tag{2.18}$$

In the case of no flow ($M = 0$), equation (2.17) simplifies to

$$\frac{d^2\hat{p}}{dr^2} + \frac{1}{r}\frac{d\hat{p}}{dr} + \left\{k^2\left[1 - \left(\frac{k_z}{k}\right)^2\right] \mp \frac{m^2}{r^2}\right\}\hat{p} = 0 \ . \tag{2.19}$$

A general solution to equation (2.18) can be written as the combination of two characteristic functions

$$a(s) = A \cdot J_\nu(s) + B \cdot Y_\nu(s) \ , \tag{2.20}$$

a *Bessel function* J_ν and a *Neumann function* Y_ν of order ν corresponding to the circumferential mode order m. The Bessel function can be written in terms of a power series

$$J_\nu(s) = \sum_{m=0}^{\infty} \frac{(-1)^m \cdot (\frac{s}{2})^{\nu+2m}}{m! \cdot \Gamma \cdot (\nu + m + 1)} \ , \tag{2.21}$$

in which Γ stands for the Gamma function which is an extension of the factorial to all real numbers. However, as in the current application only integers will be used for ν, it can be replaced by a factorial expression

$$\Gamma(n+1) = n! \qquad \text{for } n \in \mathbb{N} \,. \tag{2.22}$$

The Neumann function, which represents another infinite series, can be also related to the Bessel function

$$Y_\nu(s) = \frac{J_\nu(s)\,\cos(\nu\pi) - J_{-\nu}(s)}{\sin(\nu\pi)} \,. \tag{2.23}$$

For illustration, examples of both the Bessel and Neumann functions of integer order m are displayed in figure 2.3. As can be seen, all Bessel functions, except for the zeroth order, have a zero point at $s = 0$, whereas the Neumann functions become singular at the origin. However, both feature an unlimited number of zero points with increasing s.

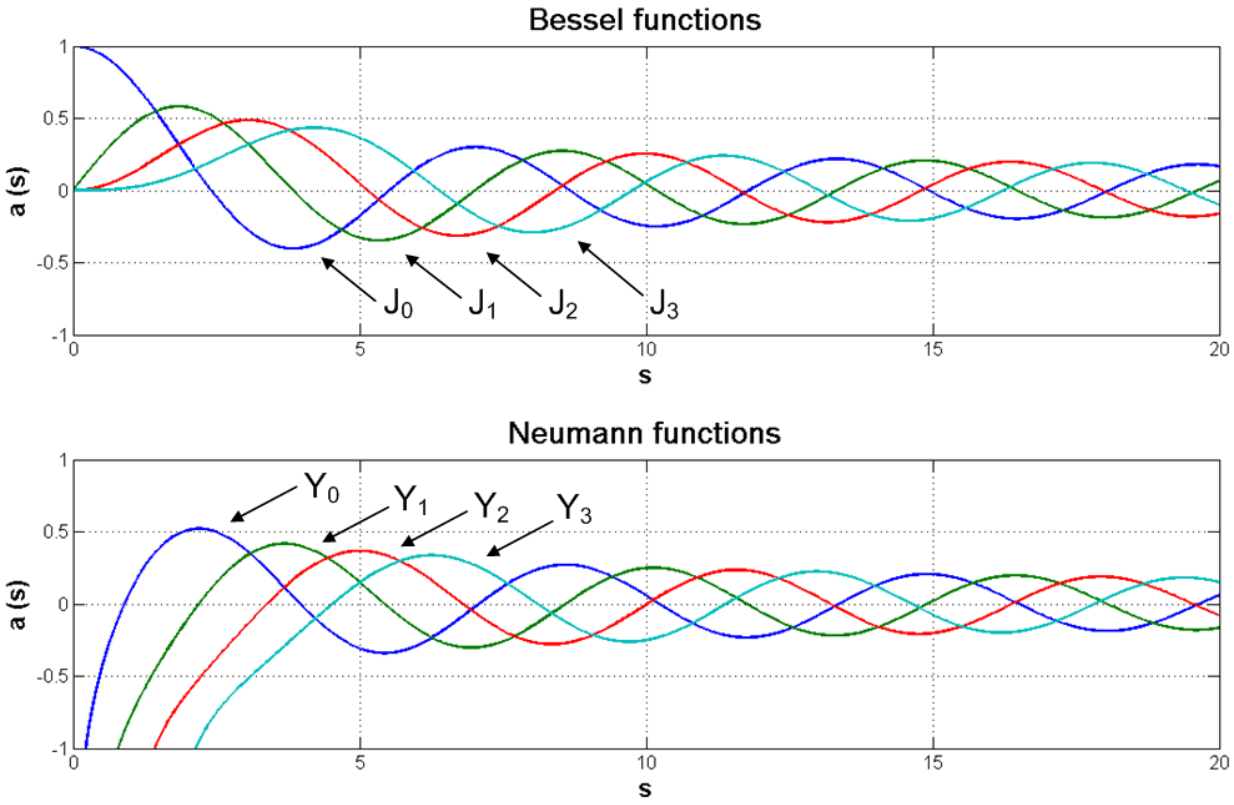

Figure 2.3: Bessel and Neumann functions

With application to a hardwalled circular duct, the boundary conditions are a zero pressure gradient at the duct wall (for reasons of simplicity chosen to be at $r = 1$) and a finite pressure value at the duct axis ($r = 0$)

$$\frac{\partial p}{\partial r}_{|\,r=1} \stackrel{!}{=} 0 \,; \qquad\qquad p_{|\,r=0} \stackrel{!}{=} \text{finite} \,. \tag{2.24}$$

The second condition prevents a singularity at the duct axis. Because of this restriction, the coefficient B in front of the Neumann function has to vanish, which leaves only the Bessel

function as a solution to the second order differential equation.[1]

As could be seen in figure 2.3, there are an unlimited number of zero values for each order ν of the Bessel function (corresponding to the azimuthal periodicity m). Accordingly, the numbering of the eigenvalues is complemented by a second parameter n

$$\hat{p}(r) = A \cdot J_m(\kappa_{mn} \cdot r) \ , \tag{2.25}$$

in which κ_{mn} are the eigenvalues of the Bessel function of order m. The condition for determination of the eigenvalues is hence

$$J'_m(\kappa_{mn}) \stackrel{!}{=} 0 \ . \tag{2.26}$$

Using a recursion formula for the derivative of the Bessel function (found e. g. in Morse and Ingard [3])

$$\frac{d}{dx} J_m(x) = J_{m-1}(x) - \frac{m}{x} J_m(x) \ , \tag{2.27}$$

the eigenvalue equation (2.26) can be solved more easily by numerical means.

$$\boxed{J_{m-1}(\kappa_{mn}) - \frac{m}{\kappa_{mn}} J_m(\kappa_{mn}) \stackrel{!}{=} 0} \tag{2.28}$$

As a result of these considerations, the expression for the sound pressure p can be now written as follows (compare Ehrenfried [2]),

$$\boxed{p(r,\theta,z,t) = A_1 \cdot J_m(\kappa_{mn}) \cdot (A_2 \cdot e^{-ik_{z_{mn}} z} + B_2 \cdot e^{+ik_{z_{mn}} z}) \cdot (A_3 \cdot e^{-im\theta} + B_3 \cdot e^{+im\theta}) \cdot e^{i\omega t}} \tag{2.29}$$

in which the radial distribution is given by the Bessel function, the variable m determines the circumferential mode number, and corresponds to the number of nodal lines in the radial direction through the origin, and the radial mode number n corresponds to the number of nodal circles in a given cross section.

An important conclusion of this section is the fact that the eigenvalues of the Bessel functions κ_{mn} determining the radial sound pressure distribution in the duct, are, for this case of a hard walled duct, dependent solely on geometrical quantities (i. e. the radius of the duct r and the azimuthal mode number m) as can be seen in equation (2.28)[2]

$$\kappa_{mn} = f(m, r) \ . \tag{2.30}$$

This characteristic will change in chapter 2.1.1.4, where an acoustic lining is added to the duct wall.

For a better illustration, sketches of the first mode shapes in the cross section of a circular duct are given in figure 2.4. Therein, dark areas indicate positive values of the sound pressure and bright ones negative values, corresponding to a snapshot of the instantaneous pressure distribution. Accordingly, in the horizontal direction, the number of radial node lines is incremented, corresponding to an increasing azimuthal mode number m. In the vertical direction, the radial mode order n increases from the top to the bottom with the number of concentric node circles.

[1] In annular ducts, e. g. in bypass duct applications, the coefficient B remains non-zero, and hence, both Bessel and Neumann functions are used in the solution.

[2] Remember that in this derivation, the radius has been set to $r = 1$ for simplification.

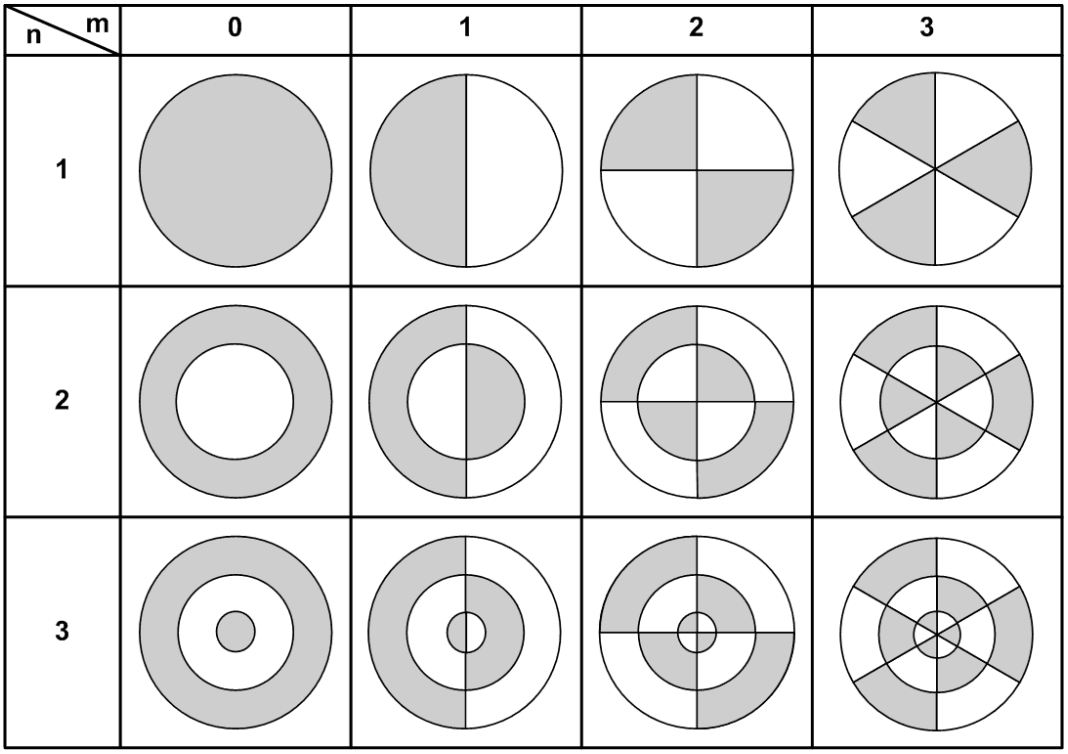

Figure 2.4: Mode shapes in circular duct

At this point, the nomenclature used within this thesis shall be pointed out. With respect to the circumferential mode number m, the notation starts at $m = 0$ for an axisymmetric mode shape, and increases accordingly with the number of nodal lines in the radial direction. Differently for the radial mode number n, which starts at the value $n = 1$ and hence is equal to the number of nodal circles + 1. This somewhat unconventional notation[3] is related to the numbering of the zero values of the Bessel equation, and has been adopted to stay in line with the notation of the BEM code ACTIPOLE which has been used for most of the computations in this thesis and will be described in chapter 2.4.3.4.

To clarify the influence of the various coefficients in equation (2.29), they will be described consecutively in the following

- A_1 : amplitude of radial pressure distribution ,
- A_2, B_2 : axial propagation characteristics ,
- A_3, B_3 : mode rotation (spinning mode character) .

Thus, the coefficient A_1 does not influence the mode shape in the radial direction, which is determined by the Bessel function, but scales its amplitude.

In contrast, A_2 and B_2 determine the axial propagation of the mode: if e. g. $A_2 = 1$ and $B_2 = 0$, the mode propagates solely into the positive axial direction, and conversely for $A_2 = 0$ and $B_2 = 1$ (negative axial propagation). For the special case $A_2 = B_2$, standing wave patterns are excited which rest at a fixed axial location.

Accordingly, but with respect to the circumferential direction, for the coefficients A_3 and B_3: for $A_3 = 1$ and $B_3 = 0$, a so-called *spinning mode* of order $+m$ can be observed within the duct which spirals in the positive rotation direction (as can be seen exemplarily for a mode ($m = 2$, $n = 1$) in figure 2.5(b)) - and analogously for the opposite case ($-m$: negative

[3]Most of the pertinent literature uses a notation starting at $n = 0$, e. g. Morse and Ingard [3] and Ehrenfried [2].

spinning direction). For the special case $A_3 = B_3$, the mode shape does not spin but creates standing wave patterns in the circumferential direction (compare figure 2.5(a)). These specific mode shapes will be called *'non-spinning' modes* within this thesis to distinguish from the spinning modes which are generally used within the field of duct acoustics as they resemble the modal pattern of a rotating noise source (as the fan, compressor, or turbine).

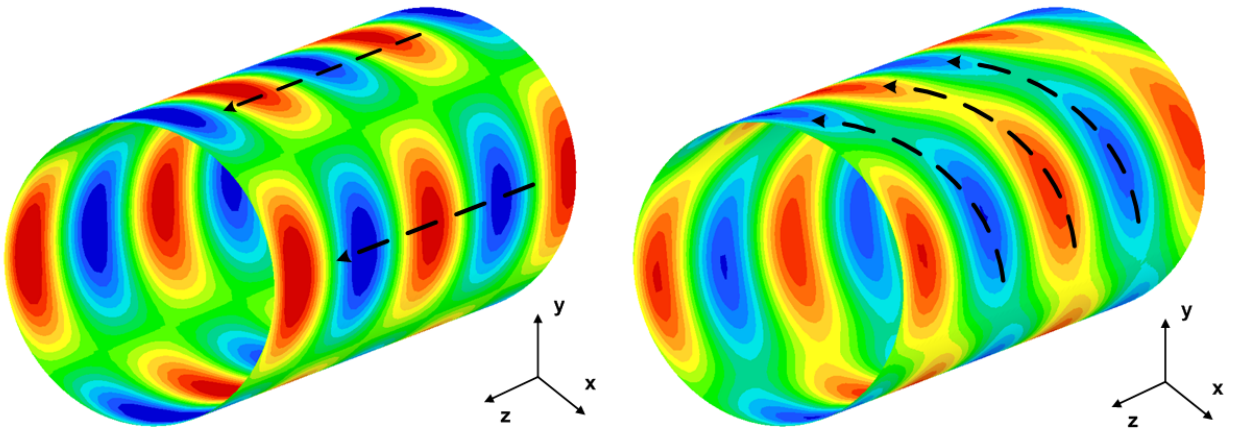

(a) 'non-spinning' mode (2/1) cos (b) spinning mode $(2/1)^+$

Figure 2.5: Comparison of spinning and 'non-spinning' mode pressure distributions

Concerning the 'non-spinning' modes, for each mode (m/n) which does not exhibit a perfect axisymmetry as the fundamental mode $m = 0$ (called an 'azimuthal mode', $m > 0$), two solutions are found mathematically which feature the same geometric shape but are azimuthally shifted against each other. For these basic (geometric) mode shapes, a certain notation will be used throughout this thesis, which relates to their symmetry conditions.

Figure 2.6 illustrates this characteristic exemplarily for the first two azimuthal mode orders. Therein, the symmetry conditions (even/odd) known from mathematical functions

$$\begin{aligned} f(x) &= f(-x) &&: \quad \text{even function} \\ f(x) &= -f(-x) &&: \quad \text{odd function} \end{aligned} \tag{2.31}$$

are used to classify the symmetry conditions of the mode shapes concerning their characteristics with respect to the coordinate axes (in the figure, the symmetry condition is assigned to the normal direction to the symmetry plane). As a result, the designation 'cos' is assigned to modes exhibiting an 'even' symmetry with respect to the y-direction ($\equiv$ xz-plane) - corresponding to the 'even' symmetry condition of the cosine function and vice versa for the sine modes. This classification is illustrated for the two cases of azimuthal modes exhibiting an even or odd number of radial node lines ($m = 2p$ / $m = 2p + 1$).

Spinning modes, as treated above, are nothing but an exponential recombination of these basic (cos/sin) mode shapes, according to Euler's formulas

$$\begin{aligned} e^{+i\varphi} &= \cos(\varphi) + i \cdot \sin(\varphi) \,, \\ e^{-i\varphi} &= \cos(\varphi) - i \cdot \sin(\varphi) \,. \end{aligned} \tag{2.32}$$

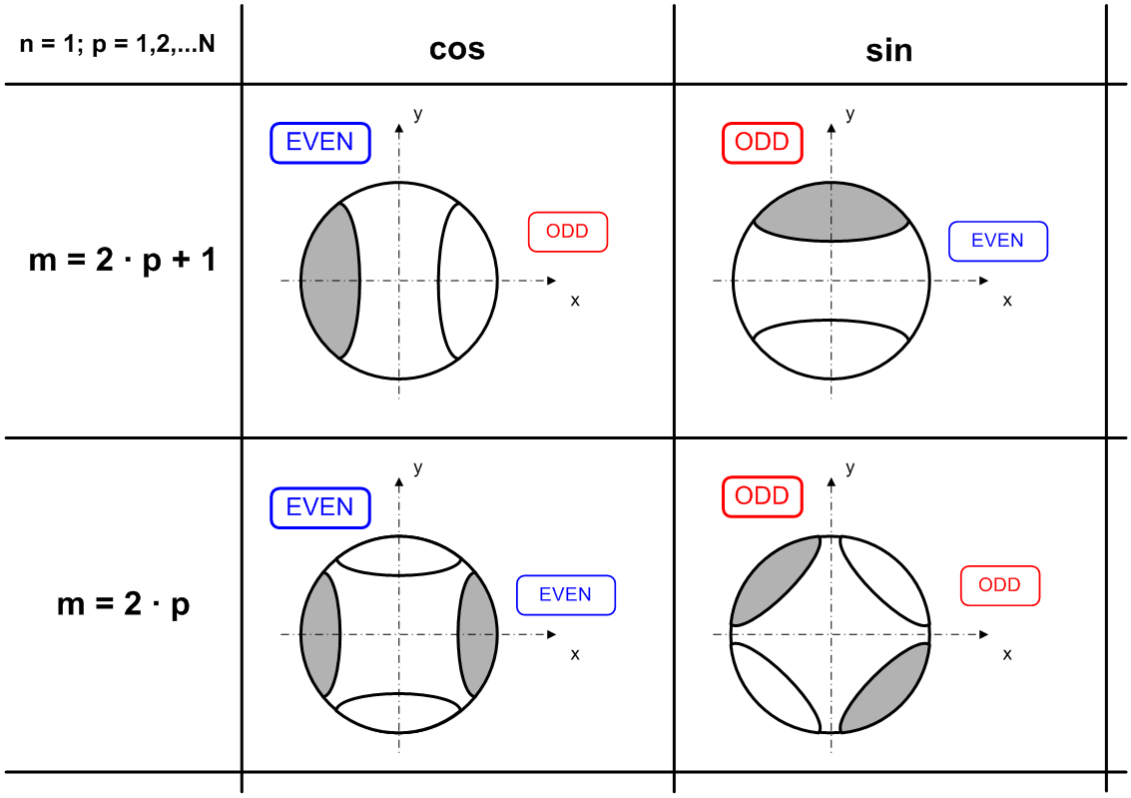

Figure 2.6: Symmetry conditions of basic (geometric) mode shapes

After this excursus into the mode shapes, an alternative, and commonly used, as more compact, formulation of the pressure distribution equation (2.29) shall be presented, which allows also for negative signs for m and $k_{z_{mn}}$, and eliminates the various amplitude coefficients. Accordingly, only the two modal numbers m and n determine the pressure distribution pattern within the duct

$$p(r,\theta,z,t) = A_{mn} \cdot J_m(\kappa_{mn}) \cdot e^{-ik_{z_{mn}}z} \cdot e^{-im\theta} \cdot e^{i\omega t} \ . \tag{2.33}$$

In the general case of a broadband sound field, solutions to the convected wave equation for a circular duct can be described by a superposition of an infinite number of eigenvalue solutions

$$p(r,\theta,z,t) = \sum_{m=-\infty}^{\infty} \sum_{n=1}^{\infty} A \cdot J_m(\kappa_{mn}) \cdot e^{i(\omega t - m\theta - k^{\pm}_{z_{mn}} z)} \ , \tag{2.34}$$

which can be written as well as a matrix equation (neglecting the time dependency $e^{i\omega t}$)

$$\{p\} = [T] \cdot \{A\} \ , \tag{2.35}$$

in which p stands for a vector of pressure values measured at $(1 \cdots N_{mic})$ microphone positions and the vector A contains the individual modal amplitudes participating at the sound field. Therein, the superscripts indicate the positive or negative propagation and spinning directions, respectively, and the elements $A^{\pm\pm}_{mn}$ each stand for the individual vector components

containing all propagating modes

$$\{p\} = \begin{Bmatrix} p_1 \\ p_2 \\ \vdots \\ p_{N_{mic}} \end{Bmatrix} \qquad \{A\} = \begin{Bmatrix} A_{mn}^{++} \\ A_{mn}^{-+} \\ A_{mn}^{+-} \\ A_{mn}^{--} \end{Bmatrix} . \tag{2.36}$$

The transformation matrix T contains the coefficients relating these two quantities to each other, i. e. the axial, radial, and azimuthal components of the individual modes as given in equation (2.34). In this matrix, the individual functions for the N_{mic} microphones are listed in the rows and the modal coefficients for each of the propagating modes in the columns

$$[T] = \begin{bmatrix} T_{mn,z_1}^{++} & T_{mn,z_1}^{-+} & T_{mn,z_1}^{+-} & T_{mn,z_1}^{--} \\ T_{mn,z_2}^{++} & T_{mn,z_2}^{-+} & T_{mn,z_2}^{+-} & T_{mn,z_2}^{--} \\ \vdots & \vdots & \vdots & \vdots \\ T_{mn,z_{N_{mic}}}^{++} & T_{mn,z_{N_{mic}}}^{-+} & T_{mn,z_{N_{mic}}}^{+-} & T_{mn,z_{N_{mic}}}^{--} \end{bmatrix} . \tag{2.37}$$

In turn, the matrix components $T_{mn,z_l}^{\pm\pm}$ are composed in the following way

$$T_{mn,z_l}^{\pm\pm} = J_m(\kappa_{mn}) \cdot e^{\pm i k_{z_{mn}} \cdot z_l} \cdot e^{\pm i m \theta} . \tag{2.38}$$

This description of a general sound field will be of importance later on in chapters 3 and 5, when an unknown input sound field (either obtained from measurements or simulation) will be decomposed into its modal components.

As mentioned above, the *axial wave number* $k_{z_{mn}}$ occurring within the exponents of the solution for the pressure, constitutes one component of the wave number vector pointing into the direction of propagation of the wave fronts. An orthogonal decomposition yields the three components k_r, k_ϑ, and k_z, as is shown in figure 2.7. The magnitude of these components determines the distribution of energy in the respective coordinate direction. For example, a zero wave number component in the axial direction ($k_z = 0$) corresponds to a non-propagating (cut-off) mode.

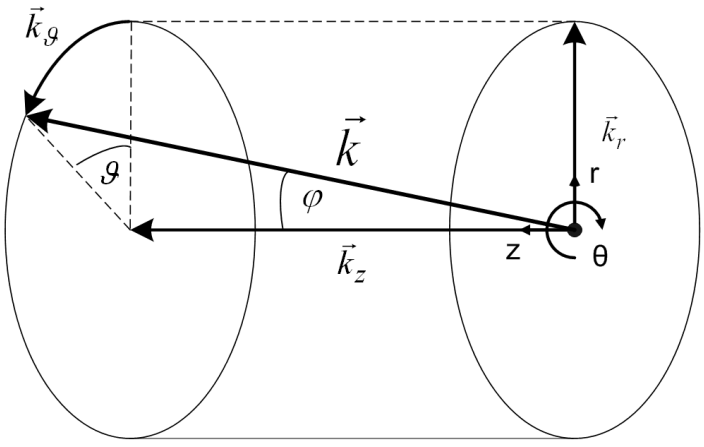

Figure 2.7: Wave number vector components

From the magnitude of the wave number vector, the *Helmholtz number* directly results

$$He = k \cdot R \,, \tag{2.39}$$

which is conveniently used in duct acoustic applications as the dimensionless frequency.

To continue with the inspection of the axial wave number k_z, it can be computed from the eigenvalue κ_{mn} according to Hubbard [1].

$$\boxed{k_{z_{mn}} = \frac{k}{1-M^2}\left[-M \pm \begin{cases} \sqrt{1-(1-M^2)\left(\frac{\kappa_{mn}}{k}\right)^2} \\ i \cdot \sqrt{(1-M^2)\left(\frac{\kappa_{mn}}{k}\right)^2 - 1} \end{cases}\right]} \tag{2.40}$$

Depending on the value of the *cut-off ratio* ξ as introduced by Rice in Ref. [4][4]

$$\xi_{mn} = \frac{kr}{\kappa_{mn}\sqrt{1-M^2}} \,, \tag{2.41}$$

the axial wave number becomes real for $\xi > 1$ (upper case in equation (2.40)) or complex for $\xi < 1$ (lower case in equation (2.40)).

In the first case, $k_{z_{mn}}$ has positive and negative values corresponding to axial waves traveling into the positive and negative z-direction, and the mode is termed *'cut-on'*. Moreover, in most cases, the sign of the root directly corresponds to the direction of propagation in the z-direction. Hence, these values of $k_{z_{mn}}$ are commonly labeled $k^+_{z_{mn}}$ and $k^-_{z_{mn}}$. Only in certain cases for $M > 0$

$$1 < \left(\frac{\kappa_{mn}}{k}\right)^2 < \frac{1}{1-M^2} \,, \tag{2.42}$$

there are two negative values for $k_{z_{mn}}$. However, it can be shown that the positive sign in equation (2.40) still corresponds to a transmission into the positive z-direction, and vice versa (according to Hubbard [1]). The same phenomenon occurs for $M < 0$ yielding two positive values for $k_{z_{mn}}$.

In the second case, where $k_{z_{mn}}$ becomes complex, equation (2.33) becomes

$$p(r,\theta,z,t) = A_{mn} \cdot J_m(\kappa_{mn}) \cdot e^{\pm im\theta} \cdot e^{-iRe(k_z)z} \cdot e^{\pm iIm(k_z)z} \cdot e^{i\omega t} \,, \tag{2.43}$$

in which

$$\begin{aligned} Re(k_z) &= -\frac{Mk}{1-M^2} \,, \\ Im(k_z) &= \frac{k}{1-M^2}\sqrt{(1-M^2)\cdot\left(\frac{\kappa_{mn}}{k}\right)^2 - 1} \,. \end{aligned} \tag{2.44}$$

The corresponding acoustic waves travel as well into the positive and negative directions but are attenuated with distance. As no acoustic power is carried substantially far away from the source and the corresponding sound field is purely reactive, they are referred to as being *'cut-off'*.

[4]Remember that for simplification reasons in this derivation, the duct radius has been chosen to be $r = 1$.

Analogous to the cut-off ratio given in equation (2.41), the *cut-off frequency* f_c is defined as the frequency above which the respective mode begins to propagate

$$f_{c_{mn}} = \frac{f}{\xi_{mn}} = \frac{c}{2\pi}\,\kappa_{mn}\,\sqrt{1-M^2}\;. \tag{2.45}$$

From the axial wave number $k_{z_{mn}}$ other important quantities can be derived, as e. g. the attenuation per length dL (in the axial direction), defined as the change in sound pressure level (SPL) over a specified length Δz. In this context, no end reflections are considered, and the attenuation is calculated separately for each mode

$$dL = 20 \cdot \log \frac{p_2}{p_1} = 20 \cdot \log \frac{p(z+\Delta z)}{p(z)} \qquad \left[\frac{\mathrm{dB}}{\mathrm{m}}\right]\;, \tag{2.46}$$

which can be transformed using a complex notation for the axial wave number k_z

$$dL = 20 \cdot log\left(e^{\beta\cdot\Delta z}\right) \approx 8.686\;\cdot\; Im(k_z)\;\cdot\Delta z \qquad \left[\frac{\mathrm{dB}}{\mathrm{m}}\right]\;. \tag{2.47}$$

This equation directly indicates the dependency of the attenuation per unit length on the magnitude of the imaginary part of the axial wave number.

An alternative method of picturing the physical behavior of an acoustic wave is the concept of the modal *propagation angle*. This concept describes the resulting pressure field as a superposition of plane waves propagating at an angle φ with respect to the duct axis (compare figure 2.7), which is directly related to their cut-off ratio. Figure 2.8 sketches the propagation angle and the direction of propagation (also known as the *phase velocity* $\boldsymbol{v_\varphi}$) normal to the wave fronts (to start, the influence of the flow Mach number should not be regarded).

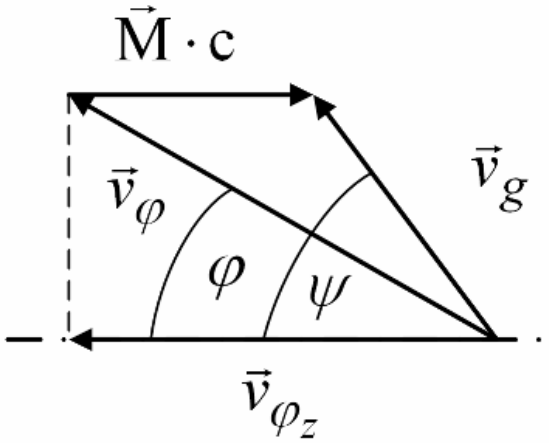

Figure 2.8: Sketch of phase and group velocity and propagation angle

For example, if the cut-off ratio is exactly equal to 1, the propagation angle is 90°, and therefore the wave does not propagate into the axial direction but stays within the same axial position. With an increasing cut-off ratio, the angle φ becomes smaller, and the wave begins to travel into the axial direction (compare Rice and Heidmann [5]).

The propagation angle φ can thus be computed by the following simple relation

$$\varphi = \cos^{-1}\left(\frac{k_{z_{mn}}}{k}\right)\;. \tag{2.48}$$

However, in the presence of a uniform mean flow, the propagation angle is shifted by the vector addition of the phase velocity vector and the flow vector, as depicted in figure 2.8.

This yields the so-called *group velocity* $\boldsymbol{v_g}$ which corresponds to the effective acoustic power flux at an angle ψ with respect to the axis.

This group velocity angle can also be computed directly from the axial wave number

$$\psi = \cos^{-1}\left(\frac{k_{z_{mn}}}{k\left(1 - M\frac{k_{z_{mn}}}{k}\right)}\right) . \tag{2.49}$$

For a closing remark to this section, it should be mentioned that above described modal solutions are up to this point only physically possible solutions within the duct. Whether they are actually present, depends on the nature of the source and the boundary conditions at the termination of the duct. In contrast to the idealized case of an infinite duct, in which waves travel only into one direction without interference, the terminations in finite length ducts introduce reflections which lead to waves traveling into both directions.

2.1.1.3 Influences of a uniform mean flow

To provide an insight into the effect of a superimposed uniform flow on the the cut-off frequency f_c and the axial wave number k_z, the following plots give examples of the results obtained for a hardwalled circular duct as functions of the flow Mach number. In this case, radial modes of the axisymmetric mode $m = 0$ at $f = 2000$ Hz have been chosen, as it yields the largest number of propagating radial modes.

Figure 2.9 shows the variation of the cut-off frequencies with the flow Mach number (in the range $-0.5 \leq M \leq +0.5$) for the first 4 radial mode orders ($n = 1 \cdots 4$). With respect to the coordinate system defined in figure 2.2, the negative sign of the Mach number corresponds to a propagation of a positively traveling sound wave against the direction of the flow, as would be the case in an engine inlet, and the positive sign to a propagation in the direction of the flow, as in an exhaust or bypass duct application. With respect to the geometric parameters, the radius of the duct model used in the numerical study in chapters 4 and 5 has been used, which corresponds to $r = 0.25$ m.

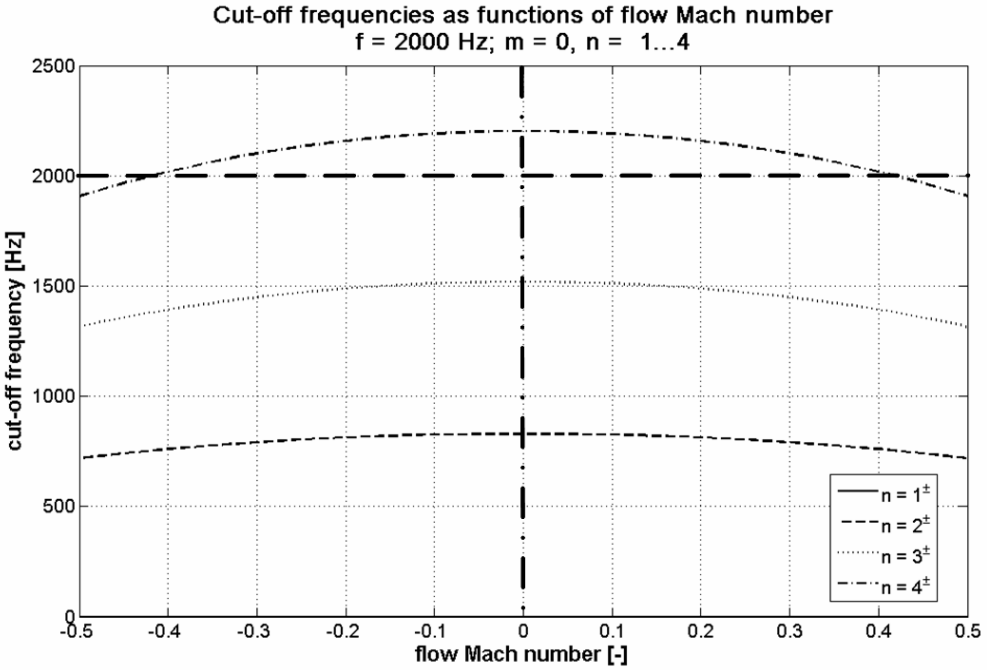

Figure 2.9: Cut-off frequencies as functions of flow Mach number; 2000 Hz; $m = 0$

The curves exhibit a maximum at the zero flow condition ($M = 0$) and decrease parabolically and symmetrically with increasing magnitude of the flow Mach number (as can be inferred also from equation (2.45)). Whereas the cut-off frequencies of the first three radial mode orders are well below the excitation frequency of $f = 2000$ Hz, mode (0/4) is cut-off in the zero flow case (its cut-off frequency yields $f_{c_{(0/4)\,|\,M=0.0}} = 2202$ Hz).[5] However, with increasing magnitude of the Mach number, f_c decreases, and at approximately $M = \pm 0.4$ the cut-off limit is reached. Accordingly, with higher negative Mach numbers, a wave starts to propagate into the positive axial direction.

This behavior can be understood when considering the convective effect of the flow on the propagating acoustic waves. Additionally, as indicated in figure 2.10, the wavelength of the waves traveling opposed to the flow direction (the positively traveling ones) decreases with an increasing negative Mach number, and increases for the negatively traveling waves propagating in direction of the flow.

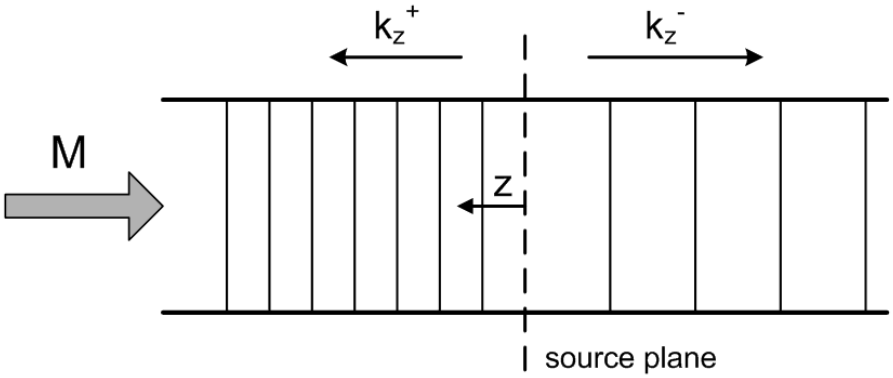

Figure 2.10: Schematic sketch of influence of flow velocity on axial acoustic wavelength

This causes a frequency shift known as the *Doppler effect*, and also influences the axial wave number. In general, it corresponds to larger wave numbers for a propagation against the flow (i. e. more wavelengths per unit length, or alternatively, an increased effective frequency), and smaller wave numbers in the direction of the flow.

In the following, this effect on the axial wave number will be studied on the basis of the example presented above. However, in contrast to the zero flow case, in which the wave number was purely real (corresponding to propagating waves) or imaginary (cut-off modes) (compare equation 2.40), in the presence of flow, it becomes a true complex value. Accordingly, the trajectories of the individual modes as functions of the flow Mach number will be studied in the complex plane.

Figure 2.11 presents the corresponding plot for the first radial modes of the azimuthal order $m = 0$. Two types of trajectories can be found within the figure: the ones whose axial wave numbers are consistently located on the real axis (purely real axial wave numbers), and the ones which move in the complex plane (as for $n = \pm 4$). The former ones correspond to the modes which are cut-on at all Mach numbers (i. e. $n = 1 \cdots 3$). Their axial wave number magnitude increases with an increasing positive (for the positively traveling waves) or negative (negative propagation direction) Mach number due to the convective effect of the flow, as indicated by the arrows on the horizontal axis.

[5] The zeroth radial mode (0/1) constitutes the special case of a constant cut-off frequency (identical to zero) since the plane wave mode is always propagative.

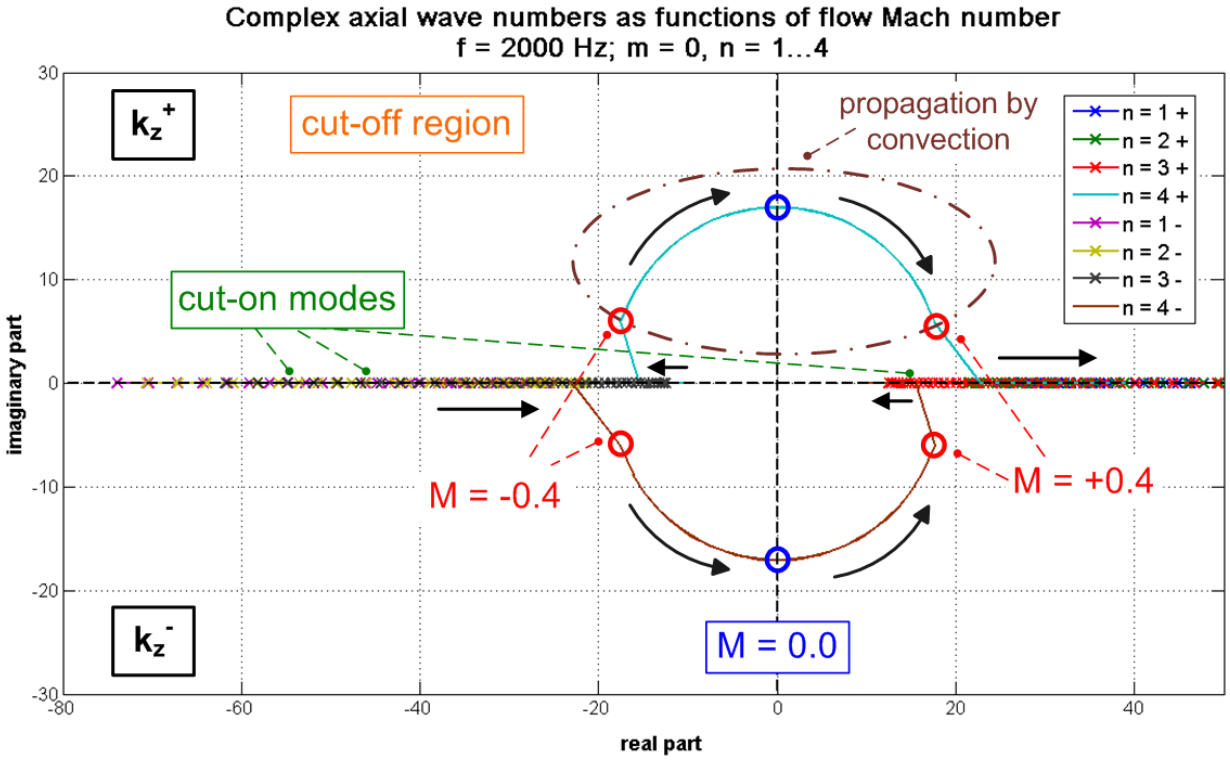

Figure 2.11: Axial wave number in the complex plane as a function of flow Mach number; 2000 Hz; $m = 0$

The other two curves represent the characteristics of the modes $n = \pm 4$ which have been discussed above, and are cut-off for most of the flow velocities. These cut-off regions are the ones in the complex plane with an imaginary part $Im(k_z) \neq 0$. In comparison of the two propagation directions (k_z^+ and k_z^-), the positive axial wave numbers yield a positive sign of the imaginary part, and opposite for the negative wave numbers. Apart from this, they might propagate into both directions depending on the superposition of the axial acoustic wave number and the flow speed (compare again figure 2.8).

At zero flow, the axial wave numbers of mode (0/4) are purely imaginary (compare e. g. the duct acoustics chapter in Rienstra and Hirschberg [6]). With increasing flow speeds, the solutions move into the complex plane, i. e. they are convected by the flow as indicated exemplarily for the positive axial wave numbers, but are still cut-off. However, at $M = \pm 0.4$ where the cut-off limit is reached, the trajectories move to the real axis to yield propagating waves into the respective directions, corresponding to the change from the second to the first solution in equation (2.40). As for the other modes which are cut-on at all flow speeds, the magnitude of the real part of the axial wave number then increases or decreases depending on the direction of propagation relative to the flow direction.

2.1.1.4 Application to acoustically treated duct

In a duct in which the walls have been treated ('lined') with a sound absorbing material, different boundary conditions have to be applied at the duct wall than in the hardwall case. Here, the radial pressure gradient is not equal to zero (as in the first condition of equation (2.24)), but related to the complex impedance (or admittance) of the lining material, as will be shown in the following.

This *acoustic impedance* Z of the material is a purely mathematical construct which is commonly used to describe the acoustic properties of a material. It is defined by the ratio of the sound pressure to the normal sound particle velocity

$$Z = \frac{p}{v_n} \, . \tag{2.50}$$

However, it can only be assumed to be a fixed value at a given frequency under the assumptions that the material is locally reacting,[6] responds linearly, and is insensitive to a grazing flow. Several issues arising with respect to an accurate impedance eduction are thus mentioned in a paper by Parrott, Jones, and Watson [7].

The reciprocal value of the impedance, which is also frequently used for the description of the acoustic properties of a material or medium, is the *acoustic admittance* A_a

$$A_a = \frac{1}{Z} \, . \tag{2.51}$$

Both values A_a and Z are, in general, complex numbers. The acoustic impedance is composed of the resistance R and reactance X, and the admittance of the conductance G and the susceptance B

$$\begin{aligned} Z &= R + i \cdot X \, , \\ A_a &= G + i \cdot B \, . \end{aligned} \tag{2.52}$$

As mentioned above, in the case of an acoustically lined duct, the normal velocities of the fluid at the duct wall and the duct wall itself have to be identical. They are, in both cases, equal to the derivative of the local particle displacement δ, which can be defined in these cases as a time-harmonic function

$$\delta = \delta_0 \cdot e^{i\omega t} \, . \tag{2.53}$$

So, for the duct wall, the normal velocity component yields

$$v_w = \frac{\partial \delta}{\partial t} = i\omega\delta \, , \tag{2.54}$$

whereas for the fluid, the substantial derivative (compare equation (2.8)) has to be taken to account for the convection effect of the flow

$$v_f = \left(\frac{\partial}{\partial t} + M \cdot \frac{\partial}{\partial z} \right) \delta = \left(i\omega + M \cdot \frac{\partial}{\partial z} \right) \delta \, . \tag{2.55}$$

Inserting the expression for δ from equation (2.54) yields

$$v_f = \left(1 - i \, \frac{M}{\omega} \cdot \frac{\partial}{\partial z} \right) v_w \, , \tag{2.56}$$

[6] In most application cases, a so-called 'locally reacting liner' will be utilized, which ensures that the incident sound wave can only propagate normal to the duct wall within the lining material. This can be achieved e. g. by partitioning of the cavity. Detailed information on this subject will be presented in chapter 2.3.

and finally, in combination with equations (2.50) and (2.51)

$$v_f = A_a \cdot \left(1 - i\,\frac{M}{\omega} \cdot \frac{\partial}{\partial z}\right) p\ . \tag{2.57}$$

In application to a circular duct, where the normal velocity component to the duct wall equals the radial one (i. e. $v_f = v_w = v_r$), this results can be inserted into the radial component of the momentum equation (2.2)

$$\frac{\partial p}{\partial r} = -\left(\frac{\partial}{\partial t} + M \cdot \frac{\partial}{\partial z}\right) v_r = -i\omega A_a \cdot \left(1 - i\,\frac{M}{\omega} \cdot \frac{\partial}{\partial z}\right)^2 p\ . \tag{2.58}$$

Using the expression for the axial pressure variation

$$\frac{\partial p}{\partial z} = -ik_z p\ , \tag{2.59}$$

equation (2.58) becomes

$$\frac{\partial p}{\partial r} = -i\omega A_a \cdot \left(1 - \frac{M}{\omega} k_z\right)^2 p\ . \tag{2.60}$$

This equation thus constitutes the first boundary condition, the second being again the finiteness of the solution at the duct center line.

At first, the simplified no flow case ($M = 0$) will be examined which leads to the following set of boundary conditions

$$\frac{\partial p}{\partial r}_{|M=0,\,r=1} \stackrel{!}{=} -i\omega A_a p\ ; \qquad p_{|M=0,\,r=0} \stackrel{!}{=} \text{finite}\ . \tag{2.61}$$

Accordingly, this yields in combination with the conditional equation for the radial sound pressure distribution given by equation (2.25), and the recursion formula for the Bessel function in equation (2.27), the eigenvalue equation for a lined duct without flow (in accordance with Hubbard [1]).

$$\boxed{\kappa_{mn} \frac{J_{m-1}(\kappa_{mn})}{J_m(\kappa_{mn})} - m = -i\omega A_a} \tag{2.62}$$

In contrast to the hardwall case discussed in the previous section, the eigenvalues are not anymore determined solely by the geometry of the duct, but also (of course additional to the complex admittance A_a) dependent on the angular velocity ω (or wave number k)

$$\kappa_{mn} = f(m, r, A_a, k)\ . \tag{2.63}$$

Thus, on the one hand, the eigenvalues have to be recomputed for each frequency. On the other hand, the solution to this transcendental equation cannot be easily found in all cases, and has to be solved possibly iteratively or numerically. More information about the various efforts to solve this equation (and the one including a uniform flow to be presented in the following) can be found in chapter 2.4.

In the case of a uniform flow of Mach number M, the eigenvalue condition becomes even more difficult to solve because of the additional factor on the right hand side in equation (2.60). As before, the recursion formula has been used to obtain the eigenvalue equation for a lined duct including a mean uniform flow

$$\kappa_{mn} \frac{J_{m-1}(\kappa_{mn})}{J_m(\kappa_{mn})} - m = -i\omega A_a \cdot \left(1 - \frac{M}{\omega} k_{z_{mn}}\right)^2\ . \tag{2.64}$$

In combination with equation (2.40) defining the axial wave number $k_{z_{mn}}$ (considered here only the upper part corresponding to cut-on modes), quite a complex equation results for the determination of the eigenvalues (Hubbard [1]).[7]

$$\kappa \frac{J_{m-1}(\kappa)}{J_m(\kappa)} - m = -i\omega A_a \cdot \left(1 - \frac{M}{\omega} \cdot \frac{k}{1-M^2} \cdot \left[-M \pm \sqrt{1-(1-M^2)\left(\frac{\kappa}{k}\right)^2}\right]\right)^2 \tag{2.65}$$

The eigenvalues κ_{mn} thereof are dependent (apart from the admittance of the lining and the geometric quantities r and m) on the wave number k and the Mach number M

$$\kappa_{mn} = f(m, r, A_a, k, M) \; . \tag{2.66}$$

As for the hardwalled duct, where the effect of the Mach number on the axial wave number has been analyzed, similar trends shall be observed concerning a variation of the acoustic impedance. Therefore, consecutively, the resistance and reactance of the acoustic lining will be varied keeping the respective other parameter fixed. Accordingly, plots of the eigenvalues and axial wave numbers (which have been shown above to be functions of the complex admittance A_a - compare equation (2.62)) will be presented in the complex plane.

At first, the resistance value will be kept fixed at $R = 500 \cdot \rho c$, a very high value which comes close to hardwall conditions.[8] In contrast, the reactance value has been varied in a wide range (from $-1000 \cdot \rho c$ to $+1000 \cdot \rho c$). Figure 2.12 presents the corresponding eigenvalue plot.

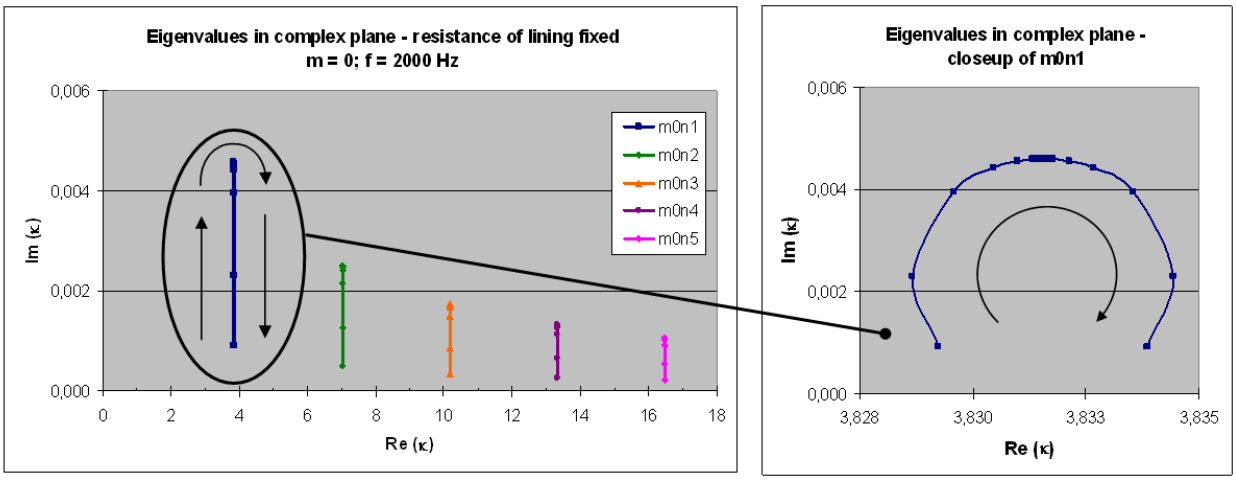

Figure 2.12: Eigenvalues in complex plane - variation of lining reactance; 2000 Hz; $m = 0$

The left hand side gives an overview of what appear to be vertical lines for the first five radial modes of the azimuthal order $m = 0$. They are located approximately at the axial positions of the hardwall eigenvalues ($\kappa = 3.8, 7.0, 10.2, 13.3, 16.5$). The closeup of the fundamental mode on the right hand side reveals the true shape of its trajectory in the complex plane. To define the sense of the curve, the arrows indicate the results for the parameters ranging

[7] In this expression, the indices m, n to the eigenvalues and the axial wave number have been omitted for reasons of clearness.

[8] This value has been chosen since the eigenvalue equation for lined ducts (equation (2.62)) is not easily solvable by analytical means, as will be explained in detail in chapter 2.4. However, keeping one of the two parameters of the complex impedance/ admittance at an almost hardwall value, the numerical problems can be circumvented.

from negative to positive (near) hardwall values. However, considering the scale of the plots, it becomes obvious that the variations take place at a very low level - with respect to both the variations in the real and the imaginary part. These tendencies are, as well, in line with the observations described in Rienstra and Hirschberg [6].

Correspondingly for the variation of the lining resistance depicted in figure 2.13. In this case, the reactance has been kept fixed at $X = -200 \cdot \rho c$, which represents the properties of a sound absorbing material in the notation used within this thesis. Again, the variation of the resistance has been performed over the complete range from $-1000 \cdot \rho c$ to $+1000 \cdot \rho c$, even if, in a real application, only positive values of R are meaningful.

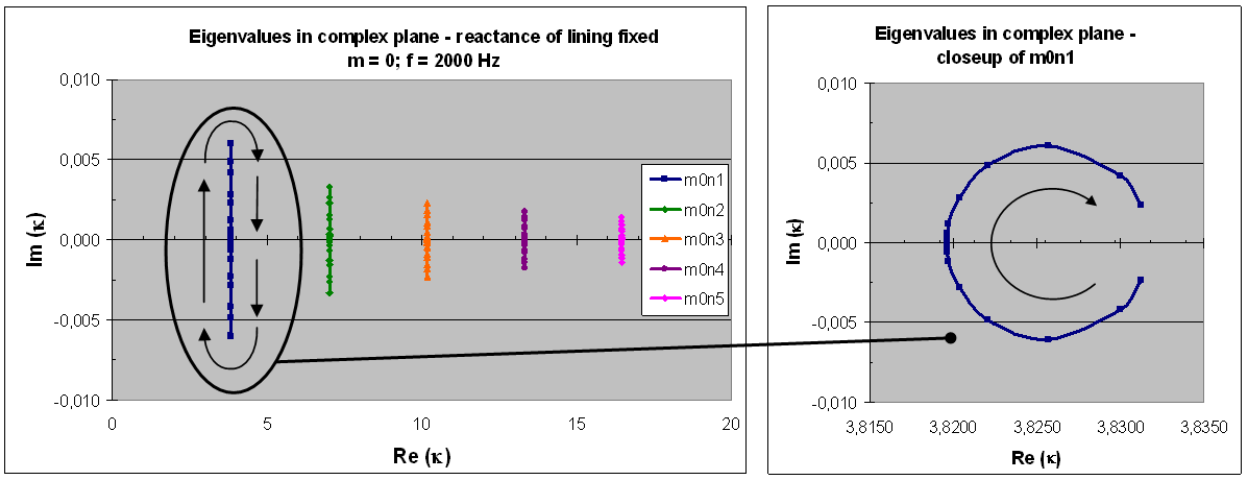

Figure 2.13: Eigenvalues in complex plane - variation of lining resistance; 2000 Hz; $m = 0$

As in the analysis above, the results for the several radial modes seem to yield lines in the complex plane in the vicinity of the hardwall solutions. At a closer look, they also exhibit the circular shape, however, rotated by 90° with respect to the previous results.

To conclude, the corresponding effects upon the axial wave number in the complex plane are summarized schematically in figure 2.14. It opposes the results of the variations of both components of the acoustic impedance (R, X), and shows the different effects for cut-on (located on the real axis in the hardwall case) as well as cut-off modes (found on the imaginary axis).

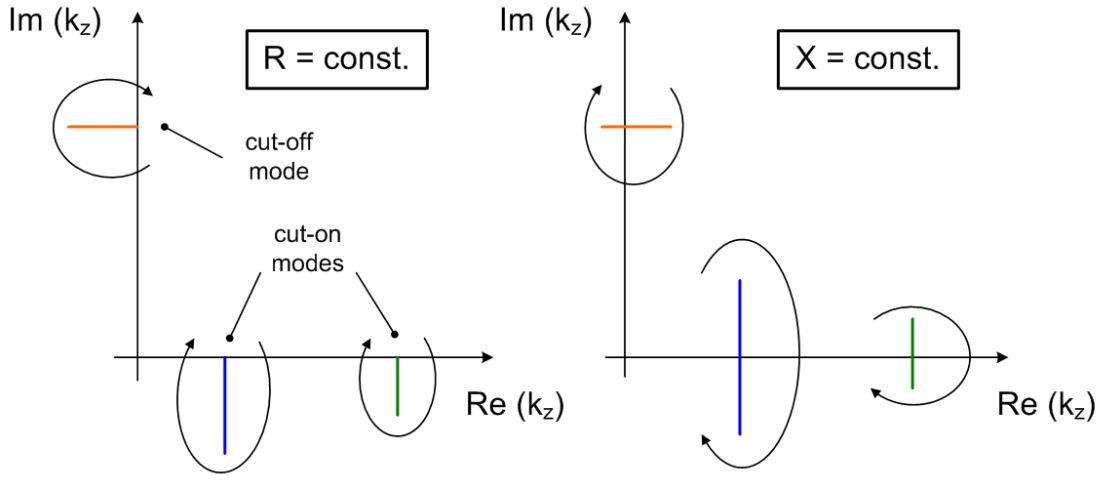

Figure 2.14: Comparison of axial wave number variations in complex plane; 2000 Hz; $m = 0$

They correspond to the observations for the eigenvalues described above, and point out once again, as mentioned during the analysis of the flow effects in the previous section, that in applications involving acoustic linings and/or a flow, the simple criterion that a real part of the axial wave number equal to zero corresponds to a cut-off mode, and a real part different from zero corresponds to a propagating mode (obtained from the analysis of hardwalled ducts) does not maintain validity in the general case. In contrast, the axial wave numbers move in the complex plane, and both the real and the imaginary part have to be considered to judge whether the mode might be cut-on or cut-off. Compared to the hardwall case, also the eigenvalues become complex in the lined duct case, as can be expected considering equation (2.62).

2.1.2 Influence of reflections and diffraction at the duct termination

Subject of this second part of the theory section will be the effects of the duct termination on the sound field. They include reflections back into the duct and diffraction effects related to the wavelength-to-diameter ratio.

As mentioned above, at any duct discontinuity, which might be a change in the acoustic boundary condition, an expansion or constriction of the duct diameter, or simply the termination of the duct open to the free space, a part of the acoustic waves is reflected which changes the energy within the propagating field as well as its modal composition.

Accordingly, the modal *reflection coefficient*, which is a measure for the amount of reflections from a duct discontinuity, can be calculated from the amplitudes of the incident and the reflected waves

$$r_{mn} = \frac{A^-_{mn}}{A^+_{mn}} \,. \tag{2.67}$$

These reflections cause standing wave patterns of a periodicity $\lambda/2$ with stationary minima (nodes) and maxima (antinodes). Depending on the properties of the discontinuity, this superposition of the incident and reflected waves exhibits different characteristics as depicted in figure 2.15 for the two idealized limits of the reflection coefficient at the example of a sound wave incident upon a wall.

The upper sketch represents the so-called *hardwall* boundary condition in which the wall is perfectly rigid, yielding a total reflectance and a reflection coefficient $r_{mn} = +1$. Directly at the wall, the sound pressure amplitude reaches twice the value of the incident wave ($p = 2 \cdot p_1$) and the normal sound particle velocity is reduced to zero ($v_n = 0$). The first maximum of the sound particle velocity is found at a quarter wavelength ($\lambda/4$) distance from the wall, where the sound pressure, in return, reaches a node. This pattern recurs with the periodicity $\lambda/2$ yielding a stationary pattern in the open half space.

Exactly reversed for the *softwall* boundary condition which models a perfectly compliant wall:[9] in this case, the sound pressure has a node directly at the wall, where the normal sound particle velocity reaches a maximum. This corresponds to a reflection coefficient $r_{mn} = -1$ and a phase reversal of the pressure.

In between these two limits, the reflection coefficient takes all possible values in practical applications. They correspond to a reflection not directly at the wall but at a certain distance inside the material (or the second medium). This causes an amplitude reduction and a shift of the sound pressure and sound particle velocity nodes from the two distinct locations at $x = 0$ or $x = \lambda/4$.

[9] This condition can be found e. g. at the boundary of liquids to air.

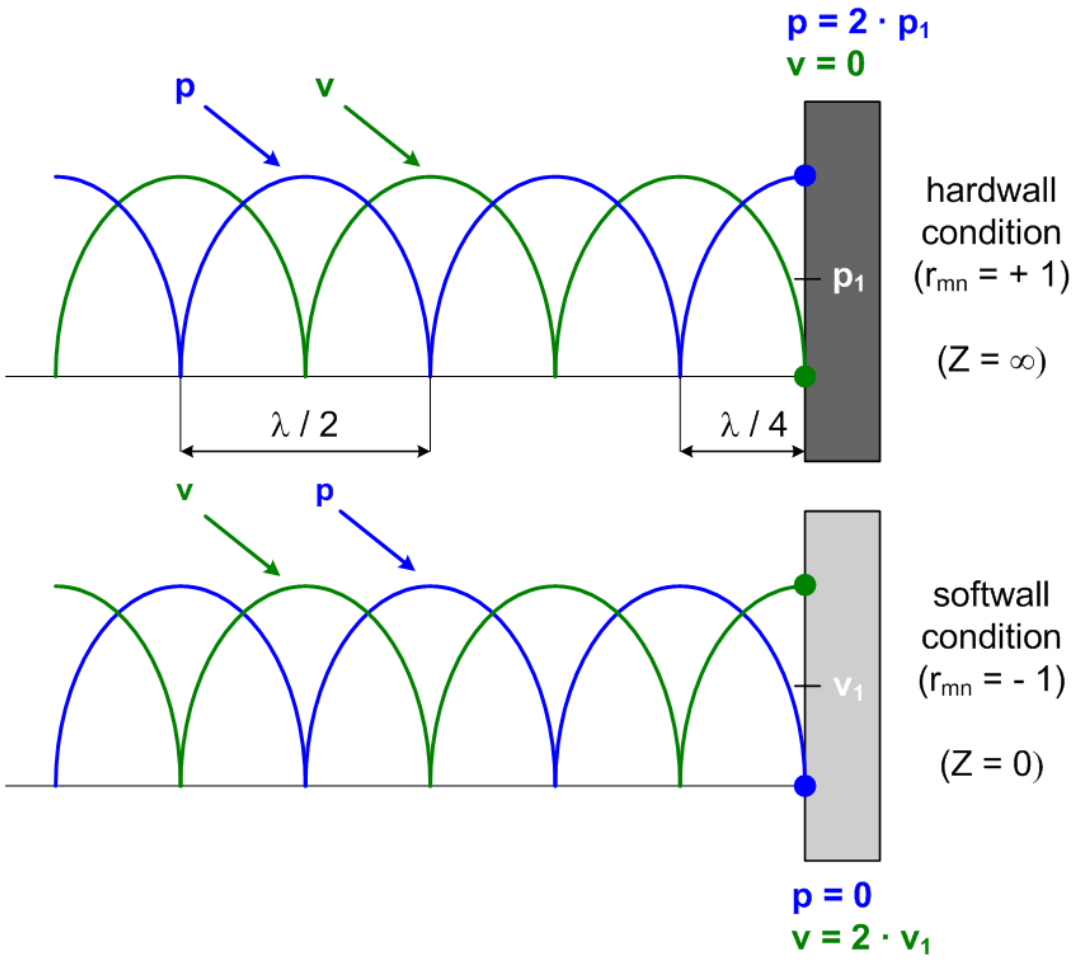

Figure 2.15: Standing wave patterns for the two limiting wall boundary conditions

A third special case concerning the impedance of a material is the *reflection-free* condition which is desired e. g. in numerical studies or test rigs to create an *anechoic termination* avoiding reflections from the opening or the end plate. It can be achieved, at least for the plane wave mode, by assignment of the characteristic impedance of the medium Z_0 to the corresponding geometry

$$Z_0 = \rho_0 \, c_0 \; . \tag{2.68}$$

Impedance values are, in practice, often normalized with respect to this characteristic impedance to yield specific values

$$\zeta = \frac{Z}{\rho_0 \cdot c_0} \; . \tag{2.69}$$

From measurements, the maximum and minimum sound pressure values of the resulting standing wave pattern can be determined, and combined to the *standing wave ratio (SWR)*

$$SWR = \frac{p_{max}}{p_{min}} = \frac{p^+ + p^-}{p^+ - p^-} \; , \tag{2.70}$$

in which p^+ and p^- stand for the sound pressure amplitude of the incident and reflected wave,

respectively. The SWR can be then related to the reflection coefficient (compare Veit [8])

$$r_{mn} = \frac{SWR - 1}{SWR + 1} \,. \tag{2.71}$$

This measurement method is used in the *Kundt's tube* or *impedance tube*, a circular tube in which an incident plane wave excited at the one end impinges on a material sample at the other end. From the measurement of the complex sound pressure at two locations, the SWR, and hence the reflection coefficient, can be determined, which is related to the *absorption coefficient* α

$$\alpha_{mn} = 1 - r_{mn} \tag{2.72}$$

and the specific acoustic impedance of the material

$$r_{mn} = \frac{\zeta - 1}{\zeta + 1} \,. \tag{2.73}$$

According to equation (2.67), a reflection coefficient can be computed separately for each contributing mode. However, at these discontinuities, the acoustic modes are not decoupled, and hence, the notation has to be extended to account for effects between the individual mode orders. This procedure is well-known as the *Wiener-Hopf technique* coupling the incident mode(s) on the one side of the discontinuity with all propagating modes on the other side and has been described in detail by Weinstein [9].

In the conventional case of an axisymmetric duct and acoustic boundary conditions, a coupling between azimuthal modes can be excluded. Thus, coupling will only occur between radial modes of the same azimuthal mode order m. Correspondingly, a third letter is added to the notation of the reflection coefficient: r_{mnl}. The first two correspond to the azimuthal and radial mode order of the incident (excited) mode, and the last one to the radial order of the reflected one (following the notation introduced by Zorumski [10]).

Depending on the respective numbers of the incident and reflected radial mode orders, the reflection coefficients r_{mnl} will be named in the following:

- $n = l$: direct reflection coefficient,
- $n \neq l$: coupling reflection coefficient.

Additionally, the sum of all single reflection coefficients of an incident mode (i. e. the sum of the direct and all coupling reflection coefficients) will be referred to as the *total reflection coefficient* r_{mnt}.

As has been reported e. g. by Felsen and Yee [11], the direct reflection coefficient at the cut-off frequency of a radial mode yields in idealized conditions the value of unity (equivalent to a total reflectance), and decreases with increasing frequency (increasing cut-off ratio). However, at the cut-on frequencies of the higher order radial modes, the direct reflection coefficient experiences a kink, leading to increased reflection levels, which can also be observed in the characteristic of the total reflection coefficient. After having passed the cut-on frequency, the levels decrease again up to the next radial mode cut-on frequency.

Additionally, the coupling coefficients become non-negligible in the presence of additional propagative radial modes. An example of this is shown in figure 2.16 for the zeroth azimuthal mode ($m = 0$) and the first two radial mode orders (at a duct radius of $R = 0.25$ m).

As can be seen, the direct reflection coefficient r_{011} (blue curve) of the zeroth radial mode (0/1) decreases continuously up to the cut-on frequency of mode (0/2) at $f = 830$ Hz.

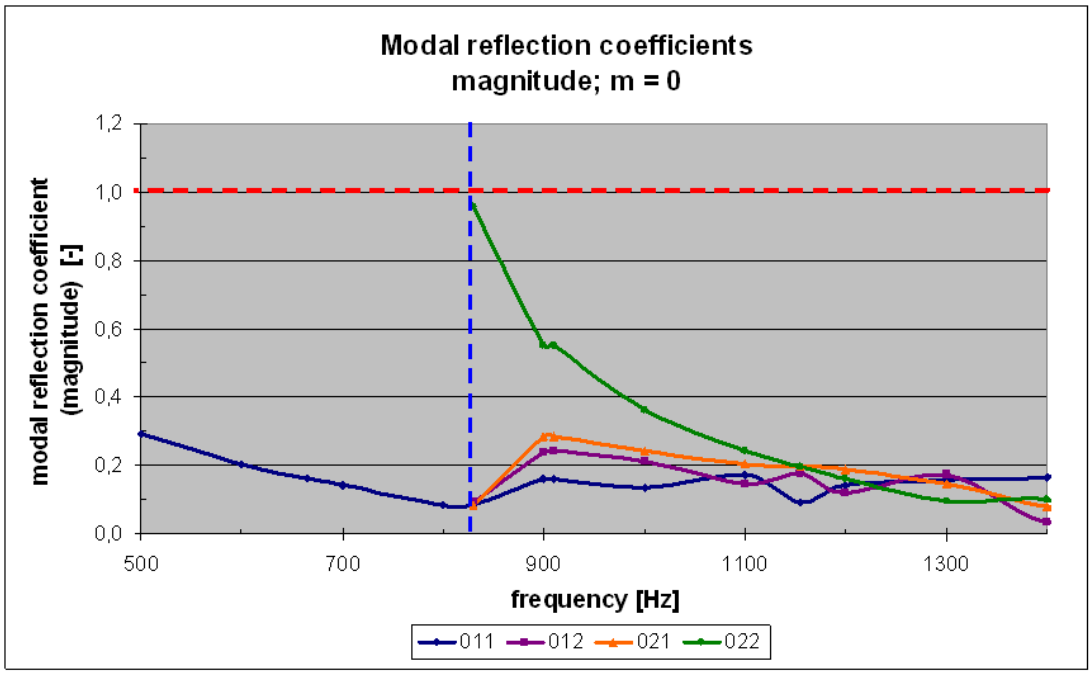

Figure 2.16: Reflection coefficients (magnitude) for circular duct ; R = 0.25 m, m = 0

From this point on, additional to the direct reflection coefficient of this first radial mode (r_{022}, green curve), decreasing from 1.0 at the cut-on frequency, the coupling coefficients r_{012} and r_{021} can be observed at approximately the same level as the direct reflection coefficient r_{011}. This corresponds to an equally distributed energy between both radial modes ($n = 1, 2$) for the excitation of the lower order one. With increasing frequency, the level of the coupling coefficient r_{012} stays even above the direct reflection coefficient, before it decreases considerably starting at approximately 1300 Hz.

Similar observations have been reported by Zorumski (compare above) for circular and annular ducts with arbitrary wall admittances terminating in an infinite baffle.[10] He also mentioned that the matrix of coupling coefficients is not symmetric but tends to convert lower radial mode orders into higher ones (in the above example, this would correspond to $r_{012} > r_{021}$).

A coupling of modes for rectangular ducts has been observed by Muehleisen [12] for step discontinuities, junctions, and duct terminations in an infinite baffle. He also reports coupling coefficients larger than unity, which might seem physically incorrect at first, but are related to the different energy levels of the affected modes.

As could be seen above, the reflection coefficient of a mode close to its cut-on frequency is close to 1 corresponding to a total reflectance. This is also valid in the long wavelength region, where only the fundamental mode (the plane wave (0/1)) can propagate within the duct. Under these conditions, the velocity distribution across the duct can be assumed constant, and the air in the opening acts like a plane piston. Depending on the frequency of excitation, it radiates sound into the open space and reflects some back into the duct.

At very low frequencies, at which the wavelength is much longer than the duct diameter, zero energy is being radiated from the duct and strong standing wave patterns are built up inside the duct. However, with increasing frequency, more and more energy is being radiated, and the reflection coefficient decreases accordingly. As well, the directivity (defined as the dependency of the pressure amplitude on the azimuthal angle) changes with frequency

[10] A baffle is an infinite plane enclosing the duct termination, which permits radiation only into the forward half space.

according to the equations given by Morse and Ingard in Ref. [3] derived from the original investigations by Lord Rayleigh in 1896 in Ref. [13].

The sound pressure at a distance r caused by a plane circular piston of radius a baffled in a rigid, infinite plane can thus be computed by the approximate equation

$$p\left(r\right) \simeq -ik\rho c \cdot \frac{e^{ikr}}{4\pi r} \cdot 2u\pi a^2 \left[\frac{2J_1(ka\sin(\theta))}{ka\sin(\theta)}\right] , \tag{2.74}$$

in which θ stands for the azimuthal angle and u for the velocity amplitude of the piston. An example of the corresponding directivity of radiation (at a distance $r = 10 \cdot a$) is given in figure 2.17 for three frequencies equivalent to $\lambda = 5 \cdot a$, $\lambda = 2 \cdot a$, and $\lambda = a$ for a piston of radius $a = 0.1$ m and a velocity amplitude of $u = 0.01$ m/s.

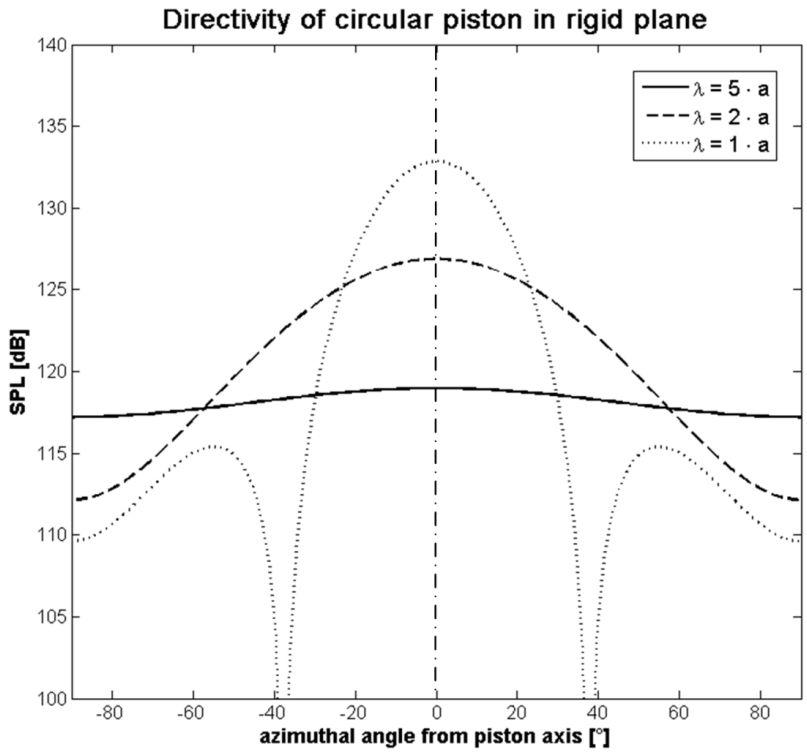

Figure 2.17: Radiation from plane circular piston of radius a baffled in rigid plane

As obvious from the figure, the directivity is very uniform at the longest wavelength ($\lambda = 5a$), and becomes more and more directional with increasing frequency ($\lambda = 2a$). At even higher frequencies, secondary maxima can be found (compare curve for $\lambda = a$), which stem from interferences between the directly radiated pressure field of the piston and reflections from the baffle plane. However, these secondary peaks range at a considerably lower pressure level, in the example almost 20 dB below the primary peak. These diffraction effects are exactly analogous to the ones observed in physical optics, e. g. the diffraction of a beam of light at a slit. However, because of the considerably longer wavelengths in acoustics, diffraction becomes much more important in this field of physics.

Similar effects can be observed for higher order modes, and will be of relevance in the analysis of the results in chapters 4 and 5. Since the waves propagate at an angle φ with respect to the axis, the axial component λ_z of the wavelength λ (or equivalently the axial wave number k_z) has to be considered when estimating diffraction effects.

2.1.3 Radiation to the far field

After these comments on the reflection and diffraction effects at the duct opening, the radiation to an observer will be treated in the last part of this section. Therefore, basic relationships between the radiated sound pressure and sound particle velocity will be analyzed, leading to a definition of the 'far field', i. e. the region a certain distance away from the source exhibiting particular properties.

The most elementary source of sound is a pulsating sphere as shown in figure 2.18. Its radius fluctuates harmonically around the mean radius a. Therefore the radiated sound field is uniform and exhibits no distinct directivity. In general, if the mean radius a is small compared to the wavelength ($a \ll \lambda$), the dimensions of this 'monopole source' can be reduced and idealized to a point.

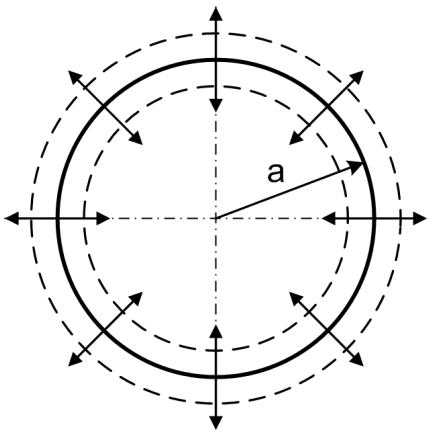

Figure 2.18: Sketch of a spherical wave source (monopole)

The monopole source, which corresponds to a harmonic mass flow, emits the sound pressure

$$p\,(r) = A \cdot \frac{e^{-ikr}}{r}\ , \tag{2.75}$$

which depends only on the distance r from the source. The corresponding sound particle velocity v is the derivative of the sound pressure with respect to the radial direction divided by a factor

$$v(r) = \frac{\frac{dp(r)}{dr}}{-i\rho\omega}\ . \tag{2.76}$$

An example of the relative trends for $p(r)$ and $v(r)$ is given in figure 2.19 for standard atmosphere conditions and a wave number of $k = 100$. It shows a snapshot of the acoustic parameters with respect to the distance from the source.

As can be seen, the sound pressure (blue curve) and particle velocity (green curve) are out-of-phase by nearly 90° in the vicinity of the source and nearly in-phase at larger distances from the source. This latter characteristic corresponds to the definition of the 'far field' for this simple source, which starts approximately at the distance of one wavelength from the source center (as indicated in the figure).

However, in duct acoustic applications, the far field definition is normally related to the diameter of the duct, which determines its diffraction effects. Thus, dependent on the literature, values of $r = 5 \cdot D$ or $r = 10 \cdot D$ are used to define the far field limit.

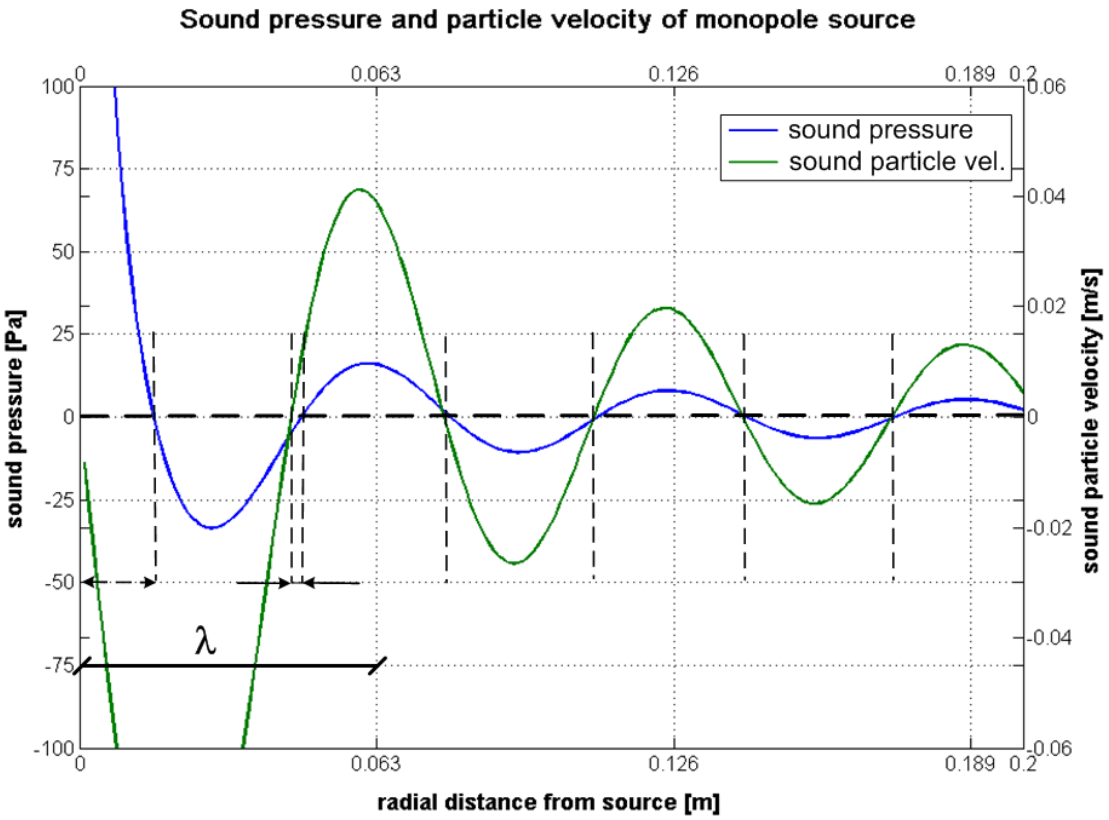

Figure 2.19: Sound pressure and sound particle velocity of monopole source as functions of radial distance

Another important acoustic quantity related to the sound pressure and particle velocity is the sound intensity I which is a measure of the acoustic energy flux. As the sound particle velocity, it is a vectorial quantity

$$\boldsymbol{I} = p \cdot \boldsymbol{v} \ . \tag{2.77}$$

In most applications, the normal intensity (denoted by I_n) with respect to a certain plane or surface is considered. It can be computed directly, if the sound pressure and normal velocity distribution are known[11]

$$I_n = p \cdot v_n^* \ . \tag{2.78}$$

The above given equation is generally valid, however, in case far field conditions can be assumed, a simplified expression, involving only the sound pressure, can be used

$$I = \frac{p_{rms}^2}{\rho c} = \frac{p_{peak}^2}{2\rho c} \ , \tag{2.79}$$

in which p_{rms} stands for the effective (or rms-)[12] pressure which is related to the peak pressure by $p_{peak} = \sqrt{2}\, p_{rms}$.

[11] The * refers to the complex conjugate of the normal velocity.

[12] rms stands for 'root mean square', the quadratic mean, a conveniently used quantity to determine the effective (time-averaged) value e. g. of the sound pressure level. rms-values will be used as well in chapters 4 and 5.

As explained in the definition of the far field above, the intensity also contains information about the phase relation between sound pressure and particle velocity. Hence, the imaginary part of the intensity becomes negligible compared to the real part far from the source, and comparable in the near field of the source, where the field is purely reactive (for more information refer to Ehrenfried [2]).

Furthermore, the intensity can be integrated over a specific area A_s to obtain the radiated power value into this region,

$$\boxed{P_{rad} = \frac{1}{2} \int_{A_s} I_n \, dA_s = \frac{1}{2} \int_{A_s} p \cdot v_n^* \, dA_s} \tag{2.80}$$

which as well consists of a real part (active power) and an imaginary part (reactive power). The reactive power value normally becomes non-negligible only close to acoustic sources, and is a measure of the power involved in the conversion of kinetic (particle velocity) to potential (pressure) energy.

2.2 Typical aircraft engine noise field

Within this section, the typical noise field radiated from a modern turbofan engine and the basic noise generation mechanisms, as well as the regulations and reference quantities applicable for aircraft certification, will be shortly presented. These are essential for the understanding of the following liner design methodologies and the objectives of the novel concept developed within this thesis.

2.2.1 Aircraft noise components

The noise field of a modern commercial aircraft powered by high bypass ratio (BPR) turbofan engines is composed of several contributions whose relative weighting depends on the flight condition. As sketched qualitatively in figure 2.20, the main contributions are the engine and the airframe (including wing and landing gear). At approach (figure 2.20(b)), both reside at nearly the same level with a slightly higher contribution by the engine. However, at takeoff (figure 2.20(a)), the engine clearly dominates the radiated noise field. This is comprehensible considering the different power settings at these two flight conditions.

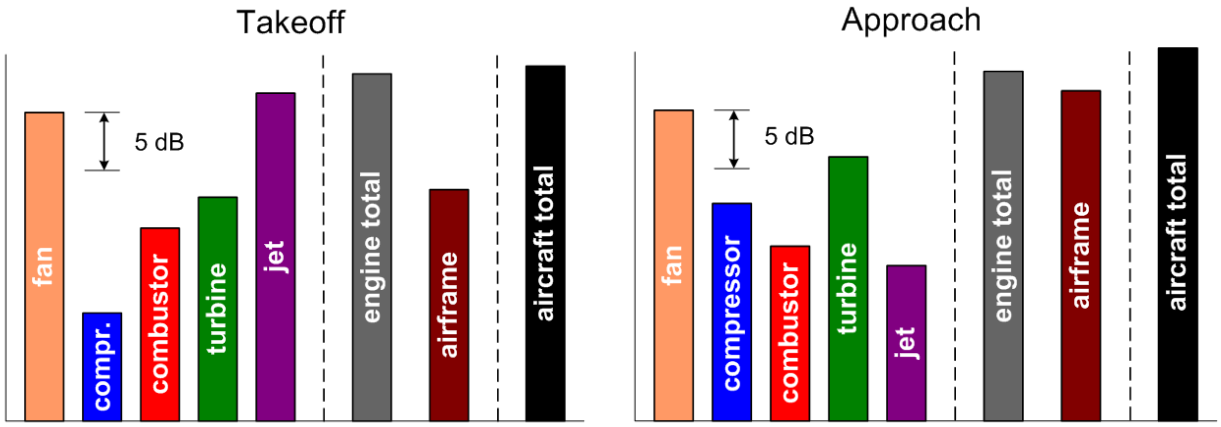

(a) takeoff (b) approach

Figure 2.20: Breakdown of aircraft noise sources (according to Batard [14])

In detail, the engine components contributing to the acoustic radiation are the fan, the compressor stages, the combustion processes, the turbine, and the jet. They each exhibit characteristic directions of radiation (a distinct 'directivity') and are of different importance with respect to forward and rearward radiated noise (compare also figure 2.21). Accordingly, in the forward sector, the fan is the dominant component, clearly separated from the compressor in terms of sound pressure level. In the rearward direction, additional to the fan, also the turbine stages, the combustion processes, and, above all, the jet contribute to the radiated noise field.

With respect to the bandwidth of the radiated noise, the turbomachinery parts (i. e. the fan, compressor, and turbine stages) produce mainly tonal noise related to the rotational frequency of the shaft or the interaction of rotating and fixed components (as will be described in the next subsection). On the contrary, the primary sources of broadband noise are the jet and the combustion processes.

Comparing these contributions of the engine components at the two flight conditions (depicted in figure 2.20), it becomes obvious that fan noise is an important factor both at takeoff and approach. Due to the full power setting at takeoff, the jet dominates the rearward radiation, and adds to the overall engine sound pressure level at this condition. In contrast,

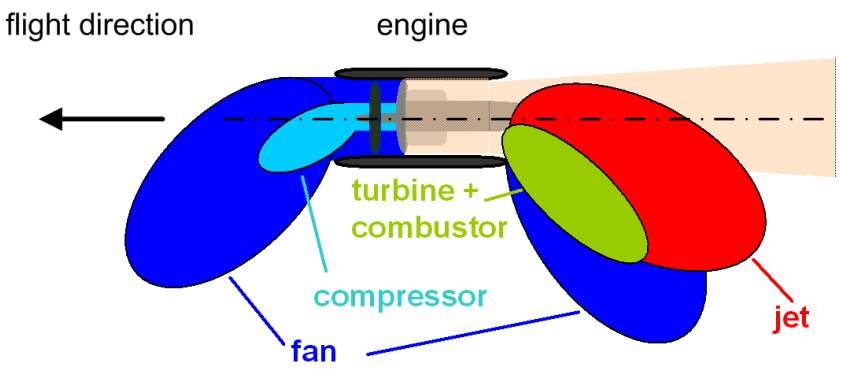

Figure 2.21: Sketch of typical aircraft engine noise sources (according to Batard [14])

at approach, jet noise becomes relatively unimportant, wherefore the turbine becomes the second significant noise source.

Especially with respect to the continuing trend of increasing bypass ratios for newly developed turbofan engines (UHBR = Ultra High BPR), the importance of the tonal components produced by the fan will increase even more. This is mainly related to two reasons: on the one hand an increase of the ratio of the diameter to the length of the engine inlet causing a reduced efficiency of the acoustic treatment. Additionally, the reduction of the rotational speed of the turbomachinery and of the number of fan blades results in lower frequencies of the tonal components, which are more difficult to handle taking into account the limited available installation space for acoustic treatments. On the other hand, the increasing BPR reduces the importance of jet noise such that recently more emphasis has been put on (rearward) fan noise and its reduction (as mentioned e. g. in Ref. [15]).

2.2.2 Fan noise generation mechanisms

In their famous paper about the prevailing duct modes within an aircraft engine inlet, Tyler and Sofrin [16] developed a simple analytical model describing the noise generation mechanism, the transmission within the duct, and the radiation to the observer. They identified the rotor as well as the interaction of the rotor and the corresponding stator to be the primary noise sources for the generation of spinning mode patterns.

The rotor alone creates a spectrum of harmonics of the *Blade Passage Frequency (BPF)*, which is the product of the shaft angular frequency Ω and the number of rotor blades N_B

$$BPF = \Omega \cdot N_B \; . \tag{2.81}$$

It consists of modal patterns of an integer multiple of the number of blades all spinning with the shaft rotation speed. Since these modal patterns are periodic (as is the stagger of the blades), their pressure distribution at a fixed axial location and radius can be described by a Fourier series

$$p(\theta, t) = \sum_{n=0}^{\infty} A_n \cos\left[nN_B(\theta - \Omega t) + \varphi_n\right] \; . \tag{2.82}$$

A radial variation of the pressure (for the higher radial mode orders) can be included by considering A_n and φ_n (the amplitude coefficients of the n-th mode) to be functions of the radial position r.

As can be deduced from the theoretical considerations in the first part of the chapter (e. g. equation (2.40)), the phase velocity in the circumferential direction (i. e. the circumferential velocity of the nodes at the duct wall) has to exceed a certain value for the mode to propagate, which is in either case greater than the speed of sound. Thus, from equation (2.45), the following condition directly follows for the zero flow case (and $r = 1$)

$$\frac{\omega}{c} \geq \kappa_{mn} \ . \tag{2.83}$$

This is the propagation condition for a mode $m = 1$, for which the pressure pattern spins by 360° (a full revolution) in one period. For higher order azimuthal modes, the angular distance and, in equal measure, the rotational speed reduce proportional to the azimuthal mode number m (e. g. for a mode $m = 2$, the angle reduces to 180°). Thus, in general, the cut-off condition in terms of the angular velocity of the mode can be expressed as

$$M \geq \frac{\kappa_{mn}}{m} \ . \tag{2.84}$$

Accordingly, the *critical Mach number* M_{crit}, at which the equation is exactly balanced, shows a decreasing tendency with increasing azimuthal mode number m and asymptotically approaches unity, as can be seen in figure 2.22.

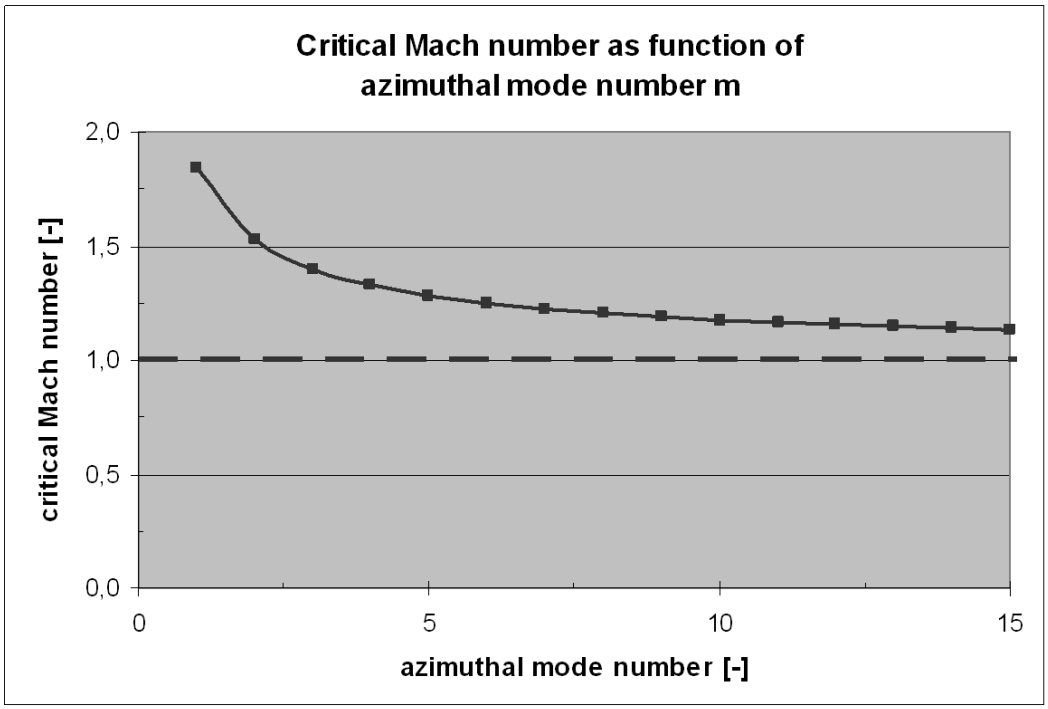

Figure 2.22: Critical Mach number M_{crit} as function of azimuthal mode number m

These findings yield the following result for the 'rotor alone tones': if the rotor tip speed exceeds the critical speed for the first BPF harmonic ($M_{tip} > M_{crit_{1BPF}}$), all harmonics of the blade passage frequency propagate as well. This is due to their constant angular speed (Ω) and the decreasing tendency of the critical Mach number with increasing m. Consequently, for a subsonic rotor, all BPF harmonics decay.

On the contrary, for the rotor-stator interaction tones, modes are excited by rotor blades cutting the wakes of upstream stators or the impingement of the rotating wakes of the rotor on downstream stators. The corresponding azimuthal mode numbers can be computed by the following relation, in which N_B stands for the number of rotor blades, N_V for the number

of stator vanes, n for the order of the blade harmonic, and k is an index ranging over all positive and negative integers.

$$m = nN_B + kN_V \; ; \qquad k = 0, \pm 1, \pm 2, \cdots \tag{2.85}$$

Accordingly, for each n-th BPF harmonic, a modal spectrum can be determined, which can be, as well, described by a Fourier series. If the effects of all blade-vane interactions are summed up, the following equation results for the pressure field at a fixed radial and axial position

$$p_{mn} = \frac{N_V}{2} A_{mn} \cos\left[m\left(\theta - \frac{nN_B}{m}\,\Omega t\right) + \varphi_n \right] . \tag{2.86}$$

Thus, in the rotor-stator interaction case, each mode has a different angular velocity (in contrast to the 'rotor alone tones' where all harmonics spun with the rotor shaft speed). This characteristic makes possible the excitation of supersonic phase velocities by a subsonic rotor, an important conclusion for understanding the noise field of an aircraft engine.

In general, the rotor-stator interaction tones of the fan at the harmonics of the BPF are the main contributions to forward radiated noise. They dominate the sound field apart from other tonal contributions by the compressor and broadband components through interactions of the flow and the airframe or nacelle. Typically, modern turbofan engines are designed using a '1BPF cut-off design', i. e. the number of rotor and stator blades has been selectively chosen to ensure that the modes excited at the first BPF are all cut-off. Hence, the acoustic liner can be designed to attenuate the higher BPF harmonics effectively.

However, during takeoff and climb the engine operates at full power and, due to the large diameters of modern turbofans, the fan tip speeds exceed Mach 1. This excites the above described rotor alone tones, also known as 'multiple pure tones' or 'buzz saw noise' (=BSN, because of their rather annoying, relatively low frequency, ragged noise). They affect both the passengers in the front cabin and the community around the airport.[13] With respect to the continuously increasing fan diameters of modern turbofan engines, the avoidance of BSN remains one of the important fields of research activity. As a result, efforts are directed at reducing the shaft rotational speed, which is however limited due to its coupling with the compressor and turbine stages. In this respect, a geared turbofan concept (GTF), in which the fan is decoupled from the turbine by a gearbox, might yield promising results.

2.2.3 Aircraft noise certification measurements

For the certification of new or modified versions of existing aircraft, the ICAO and the FAA specify in the 'Environmental Technical Manual on the Use of Procedures in the Noise Certification of Aircraft' [18] three measurement points around the airport to estimate the impact of starting and landing aircraft on the neighboring areas. These positions are sketched in figure 2.23 with respect to the runway and comprise approach, takeoff, and sideline positions.

At *approach*, the measurement position is located 2000 meters ahead of the beginning of the runway, where the aircraft should be at an approximate height of 400 ft $\approx$ 130 meters. After having passed this position, during certification runs, the aircraft does not come to a halt but performs a go-around procedure (a touch-and-go landing) and takes off again. The respective measurement point for *takeoff* is 6500 meters behind the touchdown point on the runway. It is also referred to as the *cutback* condition, which describes a standard procedure to reduce the noise exposure of the community by reducing the thrust setting at a certain

[13] More information concerning the prediction of buzz saw noise and a comparison with experimental data can be found e. g. in McAlpine, Fisher, and Tester [17].

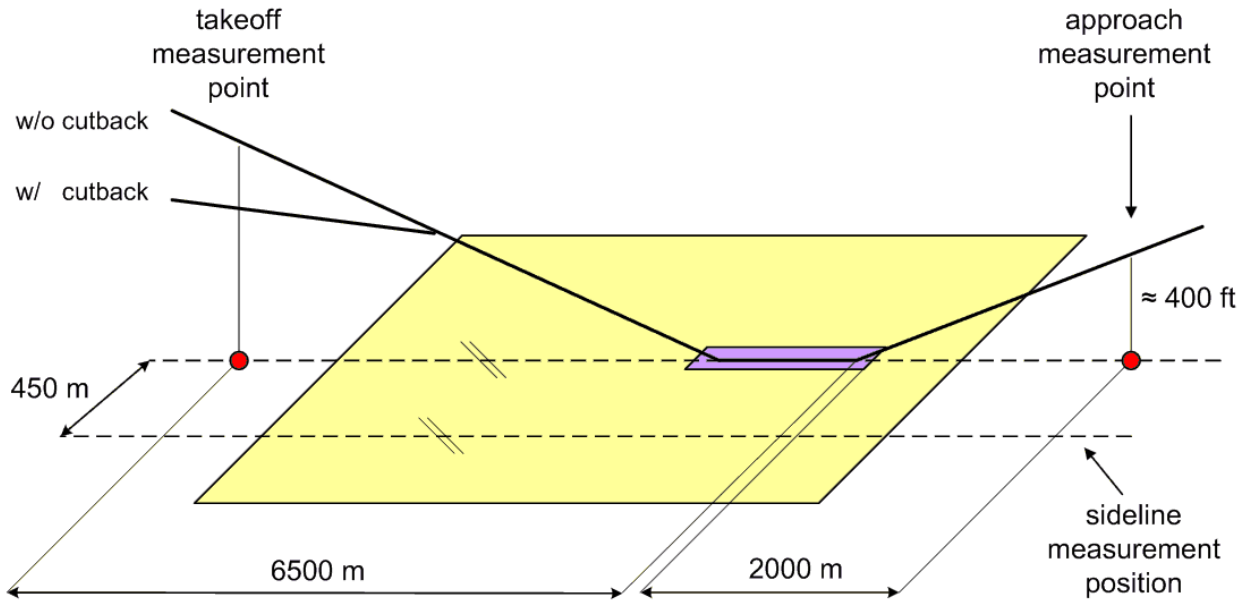

Figure 2.23: Principal sketch of noise certification measurement points

altitude. This results in reduced noise levels, but also a flatter climb angle and a longer duration in low flight levels, contrary factors which have to be balanced when designing low noise flight procedures (as mentioned e. g. in Antoine and Kroo [19]). The third certification measurement position is the *sideline* location 450 meters sideways of the runway, where the aircraft should be at a height of ≈ 300 meters.[14]

The acoustic quantity ultimately compared to the required noise standards is the *Effective Perceived Noise Level (EPNL)* (definitions taken from the Handbook of Acoustic Ecology by Truax [20]), which is a measure of the perceived noise observed on the ground. It is obtained from the Perceived Noise Level (PNL) by a tone and a duration correction, as defined in the following

$$EPNL = PNL_{max} + 10 \cdot \log\left(t_{10}/20\right) + F \; . \tag{2.87}$$

In this equation, the variable t_{10} specifies the duration (in seconds) of the noise level within 10 dB of the peak PNL and F is a tone correction for pure tones. The Perceived Noise Level scale has been developed by Kryter [21] to measure the perceived noisiness of jet aircraft, and later on been adopted by the ICAO. He used equal loudness contours to create an alternative scale (which he named 'noy') to the flat, i. e. not weighted, dB scale. To this, the PNL, which is similar to an A-weighted decibel scale (with a peak weighting at 2000 Hz and decreasing tendency towards higher and, especially, lower frequencies), can be converted by a simple relation

$$PNL = 40 + \log_2\left(\text{noy}\right) \; . \tag{2.88}$$

[14] Details on these procedures and deviations for different types of airplanes can be found in the above referenced technical manual published by the ICAO [18].

2.3 Implementation in lining concepts

Within this section, the application of the duct acoustic theory to the design of efficient lining concepts will be summarized. Therefore, the most important developments have been classified into three basic groups: uniform liners of various kinds, adaptive, active, or hybrid concepts, and non-uniform configurations, in which 'non-uniform' might refer to the liner design or the geometry of the duct itself.

2.3.1 Uniform passive liners

To start, the basic categories of acoustic absorbers and resonators as well as the commonly used materials will be presented. This will be followed by the two steps of an efficient liner design: the determination of the acoustic impedance of the concept and the calculation of the theoretical optimum for a specific application. Finally, the effect of reflections and modal coupling at impedance discontinuities as well as advanced uniform lining concepts will be shortly mentioned.

2.3.1.1 Basic liner types and materials

The three basic types of liners (or acoustic absorbers) are the ones depicted in figure 2.24 and described in Refs. [22], [23], and [24]. They can be classified with respect to different characteristics, but the most commonly used distinctive feature is the way they affect an incident sound field. Accordingly, it can be differentiated between locally (or point) reacting absorbers and non-locally reacting absorbers.

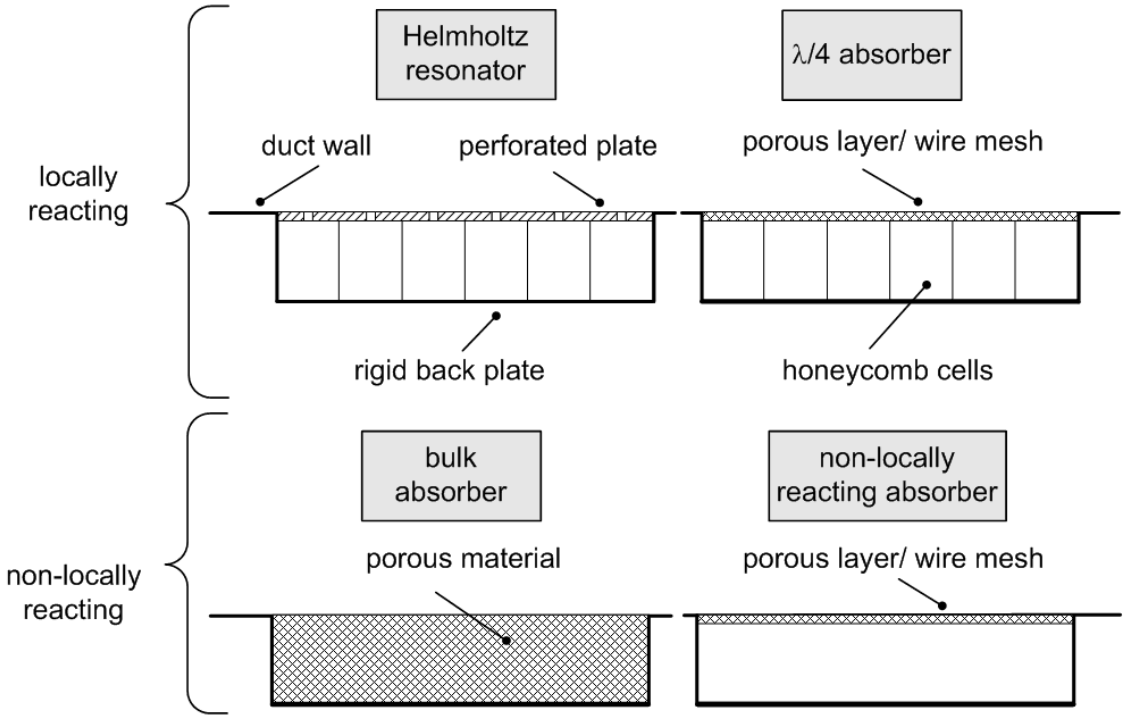

Figure 2.24: Schematic sketch of three basic types of wall linings

This naming refers to the way acoustic waves can propagate within the lining material: *locally reacting absorbers* admit only wave propagation in the direction normal to the wall by partitioning the cavity behind the facing sheet, e. g. by a honeycomb material. On the contrary, *non-locally reacting absorbers*, which are either macroscopically homogeneous bulk

absorbers (e. g. foams, glass fiber) or consist of a porous layer positioned at a certain distance from an acoustically hard wall, do not constrict the direction of propagation. They act as broadband absorbers affecting a broad frequency spectrum and are only limited by their thickness, which determines the maximum operating frequency (compare upper sketch of the absorption coefficient as a function of frequency in figure 2.25) (as defined in equation (2.72)).

The two types of locally reacting liners are the classical *Helmholtz resonator*, which has only a small opening to the duct wall compared to the volume of the back cavity, and the *resistive resonator* or $\lambda/4$ *absorber*. The latter consists of a back cavity (as the resonator) covered by a resistive facing sheet, which permits acoustic waves to enter the cavity over the whole front surface area. Their characteristic differences with respect to the absorption coefficient can be inferred from the two lower plots in figure 2.25.

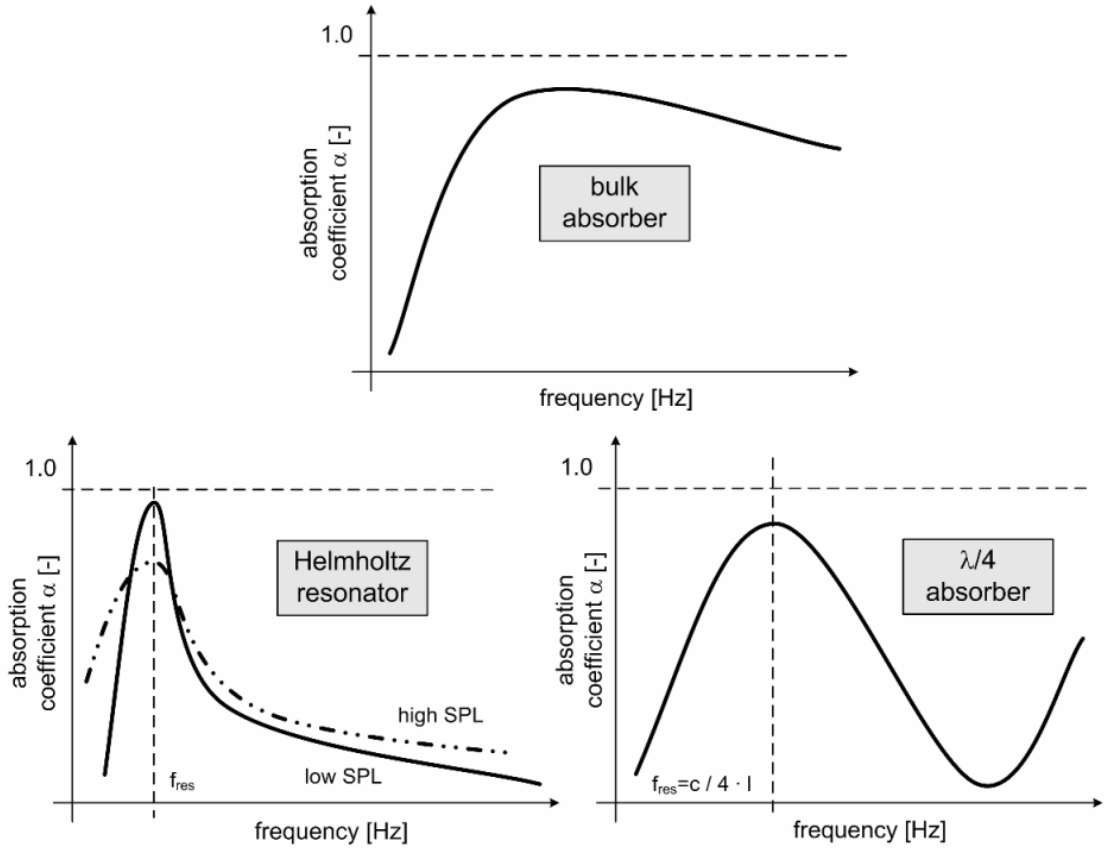

Figure 2.25: Absorption curves of wall linings

At the resonance frequency of the resonator, which is defined by its volume V, the opening surface area A_s, and the throat length l (compare schematic sketch in figure 2.26)

$$\omega_{res} = \sqrt{\frac{c^2 \cdot A_s}{V \cdot l}}\,, \tag{2.89}$$

the Helmholtz resonator shows a narrow peak at lower and medium sound pressure levels (up to $\approx$ 130 dB), and a broader attenuation spectrum at high sound pressure levels. This non-linearity, as well as its high but narrow peak absorption, are characteristic for the Helmholtz resonator.[15]

[15]In the design of acoustic resonators it is generally assumed that the dimensions of the resonator are small compared to the acoustic wavelength, which permits only a plane wave motion within the resonator.

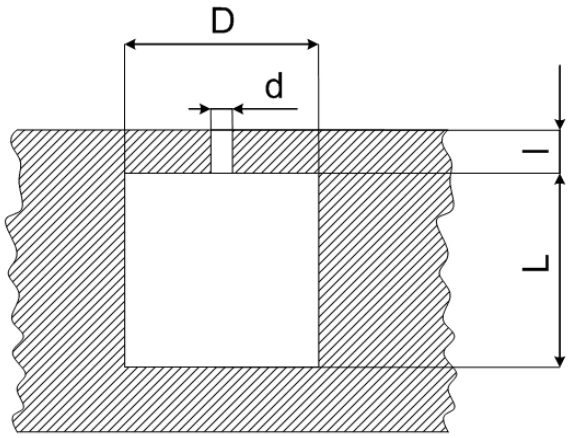

Figure 2.26: Schematic sketch of Helmholtz resonator

In contrast, the $\lambda/4$ absorber exhibits a broader peak centered at the quarter-wavelength resonance of the back cavity (and theoretically at all odd multiples). Its resistive sheet at the front side of the cavity consists of either a fine wire mesh or a (micro-) perforated plate, and becomes most effective if positioned at the peak of the sound particle velocity a $\lambda/4$ distance from the rigid back plate (compare figure 2.15). For a first approximation, the sheet can be considered to act purely resistive, and the effect of the back cavity to be purely reactive. Thus, the effective impedance of the absorber can be computed accordingly

$$\frac{Z_{\lambda/4}}{\rho c} = R_{sheet} + i \cdot \cot\left(\frac{\omega \cdot l_{cav}}{c}\right) , \tag{2.90}$$

in which l_{cav} denotes the depth of the back cavity. However, for a detailed design, several other aspect have to be taken into account, e. g. the reactive effect of the sheet (due to the air contained in the sheet), the end correction of the throat (accounting for the co-moving air mass), and flow effects changing the angle of incidence of the sound wave. Further reading on the theory and design of acoustic absorbers and resonators can be found in Ingard [25].

With respect to the decision in favor of one of the three types for a given application case, also the environmental conditions (e. g. temperature, erosion, contamination, drainage) as well as additional criteria (e. g. weight, strength, manufacturing cost) have to be taken into account (a summary of structural and environmental studies is given in Watson [26]). Because of its favorable properties and a good compromise between peak absorption and bandwidth, if properly designed, the $\lambda/4$ absorber is the one most commonly used in aircraft engine inlet and exhaust ducts.

2.3.1.2 Determination of lining impedance

The impedance of a certain material or liner design, and its respective reflection and absorption coefficients, can be determined in several ways. The most frequently used one in laboratory tests is the *Kundt's tube* or *impedance tube* technique according to ISO 10534-1 and -2. As has been mentioned in the definition of the acoustic impedance in the previous chapter, accordingly a sample of the material is mounted at one end of the tube, and a plane wave is excited at the other end. From the measurement of the sound pressure level and the relative phase by two flush-mounted microphones at two known axial positions, this characteristic quantity of the material can be computed. This Kundt's tube measurement method is, by default, limited to normal incidence, but oblique incidence values can be estimated

analytically. However, it yields accurate results within a short time frame and requires only a small sample of the material.

In contrast, the measurement of the absorption in a *reverberation room* according to ISO 354 requires much larger samples of the test object, and determines the diffuse field absorption coefficient. This method is rather suited for larger structures with varying normal directions.

For the local impedance measurement of liners, the *two microphone method* originally suggested by Sivian [27] and described also by Dean [28] is convenient to use, since it requires only the measurement of the complex sound pressure at one location within the cavity and one at the outer surface of the resistive sheet (of the $\lambda/4$ absorber). It is based on the simple relationship between cavity pressure and particle velocity and the limitation to a plane wave propagation within the liner under the condition that the size of the partitions is small compared to the wavelength.

Additionally, in the early years of modern high BPR aircraft engines, extensive parametric experimental studies with respect to the impedance of different liners designs have been conducted at specially designed test facilities in the 1970s. These aimed at the identification of the relevant parameters (Atvars and Mangiarotty [29]), the better understanding of discrepancies between measurements and analytical predictions (Wirt [30]), and the optimization of the duct treatments (Kraft et al. [31]).

Recently, a combined numerical and experimental study by Jones et al. [32] investigated the individual and mutual effects of the basic geometric parameters of locally reacting liners of the resistive resonator type. These comprised the influence of the percentage of open area of the resistance sheet, the sheet thickness, the sheet thickness-to-hole diameter ratio, and the cavity depth.

2.3.1.3 Optimization of liner performance

After the determination of the acoustic impedance of a liner design, the second step is related to the calculation of the *optimum impedance* for a specific application. This design point has probably been studied first by Cremer [33], who stated that the maximum attenuation rate, which is equivalent to the maximum imaginary part of the axial wave number (k_z), compare equation (2.47), coincides with the point in the complex wave number plane at which two modes merge (referred to as a 'branch point' by Morse [34]). His theory was limited to a rectangular duct and the first two modes,[16] but has been extended by Tester [35] to higher order modes as well as circular and annular ducts.

Tester also demonstrated why the large predicted attenuations have not been observed to this extent in practice, and explained the physical mechanism at the optimum condition using a ray model [36]. As the standard Green's function does not exist at the optimum condition (the eigenfunctions become orthogonal to themselves at the double pole position), Tester derived an alternative formulation for the case of a rectangular duct, involving non-orthogonal modes. This concept has been adopted by Zorumski and Mason [37] and applied to circular and annular ducts.

Rice published a series of papers starting in 1968 [38], in which he described an inverse approach to the determination of the optimum impedance and the maximum achievable attenuation for a given mode [39]. Instead of directly seeking eigenvalues of equation (2.62) by a series expansion or an iteration, he limited his analysis to a single mode and specified eigenvalues, for which the impedance could easily be computed. Since in the general case this procedure does not yield the desired optimum values, Rice performed a parametric variation

[16] Cremer focused his efforts on the *least attenuated mode*, which is, in general, the fundamental mode, as its attenuation value determines the maximum achievable attenuation at larger distances.

of both the real and the imaginary part of the axial wave number (which he denoted the 'propagation' (τ) and 'damping' (σ) coefficients), from which the eigenvalue κ can be derived using equation (2.40).

Keeping one of the two parameters (σ, τ) constant, contours can be plotted in the complex impedance plane, which e. g. for a constant σ are equivalent to regions of constant attenuation. By careful selection of the starting value and small increments of the damping coefficient τ, the characteristic closed ('teardrop-shaped') contours degenerate into a point representing the optimum impedance for this mode. From the corresponding damping coefficient, the maximum achievable attenuation can then be calculated. Yet, a further increase in the damping coefficient generates a new set of closed contours, which represent the solution for the next radial mode.

An example of these plots is given in figure 2.27 reproducing a figure from one of Rice's papers (Ref. [40]).

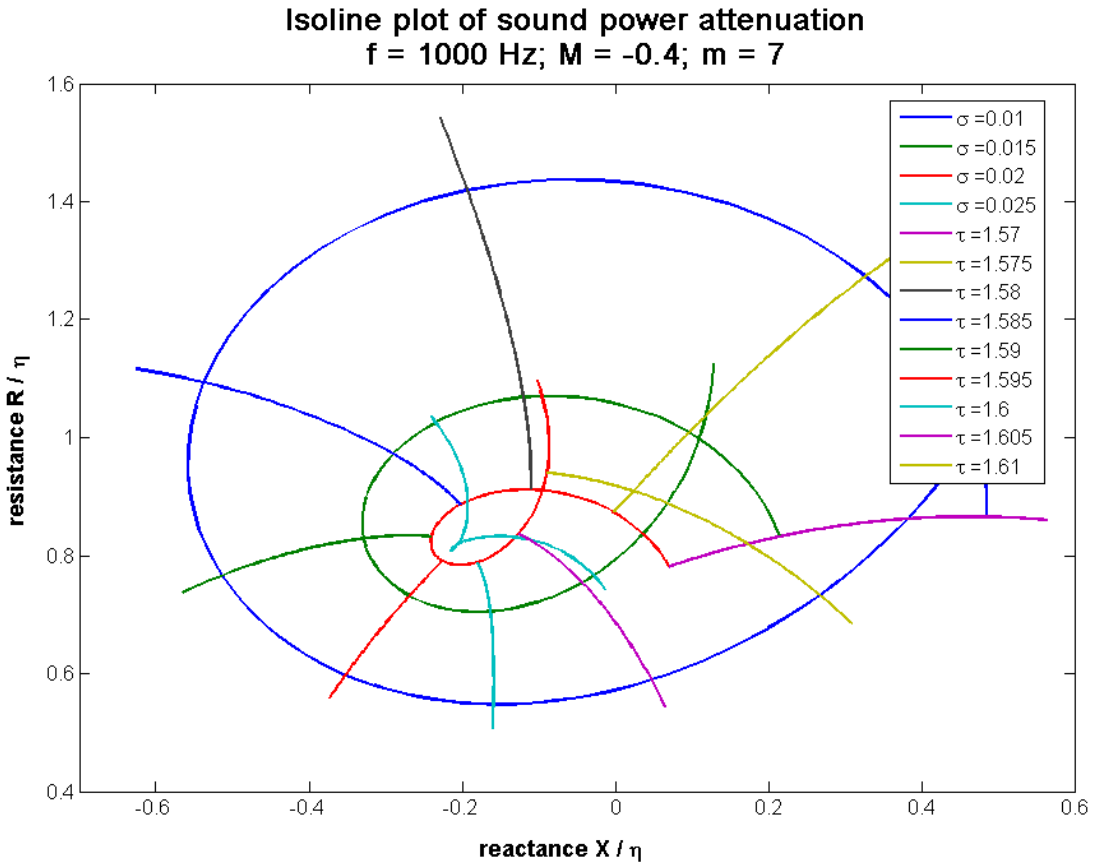

Figure 2.27: Example of iso-attenuation plot in complex plane according to Rice

Whereas, on the one hand, this method is a very fast and effective way of finding the optimum impedance, it is dependent on the careful selection of the starting values to ensure the correct radial mode order.

In parallel, Wilkinson [41] used a Boundary Element approach[17] developed by Liu and Martenson [42] coupled to a gradient technique to calculate optimized lining configurations. He compared his results to Rice [38] for a plane wave inside a circular duct and found a good correlation. However, for higher mode orders, his solution and the one obtained by Kraft [43] (who used a similar procedure as Rice) differed significantly, which he attributed to different normalization schemes and numerical errors.

[17] The concept of the Boundary Element Method will be explained in detail in chapter 2.4.3.2.

Plumblee et al. [44] presented an extensive measurement program on sound propagation in hard walled and lined annular ducts and the corresponding radiation patterns for a series of modes. They used this data to verify their duct acoustic theory, which is based on the solution of the eigenvalue problem by a finite difference scheme similar to the one Wynne and Plumblee proposed in Ref. [45]. In presence of a sheared flow, they used a Newton-Raphson iteration[18] starting from the zero flow case to ensure convergence. Their results verified most of the effects of practical interest for hardwalled and lined duct cases. Additionally, Plumblee et al. presented interesting methods for an experimental determination of the cut-on frequencies and mode shapes and the measurement of the acoustic impedance of liners.

Approximately three decades after the emergence of Boundary Element methods in the 1960s, Dunn, Tweed and Farassat [46] presented a computationally efficient tool named TBIEM3D (Thin-duct Boundary Integral Equation Method, 3-dimensional) for the calculation of the acoustic radiation from an engine duct in the presence of a uniform flow and arbitrary wall boundary conditions. They coupled it to a Newton search routine in the complex impedance plane maximizing the far field attenuation at a number of observation points [47]. An important conclusion from their results is the fact that the region of near optimum liner behavior is relatively large, corresponding to only slight losses of performance for variations in the effective liner impedance due to manufacturing imprecisions, unexpected influences on the impedance, or in-service contamination.

2.3.1.4 Effects of impedance discontinuity

Within the context of the transition from the initially used infinite duct theory (e. g. by Rice [38], granting an undisturbed axial wave propagation without reflections from the duct terminations) to ducts of finite length, reflections and changes in the modal structure have been observed. Lansing and Zorumski [48],[49] were the first to implement a so-called *mode matching method* based on the Wiener-Hopf technique (described in chapter 2.1.2) into the multisectioned duct theory, which will be referenced again later on. Yet, this technique is generally valid at each impedance discontinuity within the duct - as might be the interface between a hardwalled and a lined duct section, variations in the geometry, or the duct termination itself (compare figure 2.28).

The figure indicates reflected and transmitted waves at each impedance discontinuity which can be determined by the mode matching method. Since these components may contain not only reflections but also the coupling of modes, the radiated field might be considerably different to the one excited at the source plane. These redistribution effects of modal energy have been studied intensively by Montétagaud and Batard [50], as they are of considerable importance in the design of acoustic liners. The authors reported two types of modal conversion effects, which have been discovered during the computation of radial wave numbers [51] by the Eversman method (a numerical integration scheme) [52]. These imply the conversion, or change, of the radial mode order observed in the transition from the hardwall solution to lined duct cases, and have been named 'partial' and 'total radial mode conversion' depending on the degree of reordering.

In an attempt to eliminate the reflections from the forward end of the liner segment, and to maximize the treated area, Astley et al. [53] studied amongst others the influence of an extension of the acoustic liner to the exit plane of the inlet (including the lip area). They discovered different effects for the two flight conditions sideline and approach (an overall scaling of the attenuation at approach, at sideline mixed with scattering effects), but, in

[18] More information about iteration schemes will be presented in chapter 2.4.2.

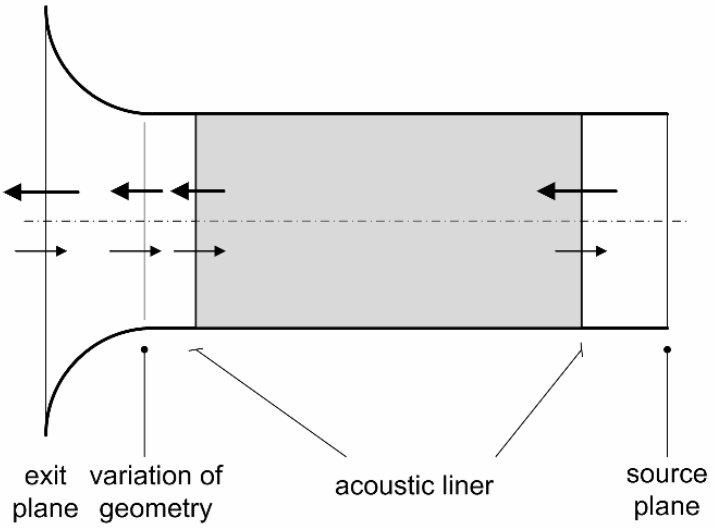

Figure 2.28: Transmitted and reflected wave components in acoustic duct

general, favorable results for the *extended lip liner* yielding increased absorption and lower reflection/ scattering levels.

The fundamental problem related to this extension of the acoustic liner deals with the integration of the anti-icing system, which is located in this lip region of the nacelle. A possible solution has been demonstrated within the Boeing QTD2 program [54], increasing the acoustically treated area by 78% relative to the baseline production inlet.

2.3.1.5 Advanced designs

After the treatment of the basic types of uniform liners, several advanced concepts will be presented in the following trying to achieve enhanced absorption properties either by an elaborate design or by a more complicated structure.

As a logical extension of the single degree of freedom (SDOF) absorber concept presented in the previous section, several researchers studied *double degree of freedom (2DOF)* [55],[56] or *multi degree of freedom (NDOF)* systems [57] to broaden the absorption characteristic or address several frequencies with one design. These, of course, imply a more complicated manufacturing process and an increased installation height, but yield quite promising results in some cases. An example of the concept of a 3DOF liner is depicted in figure 2.29. It consists of three cavities of depths l_1, l_2, l_3 connected in series and separated by two septums[19] of impedance Z_2 and Z_3. They are coupled to the duct wall by a facing sheet of impedance Z_1 and terminated at the rear by a rigid back wall. By a suitable selection of the respective cavity depths and the interconnecting septums, a broad frequency range can be covered by the design.

A completely different approach of adding degrees of freedom to the liner design has been presented in 2003 by Sijtsma and van der Wal [58]. They proposed a non-locally reacting liner consisting of helical waveguides covered by a perforate plate, and optionally filled with a porous material. The advance ratio of the waveguides and the properties of the porous material (if applied) represent two additional parameters, which can be used to optimize the liner performance. This design was mainly intended to be used for the attenuation of the rotor alone tones and, therefore, to be positioned directly adjacent to the fan as a so-called 'fan-face' liner. In this application, the *spiralling liner* achieved a 3 dB higher attenuation

[19]The septums are the horizontal walls connecting two respective cavities in the wall normal direction.

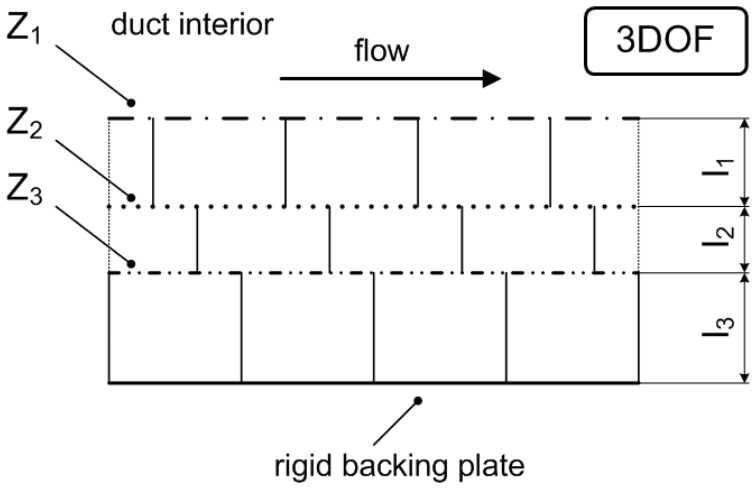

Figure 2.29: Schematic sketch of 3DOF liner

for the rotor alone noise and comparable results to an optimum locally reacting liner for a broadband input.

Not designed to increase the number of DOFs but achieve additional attenuation, the concept of the *Herschel-Quincke tube*, originally invented back in 1833 by Herschel [59], and verified experimentally in 1866 by Quincke [60] for plane sound waves, has been applied to higher order modes in aircraft engine inlet and bypass ducts by Burdisso, Smith et al. [61],[62],[63]. It makes use of the interference of acoustic waves propagating in the main duct and ones traveling through the Herschel-Quincke tube, which constitutes a kind of side branch or bypass connecting two axial stations of the duct.

Concerning new materials, the Georgia Institute of Technology developed tiny *hollow ceramic spheres* of varying diameters to be used as acoustic absorbers, especially in high-temperature applications [64]. They could be used instead of typical bulk absorbers, which cannot comply with the thermal constraints and are not as shapeable. The concept has been adopted by the French company '01dB-Metravib' [65] for the acoustic design of splitters in the bypass duct in the framework of the European research project SILENCER (Significantly Lower Community Exposure to Aircraft Noise) [66].

Concluding, it may be stated that currently used 1DOF or 2DOF uniform liners, which are typically optimized for approach conditions, are technically mature and yield quite satisfying results. However, to achieve noise reductions in line with the ACARE 2020 goals, new concepts have to be developed. One category of these approaches to increase the effectiveness of the lining will be presented in the following section.

2.3.2 Adaptive, hybrid, and active concepts

In this section, adaptive, hybrid, and active concepts will be presented, which aim at an improved flexibility and capability of the acoustic treatment. However, in general, they imply a more complicated system as they include an array of actuators and sensors.

2.3.2.1 Adaptive and hybrid liner systems

The most obvious solution to adapt the impedance of an acoustic liner is probably the *mechanical adjustment* of its characteristic dimensions, which can be either of (or both) the resistance of the facing sheet and the reactance of the back cavity. Several researchers developed concepts in which the size of the cavity could be adjusted mechanically, e. g. De

Bedout and Franchek [67] for a Helmholtz resonator and Laak and Kapsos [68], who have been granted a patent for their 'adaptive passive attenuation system' comprising multiple adjustable quarter-wavelength absorbers.

Ahuja and Gaeta [69] tried to realize an impedance tuning by sliding two perforates relative to each other in the septum of a 2DOF liner concept and achieved quite good effects on both the resonance frequency and the magnitude of absorption. In the limiting case, this design also allowed the 2DOF system to become a SDOF liner in case of a complete closure of the septum.

A different concept for the adaptation of both resistance and reactance has been presented by Pongratz [15] in the framework of the SILENCER project.[20] He designed a frequency adaptation affecting the reactance of the absorber using a flexible rubber membrane at the rear wall of the cavity, which could be deflected by pressurized air supplied to a backing cavity. Neglecting the coupling between the two cavities and the rubber membrane, the resonance length could be adjusted to meet optimum conditions. In parallel, the facing sheet resistance could be influenced by a heating foil sandwiched between two layers of the resistance sheet. The heating locally changes the properties of the medium (density, viscosity, speed of sound) and increases its flow resistance. By these two concepts, connected to a suitable control algorithm and a two microphone local impedance measurement, the impedance of the absorber could be shifted to meet a resonance frequency range between 1200 Hz and 3500 Hz and achieve optimum conditions.

Another group of researcher used the physical phenomenon studied e. g. by Ingard and Ising [70], which states that a steady *bias flow* through a perforated sheet increases its acoustic resistance. To achieve an effect not only on the resistance, but also the reactance of a liner, Dean and Tester [71] applied this concept to a multilayer design. They used a 'positive bias flow', corresponding to air blown through the liner from the backing wall. In result, the impedance of this liner system could be adapted within a certain range, however, yielding only marginal improvements probably related to an unknown modal content of the input sound field.

Several years later, Ahuja, Cataldi, and Gaeta [56] studied the same concept on a 2DOF liner, but using a 'negative bias flow' corresponding to suction from the backing wall. This approach could be combined with a flow control device, which also uses boundary layer suction to prevent separation of the flow. Positive effects have been reported for zero flow conditions in a test duct, but this enhanced absorption decreased in the presence of a grazing flow. Compared to the positive bias flow concept, which requires a considerable amount of bleed air, the negative (suction) concept has been assessed more favorable, in particular, if combined with an already existing flow control device.

Very recently, a group of researchers at the DLR (Deutsches Zentrum für Luft- und Raumfahrt) [72] again studied the effect of a bias flow on the acoustic absorption. However, their field of interest was the suppression of thermo-acoustic instabilities within the combustion chamber of an aircraft engine. They used perforated liners originally intended for cooling purposes to analyze the effect of the number of jets, the jet velocity, their mutual spacing, and the flow Mach number and found quite promising results concerning the absorption characteristics. Whereas for cooling purposes, the jet velocity should be rather high, lower velocities yielded better results in an acoustic respect. Concerning the influence of the grazing flow, the effects observed showing an increased absorption with increasing flow speeds (which is contradictory to the results of Ahuja et al. [56] as described above), have not been understood yet. Additionally, interference effects between the individual jets have been suspected to be the reason for a reduced attenuation for a large number of jets, which would

[20] The concept of this mechanically adaptive liner will be presented in detail in chapter 3.1.

normally be expected to yield favorable results. This interference effect was made possible by the missing partitioning of the back cavity which consisted of a single plenum admitting communication amongst all perforations.

The group of *hybrid liners* constitutes an intermediate step between adaptive systems and active noise control. Thus, hybrid systems contain an active element to adjust, or tune, the impedance of the system, but not directly control the sound field. Additionally, these concepts maintain part of their performance in case the control is turned off, as they also act as a purely passive absorber. Figure 2.30 shows the principal setup of a hybrid absorber concept consisting of a porous layer or resistance sheet, a cavity, and an actuator that creates a secondary sound field interfering with the primary one which propagates inside the acoustic duct.

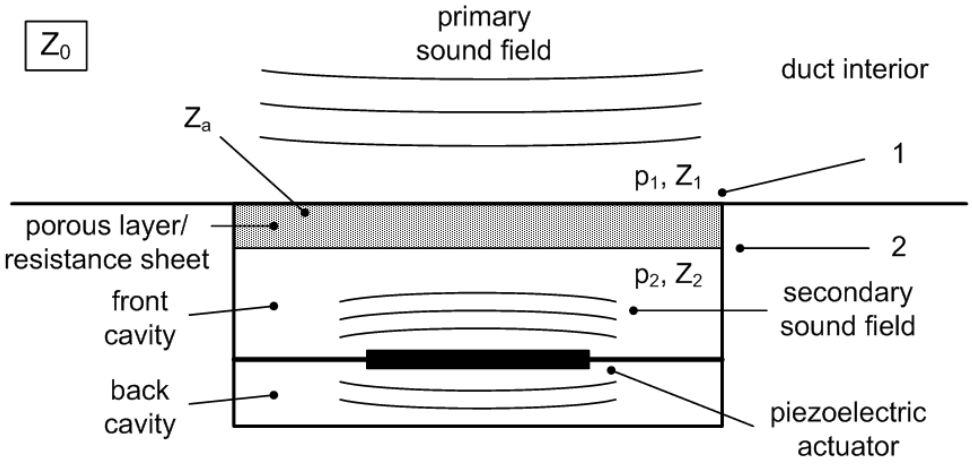

Figure 2.30: Schematic sketch of hybrid absorber

Radcliffe and Birdsong [73] named their concept, which consists of a Helmholtz resonator with an actively controlled impedance by a loudspeaker and a feedback control loop, a 'Semi-Active Helmholtz Resonator (SHR)' and demonstrated the tuning of the resonance over a range of frequencies.

Similar with respect to the working principle, but using a different actuator, Horowitz et al. [74], [75], [76] proposed a tunable Helmholtz resonator with a compliant piezoelectrically controlled backplate. This design, in general, yields the same characteristics as the above mentioned one, but is more appropriate for the application to an aircraft engine duct, since it comprises a powerful but low weight actuator based on piezoelectric technology. Additionally, the compliant backplate serves in its passive state the function of a second cavity layer emulating a 2DOF resonator. As Radcliffe and Birdsong, Horowitz et al. intended to use the tunable resonator for the adaptation to specific flight conditions or engine power settings (e. g. takeoff, approach), and not as an active noise control device.

A combination of an active wall at the rear end of the cavity and a layer of absorbing material positioned at a certain distance, has been repeatedly proposed by different researchers, e. g. by Furstoss, Thenail, and Galland [77] in 1997 (based on a concept by Thenail et al. [78]), Hilbrunner et al. [79] in 2002, and Cuesta et al. [80] in 2005. These concepts use the active wall, which could be implemented by a piezoceramic or a loudspeaker, to create a 'pressure release condition' ($p_2 = 0$, also known as a softwall condition as defined in figure 2.15) at the rear face of the porous layer. By this, and a suitable selection of the resistance of the porous layer ($Z_a = Z_0 = \rho_0 \cdot c_0$), a maximum sound absorption can be achieved even with cavity depths not sufficient for a conventional $\lambda/4$ absorber design.

Beyene and Burdisso [81] adopted in 1996 the idea of Thenail et al. [78], but showed that an 'impedance matching' (i. e. $Z_2 = Z_0$) at the rear surface of the porous layer yields better absorption characteristics than the pressure release condition. This conclusion has been confirmed by Smith, Johnson, and Burdisso [82], who compared both boundary conditions at the back surface of the absorptive layer. Additional to an enhanced attenuation, they observed a substantially reduced control effort for the impedance matching condition.

2.3.2.2 Active noise control (ANC)

Nelson [83] presented quite a comprehensive recapitulation of active techniques and their potential applications in aeronautics within the scope of his keynote lecture at the AIAA/CEAS Aeroacoustics Conference in 2000. However, in this context, only the main historical and recent contributions will be mentioned.

The first experimental observation of the interference of two sound sources has been reported by Lord Rayleigh in Volume 1 of his famous book 'The Theory of Sound' (1877) [84]. He noticed destructive interference causing spatial regions of silence, whose size depends on the acoustic wavelength.

Paul Lueg was the first to propose an Active Noise Control concept (ANC) in 1936, which he called a 'process of silencing sound oscillations' in his patent specification US 2,043,416 [85]. His idea of sensing incoming sound waves using a microphone and emitting waves from a loudspeaker with exactly the opposite phase to cancel the primary sound field (at least at a certain position or in a certain area), has been adopted later on by generations of researchers trying to implement it into an aircraft engine inlet duct.

A conceptual sketch of an ANC system applied to an acoustic duct is presented in figure 2.31. It shows a primary noise source (e. g. a rotor), error sensors in terms of microphones flush mounted to the duct wall, and actuators (e. g. loudspeakers) exciting a secondary sound field, which interferes with the primary one. Therefore, the sensor signals as well as an information from the source (e. g. the RPM of the fan), are fed to a controller, which calculates in real time the corresponding output signals driving the speakers. If properly implemented, the superposition of the primary and secondary (phase reversed) sound field should ideally cancel out, resulting in perfect silence.

Lueg's concept has been later on adopted by Conover [86] and Kido and Onoda [87] who automated an adaption of multiple loudspeakers to minimize the mean square error at several microphones.[21] Even if at that time computer technology was already reasonably mature, the multitude of ANC applications started with the invention of Digital Signal Processors (DSP) in the 1980s.

Especially in the 1990s, a large number of papers have been published dealing with Active Noise Control. For example, in 1993 Kraft and Kontos [88] studied the feasibility of an ANC system within an aircraft engine inlet including an array of error sensors and actuators. They observed difficulties in case of multiple radial modes, since the actuators can only be mounted at the duct wall, and therefore yield only limited control of the radial distribution. Additionally, they identified weight and power restraints as the critical factors for ANC applications and highlighted the need for research with respect to the development of novel lightweight but powerful transducers. Even if they did not study alternative solutions, Kraft and Kontos also mentioned the possibility to absorb or reflect sound waves by the actuators. In 1996, both inventors have been granted a patent on an 'active acoustic liner' (US 5,498,127) configured for buzz saw noise tones (compare chapter 2.2.2) for whose relatively low frequencies a conventional liner design would require too much volume [89].

[21] The algorithm used is accordingly named LMS (least mean square).

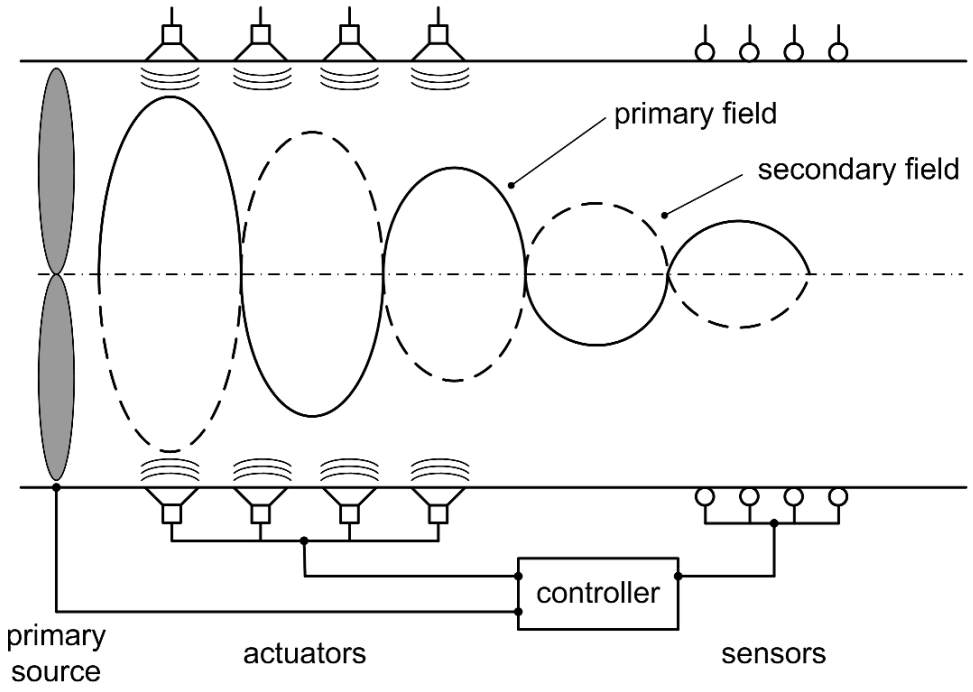

Figure 2.31: Schematic sketch of Active Noise Control (ANC) system

In the same year, Thomas et al. [90] conducted an experimental study, which verified the effectiveness of an ANC system. They demonstrated, in addition, the simultaneous control of two tones using a multichannel control system.

Risi, Burdisso, and Fuller [91] also performed an analytical investigation of the efficiency of an ANC system, but extended the concept of Kraft and Kontos [88] by using multiple axial stations for the transducers, which allows for the control of higher radial mode orders. This concept has been adopted by Joseph, Nelson, and Fisher [92], [93] who defined a kind of Nyquist criterion[22] for the number of sources in a plane and the number of axial source rings. Accordingly, the number of circumferential actuators has to be at least twice the highest propagating azimuthal mode number and the number of rings to be equal to the number of radial modes. They also stated that an array of in-duct error sensors could be used instead of a large number of far field sensors, which cannot be used in a real application case.

In 2001, Joseph, Fruteau, and Nelson [94] published results based on simulations, which show that the total number of sensors/ actuators should equal the number of propagating modes to ensure the numerical robustness of the control system. This postulation limits the frequency range of the ANC system (according to the authors to $k \cdot R_{|max} = 16$) beyond which it becomes inefficient even if the required number of sources/ sensors would be used due to the poor conditioning of the control matrix.

Within the same European research project (RANNTAC)[23], Maier et al. [95] conducted tests on a model fan using different types of error sensors and control strategies, which helped to largely reduce the number of actuators.

Even if not one of the latest publications on ANC systems, the paper by Berge, Bouty, and Cailleau [96] should be referenced at this point, in which they used a Boundary Element Method to study the efficiency of Active Noise Control not only with respect to a global

[22] In digital signal processing, the Nyquist criterion states that the sample rate has to be at least twice the highest frequency contained in the signal to accurately identify its constituents.
[23] RANNTAC = Reduction of Aircraft Noise by Nacelle Treatment and Active Control

attenuation, but also for a directivity control reducing the power radiated into certain sectors (e. g. in direction to the cabin or the ground). This objective is also being pursued by the 'Virtual Scarf' technology presented in this thesis (chapter 4), however by fundamentally different means.

In summary, the application of an adaptive liner system to an aircraft engine inlet seems to be rather complicated yielding only a limited potential. This is related to the characteristics of the sound field at the two certification conditions takeoff and approach. In general, the acoustic liners are being optimized for the dominant BPF tones at approach. At takeoff, where Buzz Saw Noise plays an important role, they perform adequately, but different measures have to be used to limit the impact of these multiple tones (as e. g. the Zero Splice Intake presented within the next part). Moreover, an adaptation of the resistance might be already accomplished by the proper selection of a resistance sheet exhibiting a suitable frequency dependence.

Concerning Active Noise Control systems, the complexity, the non-negligible additional weight of the actuators, and the power requirements prevented an application to aircraft engines up to the presence. Thus, the most important scope of work is the design and fabrication of powerful, lightweight actuators.

To create a transition to the following section on non-uniform lining design, it its referred to the 1999 NASA report by Bielak, Premo, and Hersh [97]. In this summary of current and advanced lining concepts for enhanced noise reduction and increased bandwidth (e. g. multi DOF passive liners, adaptive liners via bias flow or heating), the authors evaluate the potential of a uniform liner optimization to be limited, similar as the improvements due to increased DOFs or an adaptation of the impedance. In contrast, the authors believe that the maximization of the lined area, including also a modification of the inlet geometry (compare scarf inlet concept to be presented in the next section), offers a much larger potential. Even if not studied in detail, they consider modal scattering to be another promising method to increase attenuation of low order modes. Several of these technologies will be presented shortly in the next section dealing with non-uniform configurations - both in terms of boundary conditions and modifications of the geometry.

2.3.3 Non-uniform configurations

This final section of the state of the art of duct lining concepts addresses all kinds of non-uniform configurations, which might be either a non-uniform impedance distribution in the circumferential, axial, or both directions (compare figure 2.32) or a non-uniform inlet geometry itself. Several concepts have been studied and proposed in the literature, but only few yielded favorable results without distinct drawbacks and could be included into real engine designs.

2.3.3.1 Segmented impedance liners

The first attempt to optimize an *axially segmented liner* (top left sketch in figure 2.32) has been published by Wilkinson [41] in 1971. He used an analytical technique coupled to a gradient method for the optimization of a two segment lining configuration. However, his study resulted in quite similar impedance values of the two segments, which might suggest a near optimum efficiency of a uniform liner. Yet, Wilkinson stated numerical problems and mentioned the difficulty to define the optimization criterion (e. g. the overall radiated power into a certain reference sector or discrete pressure values in the far field).

As referenced before, Lansing and Zorumski [48] were in 1973 the first to use a mode matching method to study the effect of multiple lining segments. They stated that 'multi-

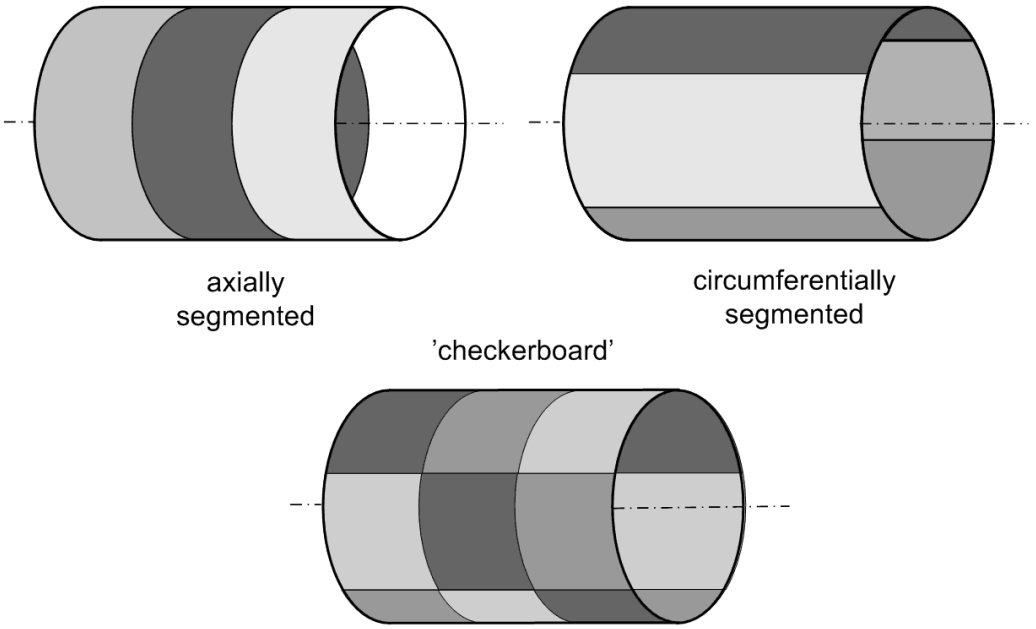

Figure 2.32: Schematic sketch of multisectioned ducts

sectioned ducts with varying admittance can be made more effective than full-length liners with constant admittance'. In a subsequent NASA report, Zorumski [49] summarized equations for the calculation of reflection and transmission coefficients of circular and annular ducts including multiple acoustic treatments. He also demonstrated that the amount of reflections is proportional to the differential acoustic admittance of the two adjacent liner segments.

Quinn [98] studied an axial segmentation using a finite difference solution scheme and maximization of the attenuation as a function of the complex impedance values of the individual segments, however confined to the plane wave mode. His results indicate a substantial improvement using three-sectional linings, and only limited potential for a larger number of axial sections, especially with respect to the considerably increasing computation time for the optimization algorithm. Concerning the reasons for this enhanced attenuation, Quinn agreed with Beckemeyer (personal communication) that the liner segmentation affects the modal composition, which leads - in favorable cases - to a more effective absorption by the subsequent panels.

Pursuing the same objective but with different means, Sawdy, Beckemeyer, and Patterson [99] tried to understand and assess the potential of the mechanisms causing increased attenuation values for axially segmented liner configurations.They, as well, identified modal conditioning as the primary reason for the improved performance. For the liner optimization, they used an analytical procedure solving the Helmholtz equation including boundary conditions at the duct walls and the junctions, and three different techniques to solve the eigenvalue equation (Newton-Raphson iteration, numerical integration, and Rayleigh-Ritz) coupled to a conjugate gradient method[24] with the total sound power attenuation as the cost function. The authors remarked that the optimum values are not necessarily global optima, but depend on the starting values and the optimization step size. For single segment liners, they found the identical optima as Rice [38], and for the two and three segment linings

[24]The conjugate gradient method is an iterative algorithm for the numerical solution of systems of linear equations, which are too large to be handled by direct methods, and can be also applied to optimization problems.

enhanced attenuation values for non-uniform liner impedances, which agreed very well with laboratory tests.

Baumeister [100] also carried out an axially segmented liner optimization using finite difference as well as mode matching methods. He started from the optimum single segment values and iterated alternately until the changes in the results became very small, which however does not indicate a global optimum. While in his results, an optimized two segment liner yielded a certain potential compared to a uniform one for a plane wave input, Baumeister evaluated the increase in bandwidth not to be significant. For a multimodal (equipartitioned) input, he observed larger degradations for the optimized two segment liner than for a uniform one, which confirms the increased sensitivity of the segmented liner to changes in the input sound field. In summary, Baumeister denied a sufficient advantage of an (axially) multisectioned liner except for the low frequency domain.

However, optimization studies concerning segmented acoustic liners have been repeatedly conducted, at last by Reimann, Tinetti, and Dunn [101] presented at the 2007 AIAA Aeroacoustics Conference. They used the acoustic power inferred from a directivity arc around the nacelle as the objective function to be minimized, and compared six optimization algorithms with respect to their sensitivity, complexity, and limitations. In result, they found a considerable potential for a segmented lining, whereas also the complexity of integration of the respective concepts into the nacelle has to be taken into account when comparing the different designs.

In subsequent studies to Baumeister [100], researchers tried not to optimize the single segments by purely mathematical optimization routines, but pursued specific objectives with an axial segmentation. One of the most promising attempts is probably the combination of a mode scattering and an absorbing element, as described and patented by McAlpine et al. in Refs. [102] and [103]. They designed a two segment inlet liner using the same resistance sheet but different cavity depths, in which the one closer to the fan serves as a scattering segment exciting primarily modes which can be attenuated very effectively by the second segment. The whole system has been optimized for a single rotor alone mode (buzz-saw noise, compare chapter 2.2). In future work, the authors plan to extend the concept to multi-modal sound fields and multisectioned liners.

Basically the same concept is used by Rice, Hersh, and Walker [104] in their patent specification of a hybrid segmented liner system. However, they used an active control component composed of a controller, a resonator, and an array of error microphones to scatter the sound field radiated from the fan. This makes the system more complicated, but, in parallel, adaptable to different conditions and input sound fields.

An alternative approach has been presented by Patrick in his patent specification [105] of a non-uniform liner. The preferred embodiments represent continuous or stepped axial variations of the acoustic impedance by changes in the perforation size and/or cavity depth. These measures aim at a selective modification of the propagation angles of the incident modes depending on their axial position within the inlet. Accordingly, a mode propagating at a small angle with respect to the duct axis (well cut-on mode), should be reflected into a steeper angle at a position far from the duct termination to maximize the effective length of the lining. Contrarily close to the exit plane of the duct, where an incident mode should be deflected into a more axial direction to increase the distance to the ground.

The first references to a *circumferential segmentation* (compare top right sketch in figure 2.32) of an acoustic treatment can be found in the patents of Lipstein [106] and Mani [107] from 1975 and 1976, respectively. While Lipstein proposes a segmentation into two semicircular liner patches, Mani uses a multitude of alternating strips of different impedances for modal scattering. By enforcing a circumferential periodicity, to which the incoming sound field has to conform, he tried to excite high order azimuthal modes which

attenuate exponentially as they are cut-off. In contrast, Lipstein reduces in his preferred embodiment the lining to the upper half of the engine inlet, which he considered most relevant for radiation towards the ground. By this measure he intends to save weight, or conversely, increases the absorption coefficient by using a different kind of material.

Concerning prediction tools, Astley, Walkington, and Eversman [108] extended their previous work [109] to be applicable also for non-uniform lining or duct geometries. Therefore, they had to solve the full 2d eigenvalue problem by means of an FE weighted residual method.[25]

Watson [110] performed extensive numerical studies with varying modal input sound fields, frequencies, and lining configurations, and compared them to test results obtained in the NASA Spinning Mode Synthesizer. He concluded that optimized segmented liners were more effective than a uniform liner for higher azimuthal order spinning modes close to the cut-off frequency. According to him, they also offer additional broadband performance and no strong dependency upon variations in the input sound field. Within his optimizations, he determined an alternating pattern of hardwall and absorbing liner strips to be most effective. In contrast, the optimization of alternating linings of different finite absorptive impedances converged to the uniform liner solution.[26]

Another optimization study comparing axially and circumferentially segmented liners to a uniform reference case by Malbéqui and Gounet presented in 2005 [111] yielded several dB of additional attenuation depending on the frequency and field of application (BPF, BSN) for the axial segmentation, and even better results for azimuthally varying impedances. However, no clear strategy has been pursued, and the optimization did not guarantee the localization of global maxima.

To conclude the treatment of segmented linings, the third alternative proposed in the lower part of figure 2.32, the so-called *checkerboard liners*, which consist of a combination of an axial and a circumferential segmentation, will be analyzed. Watson et al. [112] studied in 2002 systematically all possible variations, as well as a uniform liner, using an FE method coupled to different optimization procedures (iterative, gradient, genetic algorithms). They observed individual weaknesses in the optimization algorithms converging e. g. to the uniform liner solution or local (not global) optima. In result, a circumferential segmentation showed a superior performance compared to an axial one, whereas both were more effective than an optimized uniform solution. Contrary to expectations, the checkerboard configuration converged to a uniform liner for all optimization algorithms. Irritated by this result, and motivated by Howe's [113] statement that a checkerboard pattern should offer an improved attenuation characteristic, Watson et al. conducted additional studies and presented updated results in the subsequent year in Ref. [114]. In these, they demonstrated a considerable potential of checkerboard lining solutions of different periodicities.

Though these configurations followed a common strategy (to scatter acoustic energy into higher order azimuthal modes), the design has merely been determined by an optimization algorithm, and not by a selective assignment of characteristic boundary conditions.

Essentially also a kind of circumferentially non-uniform lining, the effect of hard strips or *liner splices* resulting from the segmentation of the acoustic liner for easier manufacturing (compare figure 2.33) on the attenuation and modal characteristic has first been studied by Rademaker, Sarin, and Parente [115] in 1996. They noticed clearly observable scattering effects in in-flight measurements of circumferential modal spectra of a real engine containing three inlet splices. Accordingly, they started a test campaign in the NLR Spinning

[25] As will be mentioned in chapter 2.4.3, for these non-uniform configurations, analytical solutions are not available.

[26] However, the question remains whether the optimization routine (a quasi-Newton algorithm) as well as the starting values were appropriate to obtain a non-uniform solution.

Mode Synthesizer to analyze the splice effects on a predefined modal sound field, and found only minor effects on the total transmitted energy for low azimuthal mode orders, although scattering effects were clearly visible in the modal spectra. For subsequent studies, they proposed to analyze high order azimuthal modes, which are characteristic for a real turbofan intake configuration, as well as initially cut-off modes, which might contribute to the sound radiation by being scattered into propagating modes. These, and additional experimental findings, have been confirmed by FE calculations performed by Regan and Eaton in 1998 [116].

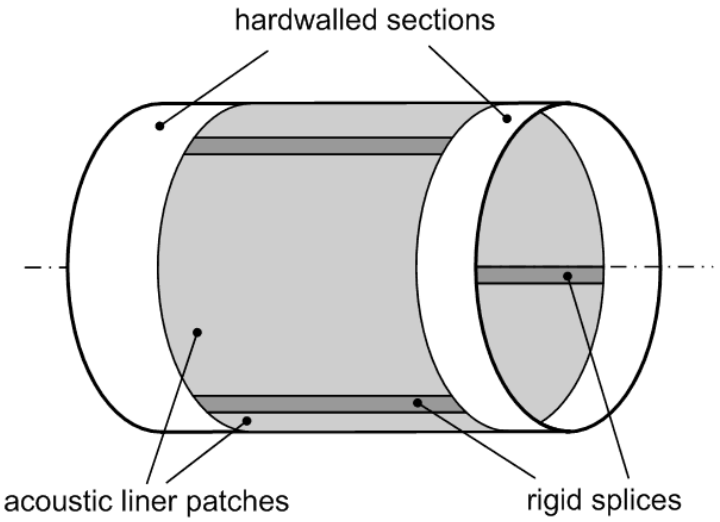

Figure 2.33: Schematic sketch of spliced inlet liner

Especially in the recent years, starting in 2002, several papers have been published dealing with the effect of liner splices. The first one of them by Elnady and Bodén [117] investigates the respective influences of splices on locally reacting and non-locally reacting liners by a collocation method (compare chapter 2.4.3.2). They found a larger impact by the liner strips on locally reacting treatments, which show a pronounced dependency of the effect on the modal order (decreasing in case of an equipartitioned sound field) compared to bulk absorbers.

McAlpine et al. [118], [119] conducted Finite as well as Boundary Element[27] computations for different flight conditions (approach, cutback, sideline) and tonal (BPF, BSN) as well as broadband noise sources. They concluded that the scattering effects are most prominent, and may dominate the overall sound field, for modes close to cut-off. These modes are in idealized (spliceless) conditions very effectively attenuated by the liner. Thus, scattering into modes of a higher cut-off ratio yields increased noise levels, which is more critical at cutback than at sideline conditions, and least pronounced at approach. Accordingly, in the conclusion the authors also mention the necessity of novel noise control methods to increase the attenuation of well cut-on, nearly axially propagating and radiating modes. The general results with respect to the modal effects have been confirmed in 2005 by Bi et al. [120]. For a more realistic sound field, these authors used a multimodal propagation method presented in Ref. [121].

To accelerate parametric studies involving liner splices, Tester et al. [122] validated an existing analytical model by a comparison to FE calculations and found an acceptable agreement for engineering purposes. Alternatively, Wright [123] proposed a hybrid approach

[27] The BE calculations have been performed using the EADS in-house BE code ACTIPOLE, which has also been used to obtain the results presented within this thesis and is described in chapter 2.4.3.4.

matching the numerically calculated eigenmodes of the spliced duct with the analytical hardwall solutions in the adjacent axial parts by means of the mode-matching method. His concept has been extended by himself and McAlpine in 2007 [124] to problems involving flow.

Based on this knowledge of the effect of rigid liner splices in engine intakes, Batard [125] and Gantie et al. [126] studied the acoustic benefits resulting from the elimination of these splices. Accordingly, they named their concept *Zero Splice Intake Liner (ZSI)* and demonstrated significant noise reductions at BPF for a range of engine operating conditions. However, they noticed that a proper manufacturing process had to be developed in parallel to achieve the desired goals. This has been done in subsequent work, resulting in an application of this technology in the nacelles of the Airbus A380 engines introduced into service in October 2007.

Boeing also conducted studies concerning the elimination of liner splices and the maximization of treated area in the context of the Quiet Technology Demonstrator 2 (QTD2) project, presented e. g. in Reed [54] and in more detail in Yu et al. [127] in 2006. Their extended liner design started closer to the fan plane and ranged up to the lip area of the inlet, where it has been integrated with the anti-icing system. This area maximization has been implemented into an acoustically smooth design, avoiding splices both in the axial and the circumferential direction. Accordingly, a significant noise reduction could be measured both in the far field and inside the cabin.

This concludes the description of the non-uniform lining configurations and the corresponding methods of computation, and leads to another embodiment of the non-uniformity: the geometry of the inlet itself.

2.3.3.2 Changes to the duct geometry / noise shielding

Already in early years, inventors proposed a modification of the axisymmetric inlet geometry of an aircraft engine to shield radiation from certain sectors, e. g. towards the ground or in direction to the fuselage. Most of these - later on called *scarfed inlets* - include movable parts to either deploy the component only during certain phases of the flight or make it adjustable to varying operating conditions. In 1968, Brown [128] filed an application for a patent (granted in 1970) comprising an extensible lower part of the front inlet, which, if deployed, yields an inlet plane at an oblique angle to the duct axis as shown in the upper sketch in figure 2.34.

Slightly different, Neumann [129] designed in 1976 a deflector, which can be moved axially and circumferentially to selectively shield noise from sectors estimated most important in the respective operating condition. This would be the region directed towards the ground at takeoff or approach, but the lateral one in direction to the fuselage during ground operations. In contrast to Brown, Neumann chose a semicircular cylindric geometry of the deflector yielding a stepped inlet geometry in a side view (lower part in figure 2.34).

Recently, Sankrithi and Nelson [130] proposed a scarf inlet configuration combined with a means to rotate the scarf to achieve optimum conditions at different phases of the flight. Their considerations were related to airflow characteristics, the ingestion of foreign objects from the runway (to prevent FOD (foreign object damage)), as well as acoustic aspects. Therefore, the rotatable asymmetric inlet portion would be directed to the sky at takeoff and towards the ground in the cruise configuration.

In general, two types of studies have been conducted with respect to the scarf inlet: the ones analyzing the acoustic benefits through shielding and influencing the directivity, and the ones investigating possible aerodynamic penalties by inflow distortions and separations. Starting with the acoustic part, a study comparing different inlet designs (short and long

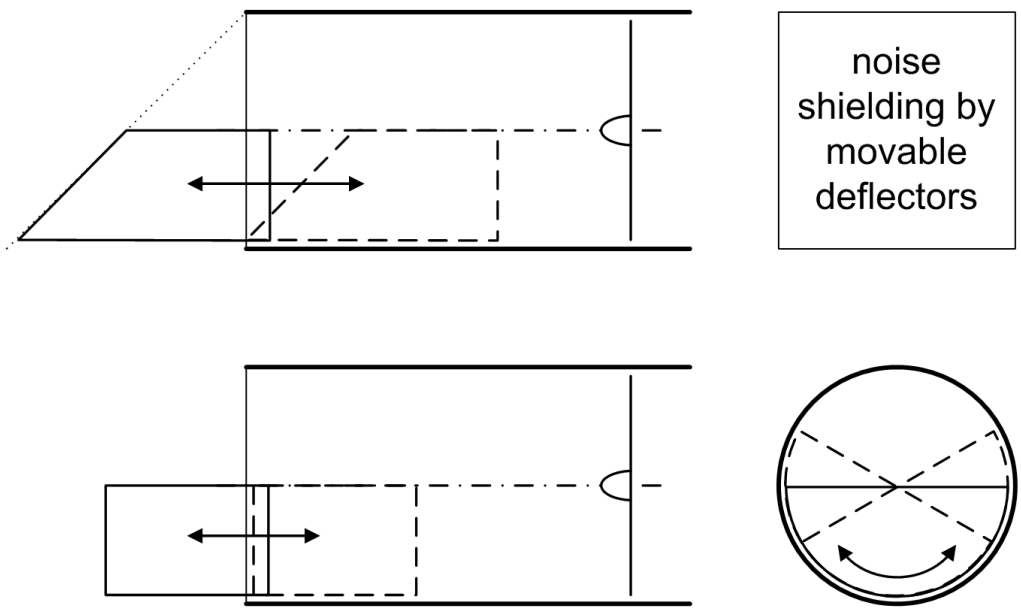

Figure 2.34: Schematic sketch of noise shielding mechanisms involving movable deflectors

symmetric inlet, scarfed inlet, elliptical inlet) by acoustic wind tunnel measurements and raytracing predictions[28] has been presented by Clark et al. [131]. They found differences for tonal and broadband noise and emphasized the possibly important effect of the boundary layer on the noise generation mechanism. However, in general, the scarf intake yielded quite promising results.

Within the framework of the European research project SILENCER, Airbus France performed intense investigations related to a design named the 'Negatively Scarfed Intake (NSI)'. At the 2005 AIAA Aeroacoustics Conference, Montétagaud and Montoux [132] presented a synopsis of the results ranging from numerical computations (BEM and raytracing), validation experiments in an anechoic chamber, a brief summary of CFD analysis (Computational Fluid Dynamics) and wind tunnel measurements,[29] and estimations of the overall impact on fan, engine, and total aircraft noise. As well, first result of a flight test campaign performed in December 2004 could be shown. These results indicate a considerable acoustic benefit of the NSI in the lower forward sector and demonstrated the shifting of the directivity curve to more positive angles (corresponding to a radiation more focused on the upper sector). This generates benefits both in takeoff and approach conditions measurable also in context of the overall aircraft noise with reductions of -1.1 EPNdB and -1.4 EPNdB, respectively.

Aerodynamic penalties resulting from the extension of the lower inlet lip have been seen as one of the major drawbacks of this technology. Thus, several attempts have been made to reduce the inflow distortion while maintaining the scarf effect concerning the acoustic radiation. Exemplarily, only two attempts will be mentioned here, namely the patents by Kutney and Mishler [134] and Curtin et al. [135] who both tried to create smooth transitions from the asymmetric inlet to the symmetric inner duct.

Abbott and Slater [136] performed a CFD study comprising three parameters: the lip thickness and the axial and circumferential extent of the lower lip extension. As found in a previous paper [137], they showed that the scarf effect can enable the aircraft to operate at

[28]The basic concept of raytracing will be summarized in chapter 2.4.3.
[29]More details of the aerodynamic analyses can be found in Smith et al. [133].

higher angles of attack (AOA) at takeoff conditions due to the upward shift of the streamlines (resulting in a reduced effective AOA). This could permit a thinner lip design reducing drag and weight. However, on the downside, the scarfing also implicates aerodynamic problems at other flight conditions. Especially at low airspeeds (as during approach), the flow might separate at the upper lip due to an elongated path of the streamlines implicating increased velocities. A second drawback might be the increased drag in the cruise condition due to the asymmetric spilling at the upper lip.

The problems of inflow distortion at low airspeeds, and even more on static test rigs, have also been mentioned by Gerhold, Clark, and Biedron [138]. They tried to counteract the increased turbulence level due to the asymmetry of the inlet and the resulting elevated noise levels at BPF by an inflow control device (using boundary layer suction), but did not succeed satisfactorily, for which they blamed the controller and the arrangement of suction holes.

Within the AIAA paper by Montétagaud and Montoux [132] and the companion paper dealing with the aerodynamic aspects (Ref. [133]), the three critical conditions static operation, crosswind ground operation, and high AOA, have been studied by CFD simulations and wind tunnel experiments. After completion of the analysis of several designs, the authors subsumed with the statement that a NSI design capable of fulfilling all requirements can be accomplished using state of the art design tools. However, a weight and drag penalty resulting from the extension of the lower inlet lip has to be balanced with the acoustic advantages in the design of novel aircraft.

2.4 Analytical and numerical methods

As has been mentioned in the first section of this chapter (section 2.1.1.4, in the context of the derivation of the eigenvalue equation for a lined duct), the determination of the eigenvalues involves the solution of a complex transcendental equation (2.62) which, in general, cannot be solved directly.

However, several attempts have been made to find a fast and dependable method for the general case involving an acoustic lining of an impedance $Z = R + i \cdot X$ and a flow of Mach number $M \neq 0$.[30] Starting from simple chart procedures and direct analytical solutions, more and more elaborate procedures have been developed up to the use of discretization techniques as the FEM and the BEM.

Within the following, a short summary of the various methods will be given including their individual advantages and drawbacks.

2.4.1 Chart procedures

The first attempts of finding solutions to the lined duct problem have probably been made by Sivian in 1937 for a plane wave propagation [139] and Morse in 1939, who applied room acoustic theory [140] to the transmission and attenuation of sound in pipes of rectangular and circular cross section [141]. He defined a dimensionless frequency parameter $\eta = f \cdot D/c$ and related the complex distribution parameter $\mu + i\kappa$ describing the distribution of pressure across the tube to a transmission parameter $\sigma + i\tau$, which determines the propagation and attenuation of the wave throughout the duct in the presence of an acoustic lining.

In a two-step procedure, *Morse's method* thus allows for the calculation of the attenuation and propagation properties of an arbitrary mode by relation of the wall impedance to the distribution parameter, and subsequently, of the distribution parameter to the transmission parameter. By the use of charts, conformal transformations have been facilitated for the whole range of relevant impedance values.

Morse's procedure has been extended for circular ducts by Molloy and Honigman [142] (using a series expansion for the Bessel function), and applied to the two general types of problems:

- *the direct problem* involving the determination of the optimum lining impedance for a given distribution parameter (mode), duct dimension, and frequency,
- *the indirect problem* of determining the attenuation of a given mode in the presence of a lining.

Though of considerable value for quick estimates, and practical, as only one chart is required for all duct configurations, the Morse charts become impractical in the presence of a flow due to their limitation to a single Mach number. However, the values obtained from the Morse charts might still serve as starting values for an iterative scheme (as will be presented in the following).

An alternative to the solution of Molloy and Honigman [142] has been published by Fisher in 1945 [143] for the plane wave mode and adopted by *Rice* in 1968 [38] in his first of a series of papers dealing with the attenuation of sound in ducts with an acoustic treatment. In this publication, Rice extended Fisher's solution to higher order axisymmetric modes (i. e. $m = 0$), and showed that Morse's solution represents a good approximation for 'nearly hardwalled' ducts (i. e. walls with a low attenuation), but loses validity in realistic applications involving an acoustic lining of a considerably reduced impedance.

[30] Within this thesis, the influence of the flow will be confined to a uniform mean flow of Mach number M.

In the impedance plane, contour plots of constant attenuation form closed shapes (compare also figure 2.27), which can be approximated by circles as would be the case in Morse's solution. This remains true - with an adequate accuracy - also for high attenuation values. However, as presented by Rice for a finite absorptive impedance, the centers move towards negative reactance values and positive resistances compared to the Morse charts, in which the maximum attenuation occurs at a zero reactance ($X = 0$).

With increasing attenuation values, the contour plots converge to a point, which represents the maximum achievable attenuation. Beyond this attenuation value, another closed shape is being formed, corresponding to the next higher radial mode of the same azimuthal mode order m. An example of this characteristic is depicted in figure 2.35 for the axisymmetric modes at a fixed dimensionless frequency and duct length-to-diameter ratio (L/D). It shows, on the left hand side, the solution for the zeroth radial mode with the centers of the circular attenuation contours located on the real axis (at $X = 0$). In contrast, for increased attenuation values (higher attenuation constant σ), the contours delineate a different closed contour (as described above), whose center point has moved into the complex impedance plane.

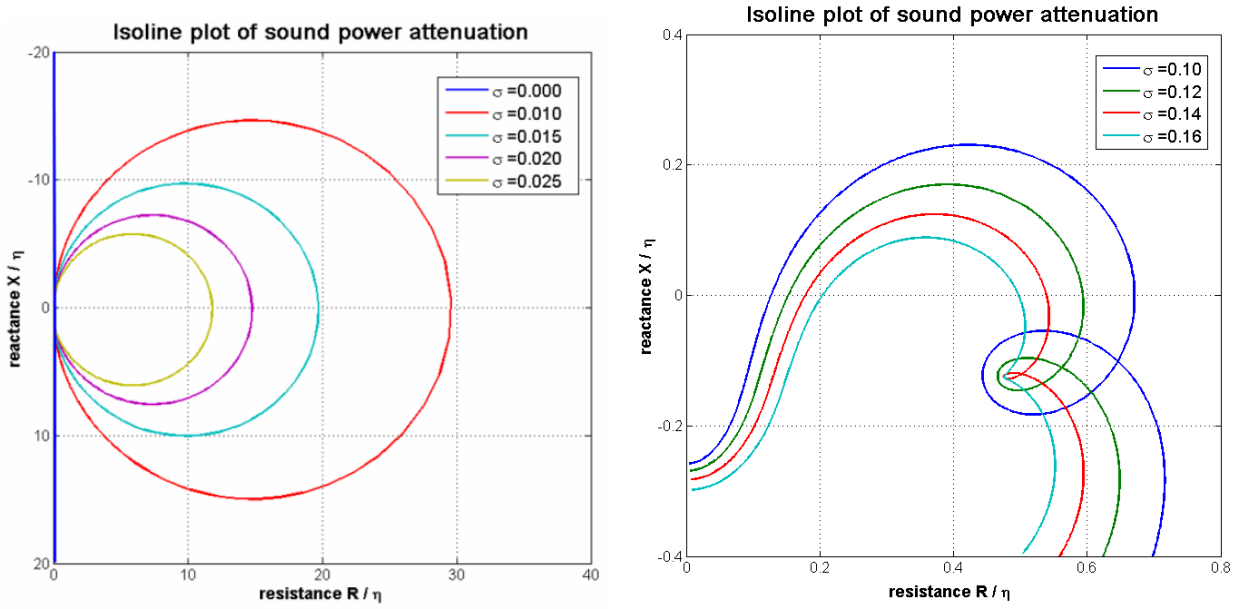

(a) near hardwall solution

(b) increased attenuation values

Figure 2.35: Example of sound power attenuation contours in impedance plane

In subsequent papers, Rice extended his theory to include flow effects (Ref. [144]), and later on generalized it to spinning modes of azimuthal order $m \neq 0$ (Refs. [39], [40]). Additionally, he reduced the amount of input parameters to solely the eigenvalues and derived correlating equations to determine these analytically from the corresponding zeroth radial solutions (Ref. [145]).

This method of finding the optimum impedance value and the maximum achievable attenuation, even if generally applicable and widely elaborate, still constitutes a search technique, which requires a certain knowledge of adequate starting values for the propagation and attenuation coefficients to prevent an omission or misinterpretation of the zero points. However, if approximate eigenvalues have been determined by other means, this technique might serve to refine the results.

2.4.2 Iteration schemes

As an alternative, iterative numerical methods have been employed, the most established one being the *Newton-Raphson iteration scheme*. It can be applied to finding the zero points of the eigenvalue function (equations (2.28), (2.62), and (2.65)) of hardwalled or treated ducts, possibly including a uniform flow. For the hardwall condition, both in the zero flow ($M = 0$) and uniform flow case ($M \neq 0$), this method proves to be very efficient and reliable, as has been shown in the examples in figures 2.9 and 2.11.

In contrast, in lined duct configurations, where the eigenvalues are complex values, the Newton-Raphson scheme becomes unreliable for low wall impedances. This is related to the requirement of adequate starting values for the iterative procedure. Otherwise, the method might not converge, or yield incorrect results related to the convergence to a wrong root.

For the zero flow case, Christie [146] published results of his study using the Newton-Raphson scheme, in which he started at a low frequency and iteratively used the results of one frequency step as the starting value for the next frequency step. This procedure seems to increase the reliability, but obviously is quite time consuming.

In presence of a uniform flow, Ko [147], [148] used a similar procedure of stepwise increments up to the frequency of interest. Additionally, he included a wall impedance iteration within each frequency loop starting from the hardwall solution.

Contrarily Eversman [149], who directly solved the eigenvalue problem using a Newton-Raphson procedure for the zero flow condition, and then gradually incremented the Mach number within the iteration loop. However, his results were limited to the plane wave mode within a rectangular duct. In a subsequent approach, Eversman [52], [150] transformed the two coupled transcendental non-linear equations (2.64) and (2.40) into a first order differential equation, which can be integrated using a Runge-Kutta algorithm with variable step size, coupled to a Newton-Raphson algorithm to reinitialize the process in case error bounds are exceeded.

An alternative to this approach used for the validation of the numerical results obtained from Boundary Element calculations within the context of this thesis is presented in the following. It starts from the hardwall condition, in which the eigenvalue is a real number, and gradually reduces the impedance to the desired value. The general process of finding the eigenvalues, which is equivalent to finding the zeros of the eigenvalue function (EVF), is depicted in figure 2.36.

On the left hand side, an overview is given of the complete process for a fixed azimuthal mode order. In the first iteration, the imaginary part of the eigenvalue $Im(\kappa)$ is set to zero which corresponds to the hardwall solution. Subsequently, the real part of the eigenvalue $Re(\kappa)$ is treated, the process of which can be observed in detail on the right hand side of the figure.

It consists of an additional loop for each radial mode order, which constitutes the respective N-th zero point of the EVF. For the determination of the approximate zero position, $Re(\kappa)$ is varied within an appropriate interval, which has been chosen at initialization, or, in the next iterations, has been determined in the previous cycle. With these values ($Re(\kappa)$ defined within the current loop and $Im(\kappa)$ from the previous iteration), the EVF is being computed and the sign change detected. This yields the approximate zero position as an input to the next part of the computation, the imaginary part loop.

The loop over the imaginary part of the eigenvalue is exactly analogous to the real part loop described above, but with interchanged functions of the real and imaginary parts. After a successful completion of this loop, the resulting EVF is computed and compared to the predefined error limits. If these conditions are satisfied, the computation of the next azimuthal mode number m starts. Otherwise, the next iteration is launched after an

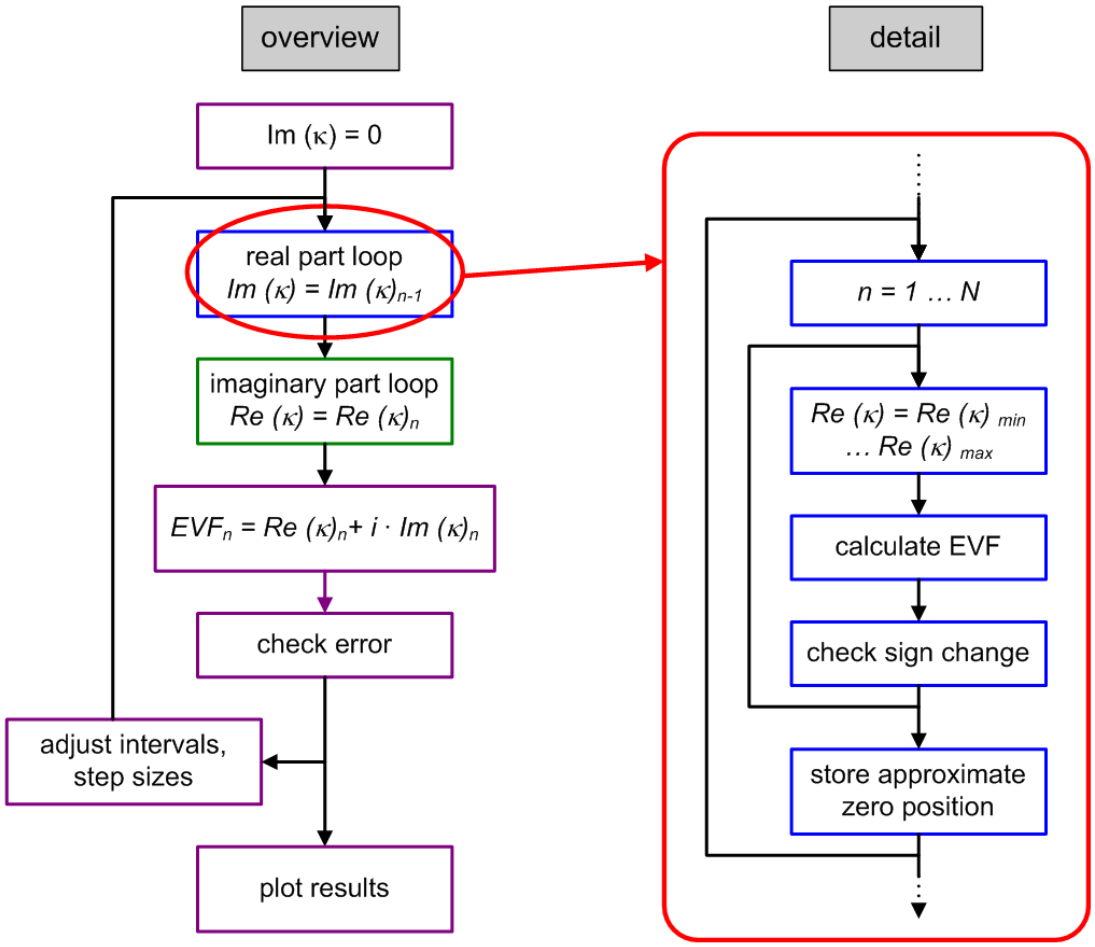

Figure 2.36: Schematic sketch of eigenvalue search procedure

adjustment of the search intervals and step sizes.

In practice, the finding of the zeros of the EVF is unproblematic for the hardwall and near-hardwall cases, which are indicated blue and green in figure 2.37, respectively. It shows an example of the characteristic of the EVF for the first five solutions ($n = 1 \cdots 5$) of the axisymmetric modes $m = 0$.

As can be clearly seen, the characteristic of the EVF changes from the derivative of the Bessel function (compare blue curve in the current figure and upper plot in figure 2.3) to a periodic function including poles (similar to the cotangent function) when reducing the wall impedance from infinity to a finite value. However, for a comparatively large impedance (as for the green curve in figure 2.37), the EVF yields nearly exactly the same zero positions as the hardwall solution, in particular the first zero point of the axisymmetric modes at $\kappa = 0$. Accordingly, the eigenvalue search routine converges quite fast, generally within two or three cycles.

If the impedance of the duct wall is reduced to a value representative of a real engine liner as in the example using $Z = (1 - i \cdot 0.5) \cdot \rho c$, the EVF function is being shifted downward and to the left as shown by the red curve in figure 2.37. This eliminates the first eigenvalue (first zero point at $\mathrm{Re}(\kappa) = 0$), which causes the algorithm to diverge. Up to a certain amount, this divergence problem can be avoided by iterating the eigenvalue from the hardwall solution and decreasing the step size between succeeding iterations. However, without an extensive effort, the divergence problem remains for a certain low impedance range.

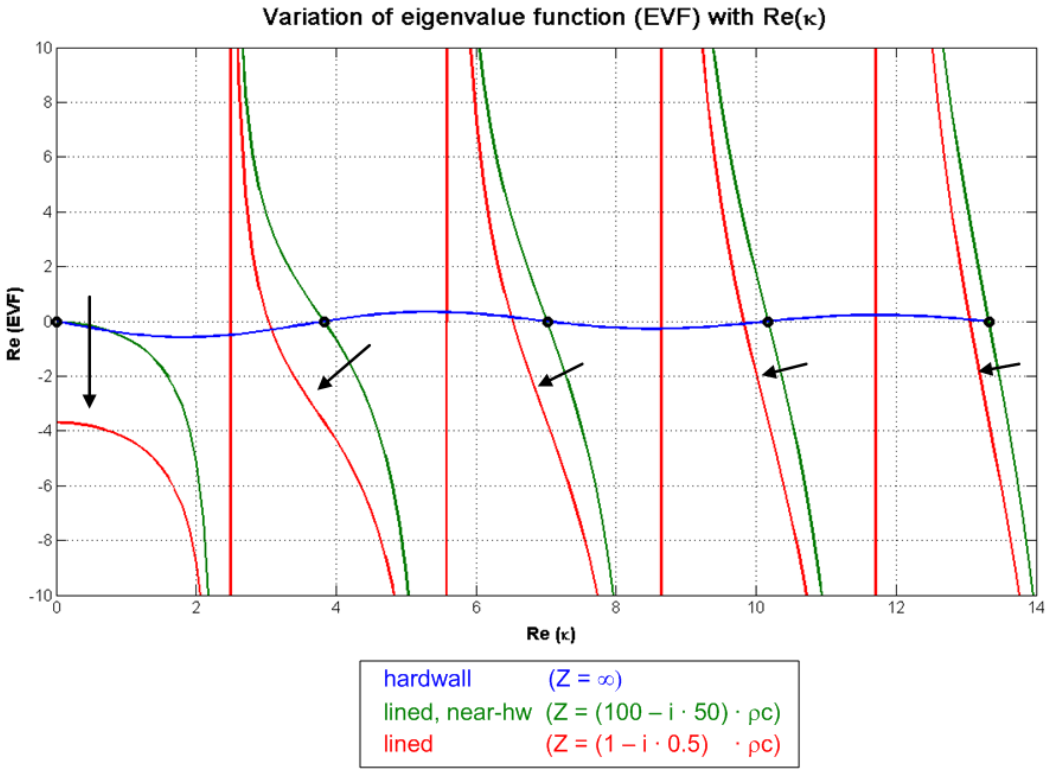

Figure 2.37: Eigenvalue function (real part) as function of complex wall impedance; m = 0

Figure 2.38 shows an example of the corresponding variation of the real part of the eigenvalue with the real part of the wall impedance for various iteration step sizes.

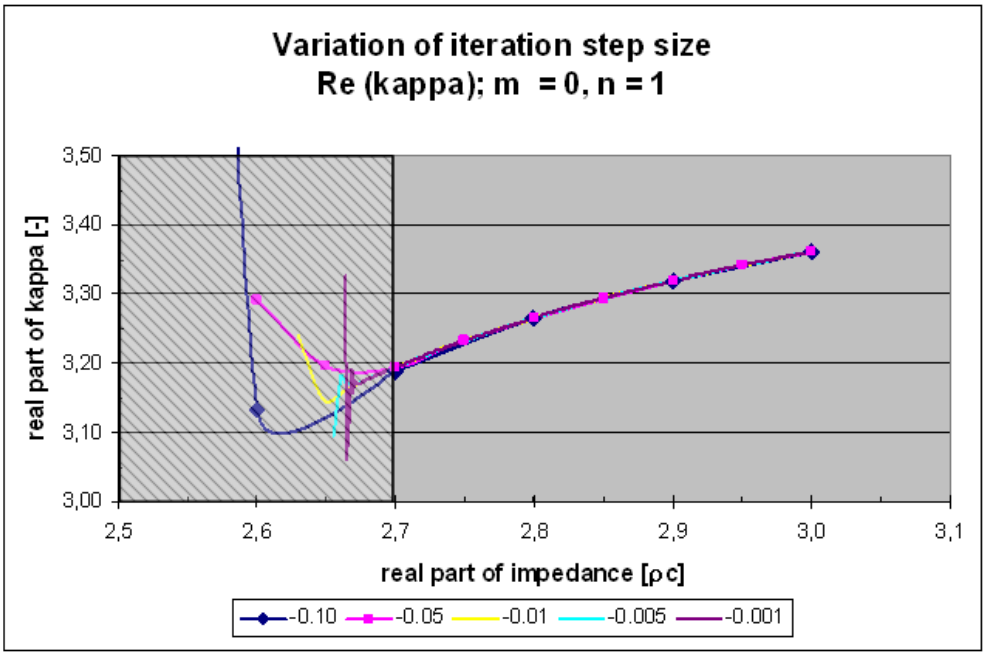

Figure 2.38: Dependency of the eigenvalue function upon iteration step size; m = 0, n = 1

It appears that the divergence problem does not directly depend upon the step size, since the wall impedance and the eigenvalue lose their clear correlation at a fixed lower limit of the impedance (at approximately $R = 2.7 \cdot \rho c$) independent of the step size.

2.4.3 Discretization methods

Discretization methods, which are considerably more time-consuming than the procedures presented above, are mainly used in applications involving non-uniform liners in the circumferential direction, which cannot be solved by analytical means or continuous numerical methods. Furthermore, these methods yield a complete set of eigenvalues and do not bare the risk of omission or duplication of certain eigenvalues, as experienced with continuous methods. However, this is granted only if performed at a sufficient discretization accuracy.

In the field of numerical acoustics in the frequency domain,[31] several fundamentally different methods are used depending on the frequency range and application case. Figure 2.39 presents the most important methods grouped with respect to these two categories.

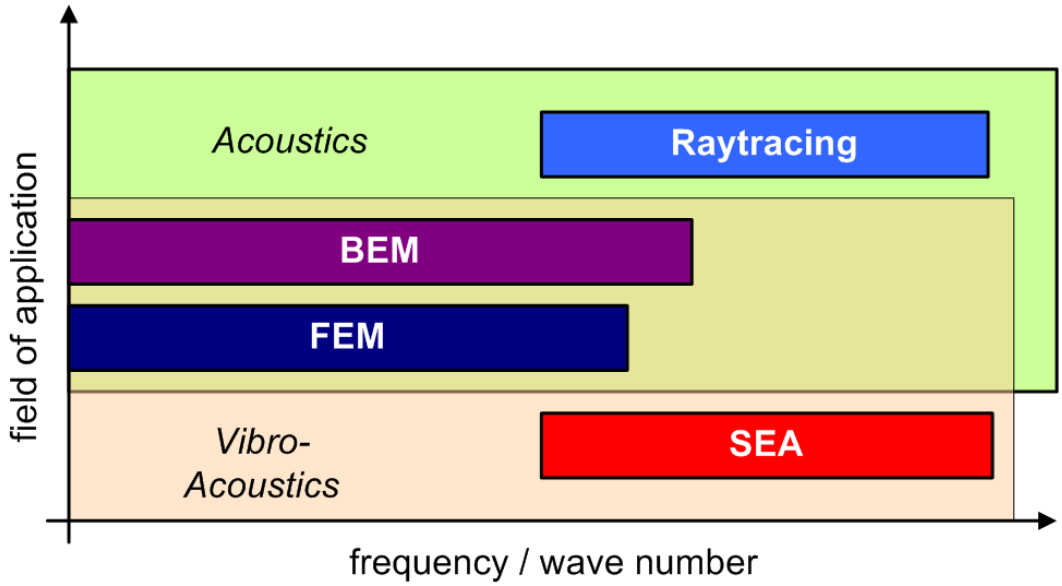

Figure 2.39: Frequency ranges and fields of application of frequency domain numerical methods (according to v. Estorff, TU Hamburg-Harburg [151])

In acoustic applications, the *Boundary Element Method* and the *Finite Element Method* are conveniently used in the low and mid-frequency range (up to several Kilohertz). Whereas the FEM is mainly used for acoustic problems within closed structures as the interior of a car or an aircraft passenger compartment, or in case structural-acoustic coupling has to be taken into account (for *vibroacoustic* applications), the BEM is conveniently employed for radiation and scattering problems dealing with the interference of rigid or acoustically treated bodies with acoustic fields. Both methods use discretized meshes and a deterministic excitation, however, with different characteristics in respect to a number of categories, as will be presented in the next subsection.

In the high frequency range, both methods become impractical because of the large number of elements involved. Therefore, alternative numerical methods have to be applied, which make use of additional simplifications or generalizations reducing the computation time and the storage space.

For purely acoustic problems, *raytracing* procedures can be used which approximate the acoustic propagation and radiation by rays, a tolerable simplification in the high frequency

[31] Time domain methods are mainly used in applications involving the exact computation of flow fields by CFD codes. In these cases, the formulation of the acoustic propagation in the time domain is convenient to avoid a transformation into the frequency domain. A second field of application are broadband noise fields spanning the whole frequency range, which would require a large number of runs using frequency domain methods, but only one computation using a time domain procedure.

range where diffraction effects become negligible. Raytracing originates from the field of optics and uses a backward procedure to determine possible origins of a ray detected by an observer. By assigning the corresponding boundary conditions to the surfaces of the bodies, also absorption, reflection, and refraction effects can be accounted for.

With respect to the applications of this method to duct acoustic problems or engine radiation, more information can be found in Tester [36], who showed that ray models may provide a sufficient accuracy for short ducts, and Boyd, Kempton, and Morfey [152] who included diffraction effects using a statistical assumption. Dougherty [153] used a raytracing procedure to determine the more and less important lining regions within an engine inlet and studied the suspected positive effects of a scarfed inlet. Within the European project DUCAT, Malbéqui [154] compared ray theory results with analytical calculations using a modal approach, which showed a good agreement at Helmholtz numbers $He > 30$.[32] He also analyzed the effect of circumferentially non-uniform liners and observed modal scattering or redistribution effects.

For vibroacoustic problems dealing with higher frequencies, a statistical approach is used to determine the characteristics of structures and cavities. The basic concept of the *Statistical Energy Analysis (SEA)*, which has been introduced in the 1960s, is the breakdown of a complex structure into subsystems, which are excited by external forces and acoustic sources, and are able to store energy or exchange it with other subsystems. In the SEA formulation, only energy or power values are regarded, which constitutes the postulation of an adequate number of propagating modes to average out preferred directions or spatial inequalities. Thus, all modes experience the same energy input, corresponding to a broadband excitation. More information on the theory of the SEA can be found in Ref. [155].

2.4.3.1 Comparison of FEM and BEM

Since they are the two most commonly used numerical methods for the applications considered within this thesis, the BEM and FEM will be compared to each other in the following with respect to a number of categories.

The first, and probably the most noticeable difference between the two concepts is the discretized domain. In the FEM, the whole domain of computation - which, in acoustic applications, is the medium air - has to be discretized by suitable (in general 3d) elements (equivalent to the discretization of bodies in its main field of application, the analysis of structural behavior). This requires quite a large number of elements in case of large cavities, e. g. an aircraft cabin. In contrast, in the BEM only the boundary of the bodies has to be discretized by 2d shell elements, and not the fluid which is treated as a homogeneous medium. This helps to reduce the necessary number of elements by large in most application cases. In figure 2.40, an example of the two different discretization schemes is depicted in terms of a cross-sectional view of a generic aircraft cabin.

However, concerning the relative solution effort, the BEM is less attractive than the FEM, which yields band structured matrices that can easily be solved by standard Gauss elimination techniques. In contrast, the matrices involved in the BEM are, in general, fully populated and require more sophisticated approaches to reduce the solution time.

A possibly advantageous alternative to the direct computation of the FE solution to a given problem can be the use of the modal space. Therefore, at first, a modal basis has to be computed containing the eigenshapes of the structure. This can then be used in a second step to compose an approximate solution at arbitrary frequencies in a considerably reduced time compared to the direct approach. Accordingly, the modal solution space might be interesting in case of a large number of frequencies to be computed. In contrast, due

[32] To recall, $He = k \cdot R$, in which k is the acoustic wave number and R the duct radius (equation (2.39)).

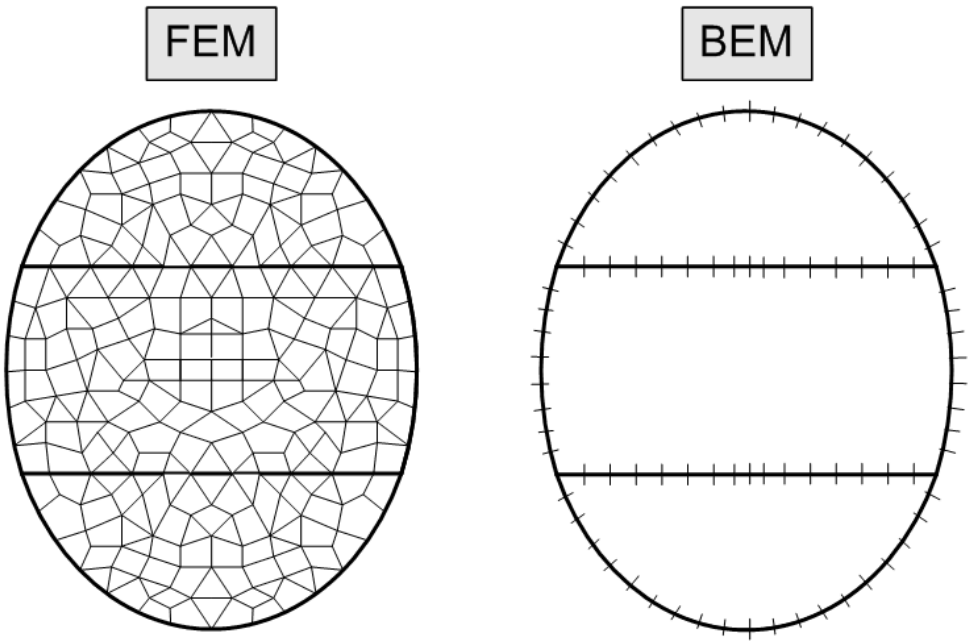

Figure 2.40: Comparison of discretization schemes of the FEM and the BEM

to the transcendental formulation of the frequency in the fundamental solution of the BEM (the Green's function), the matrices are frequency dependent, wherefore the modal approach is not available.[33]

With respect to the variables used in the respective formulations, the matrices in the FEM contain only one variable, which is the sound pressure p in acoustic problems and the displacement δ in structural applications. All other quantities can be derived by differentiation (e. g. the sound particle velocity $v = dp/dn$ in acoustics or the strain $\varepsilon = d\delta/dn$ in structural mechanics). In contrast, in the BEM both acoustic variables p and v are directly used within the equations, wherefore its called a 'mixed formulation'.[34]

As mentioned shortly in the previous subsection, acoustic calculations can be classified into two categories: interior and exterior problems. Their names refer to the domain of computation, which is either the interior of a closed structure or the radiation (to the exterior) and diffraction from rigid or vibrating bodies. In this respect, the FEM is mainly being used for interior problems, in which the fluid has to be discretized by appropriate solid elements (e. g. hexagons or tetrahedrons). As the calculation of exterior problems would require a very large, and in the limit infinite number of elements (the whole fluid domain from the surface of the body to the desired evaluation points would have to be discretized), this approach is not practicable. Hence, so-called Infinite Elements (IE) can be used, which model the transition to the far field. Yet, the use of Infinite Elements requires a sophisticated meshing effort, since the surface has to be mapped to an ellipsoidal surface for radiation problems. Contrarily for the BEM: due to its fundamental principle of discretizing only the surface of the bodies, both interior and exterior problems can be solved equally. Additionally, as will be mentioned in the next section dealing in detail with the assumptions and basic equations of the BEM, two types of formulations of the BEM are available, the Direct and the Indirect BEM.

[33] Solutions to this problem can be found e. g. in Refs. [156] and [157]. More details about the solution process of the BE problem are given in the next section.

[34] The usage of both variables in the solution process of the BEM eliminates a source of error originating from the derivation of secondary variables, as e. g. the particle velocity.

Concerning the inclusion of flow effects, both methods can incorporate a mean flow. Whereas this is limited to a uniform profile for the whole computation domain in the BEM (the fluid is assumed to be a homogeneous medium), the FEM can account for a non-uniform flow velocity distribution.

The last difference consists in the solution process of the two methods. Whereas the FEM uses a one-step procedure, in which the variables of interest at all nodes of the discretized mesh are being solved for at the same time, the BEM computes in the first step only the solution on the boundary of the body. The acoustic variables at arbitrary evaluation points, the so-called field points (FP), can then be easily found in a second step by the use of the laws of radiation from the equivalent source distribution on the boundary added to the direct contribution from the acoustic sources within the volume.

To conclude, table 2.1 summarizes the basic differences and similarities of the FEM and BEM. The question, which of the two is the adequate numerical method for a given problem, thus depends upon several factors, and can only be answered considering all aspects of the problem. Although one of the main factors might be the ratio of the fluid volume to the surface area of the body (which corresponds to the number of solid to shell elements), the question of whether a radiation problem has to be solved, will obviously influence the decision. Additionally, several other factors, as e. g. the number of frequencies to be computed or the type of flow field to be included, will play a role in the selection of the adequate numerical method.

Table 2.1: Comparison of FEM and BEM

criterion	FEM	BEM
discretization	3-d	2-d
formulation	only p used, v by diff.	mixed (p, v used)
procedure	1 step	2 steps
solution effort	low (band matrix)	high (fully pop. matrix)
solution space	direct / modal	direct
interior problems	✓	✓
ext./ radiation problems	only using IE	✓
flow effects	non-uniform mean	uniform mean

Due to the reasoning presented above, and with respect to its superior applicability to radiation problems, the Boundary Element Method has been selected for the acoustic computations performed within this thesis. Its basic equations and assumptions will be presented in the next section followed by a short summary of another state of the art numerical technique which can be integrated beneficially into the solution process - the Fast Multipole Method (FMM). Concluding this section about numerical discretization methods, a comparison of the two BEM codes used in the computations presented in this thesis will be given, the commercially available code LMS SYSNOISE and an EADS/ Airbus in-house code called ACTIPOLE.

2.4.3.2 Basics of the Boundary Element Method

The basic idea of the BEM has been promoted mainly by Chen and Schweikert [158] and Chertock [159] in the 1960s, at first with respect to the application to underwater acoustics. However, it became more and more popular in the subsequent decades with the boom of computing power facilitating the calculating of arbitrary problems with a larger numbers of elements. As mentioned above, the BEM can be subdivided into two distinct methods, the *Direct (D-BEM)* and *Indirect BEM (I-BEM)*. The former one, which will be presented first, corresponds to the solution of either an interior or an exterior problem.

Following the derivation of Moosrainer [160] for an exterior problem, the basic concept of the BEM is based upon the *method of weighted residuals* applied to the fluid volume (which will be assumed finite at first, and then transfered to infinity) and the boundary of the body. Accordingly, in acoustic applications, three types of boundary conditions (BC) can be assigned to a boundary element:

- a Dirichlet BC : $p = p_1$ on A_{s_1} ,
- a Neumann BC : $v_n = v_{n_2}$ on A_{s_2} ,
- a Robin BC : $A \cdot p_3 + B \cdot v_{n_3} = C$ on A_{s_3} .

The first two correspond to the specification of a fixed acoustic pressure or normal velocity value on the boundary element, and the third one is generally applied in terms of an impedance BC. However, due to the mixed formulation of the BEM, it is possible to start only with Dirichlet and Neumann BCs and to incorporate an impedance BC later on in the solution process as a quotient of these two.

The fundamental solution of the acoustic radiation in the free field is the *Green's function* defined e. g. in Ref. [3]

$$G(\boldsymbol{x},\boldsymbol{y}) = \frac{e^{ikr(\boldsymbol{x},\boldsymbol{y})}}{4\pi r(\boldsymbol{x},\boldsymbol{y})} \qquad \text{with} \qquad r(\boldsymbol{x},\boldsymbol{y}) = |\boldsymbol{x}-\boldsymbol{y}| \,, \tag{2.91}$$

which describes the free field variation of the sound pressure[35] at a point $\boldsymbol{y}$ due to a monopole source of unit strength at location $\boldsymbol{x}$. Using it as the weighting function, the following integral equation[36] can be derived by equating the Helmholtz equation (2.15) for the fluid volume V and the surface integrals of the two residuals on A_{s_1} and A_{s_2} for a general point in space $\boldsymbol{x}$

$$\int_V \left(\nabla^2 p(\boldsymbol{x}) + k^2 p(\boldsymbol{x})\right) G \,\mathrm{d}V_x = \int_{A_{s_2}} \left(\frac{\partial p(\boldsymbol{x})}{\partial n_x} - \frac{\partial p(\boldsymbol{x})}{\partial n_{x_0}}\right) G \,\mathrm{d}A_{s_x} - \int_{A_{s_1}} \left(p(\boldsymbol{x}) - p_0(\boldsymbol{x})\right) \frac{\partial G}{\partial n_x} \,\mathrm{d}A_{s_x} \,. \tag{2.92}$$

In this equation, the subscripts '0' indicate a steady state and terms without a subscript the acoustic fluctuations. Due to the choice of the weighting function, after a double partial integration, the volume integral and the surface integral over the infinite domain vanish, yielding a pure boundary integral formulation (the so-called weak form),

$$\boxed{\int_{A_s} \left[p(\boldsymbol{x}) \frac{\partial G(\boldsymbol{x},\boldsymbol{y})}{\partial n_x} - \frac{\partial p(\boldsymbol{x})}{\partial n_x} G(\boldsymbol{x},\boldsymbol{y})\right] \mathrm{d}A_{s_x} = \begin{cases} p(\boldsymbol{y}), & \boldsymbol{y} \in V_{ext}, \\ 0, & \boldsymbol{y} \in V_{int}. \end{cases}} \tag{2.93}$$

[35] The Green's function is an exact solution to the Helmholtz equation except for the location of the source, where the denominator becomes singular.

[36] Presented here in the formulation without flow. For reasons of compactness, the term $G(\boldsymbol{x},\boldsymbol{y})$ has been abbreviated simply by G.

in which the subscripts '*ext*' and '*int*' refer to the exterior and interior fluid volume, respectively, with respect to the boundary of the body, as can be seen in figure 2.41. This integral is known as the *Kirchhoff-Helmholtz integral* and makes possible the calculation of the sound pressure at a point in the volume V_{ext} solely from the boundary values. It can be seen as a superposition of weighted monopoles ($\partial G/\partial n_y$ term) and dipoles (G term) on the boundary.

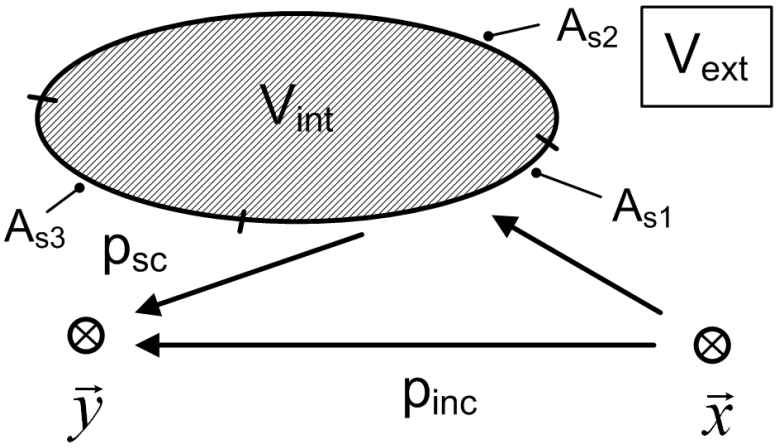

Figure 2.41: Superposition of incident and scattered sound pressure components

A characteristic property, which makes the BEM especially useful for acoustic radiation problems, is the fact that it satisfies the *Sommerfeld radiation condition* [161] exactly by default, as it does not utilize a discretized mesh except for the boundary.

On the other hand, one of the drawbacks of the BEM is the non-uniqueness of the solution at so-called *irregular frequencies*. For the exterior problem, these frequencies correspond to resonance frequencies of the corresponding interior problem. At these frequencies, the matrix becomes singular due to a purely mathematical problem and has no physical meaning. To avoid the problems arising from this constellation, a number of strategies have been invented, one of which uses additional points inside the domain at which the sound pressure is forced to zero to suppress the resonant solutions.[37]

As mentioned in the comparison of the BEM and FEM, the solution of the boundary integral equation (2.93) is only the first step in the solution process. To obtain the sound pressure at an observation point $\boldsymbol{y}$ within the volume, two components have to be separated: the direct (incident) radiation from the acoustic sources and the indirect (scattered) part due to the presence of the scattering bodies, as sketched schematically in figure 2.41.

The total sound pressure is thus the sum of the direct component, which results from the laws of radiation (e. g. for a monopole source by equation (2.75)), and the scattered part due to the equivalent source distribution on the boundary

$$p_t = p_{inc} + p_{sc} \,. \tag{2.94}$$

This yields, using the previously obtained result, the following integral equation, which includes scattering, diffraction, and reflection effects

$$p_t(\boldsymbol{y}) = p_{inc}(\boldsymbol{y}) + \int_{A_s} \left[p(\boldsymbol{x}) \frac{\partial G(\boldsymbol{x},\boldsymbol{y})}{\partial n_x} - \frac{\partial p(\boldsymbol{x})}{\partial n_x} G(\boldsymbol{x},\boldsymbol{y}) \right] \mathrm{d}A_{s_x} \,. \tag{2.95}$$

[37] These virtual points are called CHIEF points (= Combined Helmholtz Integral Equation Formulation) by Schenck [162], and 'Overdetermination Points' in LMS SYSNOISE.

In a discretized formulation, the nodal sound pressure and particle velocity values of the discrete elements as well as interpolation functions (ansatz functions) describing the variation of the variables throughout the elements are assembled in terms of vectors, similarly for the Green's function and the pressure values due to the incident waves. This yields a discretized version of equation (2.95), which is conveniently solved using a *collocation procedure*, a kind of implicit Runge-Kutta procedure, placing the observation point successively at all nodes of the boundary (more information can be found e. g. in Ref. [163]).

The result of this approach is the linear equation system of the D-BEM

$$\boldsymbol{A}(\omega) \cdot \boldsymbol{P} = -\boldsymbol{P}_{inc} + \boldsymbol{B}(\omega) \cdot \boldsymbol{V}_n \ , \tag{2.96}$$

in which the matrices $\boldsymbol{A}$ and $\boldsymbol{B}$ contain the integral expressions. They can be integrated numerically using a Gauss-Legendre algorithm except for the elements of the main diagonal, for which the distance r between the source and the observation point goes to zero and the denominator in the Green's function (2.91) becomes singular. However, these terms can be evaluated using different numerical integration schemes, e. g. the *Gaussian quadrature* which is as well explained in Ref. [163].

Unlike the band structured matrices in the FEM, the matrices $\boldsymbol{A}$ and $\boldsymbol{B}$ are fully populated, not symmetric, and complex, properties which prevent the usage of simple solver algorithms. However, in comparison, the matrices are of reduced dimensionality, and hence considerably reduced size, since they contain only the boundary nodes and not the complete fluid domain.

Another aspect of the BEM is the frequency dependency of the matrices as the matrices contain the frequency in a transcendental formulation in the Green's function. This requires a re-calculation for each frequency step and prevents a modal solution approach as for the FEM. Thus, Benthien and Schenck [164] proposed the use of so-called master frequencies between which the matrix elements are interpolated, a feature which has been implemented as well in commercially available BE codes (compare e. g. the SYSNOISE User Manual [165]).

After calculation of the primary surface results (the nodal values on the boundary), the sound pressure (and analogously the normal particle velocity) can be determined at any arbitrary point in space using a discretized version of equation (2.95).

A problem arises for the calculation of thin walled structures with the *D-BEM*: to avoid 'numerical leakage' due to the influence of the $1/r$ term in the Green's function, a very fine mesh has to be used for the modeling of the structure. This can lead to economically intolerable computation times.

Thus, a second BE method has been developed, which does not use the acoustic variables p and v_n directly in the equations, but pressure and particle velocity differences between the two faces of an element, the so-called *double* and *single layer (DL/SL) potentials* $\bar{p}$ and $\bar{q}$.

$$\begin{aligned} \bar{p} &= p^+ - p^- \ , \\ \bar{q} &= \frac{\partial p^+}{\partial n} - \frac{\partial p^-}{\partial n} \ . \end{aligned} \tag{2.97}$$

Accordingly, using this method called the *Indirect BEM*, the finite thickness of the boundary can be reduced to zero as indicated in figure 2.42. This reduces the number of elements and, as a result, also the computation time.

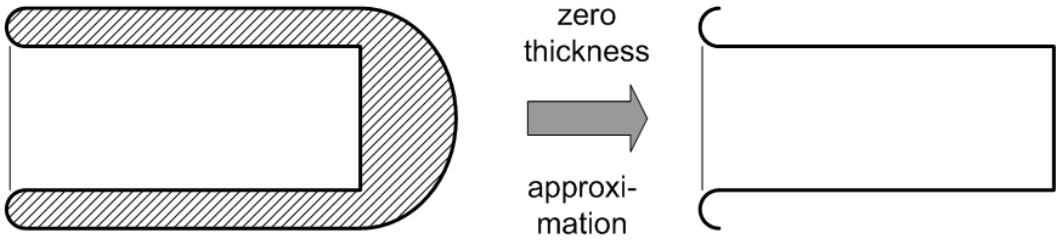

Figure 2.42: Zero thickness approximation applied to engine inlet configuration

The I-BEM solves the interior and exterior problem within one step. Since this leads to a hypersingular integral equation,[38] the collocation procedure is replaced by a Galerkin procedure involving the variation of a potential (*variational procedure*). The basis of this method, which is most commonly used in commercially available BEM codes due to its universal applicability, is the work of Hamdi [166].

The use of the potential formulation leads to a modified version of the integral equation (2.95)

$$p(\boldsymbol{y}) = p_{inc}(\boldsymbol{y}) + \int_{A_s} \left[\bar{p}(\boldsymbol{x}) \frac{\partial G(\boldsymbol{x},\boldsymbol{y})}{\partial n_x} - \bar{q}(\boldsymbol{x}) G(\boldsymbol{x},\boldsymbol{y}) \right] \mathrm{d}A_{s_x} \qquad \forall\, \boldsymbol{y} \in \{V \setminus A_s\}\,, \tag{2.98}$$

which is valid for all observer points $\boldsymbol{y}$ except for the boundary.

The discretization of the structure is implemented analogous to the D-BEM, leading to a system of equations corresponding to equation (2.96)

$$\begin{bmatrix} B & C^T \\ C & D \end{bmatrix} \begin{Bmatrix} \bar{q} \\ \bar{p} \end{Bmatrix} = \begin{Bmatrix} f \\ g \end{Bmatrix}, \tag{2.99}$$

in which f and g stand for the excitation vectors in terms of predetermined surface velocities and pressure values. As for the D-BEM, the matrix on the left hand side is complex and fully populated, but at least symmetric, which reduces the computation time and makes the I-BEM more attractive for numerical calculations. As mentioned above, also its general applicability (for interior as well as exterior problems) and the advantages with respect to slender structures contribute to its predominance.

This concludes the section about the theory of the BEM and leads to a quite novel numerical technique, which can be applied to the BEM solution process to reduce the computational effort: the Fast Multipole Method (FMM).[39]

2.4.3.3 Application of the Fast Multipole Method to the BEM

As has been mentioned above, the matrices involved in the BEM solution process are dense (i. e. fully populated), and thus cannot be easily solved by standard Gauss elimination techniques. In parallel, the size of the matrices grows with the square ($\mathcal{O}(N^2)$) and the computation time with the cube of the number of elements ($\mathcal{O}(N^3)$), which quickly leads to dimensions beyond practically solvable limits. Even neglecting the computation time, the

[38] This strongly singular property results from the vanishing distance between the two sides of the structure.
[39] Extensive information about the Boundary Element Method can also be found in Gaul, Kögl and Wagner [167].

storage space for an in-core computation (i. e. keeping the full matrix within the core memory of the computer) determines the maximum number of elements. Duraiswami [168] presents in his lecture about the Fast Multipole Method an example for a 1 GB computer: this limits the number of elements to just 32,768, a relatively small number considering the '6 (or even 10) elements per wavelength' rule proposed, respectively, by the SYSNOISE [165] and ACTIPOLE [169] manuals to ensure a proper representation of the wave propagation by the discretized mesh. Figure 2.43 illustrates the resulting rapid growth of required core memory for an increasing number of elements.

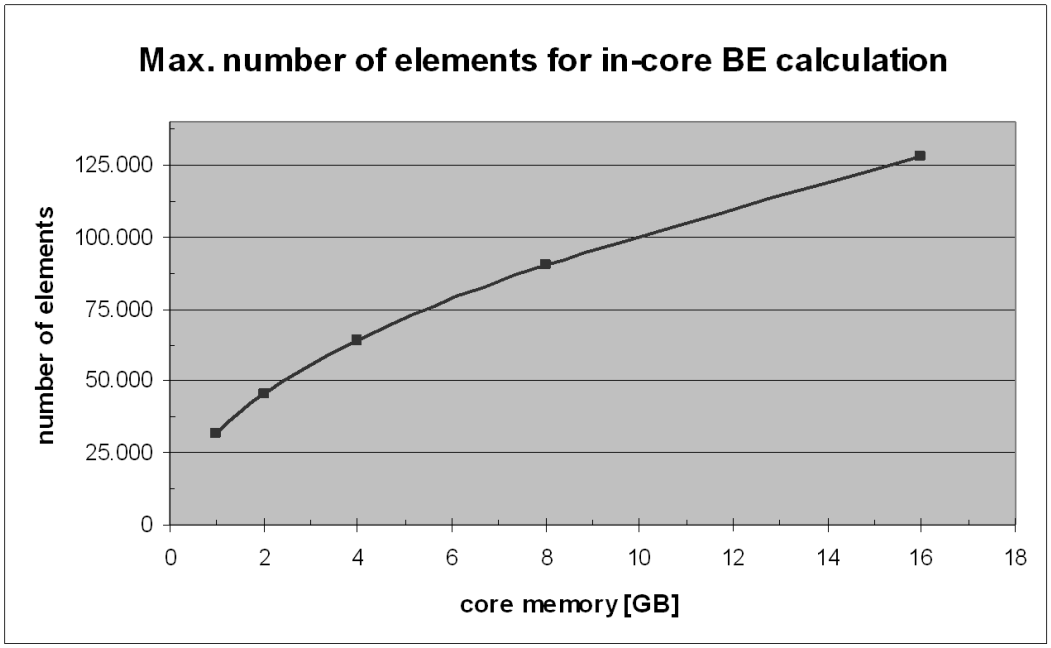

Figure 2.43: Maximum number of elements as function of in-core memory size [GB]

This example demonstrates the physical limits of BEM calculations, since out-of-core calculations become even more time-consuming. As well, simple iterative solver algorithms, which are commonly used in the FEM, do not yield satisfying time savings for the BEM due to the dense matrices. Not even Moore's law, which states that the processor speed doubles every 18 months, helps to circumvent these time and memory requirements because of the non-linear increase with the number of elements.

All these facts reason the use of alternative solver algorithms, which reduce the complexity of the problems. A very promising technique thereof is the *Fast Multipole Method (FMM)* introduced in 1987 by Greengard and Rokhlin [170] originally for the application to particle physics involving a large number of elements. It quickly became popular in several fields of physics as molecular dynamics, electromagnetics, fluid mechanics, and acoustics, and was named one of the 10 most significant advances in computing in the 20^{th} century (alongside innovations as e. g. the FFT) and won their authors the Steele prize of the American Mathematical Society.

The FMM is an innovative way of solving large matrix-vector problems by manipulation of the series and solution of an approximate problem. In this respect, adequately accurate approximate solutions can generally be accepted in scientific computations, considering as well the finite precision of the calculating machines. However, the accuracy can be made arbitrarily high at the expense of computation time.

Figure 2.44 illustrates the working principle of the FMM by means of a simple problem, i. e. the determination of the number of interactions between N sources and M evaluation points.

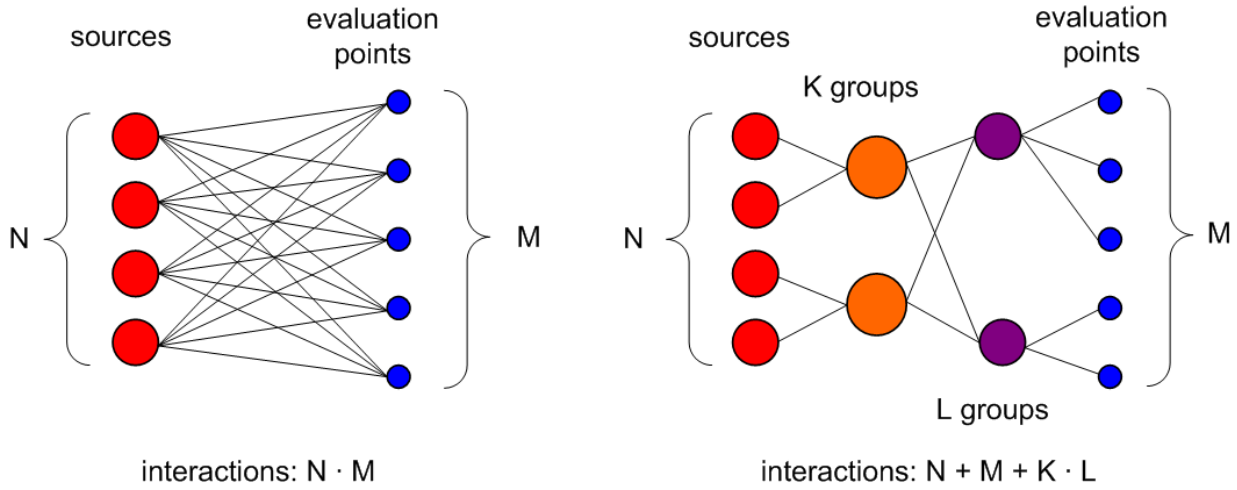

Figure 2.44: Comparison of interactions using standard algorithm and SL-FMM

Using a classical algorithm, each source has to be linked to each observation point, yielding $N \cdot M$ interactions. By a grouping of the sources and the observers, the number of interactions can be reduced to $N+M+K \cdot L$. In the example, this is equivalent to 13 interactions compared to 20 for the classical approach, or a reduction by 35%. This *Single Level FMM (SL-FMM)* already achieves quite a considerable effect with respect to the number of interactions, which can be maximized by a grouping at different levels in the *Multi Level FMM (ML-FMM)*. Its working principle is depicted in figure 2.45.

As a generalization of the SL-FMM, the ML-FMM integrates elements into groups and then re-groups these at the next level to even larger ones. By this procedure, the number of direct interactions at the highest level is reduced to a minimum.

In effect, this is equivalent to a separation of the near field and the far field interactions. 'Near field' in this context refers to the elements which are directly neighboring at the lowest level, for which the interaction is treated classically as in the standard BEM. For all other elements, the interaction is carried out by the subsequent grouping and distribution throughout the tree at the different levels using a 'bottom up' - 'top down' approach. Between the levels, and within one level (except for the lowest one), the interaction is implemented using different transfer operators consisting of expansions into infinite series involving Bessel and Neumann functions and Legendre polynomials. More information on this can be found in Refs. [168], [171], and [172]. This systematic subdivision and grouping leads in the limit to a complexity reduced to the order of $\mathcal{O}(N \cdot \log N)$, and hence, a nearly linear dependency with respect to the number of elements compared to the quadratic increase ($\mathcal{O}(N^2)$) using the classical approach.

A quite demonstrative description of the upward and downward passage through the cluster tree is contained in Gaul [173]. It points out that the upward shifting of information is being carried out up to the level where no interaction clusters are found anymore, but only neighboring cells. In this context, 'neighboring' clusters or cells are the ones directly adjacent to each other on a specific level, and 'interaction' cells are defined by the fact that their parent cells are 'neighboring' cells, but they are not direct neighbors of each other (compare also figure 2.46).

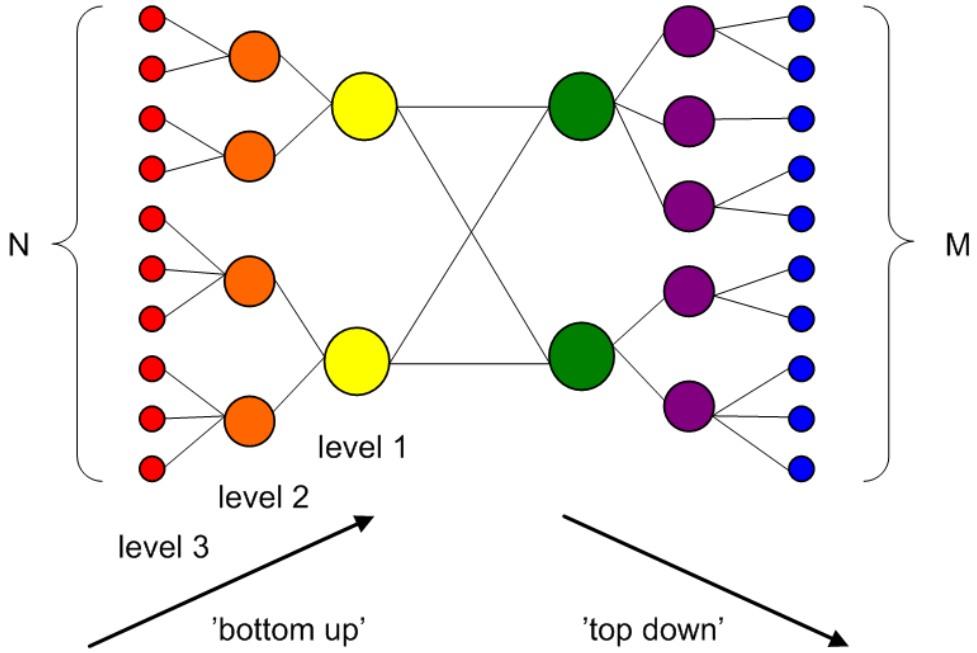

Figure 2.45: Basic concept of Multi Level FMM

Accordingly, the computation process is divided into a setup phase, in which the transfer operators (which can be reused during the computation) are created, and the iteration phase, which is carried out at the various levels. If a parallelization is to be used, which is still necessary for larger problems, the matrix should be equally distributed between the processors at each level to ensure an equally distributed computational load and a maximum performance of the code. As symptomatic for parallelized codes, each phase (initialization, ascent or descent between the levels, transfers, and integrations) is preceded by a communication phase between the processors, which needs to be balanced accordingly (as described e. g. in Alleon et al. [174]).

Due to its largely reduced complexity of a given problem, the FMM represents a particularly interesting extension of the BEM, increasing the maximum number of elements, or in return, the maximum frequency range (maximum $k \cdot R$), thus enabling the solution of realistic application cases.

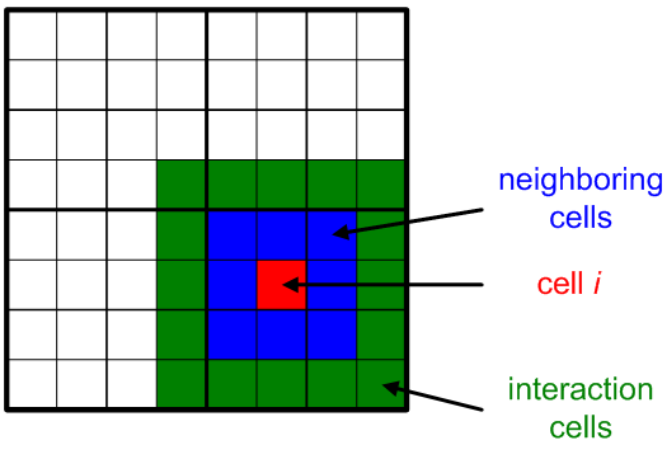

Figure 2.46: Neighboring and interaction cells on specific level in ML-FMM

2.4.3.4 Comparison of the BE codes LMS SYSNOISE and ACTIPOLE

In this closing section, the general features and differences of two BE codes, which have been used for the work included in this thesis, will be presented: the commercially available code LMS SYSNOISE and an EADS/ Airbus in-house BE code called ACTIPOLE.

To start with the former one, *LMS SYSNOISE* has been originally developed by the company IABG mbH (Industrieanlagen-Betriebsgesellschaft mbH) and then been taken over by LMS International and been integrated into LMS Virtual.Lab [175]. The SYSNOISE kernel includes acoustic, aeroacoustic, and vibro-acoustic solutions by means of FE and BE solvers. Concerning the BEM, both the Direct and Indirect approaches are implemented. For radiation problems, either the I-BEM, a 'Multi-Domain' D-BEM, or a coupled FEM-BEM approach may be selected.

The Multi-Domain D-BEM links two D-BEM domains by a coupling surface. Thus, for example an interior problem might be coupled to an exterior problem. With application to an acoustic duct, the interior problem describes the in-duct propagation coupled at the duct exit plane to the exterior domain solving the radiation problem. This approach might be useful to circumvent possible numerical problems resulting from the potential formulation of the I-BEM and the zero thickness approximation. However, it involves the twofold solution of the acoustic problem and some coupling terms, and thus generally becomes less attractive in terms of computation time.

The third solution type couples an interior FE model, in which the complete fluid domain has to be discretized, to a BE mesh on the surface of the body for a solution of the corresponding radiation problem. This might yield advantages due to the applicability of the modal solution space to the interior part. However, this approach also involves the solution of two problems increasing the computational cost. As well, the relative advantages of the BEM and FEM for a given ratio of fluid volume to surface area have to be considered (as discussed in chapter 2.4.3.1).

As expectable for a commercial code, SYSNOISE includes a variety of pre- and postprocessing features ranging from mesh checking and adaptation, an automatic launch of the computation using script files, data storage, to the plotting or display of the available data in a variety of styles, e. g. in terms of color plots, directivity curves, or radiated power values.

The second BE code *ACTIPOLE* [169], which has been developed at EADS Innovation Works in cooperation with Airbus France, uses only the generally valid I-BEM. Even though containing a universal core BE solver, it has been adapted especially to duct acoustic problems by the use of so-called 'modal surfaces' which facilitate the specification of incident and reflected modes at a specific location by the analytical model of a semi-infinite duct. This concept ensures an anechoic (i. e. reflection-free) downstream termination of the duct (as mentioned in chapter 2.1.1.2).[40]

ACTIPOLE additionally allows for the inclusion of a uniform mean flow, which is only supported in the FEM option of SYSNOISE. This feature might help to estimate the effect of a (however rather simplified) flow field on the acoustic propagation and radiation. However, within the scope of this thesis, which concentrates on the analysis of basic physical effects, flow effects will not be taken into account. Moreover, its influence is assumed to be of only minor importance causing essentially a frequency shift, but not a general change in the relevant physical phenomena.

For the faster and easier execution of parametric studies, ACTIPOLE offers so-called 'mobile parts'. By assignment of a mobile part, which is the variable part of the structure in terms of the geometry and/or the boundary conditions, and a fixed part, the size of the

[40] More information on the theoretical implications of the code ACTIPOLE and a validation with an analytical formulation can be found in Lidoine et al. [176].

matrix in subsequent BE calculations involving alternative configurations can be reduced considerably.

An additional and very significant advantage of ACTIPOLE is the implementation of elaborate iterative solvers (BlockGCR: block generalized conjugate residual solver, Gmres: generalized minimal residual, SyncGmres: synchronized Gmres) in combination with a SPAI (sparse approximate inverse) preconditioner and the ML-FMM according to the formulation of Chew (Ref. [177]). This makes possible the computation of much larger problems or, on the other hand, significantly reduces the computation time for a given problem size.

Additionally, ACTIPOLE is fully parallelized to be used on a LINUX cluster for large problems. As mentioned in the description of the FMM, in this case, the matrices are evenly distributed between the processors at all levels to minimize the idle time in the solution process.

And finally, as an open tool, ACTIPOLE uses text based input, output, and control files, and stores results in the *universal file format*. This greatly facilitates the data exchange and the postprocessing, and makes the code customizable for a particular task. On the contrary, the text based approach is not very descriptive and user-friendly. Overall, the computational process requires a relatively large number of input files and the processing of a number of steps involving different tools to obtain the final results (e. g. the sound pressure level at a field point). It also contains only the main computational steps and no graphical analysis tools.

For these reasons, an integrated user interface combining the setup process of a database, the generation of input and control files, the automated launch of the solver steps, and an elaborate set of postprocessing tools, has been implemented in MATLAB. This choice makes it possible to extend the functionality, or adapt it to special needs, and make use of existing tools as well as the standard MATLAB features (e. g. for the plotting of the results). Corresponding to the name of the BE code, this integrated tool has been named *ActiPRO*, an abbreviation for *ACTIPOLE PRe and Postprocessing*.

Figure 2.47 depicts on the left hand side the process chain for an ACTIPOLE computation using the standard way of working with the text files and a variety of tools for pre- and postprocessing, and on the right hand side the novel approach linking all ACTIPOLE components to a single, integrated tool which accompanies the complete solution process.

It becomes obvious, that without the ActiPRO tool, a large number of operations and data transfers had to be performed, starting with the conversion of the numerical mesh, which has to meet certain requirements to be compatible with ACTIPOLE. Additionally, control files had to be written for the different components of ACTIPOLE shown in the purple box (preprocessing, solving, postprocessing). For a display or further analysis of the results, an additional MATLAB tool had to be used to make them compatible with the Virtual.Lab (VL) universal file interface. The possibilities of the data interpretation are then limited to the standard features available in VL.

Differently for the new approach, in which, after the mesh has been created e. g. in MSC PATRAN, all data is entered into the ActiPRO Graphical User Interface (GUI) guiding the user throughout the complete process. In this context, a clearly visible structure, a gathering of all necessary data at the particular step within the active window, and a consistency check before to proceed, contribute to the user-friendliness of the tool. Moreover, all data is stored in a database that can be reloaded, modified, and compared to the currently loaded results at any time. ActiPRO generates the corresponding input and control files for the ACTIPOLE computation as well as script files calling the individual ACTIPOLE components. After the computation, the data is reimported into ActiPRO and can then be analyzed and plotted in several ways depending on the type of data selected (e. g. directivity and color map plots, radiated power computation, analysis of reflection coefficients, modal analysis).

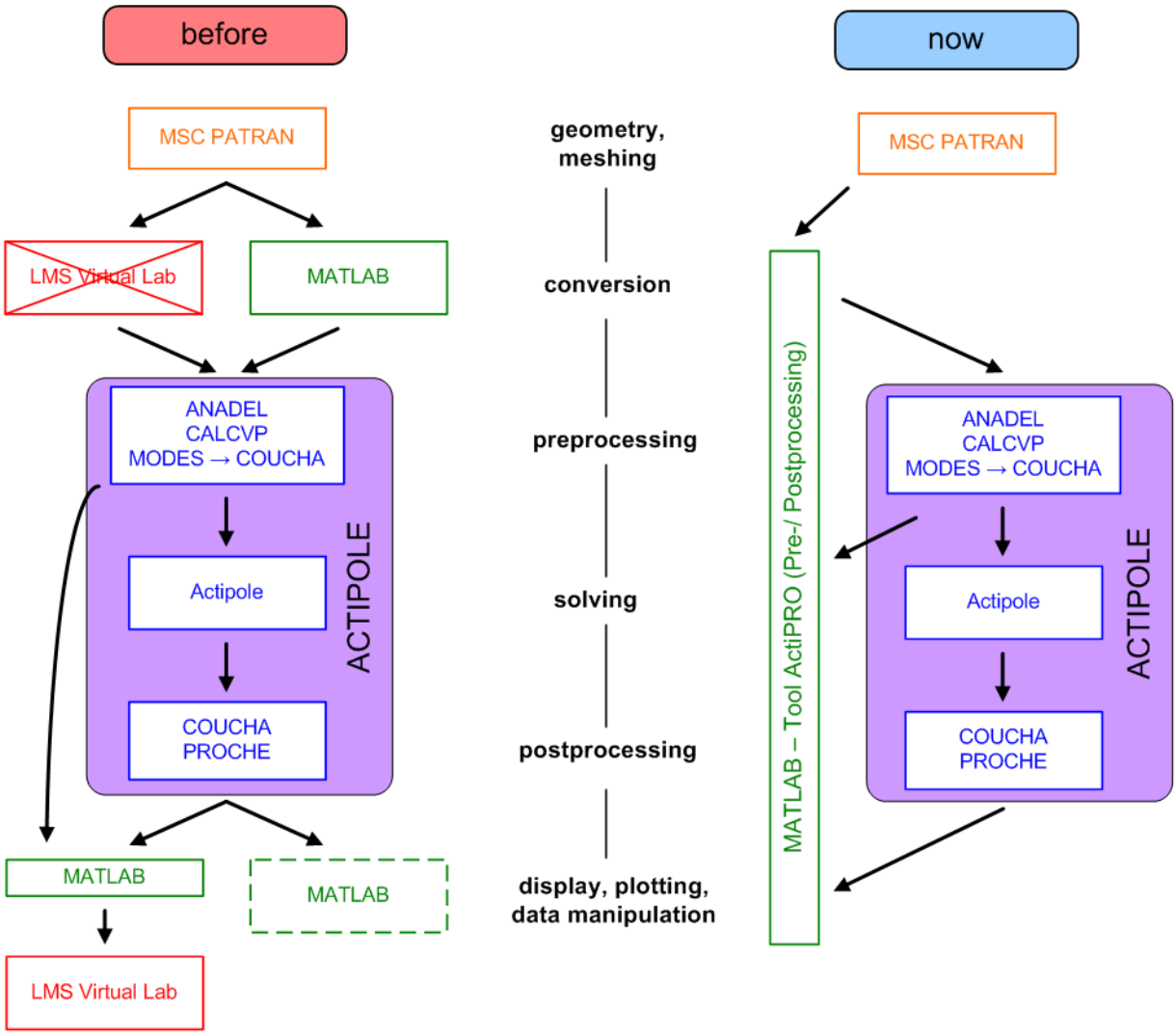

Figure 2.47: Process chain ACTIPOLE (plain) ↔ ACTIPOLE / ActiPRO

Chapter 3

Analysis of an adaptive liner concept

This chapter contains the results of a combined numerical and experimental study investigating the effects of a special type of a Mechanically Adaptive Liner (MAL) on a clearly defined modal sound field inside a rectangular duct without flow. It may serve, on the one hand, to validate the application of numerical Boundary Element (BE) calculations for duct acoustic problems involving non-uniform acoustic treatments. On the other hand, the concept of an adaptable acoustic impedance to achieve optimum values at all flight conditions, will be found in some of the advanced engine liner concepts proposed in chapter 6.

The results presented in this chapter have been obtained within the scope of the European research project SILENCER It was a medium-sized technology platform within the X-Noise technology network lasting from 2001 to 2007 and addressed noise issues related to the aircraft engine, nacelle, and airframe. The main objectives were the achievement of noise reduction and abatement measures to meet the schedule of the ACARE goals of reducing e. g. the Perceived Noise Levels by 50% (-10 EPNdB) by the year 2020. Figure 3.1 shows an overview of the different measures related to the engine and nacelle, one of which is the adaptive liner to be integrated into the lower front inlet area.

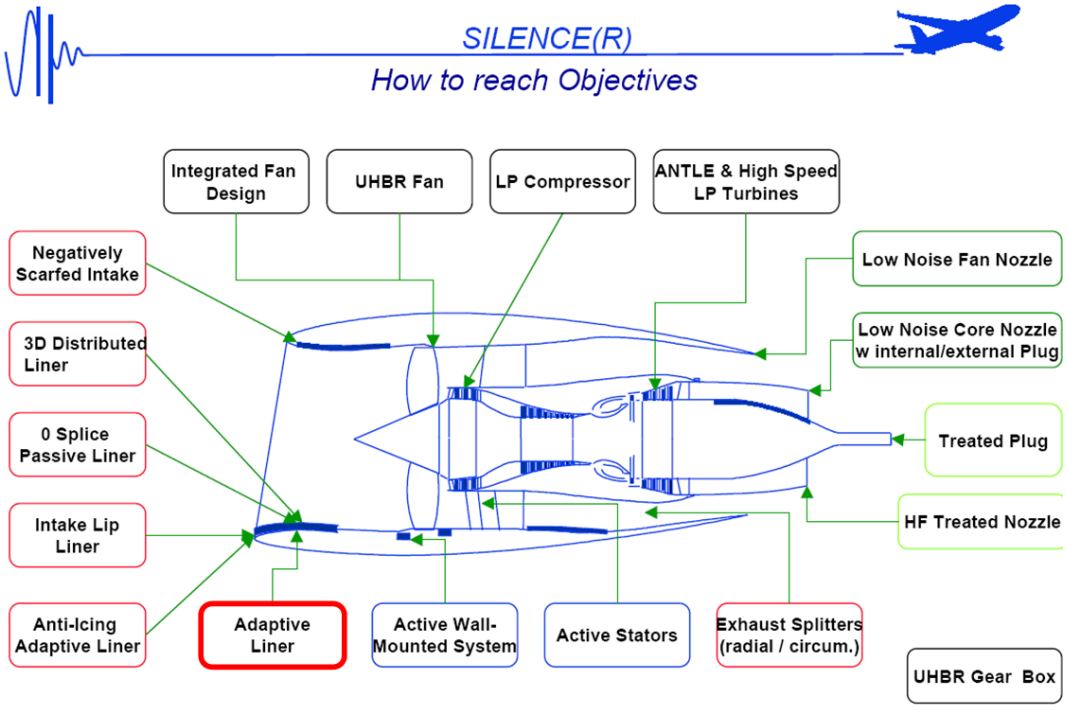

Figure 3.1: SILENCER noise reduction measures related to aircraft engine [178]

In one of the work packages, an especially designed test rig (MALTA = Mechanically Adaptive Liner Test Assembly) has been built, enabling the excitation of a single propagating mode, and the determination of the characteristics of the sound field ahead of and behind a test section containing exchangeable liner test panels. Its purpose was to clarify the acoustical behavior of the MAL designed in a previous work package, and to understand the discrepancies between wind tunnel results and corresponding acoustic predictions. Test objects were rectangular panels containing an array of MALs, as well as a set of equivalent uniform liners. In parallel, a numerical Boundary Element study resembling the duct and the test objects has been performed, enabling a comparison with the results obtained from the acoustic measurements.

The following sections of this chapter present, at first, the basic concept of the MAL and the setup and test matrix of both the experimental and numerical models. Subsequently, the results of both studies will be compared to each other with respect to consistency and deviations.

3.1 Basic concept of the Mechanically Adaptive Liner (MAL)

The mechanically adaptive liner developed at EADS Innovation Works (detailed information can be found in the corresponding SILENCER deliverables [179], [180]) is based on a $\lambda/4$ absorber design (compare chapter 2.3.1.1) with the possibility to adapt the specific impedance of the discrete elements. In detail, the resistance of the front sheet of the absorbers can be adjusted by a heatable foil in between two layers of a wire mesh resistance sheet. By variation of the electric current supplied to this heating foil, the physical properties of the medium air (ρ, c, μ) can be influenced yielding a variation of the acoustic resistance. Additionally, an adaptation of the reactance of the element can be achieved by changing the resonance length by means of a flexible silicone rubber membrane at the rear end of the cavity. It can be deflected from its neutral shape by feeding compressed air to the back cavity of the absorber element.

To determine the actual impedance of the element, the sound pressure has to be measured at two locations by means of microphones: one in front of the resistance sheet and one behind it within the cavity (according to the two microphone method described in chapter 2.3.1.2). The acoustic impedance derived from these measurements is then fed back to a controller trying to achieve the prescribed optimum impedance by variation of the heat current and the back cavity pressure. Figure 3.2 presents a sectional view of a single MAL element and its main components.

After initial testing of the single elements, two rectangular frames consisting of 48 MAL elements each have been constructed and built for subsequent tests at a rectangular acoustic flow duct facility at the 'Centre Acoustique' of the Ecole Centrale de Lyon (ECL). These panels are shown in figure 3.3 by means of a conceptual sketch (figure 3.3(a)) and a photography of the assembled configuration including the equipment for the air and electric current supply (figure 3.3(b)).

3.2 Design of experiment and setup of test matrix

For the assessment of the MAL performance compared to a set of equivalent uniform liners, an acoustic duct of the same cross section as the above mentioned flow duct has been designed. An important objective in the design of this test rig was to ensure minimum

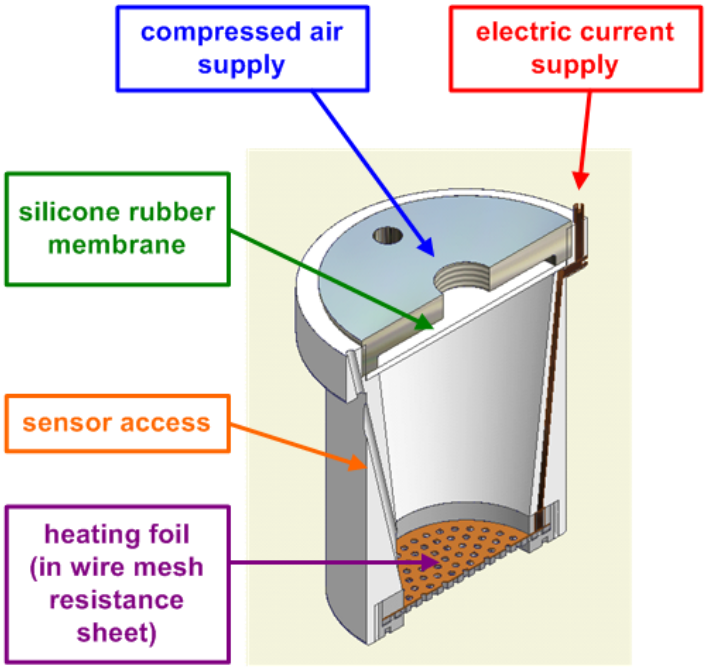

Figure 3.2: Single Mechanically Adaptive Liner (MAL) element

disturbances, which were suspected to be responsible for the discrepancies between the flow duct test results and analytical predictions. Thus, a controllable single mode excitation has been selected in combination with a modal analysis means ahead of and behind the test section. For the excitation, an array of loudspeakers has been positioned at the upper and lower duct walls, which are controlled by a Digital Signal Processor (DSP) in amplitude and phase. On the sensor side, a corresponding microphone array has been used to record the signals and convert them into the modal domain by a transfer matrix procedure. And finally, to ensure minimum reflections from the duct terminations, an anechoic condition has been applied at both ends of the duct. The corresponding general arrangement of the acoustic test rig (MALTA) is given in figure 3.4.

As can be seen, all dimensions (except for the test section defined by the length of the MAL panels) have been related to the cross section of the duct measuring 320 x 240 mm^2,

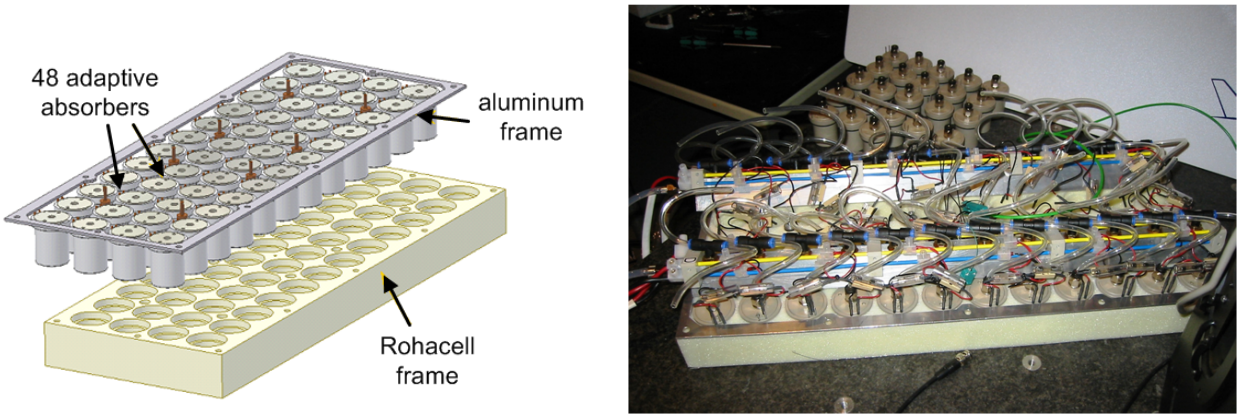

(a) conceptual sketch of MAL panel

(b) picture of assembled MAL panel

Figure 3.3: Rectangular MAL panel for acoustic testing

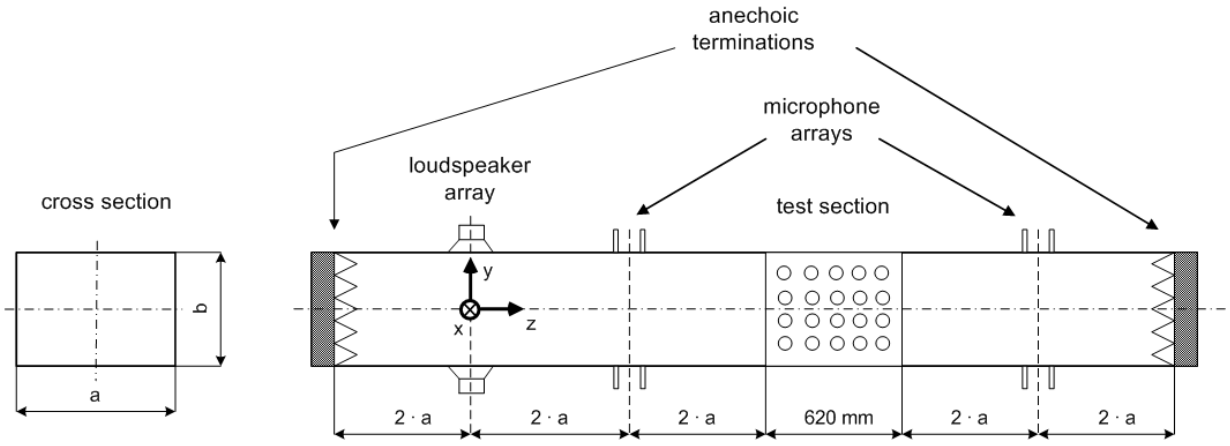

Figure 3.4: Sketch of the acoustic test rig (MALTA)

yielding an overall length of the duct of 3.90 m. The distance of two times the width of the duct cross section between two adjacent sections has been chosen to ensure a clear formation of the wave patterns and to eliminate near field effects of the respective influences (excitation, liners).

To simplify the excitation algorithm, loudspeakers have only been positioned on the upper and lower duct walls. By these means, the mode shape can be controlled in the horizontal direction, whereas the vertical pressure distribution is only defined by the wall boundary conditions and the frequency of excitation. Accordingly, in some cases, two mode shapes of the same horizontal modal number (m) but a different vertical modal number (n) are equally excited and propagate within the duct (as will be seen in the results).

To determine the number of speakers and microphones necessary to excite or detect the modal sound field, the *Nyquist criterion* (compare chapter 2.3.2.2) has been used ensuring a sufficient number of sources and sensors for a given mode number. Applied to this application, the number of speakers or microphones depends on the maximum horizontal mode number m_{max}

$$N_{mic/sp} \geq m_{max} + 1 \; . \tag{3.1}$$

Due to geometrical restrictions of the loudspeakers, a maximum number of four speakers can be positioned next to each other in the same axial plane on the upper and lower walls of the duct. This determines the maximum modal number in the horizontal direction: $m_{max} = 4$.

For the direction perpendicular to the line of speakers (y-direction), the modal number is not limited by actuators but has been determined from the modal cut-off frequencies. These are, for the case of a rectangular duct at zero flow, calculated by the following equation

$$f_{c_{mn}} = \frac{c}{2} \cdot \sqrt{\left(\frac{m}{a}\right)^2 + \left(\frac{n}{b}\right)^2} \; . \tag{3.2}$$

Accordingly, the cut-off frequencies of the first propagating modes are summarized in table 3.1. From this, the excitation frequency has been chosen to be $f = 2000$ Hz (equivalent to $k \cdot a = 11.83$), yielding a total of 11 cut-on modes (marked green in the table) and a maximum modal number in the y-direction of $n_{max} = 3$.

Table 3.1: Cut-off frequencies of first relevant modes (MALTA duct)

n \ m	0	1	2	3
1	0	536	1072	1608
2	715	893	1288	1759
3	1429	1526	1786	2151
4	2144	2210	2397	2680

To illustrate these results, figure 3.5 schematically plots the pressure distributions within the duct cross section (defined by cos-functions, compare equation 3.9) for the first propagating mode numbers in both the x- and y-direction.

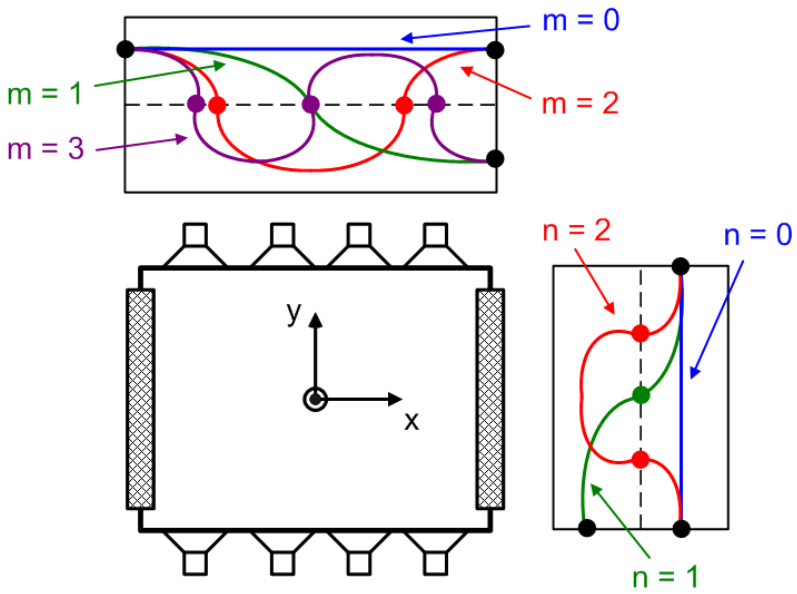

Figure 3.5: Mode shapes in duct cross section

With respect to the microphone arrays used to detect the incident sound field (ahead of the test section, on the left in figure 3.4) as well as the one modified by the presence of the different liner panels mounted into the side panels of the test section (on the right in figure 3.4), the same number of sensors ($N = 4$) has been used in the x-direction as the number of sources (loudspeakers), both on the upper and lower duct walls. Additionally, to separate the positively (emitted) and negatively (reflected) traveling waves, at each location two axial planes of microphones are needed, which yields a total of 32 microphones.

Concerning the liner configurations that have been tested/ computed, apart from the hardwall reference case (the test section enclosed by acoustically untreated walls), a passive and an active MAL configuration have been regarded. In this context, *passive* refers to the MAL elements remaining unpressurized and unheated, which could be also named a 'control off' condition. The corresponding impedance value has been determined by a Kundt's tube measurement of a single MAL element (compare figure 3.6).

The impedance assigned to the absorber elements in the numerical study in the passive configuration thus yields

$$Z_{abs_{pass}} = (1.75 + i \cdot 1.32) \cdot \rho c \, . \tag{3.3}$$

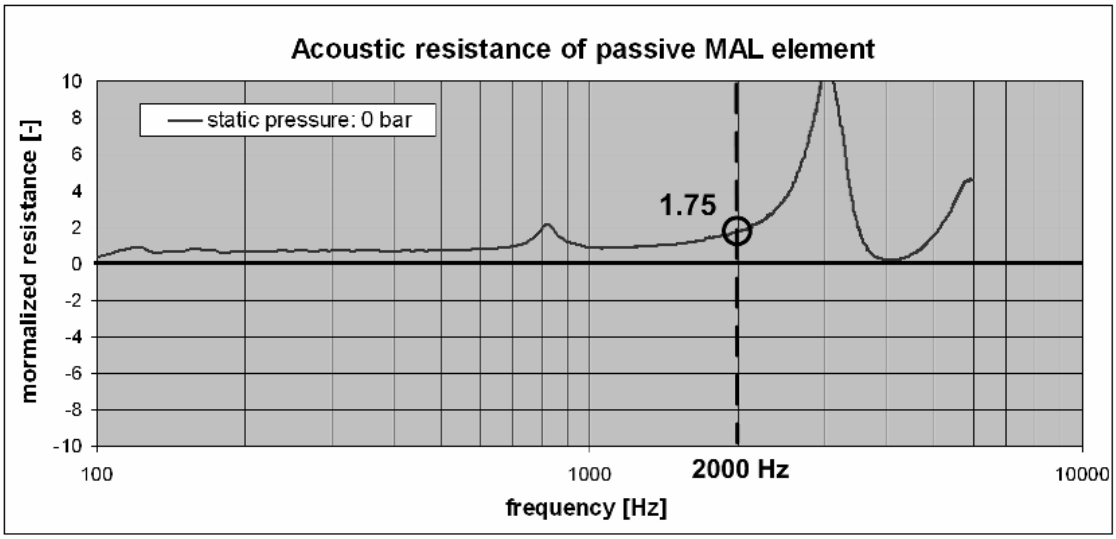

(a) resistance

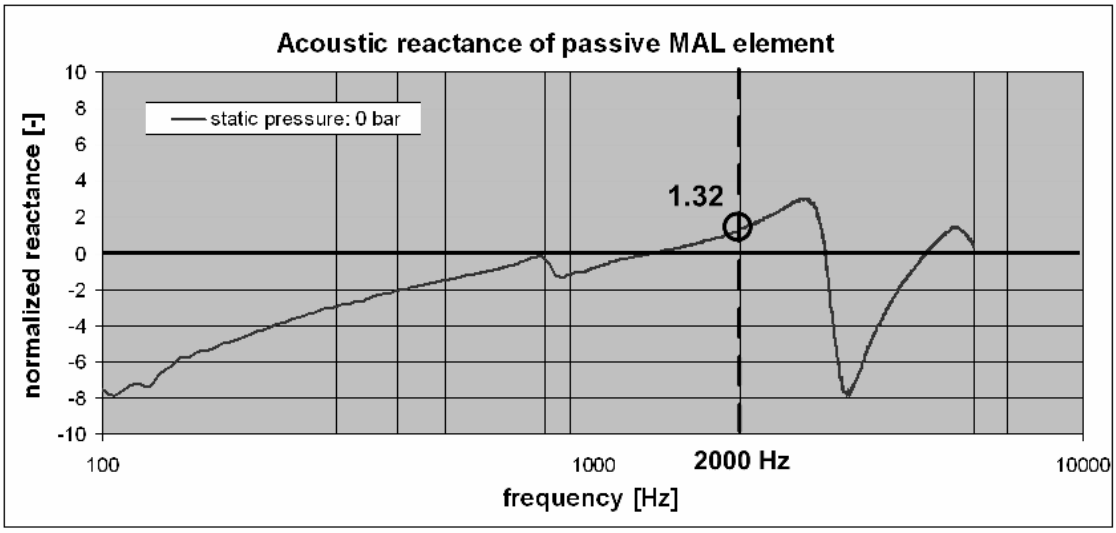

(b) reactance

Figure 3.6: Normalized impedance of single passive MAL element

In contrast, in the *active* configuration, the MAL panels have been controlled to achieve the optimum impedance value which has been provided in a corresponding SILENCER report [181]

$$Z_{abs_{opt}} = (1.30 - i \cdot 1.04) \cdot \rho c \, . \tag{3.4}$$

Additional to these two MAL configurations, two types of equivalent uniform liners have been tested: an *area-equivalent (equiv_A)* and an *averaged impedance (equiv_Z)* liner. The former one has the same acoustically effective area and impedance as the MAL panels, but concentrated on a small section. Its axial length can thus be computed as follows

$$l_{equiv\_A} = r_{\text{eff}} \cdot l_{TS} \approx 0.094\,\text{m} \, , \tag{3.5}$$

in which l_{TS} stands for the length of the test section (TS) and r_{eff} for the effective area ratio

of the MAL panels computed as follows

$$r_{\text{eff}} = \frac{A_{\text{eff\_}abs}}{A_{TS}} = \frac{N_{abs} \cdot \pi \frac{D_{abs}^2}{4}}{h_{TS} \cdot l_{TS}} = 0.1522 \equiv 15.2\% \; . \tag{3.6}$$

The second equivalent liner, the averaged impedance liner, has the same circumscribed area as the MAL panels, but an area-weighted averaged impedance (assuming ideal hardwall conditions for the area in between the discrete absorber elements)

$$Z_{equiv\_Z} = Z_{abs_{opt}} \cdot \frac{1}{r_{eff}} = (8.54 - i \cdot 6.83) \cdot \rho c \; . \tag{3.7}$$

For a better illustration, figure 3.7 depicts the two types of equivalent liners relative to the test section.

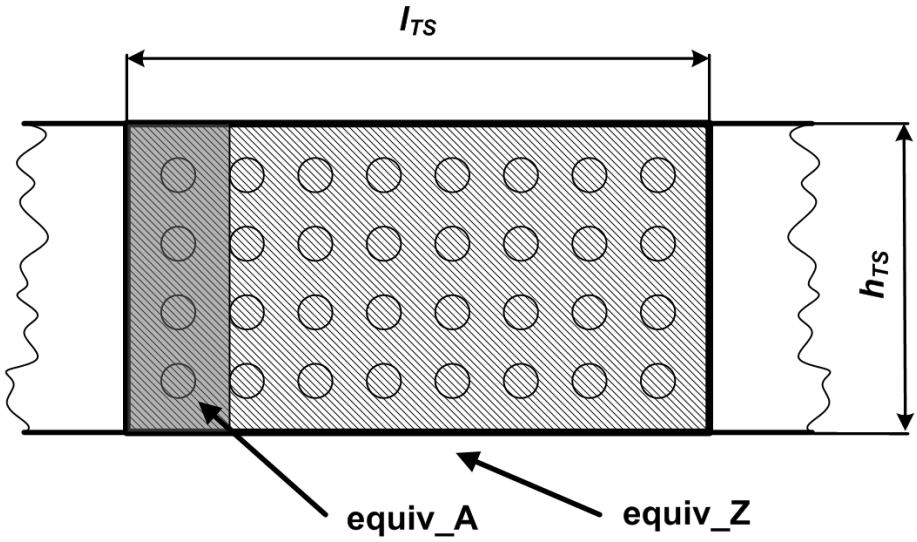

Figure 3.7: Sketch of equivalent liner configurations

3.3 Experimental setup of test rig

For the construction of the acoustic duct sketched in figure 3.4, MDF (medium density fiberboard) has been selected due to its favorable acoustic properties (hard wall conditions), good machinability, and its relatively low price. To allow for an exchangeable test section, aluminum profiles have been added in the center part, to which either the side walls, the MAL panels, or the equivalent liner panels can be attached. The two duct sections to the left and right of the test section have been placed upon framework sections, which can be moved relative to each other on aluminum tracks on the ground for easier assembly and reconfiguration (compare figure 3.8).

The anechoic terminations were designed to reduce reflections from the end plates of the duct to a minimum to allow for an undisturbed axial wave propagation. Therefore, an acoustic foam has been selected (Illbruck Waffel Dämm, figure 3.9) which - according to the manufacturer - provided a very high absorption coefficient for frequencies above 500 Hz.

To verify its performance, sample test have been conducted inside a Kundt's tube (yielding a plane wave excitation up to 1600 Hz). As can be seen in figure 3.10, an absorption coefficient (green line) $\alpha \geq 0.9$ can be ensured for frequencies above 800 Hz.

Figure 3.8: MALTA duct and subframe

Figure 3.9: Illbruck Waffel Dämm acoustic foam

However, the performance of the acoustic foam was shown to be different for a higher order modal excitation (because of the propagation angles of the respective modes), which could not be tested inside the Kundt's tube and will be assessed in the analysis of the measurement results.

Concerning the choice of a suitable loudspeaker for the acoustic excitation, it was important to have a small but powerful, reliable, and accurate component. These requirements seemed to be fulfilled by the BMS H4540 ND 1" compression driver (specification sheet in appendix A.1). To integrate the loudspeakers as closely as possible into the MDF duct walls, special inserts had to be manufactured. These, as well as two of the speakers mounted into the duct wall, can bee seen in figure 3.11. To influence the sound field in the vertical direction, at least as far as possible without speakers on the y-axis, the same number of speakers have been placed both on the top and bottom duct wall.

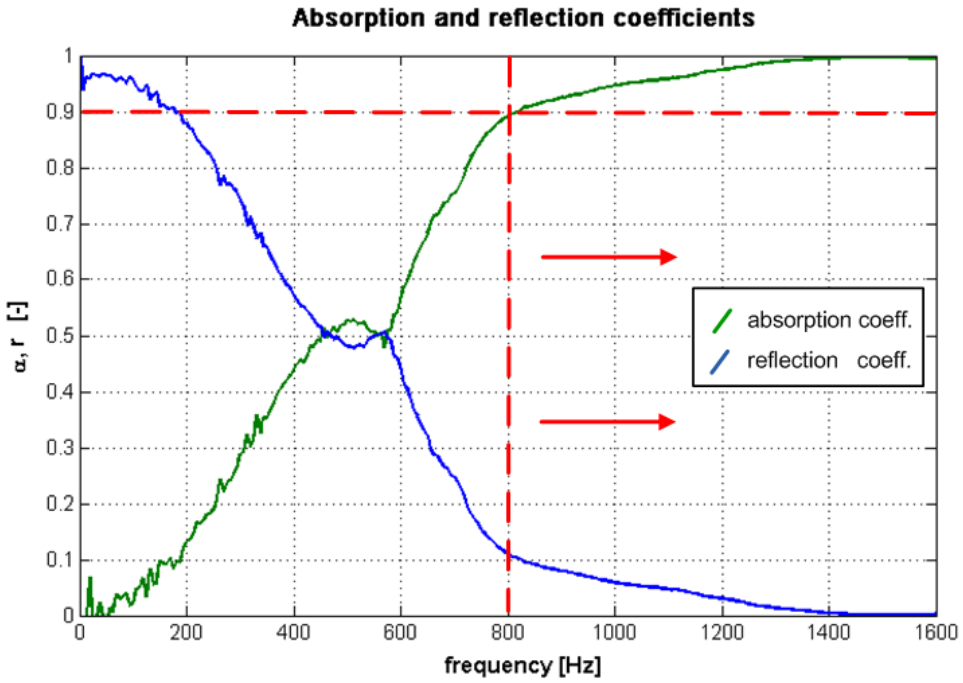

Figure 3.10: Sample impedance measurements of acoustic foam

Figure 3.11: Integration of speakers into duct wall

The 1/4" Brüel & Kjær microphones of type 4196 (specification sheet in appendix A.2) have been positioned in drilled holes and fixed by screw connectors to be flush mounted to the inner duct walls. One of the microphone arrays can be seen in figure 3.12, together with one of the speaker arrays in the background.

After minor changes to the MAL panels used in the previous flow duct tests, these could be implemented into the test section as can be seen in figure 3.13. Again, care was taken that the panels were exactly aligned with the inner duct walls. Additionally, the figure shows the integration of the two microphones for the local impedance measurement of the MAL panel.

Additionally, a pair of liners has been manufactured resembling the area-equivalent liner (equiv_A). The averaged impedance liner (equiv_Z) has not been tested but included in the numerical study. For the area-equivalent liner, a conventional $\lambda/4$ absorber design consisting of a locally reacting core material (circular thermoplastic honeycomb cells) and a facing wire mesh resistance sheet has been chosen. From the simple analytical equation determining the reactance of the cavity (equation (2.90)), the required depth of the core material has been

Figure 3.12: Microphone and speaker array

deduced, in this case $l_{cav} \approx 21$ mm

$$\frac{X}{\rho c} = cot\left(\frac{\omega \cdot l_{cav}}{c}\right) . \tag{3.8}$$

For the sheet material, two layers of Robusta 600 x 125 (Spörl KG, specification sheet in appendix A.3) were selected yielding a resistance value of $R = 1.43 \cdot \rho c$ at 2000 Hz, which is quite close to the optimum value of $R_{opt} = 1.3 \cdot \rho c$ (+ 10% error).[1]

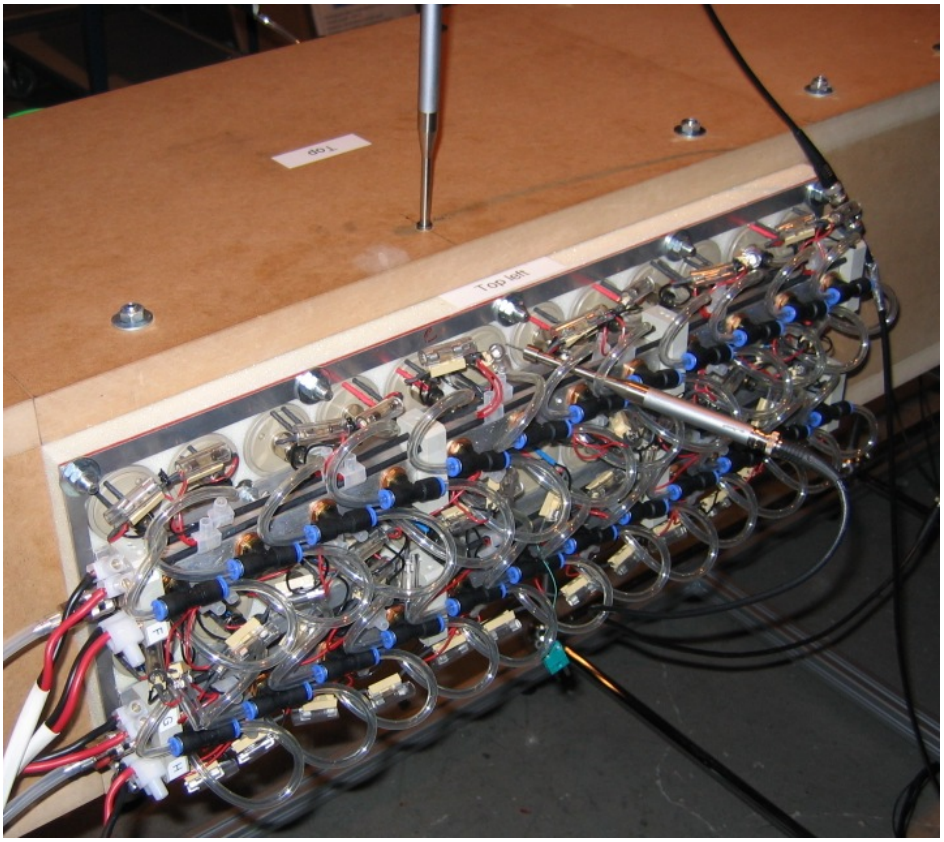

Figure 3.13: MAL panel integrated into test section and sensor access

[1] As has been analyzed in a sensitivity analysis within the numerical study, this small deviation does not influence the performance of the liner considerably.

The liner materials then had to be included into the side panels of the test section in a kind of pocket as can be seen in figure 3.14(a) showing the core material inserted into the side panel and the resistance sheet on the left hand side. Figure 3.14(b) illustrates the integration of the equivalent liner panel into the test section. For a better sealing, and to avoid secondary paths into the core material, aluminum tape has been attached at the side edges of the liner.

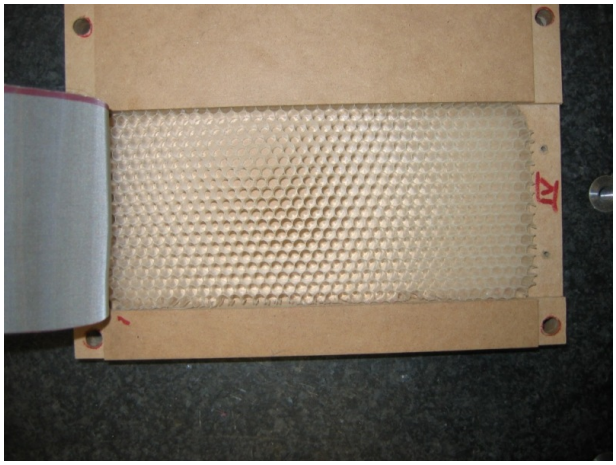

(a) assembly of area-equivalent liner

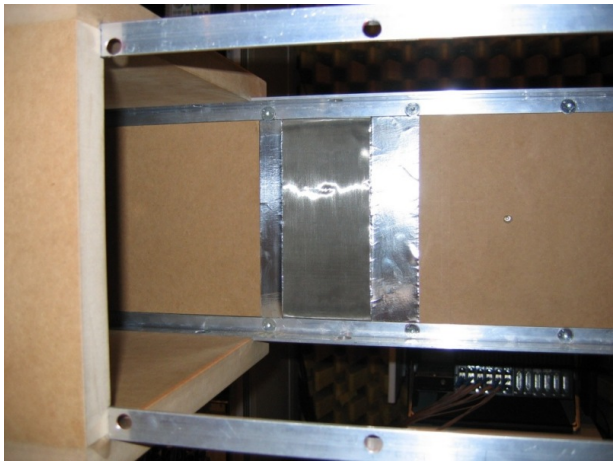

(b) integration of equivalent liner panel into test section

Figure 3.14: Assembly and integration of area-equivalent liner

After these details concerning the construction and assembly of the acoustic duct, the overall setup of the test rig and the measurement equipment is depicted schematically in figure 3.15. Within the figure, red lines and boxes indicate the excitation part of the test rig and green ones the sensoring and recording paths. Blue colors stand for the control loop related to the adaptive liners and black lines or boxes indicate data transfer paths and additional equipment as e. g. the DSP and the computers.

On the *excitation* side, the signals for the individual loudspeakers have been generated by a mode synthesizer which has been used and developed in previous research projects (e. g. TURNEX = Turbomachinery Noise Radiation through the Engine Exhaust) and adapted to the rectangular geometry for this application. It has been implemented in a real-time environment (dspace ControlDesk) connected to a DSP (dspace Autobox) and uses the solution to the wave equation of linear acoustics for a rectangular duct to compute the complex sound pressure values for a modal excitation at each time step

$$p(\boldsymbol{x}, t) = [A_x \cdot A_y \cdot \cos(k_{x_m} \cdot x) \cdot \cos(k_{y_n} \cdot y)] \cdot e^{i\omega t} \,, \tag{3.9}$$

in which k_{x_m} and k_{y_n} are the modal wave numbers in the x- and y-direction, respectively

$$k_{x_m} = \frac{m \cdot \pi}{a} \,; \qquad k_{y_n} = \frac{n \cdot \pi}{b} \,. \tag{3.10}$$

Via a Graphical User Interface (GUI), the mode synthesizer allows for the setting of the modal numbers (m, n), the frequency and amplitude of the desired mode (A_x, A_y), and plots the corresponding time signals for verification purposes (on the right hand side in figure 3.16). The signals are then fed through a combined high-pass/ low-pass (HP/LP) filter and a power amplifier to each individual speaker.

To compensate for differences in the amplifier channels, the signals supplied to the speakers have been measured, and calibration factors have been included into the DSP algorithm to ensure the same signal output for the same input level at all positions.

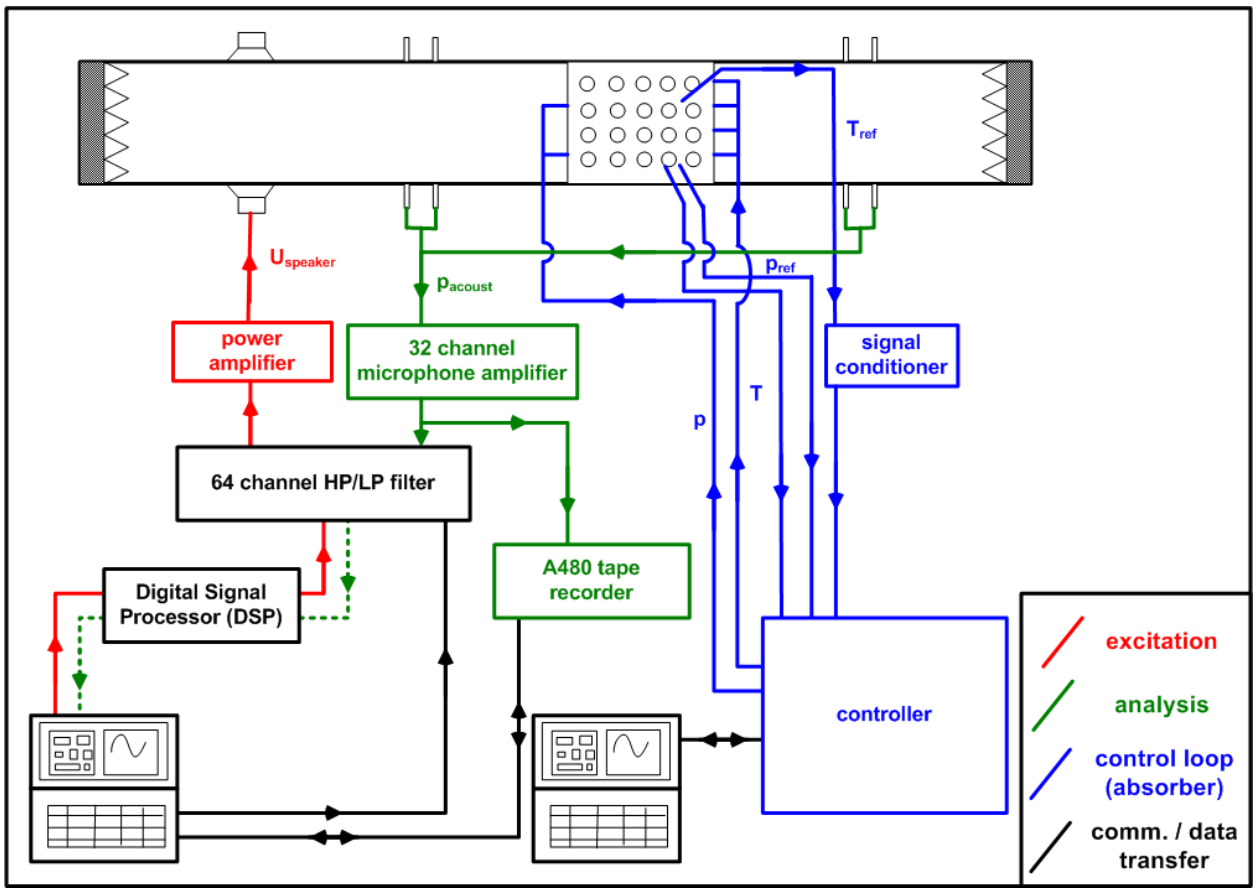

Figure 3.15: Measurement setup of MALTA test rig

Concerning the *data acquisition*, the microphone signals measured at each of the 32 sensors have been amplified by a 32 channel microphone amplifier and recorded by a RACAL A480 tape recorder controlled by a laptop computer. In the subsequent analysis part, these binary time signals have been processed by a MATLAB algorithm, which will be presented in the following.

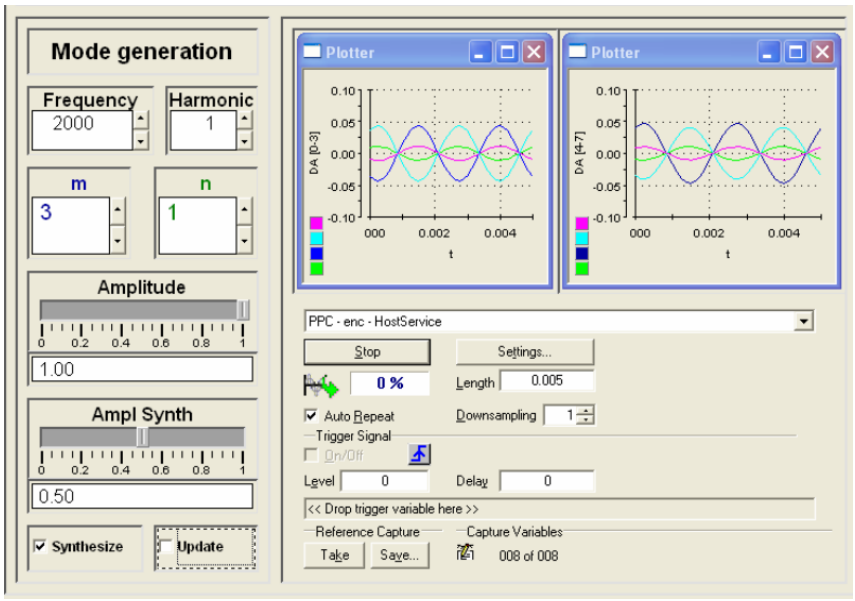

Figure 3.16: Screenshot of mode synthesizer GUI

The second (dashed) path of the time signals to the DSP for feedback has not been implemented in this task due to the limited time available, but may constitute an improvement because of the online verification possibilities (of the quality of the modal composition). It may also serve to implement a feedback loop for the modal excitation for an optimum signal generation.

The blue components and connectors in figure 3.15 are all related to the *control process* of the MALs and will not be explained here in detail.[2] However, they include the provision of the correct air pressure to the back cavity of the MALs and the electric current supplied to the heating foil included in the wire mesh resistance sheet. Additionally, sensor data measuring the temperature of the sheet and the acoustic pressure on both sides of it for the impedance eduction serve as input variables to the control process.

For the analysis of the measured microphone data, the process chain depicted schematically in figure 3.17 has been developed.

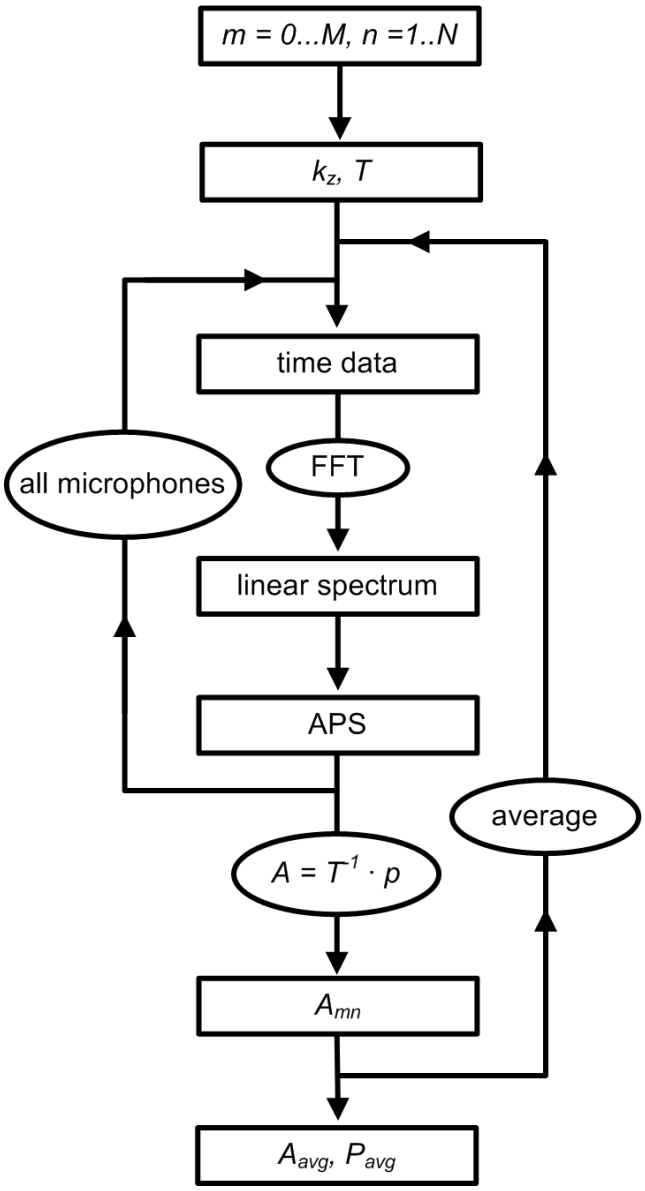

Figure 3.17: Process chain used in analysis process of measured sound field

[2]More information on the control strategy can be found in Ref. [180].

Therefore, in accordance with Gerhold, Cabell, and Brown [182], at first, the axial wave numbers had to be determined to assemble the transformation matrix T (analogous to equation (2.37) but using the modal numbers for the rectangular duct as in equation (3.10)). They can be derived from the known wave number components for each mode using the theorem of Pythagoras

$$k_{z_{mn}} = \sqrt{k^2 - k_{x_m}^2 - k_{y_n}^2} \, . \tag{3.11}$$

By an inversion of the corresponding matrix equation (given in equation (2.35)), the modal amplitude vector can be obtained. As the matrix T is, in general, not a square matrix, the inversion has to be carried out using a suitable algorithm. In this case, the Singular Value Decomposition (SVD) has been used, which is a way of factorizing a rectangular real or complex matrix, and represents a generalization of the spectral theorem (stating that a square matrix can be diagonalized by an orthogonal basis of eigenvectors) to arbitrary, not necessarily square, matrices. In detail, the SVD decomposes the matrix T into two unitary matrices[3] U and V and a real matrix D containing the singular values (equivalent to the eigenvalues of square matrices) in its main diagonal

$$T_{mn} = U_{mm} \cdot D_{mn} \cdot V_{nn}^{*T} \, , \tag{3.12}$$

in which the superscript ^{*T} denotes the complex conjugate transpose of the matrix. After determination of these matrices, the inverse of T_{mn} can be obtained quite easily by the following relation

$$T_{mn}^{-1} = V_{nn} \cdot \frac{1}{D_{mn}} \cdot U_{mm}^{*T} \, . \tag{3.13}$$

By means of these transformations, the time data of all microphones converted into the frequency domain by an FFT (Fast Fourier Transform), has been transformed into the desired modal amplitude spectra. However, to ensure representative results, an averaging process with respect to the time intervals has been applied to the analysis process (as depicted in figure 3.17).

The final results of the process are the averaged modal amplitudes ($A_{01}^{\pm} \cdots A_{mn}^{\pm}$) and the overall power of the modal spectrum

$$P_{modal} = \sum_{i=1}^{N_{modes}} A_i^2 \, . \tag{3.14}$$

However, this modal power value does not automatically reflect the actual acoustic power radiated through a cross section, as it has only been deduced from the boundary values (the microphone measurement positions). However, for the experimental part, it is the only power quantity that can be determined, and has its relevance as it allows for the comparison with the numerical results for which it will be computed following the same procedure.

An example of the final results of the analysis process is shown in figure 3.18 for mode (1/1) at 2000 Hz in the hardwall condition (test section closed by perfectly reflecting wooden panels). In the upper half of the plot, the characteristics of the microphone pressure values over the duct cross section are plotted for the first microphone array (ahead of the test section). In this case, the excited mode (1/1) can be clearly identified. The plot in the lower half shows the resulting modal amplitude distribution obtained by the analysis process presented above. From the amplitude representation in the dB scale, the good quality of

[3] A unitary matrix is a complex n by n matrix satisfying the condition that its inverse is equal to its complex conjugate transpose ($U^{-1} = U^{*T}$).

the excited mode can be deduced. With the 'primary' peak at 108 dB , the next highest amplitudes are 90 dB for modes (1/2) and (3/1) which yields an adequate separation from the primary mode (-18 dB).

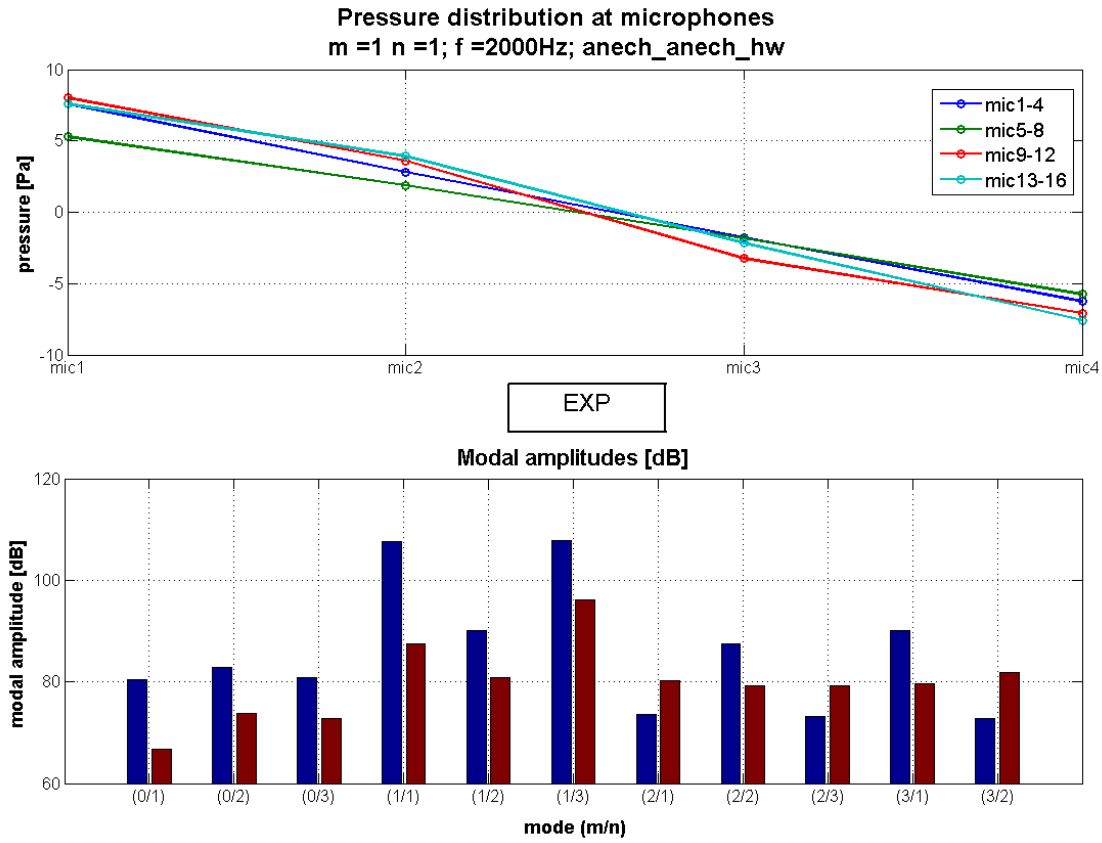

Figure 3.18: Example of modal amplitude spectra - EXP; m1n1; 2000 Hz; hardwall

As mentioned in the design of the test rig in the previous section, due to the location of the loudspeakers only at the upper and lower duct walls, the controllability of the mode shapes in the vertical direction is limited. Thus, as observable in the example, additional to mode (1/1), the mode (1/3) (i. e. the mode $(m/n+2)$, compare figure 3.19) is propagating as well (compare table 3.1), and both will be named *primary modes* in this context.

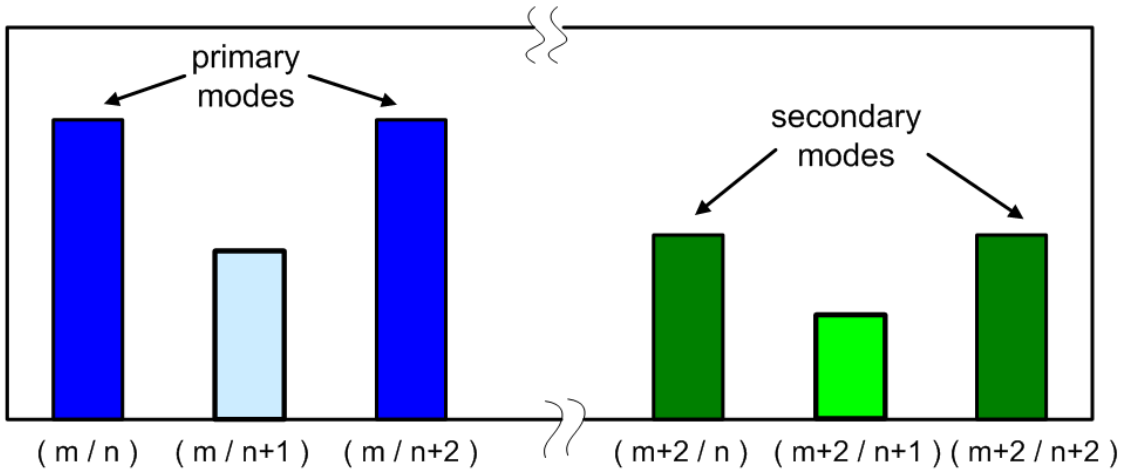

Figure 3.19: Principal sketch of primary and secondary modes

Additionally, the figure indicates a certain relationship to the *secondary modes* of mode order $(m \pm 2/n)$ and $(m \pm 2/n \pm 2)$, which in most cases exhibit the second largest amplitudes. They share the same boundary conditions on the side walls (the test section panels) with the primary modes, but feature an even number of additional (or fewer) pressure nodes in between in the horizontal direction.

From the figure, as well, the modal reflection coefficient of the acoustic foam at the front duct termination can be determined and compared to the Kundt's tube measurement presented in figure 3.10. The normalized linear amplitude coefficient of mode $(1/1)^-$ yields in this case $r = 0.0976$ corresponding to an absorption coefficient of $\alpha = 0.9024$ (using equation (2.72)). This is in good agreement with the Kundt's tube results ($\alpha \approx 1.0$ at 2000 Hz), even if these are only valid for the plane wave mode. Concerning mode (1/3), the absorption coefficient is slightly lower ($\alpha = 0.7381$), which might be explained by standing wave components inside the duct, as will be reported later on in the analysis.

3.4 Implementation into Boundary Element model

The numerical model of the MALTA test rig (depicted in figure 3.20) has been created in MSC PATRAN using triangular and quadrangular shell elements meshed onto the geometry defined previously (figure 3.4). Their size and shape has been chosen to suit the different geometrical parts (e. g. a finer element size for the absorber panel test section) and the frequency range of interest. This ensures that the same model can be used for all configurations, and differences in the results originating e. g. from discretization errors can be avoided.

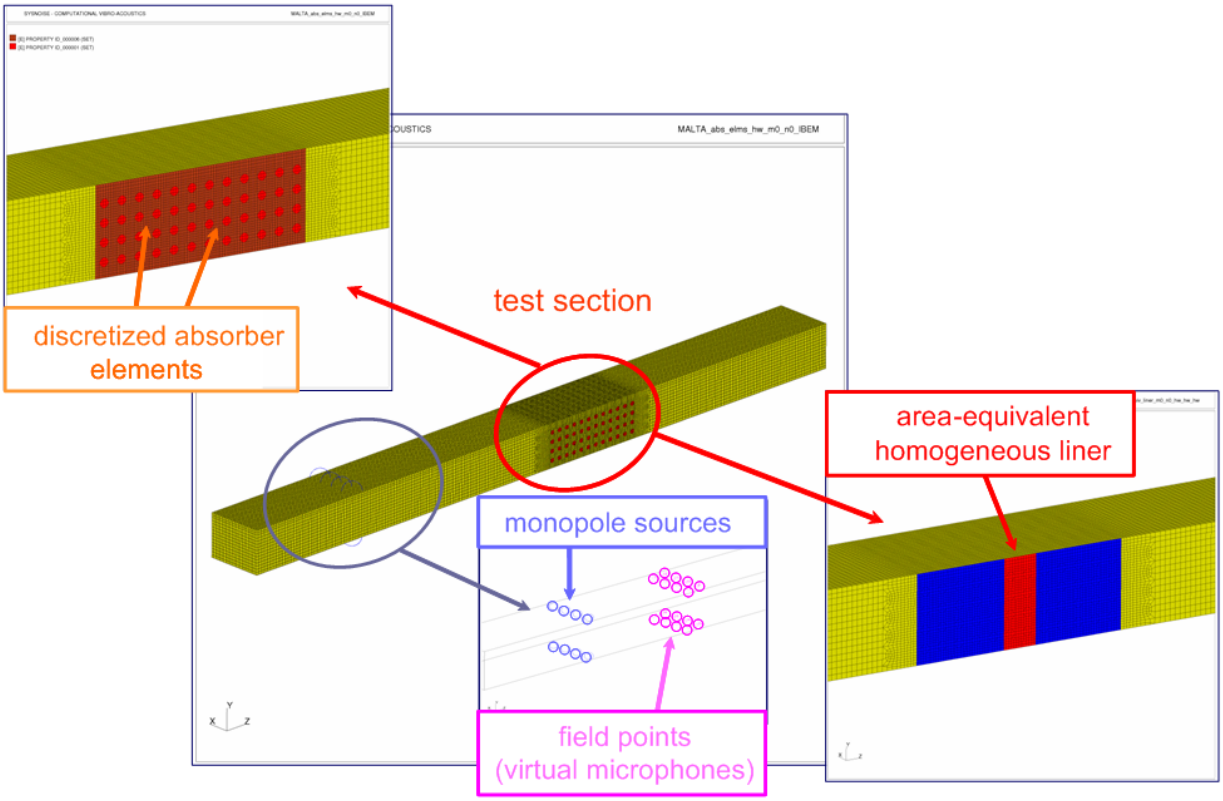

Figure 3.20: BE model of MALTA test rig

The figure shows an overview of the complete test duct as well as enlargements of the test section for two of the configurations: the discretized absorber elements (on the left hand

side) and the area-equivalent liner (on the right). Additionally, a closeup in the lower center part pictures the equivalent acoustic sources and sensors on the upper and lower duct walls.

Especially the test section had to be meshed carefully to represent the actual geometry, using appropriate simplifications to avoid too much detail and reduce the computation time. Because of this, the originally circular absorber elements have been approximated by refining and splitting the mesh in this area, as can be seen in figure 3.21. This simplifies the meshing task, and creates only a negligible change in effective area of less than 1%.

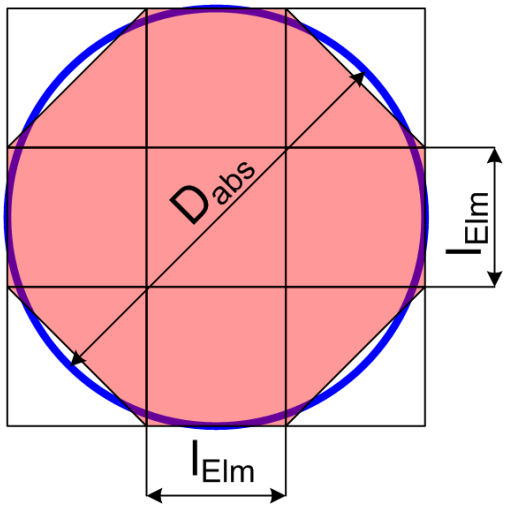

Figure 3.21: Discretization of absorber elements

Altogether, the BE model of the MALTA duct contains 36,000 elements in the model, enabling calculations up to 3.4 kHz following the '6 elements per wavelength' rule mentioned in chapter 2.4.3.3 which specifies the required fineness of the numerical mesh. The discretized model has then been imported into LMS SYSNOISE (the BE simulation environment selected for this task) and adapted to the needs of the BE solver. As well, standard atmosphere conditions have been assigned to the medium (ρ = 1.2 kg/m^3, c = 340 m/s), and the impedance values to the respective sections in the different configurations. Furthermore, the loudspeakers have been represented by acoustic monopole sources at the respective locations. For being able to analyze the sound field following a similar procedure as in the experimental results, field points (i. e. evaluation points at which the sound pressure can be 'measured') have been positioned at the exact microphone positions. These have been later on analyzed by a MATLAB algorithm similar to the one presented in the previous section (figure 3.17). Concerning the anechoic terminations of the duct, these have been approximated by assigning the characteristic impedance of the medium ($Z_0 = \rho_0 \cdot c_0$) to the end plates.

As just mentioned, for the analysis of the sound field at the two duct stations, an algorithm similar to the one described in the experimental part has been used. Indeed, only part of the process was necessary, since the results were already available in terms of pressure values instead of time series. Because of this, the FFT process and the averaging routine could be omitted and only the matrix inversion and multiplication had to be conducted after reading the SYSNOISE results file. However, for a comparison of the results, a correction factor had to be applied to account for the different levels of the excitation amplitude and the amplification in the measurement chain.

In comparison to the example of the results presented in the previous section (figure 3.18), figure 3.22 shows the results of the BE calculation for mode (1/1) at 2000 Hz in the hardwall configuration.

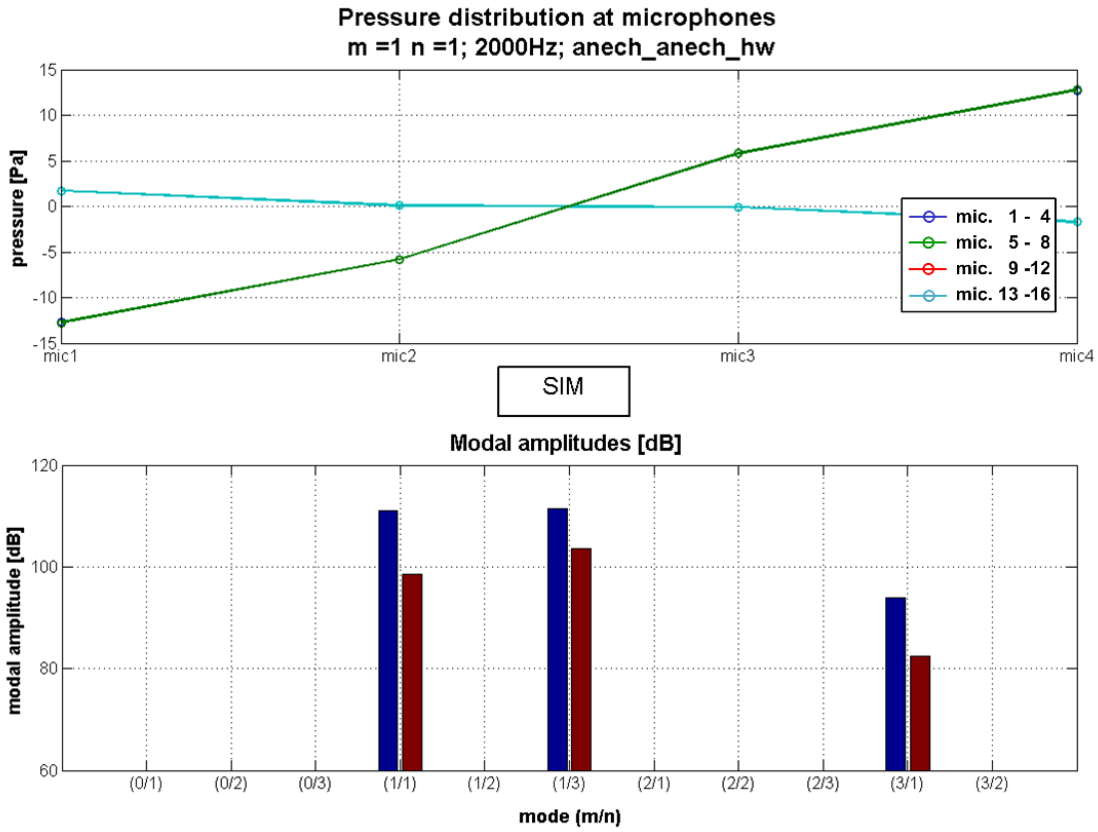

Figure 3.22: Example of modal amplitude spectra - SIM; m1n1; 2000 Hz; hardwall

At first glance, the pressure distribution in the cross section looks different to the experimental results. However, this is related to slightly different boundary conditions concerning the anechoic terminations (remember that both the experimental and numerical duct terminations are not perfect, and could only be measured/ defined for the fundamental mode) causing a different level of reflections in the two models. Considering the modal amplitudes, it is obvious that the numerical results yield a much clearer picture of the contributing modes. Only the two primary modes (1/1) and (1/3), as well as the secondary mode (3/1) at a level of 94 dB, i. e. 17 dB below the primary amplitudes, are observable in the amplitude range plotted (60 dB). This separation is nearly identical to the one observed in the experimental results, however, the overall level is 3 dB higher.

Concerning the modal absorption coefficients, they yield for the numerical results $\alpha = 0.7638$ for mode (1/1), and $\alpha = 0.5890$ for mode (1/3), which indicate higher reflection levels compared to the experimental results. This is probably due to the better absorption characteristics of the 3d-shaped acoustic foam used in the test rig (compare figure 3.9).

3.5 Comparison of numerical and experimental results

In this section, the results of the experimental and the numerical studies will be compared to each other and reasons for the deviations will be analyzed. This will be conducted, at first, for the hardwall case, which all results will be referenced to, then for the two equivalent liner configurations (the area-equivalent liner and the averaged impedance liner), and finally for the MAL configurations (active and passive). Concerning the quantities to be compared, the modal power obtained from the summation of the individual modal amplitudes (as defined in equation 3.14) will be considered in the beginning, as it yields an overview of the general

tendencies. Subsequently, also the modal amplitude spectra resulting from the different liner panels will be compared. Concluding, the degree of agreement with respect to attenuation values and modal effects, as well as differences observed, will be summarized.

3.5.1 Hardwall reference case

To start, figure 3.23 compares the modal power variations of the experimental and the numerical study from microphone array 1 to array 2 (i. e. across the test section).

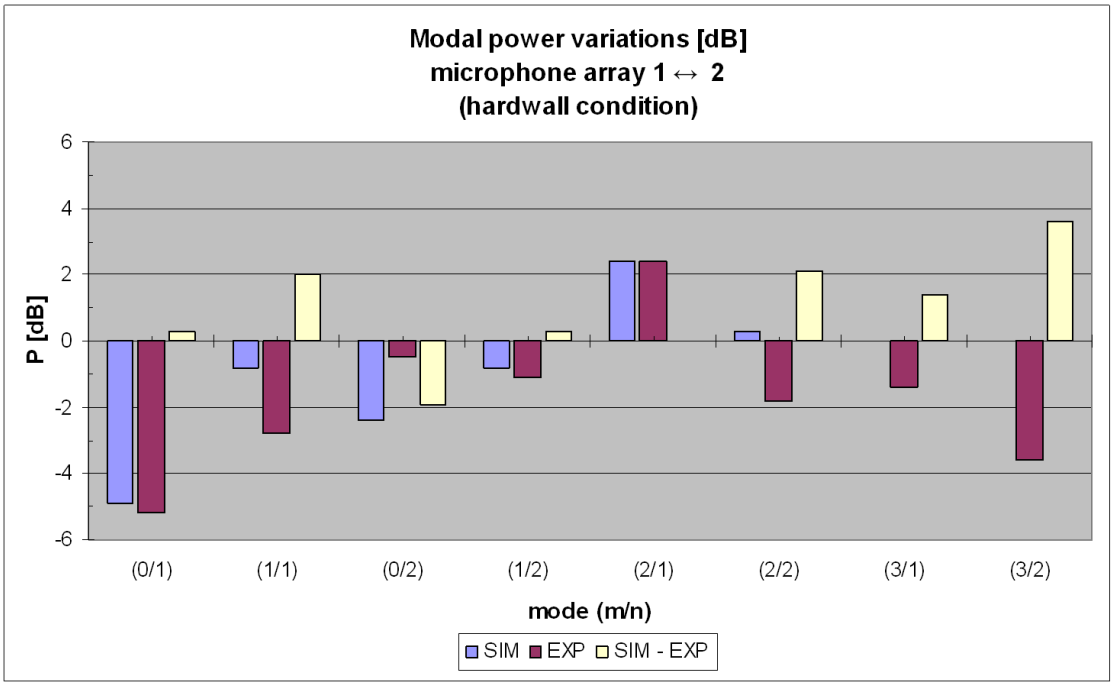

Figure 3.23: Comparison of modal power variations; microphone arrays 1 ↔ 2; EXP ↔ SIM

As can be seen, the power differences across the test section reach up to 5 dB for both studies, a noticeable value with respect to the fact that no sound absorbing materials have been included in the duct in this hardwall configuration. However, in comparison, both analyses (SIM & EXP) show a similar behavior ensuring a maximum deviation below 2 dB except for the highest propagating mode (3/2).

To explain this effect, a cross-sectional plot of the sound pressure amplitude of mode (0/1), the plane wave, will be compared at both axial duct stations. Figure 3.24 shows on the left hand side the pressure distribution at the rear microphone array center plane (between the excitation and the test section), and on the right hand side the result at the front array plane (behind the test section) obtained by two numerical field point calculations at the respective positions.

It can be clearly seen how the pressure distribution, and hence the relative modal amplitudes, change with the axial position inside the hardwalled duct. Additionally, the presence of the 2nd y-mode ($n = 3$) is obvious. In effect, at array 1, the energy is concentrated more at the upper and lower duct walls, whereas at array 2, the maximum sound pressure levels can be found located around the center line. This is related to standing wave components stemming from the imperfection of the desired reflection-free terminations of the duct both in the numerical and experimental model. Accordingly, these different pressure levels at the duct wall cause the apparent 'attenuation' that could be deduced from the results in figure 3.23.

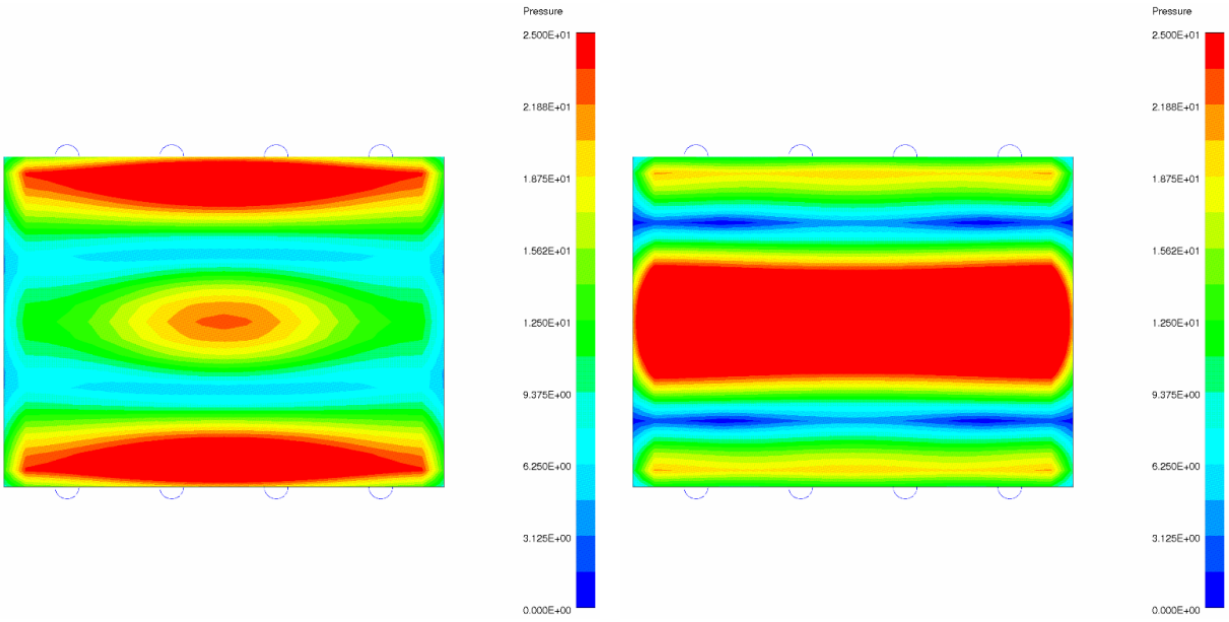

(a) rear microphone array (z = 0.65 m) (b) front microphone array (z = 2.57 m)

Figure 3.24: Cross-sectional pressure plots (amplitude) at array planes; (0/1); hardwall

This effect highlights the deficiency of the pressure determination only at the duct wall and the subsequent deduction of the modal amplitudes. However, it has been chosen to ensure the same conditions for the BE calculations and the experimental work, in which sound pressure could only be measured at the duct wall using flush-mounted microphones.

For an additional check of the consistency of the numerical model, as well the radiated power through the cross-sectional planes at the two array locations has been calculated. The two corresponding curves are depicted in figure 3.25.

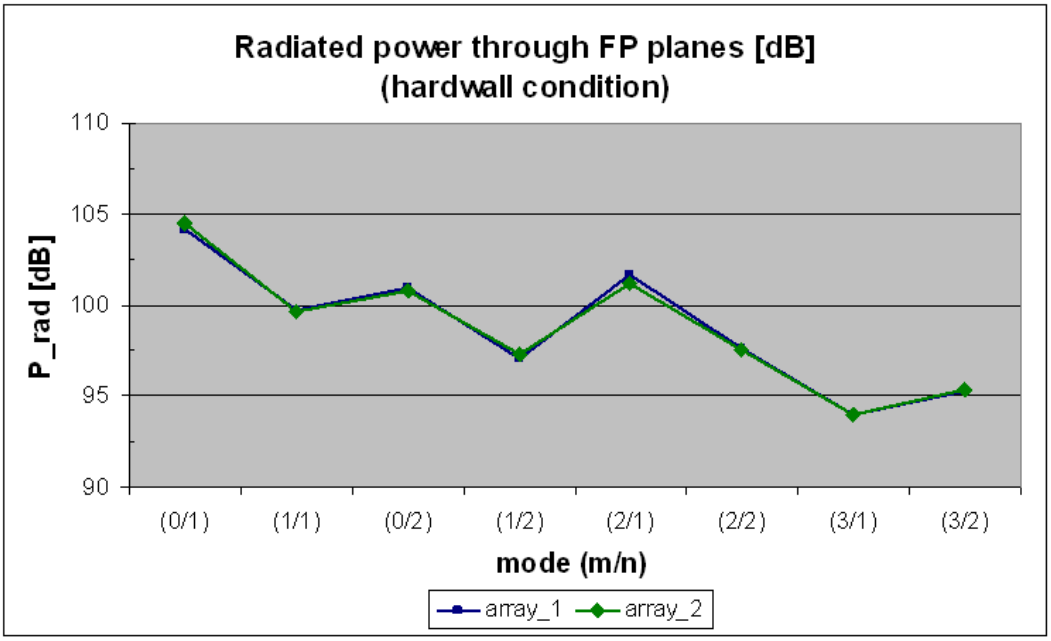

Figure 3.25: Comparison of radiated power through array planes

As can be seen, the radiated power values at both microphone array positions yield nearly exactly the same levels which confirms the reasoning given above.

After this assessment of the differences in modal power, the modal amplitudes of both simulation and experiment will now be compared to each other for the hardwall configuration. This has been done at the example of mode (1/2) at array 1 in figure 3.26.

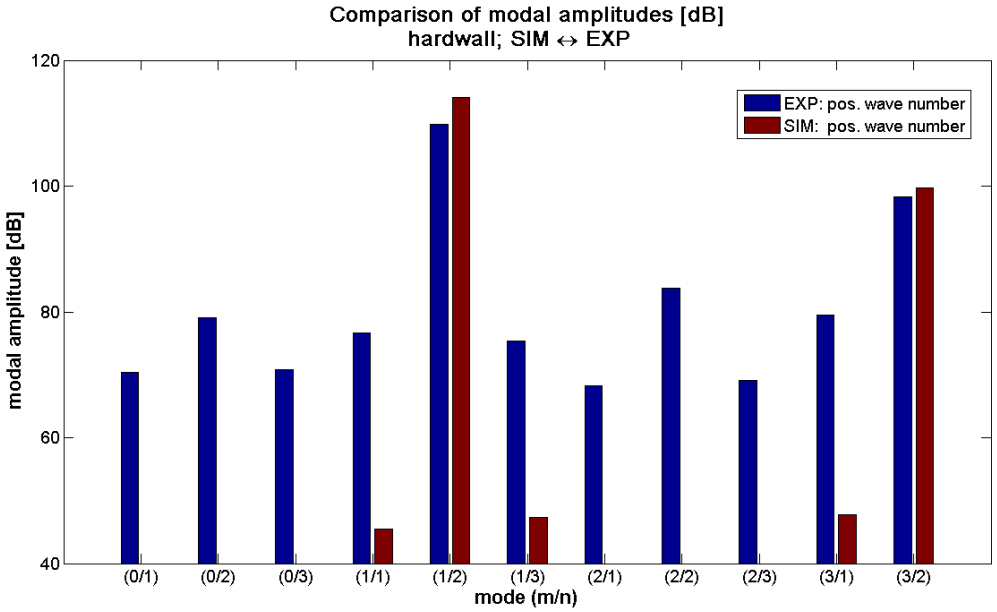

Figure 3.26: Comparison of modal amplitudes - SIM ↔ EXP; (1/2); hardwall configuration; array 1

The first observation is, that in the experimental results, all cut-on modes contribute to the modal spectrum, however at quite low amplitudes compared to the primary modal peak (on average -30 dB to -40 dB). In contrast, in the numerical simulation, only the primary mode (1/2) and the secondary mode (3/2) contribute significantly to the modal spectrum yielding a much clearer picture, as could be expected. Relative to each other, the modal amplitudes of the simulation and the experiment are quite close, differing by 4 dB and 2 dB for the primary and secondary mode, respectively.

3.5.2 Equivalent liners

Figure 3.27 shows the modal power reduction between the hardwall configuration and the area-equivalent liner (to remember, the averaged impedance liner has not been tested experimentally). In the diagram, the blue bars indicate the numerical results (SIM), the green ones the measured values (EXP), and the red bars the modulus of the difference between the two in dB.

Except for the plane wave mode, which exhibited quite a pronounced virtual attenuation in the hardwall case (as clarified above), the equivalent liner yields a modal power reduction of between 1 dB and 5 dB for both the experimental and numerical results. The difference between the two studies ranges between 0.3 dB and 2.0 dB, yielding an average of $\approx$ 1 dB, an acceptable agreement for this investigation.

Furthermore, no distinct scheme could be derived from the results indicating higher attenuations for the experimental or the numerical study. In contrast, the results change from mode to mode, and also show no clear dependency of the deviation upon the modal numbers (which could be related to the propagation angle).

In addition to the results presented above, figure 3.28 shows a comparison of the effects of the area-equivalent liner (as above) and the averaged impedance liner which has only been tested numerically.

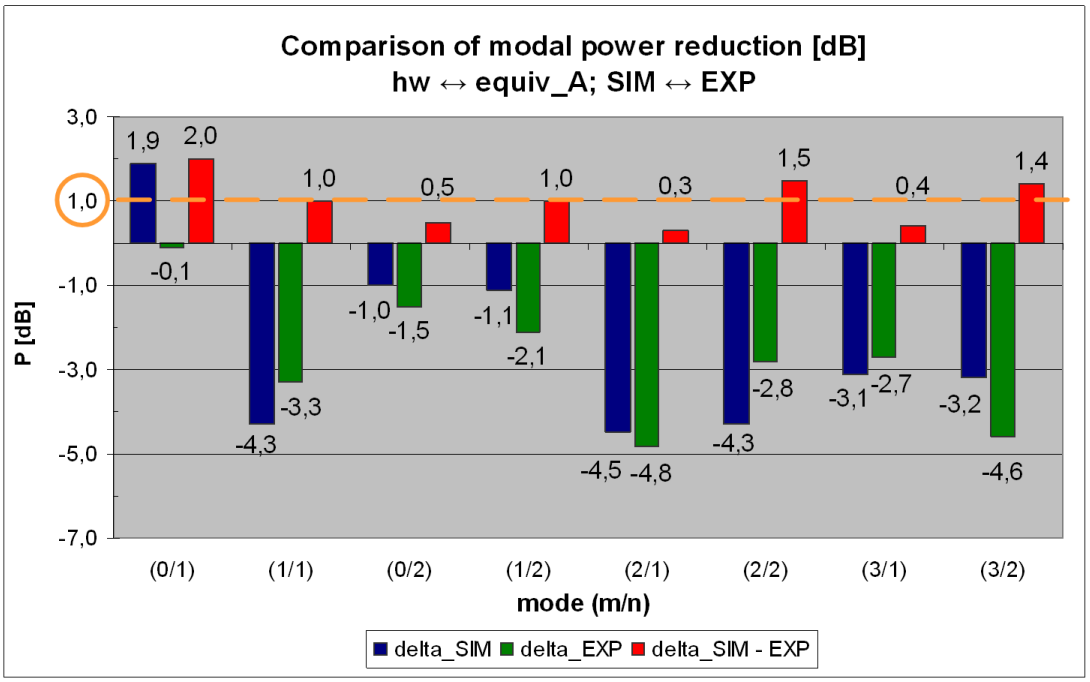

Figure 3.27: Comparison of modal power reduction - equiv_A; 2000 Hz; SIM ↔ EXP

The figure shows variations of the performance of both equivalent liner types from mode to mode. Hence, a general statement cannot be given at this point concerning the favorable conditions for either of the two configurations. However, in comparison to the MAL results later on in this chapter, it will become more obvious which variant yields the closest agreement with the adaptive liner results. Concerning the characteristic variations in the attenuation level depending on the modal numbers, the 'absorber effectiveness parameter' defined in the corresponding SILENCER report [183] shall be referenced, which incorporates

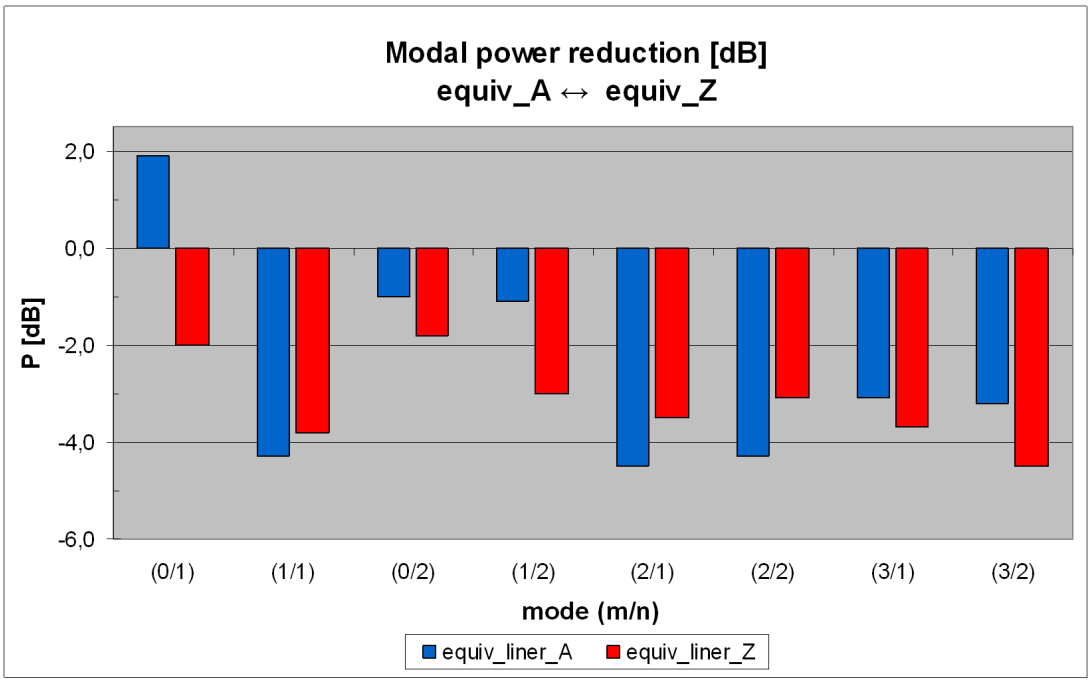

Figure 3.28: Comparison of modal power reduction - equiv_A ↔ equiv_Z; SIM; 2000 Hz

both the effective panel length (dependent on the modal propagation angle) and the effective absorber pressure (averaged over all four rows of absorber elements).

With respect to the individual modal effects, a consistent mechanism has been observed both in the experimental and numerical results of the area-equivalent liner, which will be described in the following. Therefore, figures 3.29(a) and 3.29(b) present the modal amplitude spectra determined at the two array positions (blue: experiment, red: simulation) and 3.29(c) and 3.29(d) the relative changes between microphone arrays 1 and 2.

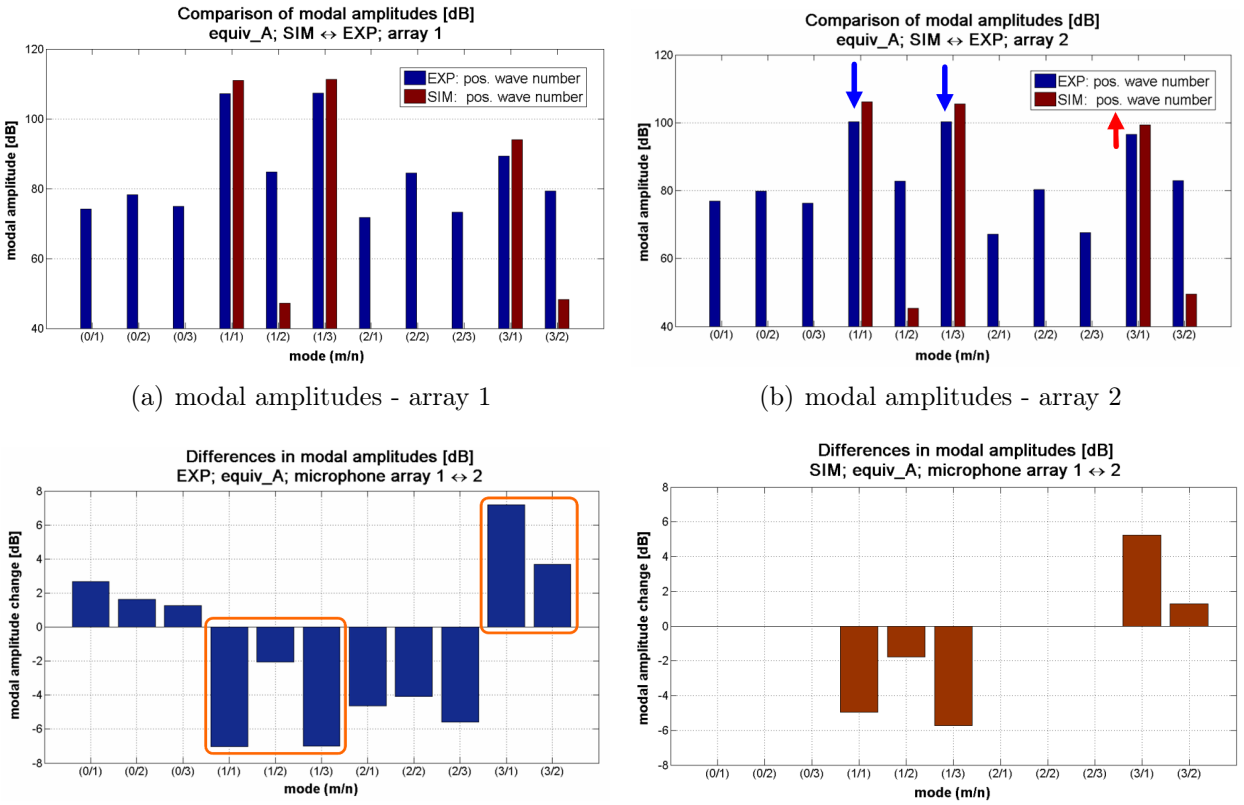

(a) modal amplitudes - array 1

(b) modal amplitudes - array 2

(c) modal amplitude changes - EXP

(d) modal amplitude changes - SIM

Figure 3.29: Comparison of modal amplitude spectra and relative changes; array 1 ↔ 2; equiv_A; EXP ↔ SIM; (1/1); 2000 Hz

First of all, as observed for the hardwall reference case in figure 3.26, the numerical results yield a much clearer picture of the contributing modes compared to the experimental values. These, however, still show an adequate separation between the primary and the secondary modes (-20 dB), as well as all other modes involved (-30 dB). As before, the modal amplitudes obtained from the simulation range ≈ 4 dB higher than the experimental ones.

Comparing now the results at both microphone arrays (top left and right), as indicated by arrows, the primary peaks have been reduced by 7 dB in the experiment, and by 5 dB/ 6 dB in the simulation. In parallel, the secondary modal amplitude (in this special case only one mode, as (3/3) is not propagating at this frequency, compare table 3.1) has been raised by 7 dB (EXP) and 5 dB (SIM), respectively. This leads to nearly equal amplitude levels of the primary and the secondary modes, especially in the experimental case (Δ SIM = 7 dB, Δ EXP = 3 dB).

This effect of a modal redistribution from the primary to the secondary mode(s) has been observed for nearly all excitation cases both in the simulation and the experiment. It probably has to do with the short length of the liner (l_{equiv_A} = 94 mm) compared to the wavelength at the frequency of excitation ($\lambda_{2000\,\mathrm{Hz}} \approx 170$ mm) imposing two jumps of impedance on the traveling waves within approximately half a wavelength.

Figure 3.30 depicts this characteristic effect schematically, pointing out again the common boundary condition of the primary and secondary modes at the vertical duct walls (where the liner panels are installed). Thus, it seems that the area-equivalent liners tend to balance the modal energy between the two physically possible solutions of the duct pressure distribution preserving the boundary values at the liner locations.

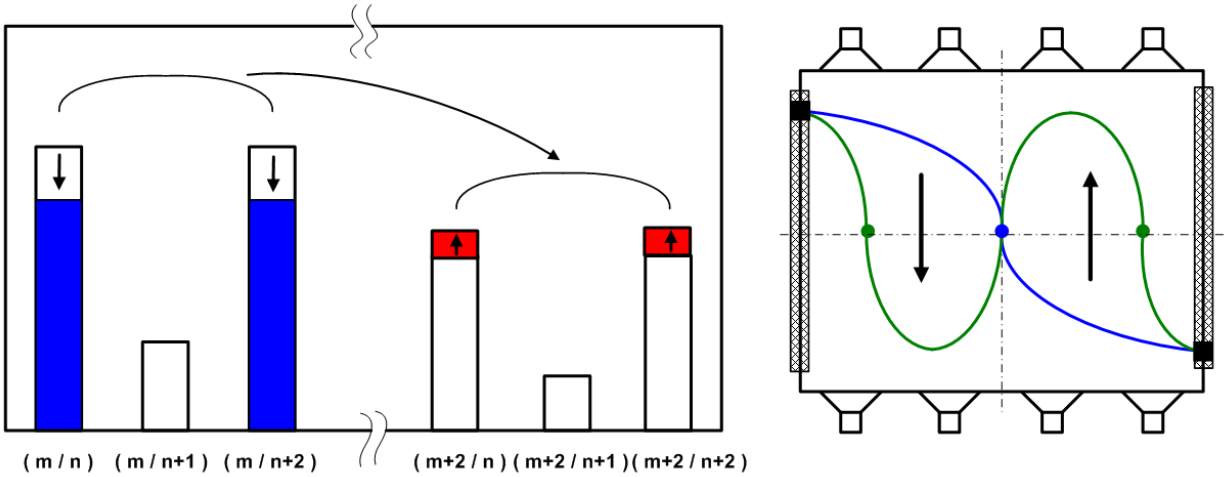

Figure 3.30: Modal amplitude effect for area-equivalent liner

In contrast, the numerical results of the averaged impedance liner (equiv_Z) are shown exemplarily for the same mode (1/1) in figure 3.31. The comparison of the modal amplitudes at array 1 and array 2 shows a reduction of all relevant participating components by -4 dB/ -5 dB for the primary modal amplitudes and -3 dB for the secondary mode. This corresponds to a purely absorptive effect, as would be desirable for most types of liners to avoid possible negative implications caused by mode scattering (as described in chapter 2.3.3).

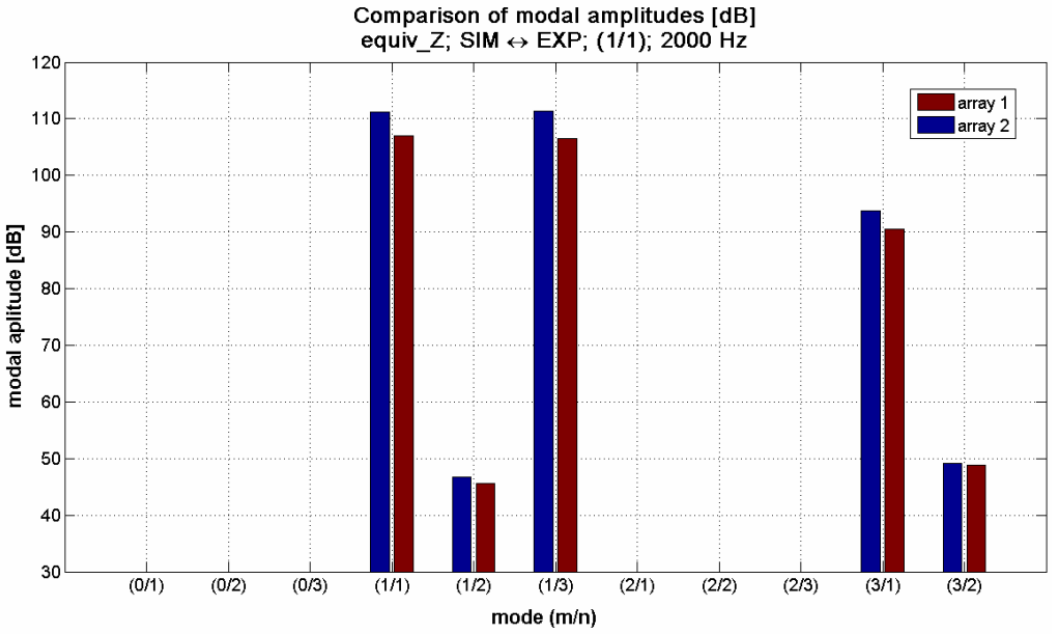

Figure 3.31: Comparison of modal amplitude spectra; array 1 ↔ 2; equiv_Z; SIM; (1/1); 2000 Hz

3.5.3 Absorber panels

Concerning the results for the MAL panels, both the *passive* and the *active* absorber performance will be presented (the terms 'passive' and 'active' corresponding to the state of the control loop as explained in chapter 3.2).

As depicted in figures 3.32 and 3.33, the results of the numerical and experimental study yielded qualitatively similar results, however at a different level. For all modes, the experimentally determined modal power reduction was considerably higher than the one obtained from the BE calculations. Moreover, the difference increases with an increasing mode order (decreasing cut-off ratio). This indicates a dependency of the effect on the propagation angle.

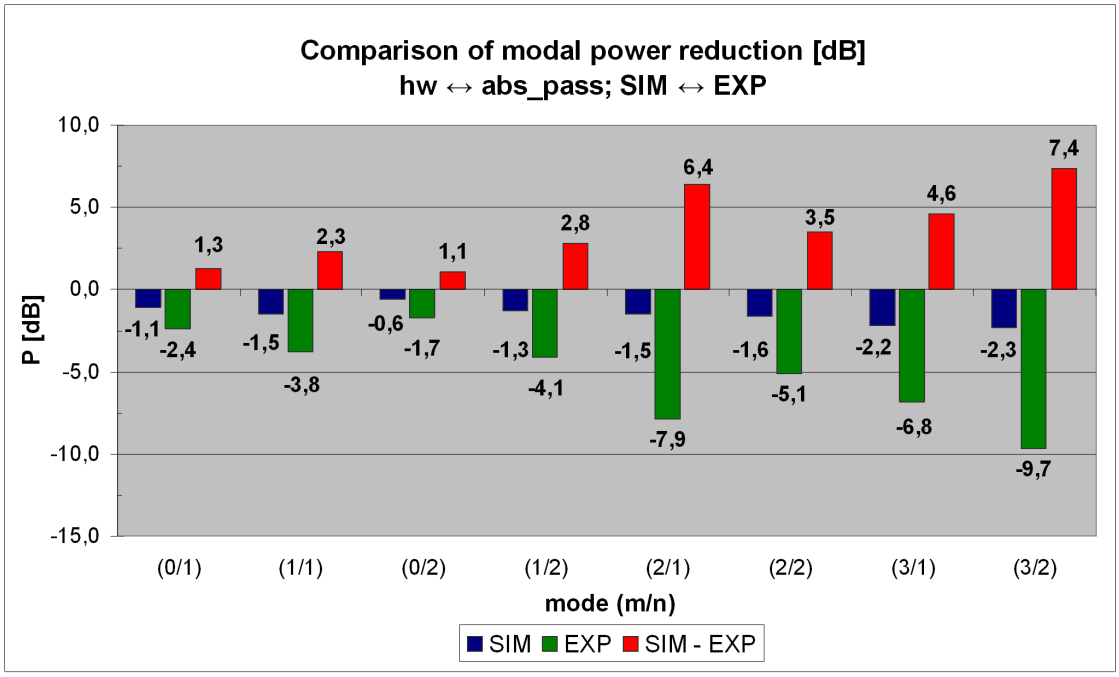

Figure 3.32: Comparison of modal power reduction - passive MAL panels ('control off'); SIM ↔ EXP; 2000 Hz

To understand this phenomenon, several modifications have been included in the numerical model. The first one includes a modeling of the Rohacell foam which has been used for embedding the MAL elements (visible in figure 3.3). Even if quite stiff and closed porous, which suggests no or only little impact on the acoustic field, due to its large area (approximately 5 times the effective area of the absorbers) it might have a non-negligible contribution to the absorption. Using its impedance value ($Z_{\text{Rohacell}} = 25 \cdot \rho c$), which has been obtained from a Kundt's tube measurement, the results improve by between 0.1 dB and 0.6 dB dependent on the mode order, at least in the passive configuration (again, increasing with increasing mode order).

The second attempt was to measure the effect of the foam on the test rig. Therefore, the absorber openings have been covered by aluminum tape, as shown in figure 3.34. This prevents any effect of the absorbers and should disclose the effect of the MAL foam panel on its own. After this measurement of the MAL panels, the results have been subtracted from the previous experimental results to ensure the same conditions as in the numerical results. This strongly reduced the discrepancy between simulation and experiment, but does not fully explain the observed differences.

Indeed, the reference measurement described above yielded a much stronger effect (pictured in figure 3.35) than could be expected from the impedance of the Rohacell foam and the numerical simulation of its effect (between 0.1 dB and 0.6 dB of additional attenuation).

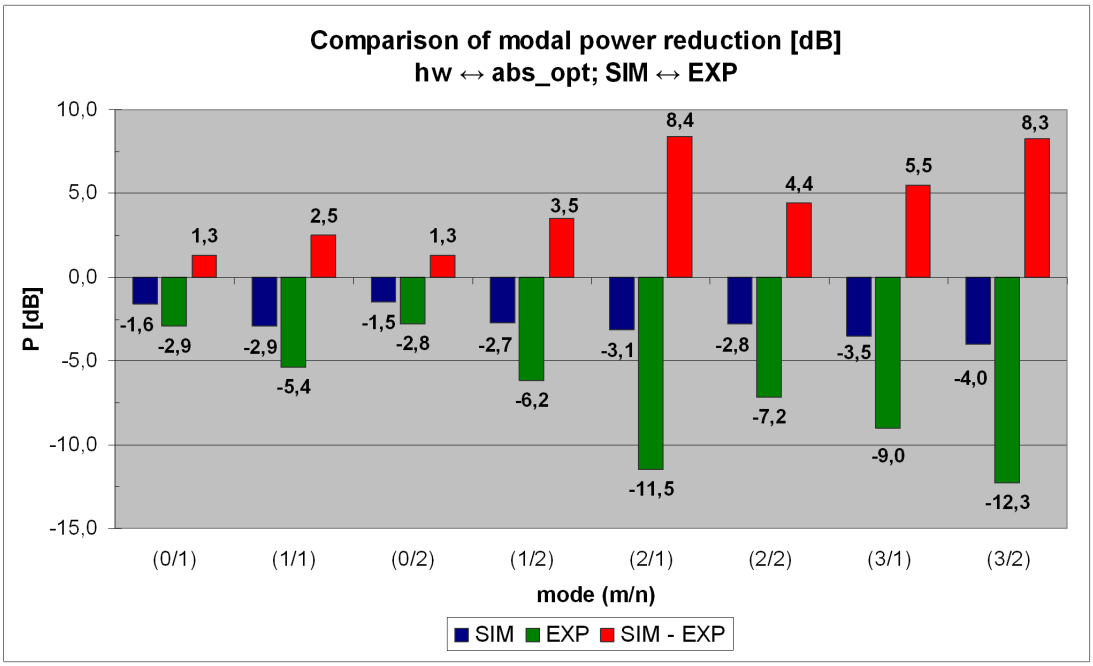

Figure 3.33: Comparison of modal power reduction - optimum impedance ('control on'); SIM ↔ EXP; 2000 Hz

Thus, the measurement setup seemed to comprise a certain detail that had not been included in the numerical modeling of the test rig.

According to these results, an additional cavity resulting from the placement of the MALs slightly behind the front side of the Rohacell panel (as can be seen in the close-up on the right hand side in figure 3.36) has been suspected to be responsible for the differences. Such a kind of cavity resonator would also explain the dependency upon the modal propagation angle, and the increasing effect for the higher mode orders.

Hence, the BE model has been modified to account for this geometric detail, as is shown in figure 3.37 in which the individual absorbers surfaces (to which the impedance boundary condition is assigned) have been shifted to the outside by 5 mm. This, in combination with the inclusion of the Rohacell foam effect, results in a considerably improved correlation between the measured data and the numerical solution.

Figure 3.34: Absorber elements covered by aluminum tape on test rig

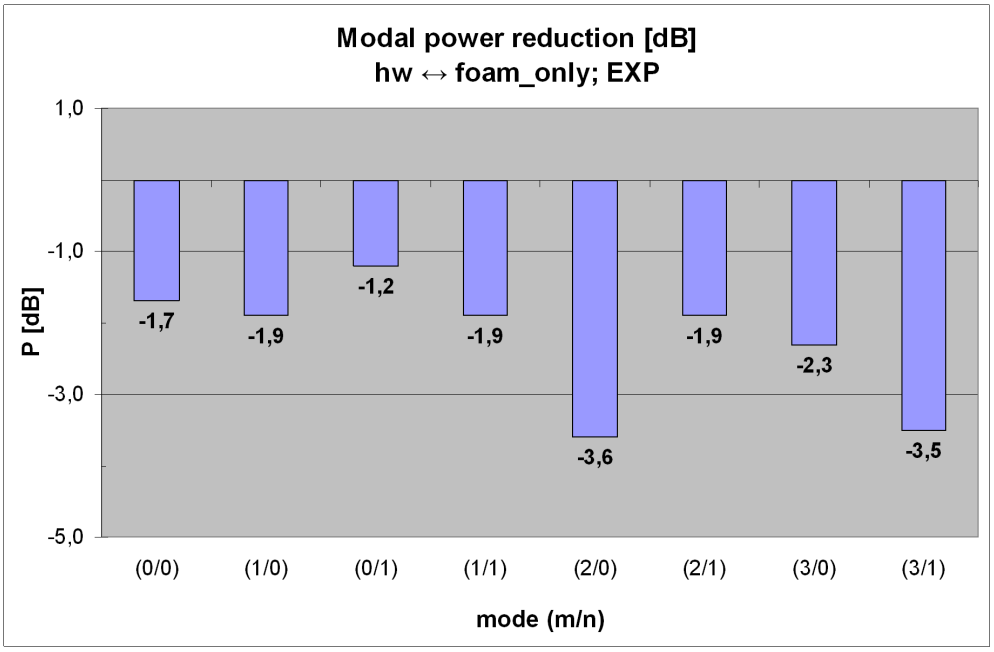

Figure 3.35: Modal power reduction measured on test rig with absorber elements covered by aluminum tape; 2000 Hz

Figure 3.38 presents the corresponding comparison of the modal amplitude reductions for the optimum impedance condition. Compared to figure 3.33 above, the maximum difference between the numerical and the experimental study could be reduced from 8.4 dB to 3.4 dB for the optimum impedance condition (and from 7.4 dB to 2.3 dB for the passive configuration not presented here).

The remaining deviation is supposed to be related to the presence of the flow fence (visible in figure 3.36 on the left hand side), which had been added to avoid an interference of the grazing flow with the microphone measurements in the flow duct facility, and not been included in the computations, as well as another small geometric detail of the absorber related to a ceramic ring enclosing the resistance sheet (compare close-up on the MAL panel in figure 3.36).

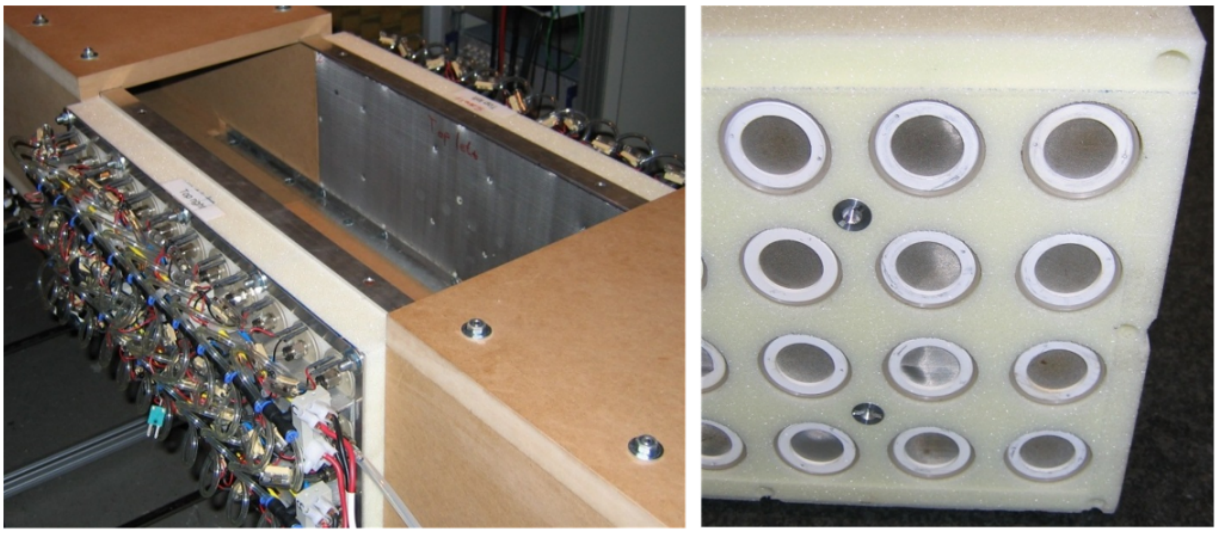

Figure 3.36: Test section of MALTA duct and close-up of absorber panel

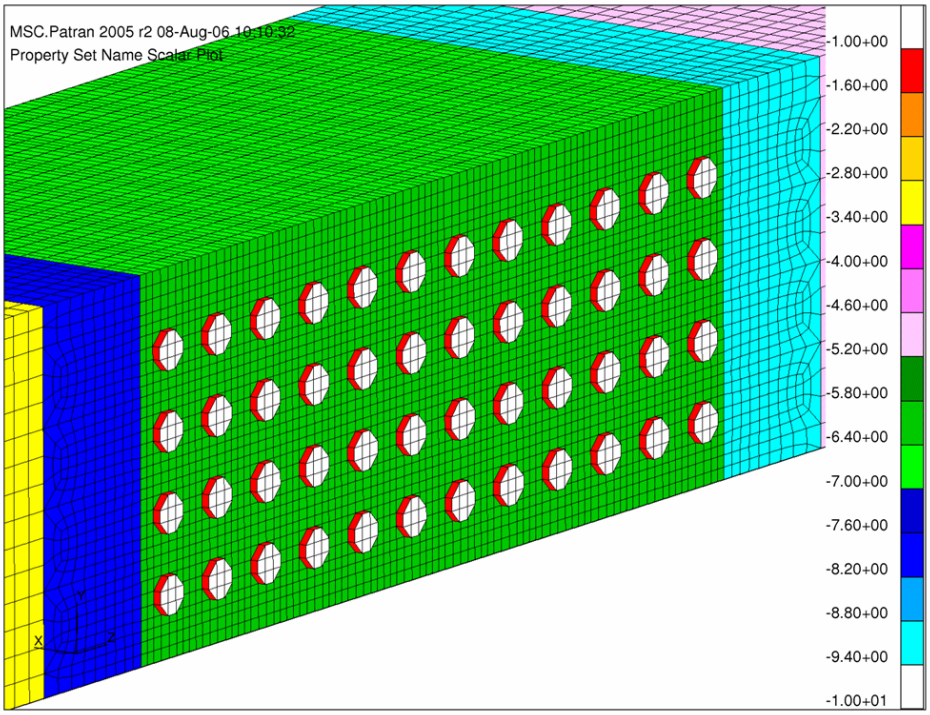

Figure 3.37: Close-up of test section of modified BE model (absorbers shifted)

After these considerations related to the modal power, the individual modal effects will be analyzed in the following, as has been done before for the equivalent liner panels. In analogy to the analysis of the area-equivalent liner, figure 3.39 shows the modal amplitude spectra due to the modal excitation (1/1) / (1/3) at the two array positions, as well as the relative changes between microphone array 1 and 2 for both the measurement (blue bars) and the simulation (red bars) in the passive configuration.

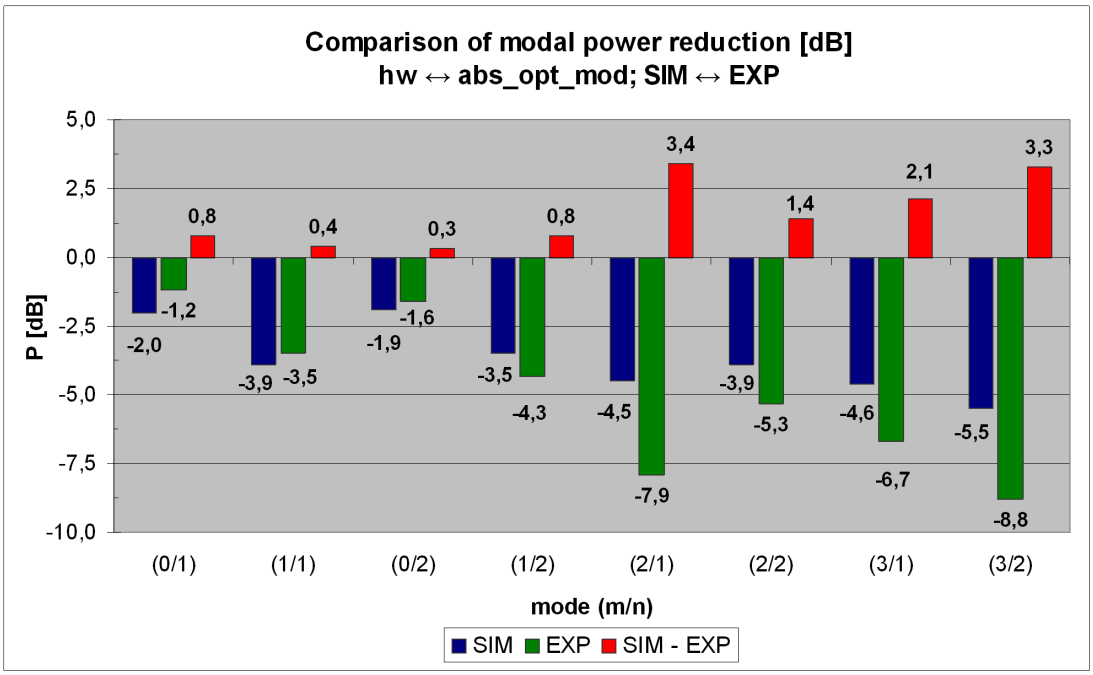

Figure 3.38: Comparison of modal power reduction - modified MAL panels, optimum impedance ('control on'); SIM ↔ EXP; 2000 Hz

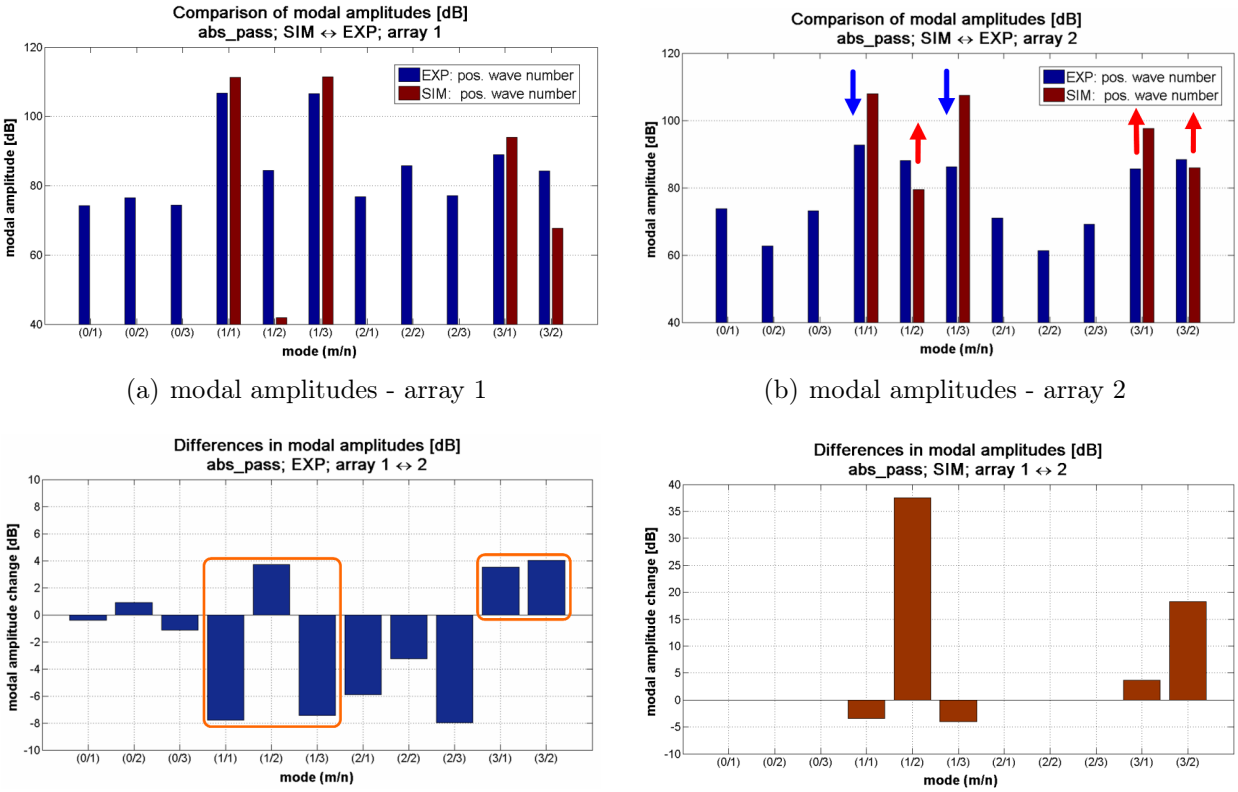

(a) modal amplitudes - array 1

(b) modal amplitudes - array 2

(c) modal amplitude changes - EXP

(d) modal amplitude changes - SIM

Figure 3.39: Comparison of modal amplitude spectra and relative changes; array 1 ↔ 2; abs_pass; EXP ↔ SIM; (1/1); 2000 Hz

Again, a certain kind of modal redistribution mechanism can be derived from the data: throughout the test section, the amplitudes of the primary modes are reduced by several dB (-8 dB/ -7 dB in the experiment and -3 dB/ -4 dB in the simulation). In parallel, the modes of the same horizontal modal order (same m) but a different vertical modal order (different n) are raised in level. This effect is much more pronounced in the numerical results, where e. g. mode (1/2) experiences an increase by +38 dB (compared to +4 dB in the experimental results). However, this raise has to be related to the starting position which - as the overall noise level ahead of the test section in the simulation - is extremely low compared to the measurements.

Similarly, the secondary mode(s) and its 'neighboring' modes (same m, different n) have been raised in level, which leads, at least on the experimental side, to a nearly balanced modal amplitude spectrum. In detail, in the measurement data, the amplitude of mode (1/3) equals the one of the secondary mode (3/1), mode (3/2) is even 2 dB higher in level, and the second primary mode (1/1) protrudes by only 7 dB from these results. On the simulation side, the separation is considerably higher, being 10 dB between the primary peaks and the secondary one, and 20 dB with respect to mode (3/2).

As for the equivalent liners, the effect on the modal amplitude spectra (depicted schematically in figure 3.40) could be observed for nearly all modes under consideration both in the simulation and the experiment. It redistributes energy from the primary peak(s) to the secondary ones (insofar analogous to the area-equivalent liners), but much more prominent, to the y-modes of the same modal parameter m as the primary and secondary modes (the so-called 'neighboring' modes).[4]

[4]Not directly equivalent, but of a similar relation to the radial modes of an azimuthal mode order for the case of a cylindrical duct.

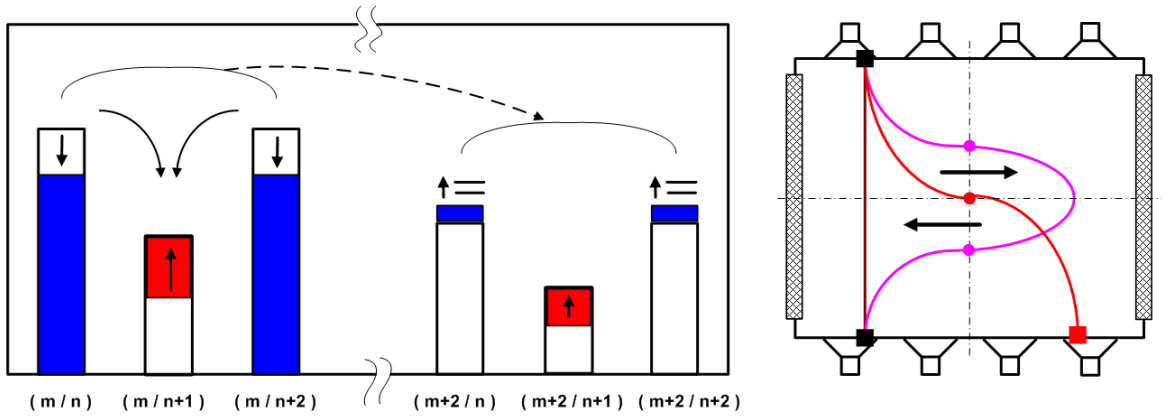

Figure 3.40: Modal amplitude effect for MAL panels

As it was not exactly clear at this point if this effect related to the y-modes occurs for all cut-on y-modes or only special ones (e. g. $n \pm 1$), additional calculations have been carried out at higher frequencies. These include $f_2 = 2800$ Hz $\equiv k \cdot a = 16.6$ (equivalent to the $k \cdot R$ value which is conveniently used in the investigation of cylindrical ducts, compare also equation (2.39)) and $f_3 = 3400$ Hz $\equiv k \cdot a = 20.1$, and yield additional cut-on modes in both the x- and y-direction (still satisfying the '6 elements per wavelength rule' for the BE model). The respective maximum mode numbers are $m = 5$, $n = 4$ at 2800 Hz, and $m = 6$, $n = 5$ at 3400 Hz.

These calculations resolve the characteristics of the MAL effect on the modal amplitude spectra: the discrete absorber elements cause scattering into the secondary modes $(m \pm 2l)$ with $l = 1, 2, \cdots N$ and all y-modes of the primary and these secondary x-modes. An example of the results is given in figure 3.41 for mode (0/2) at 2800 Hz.

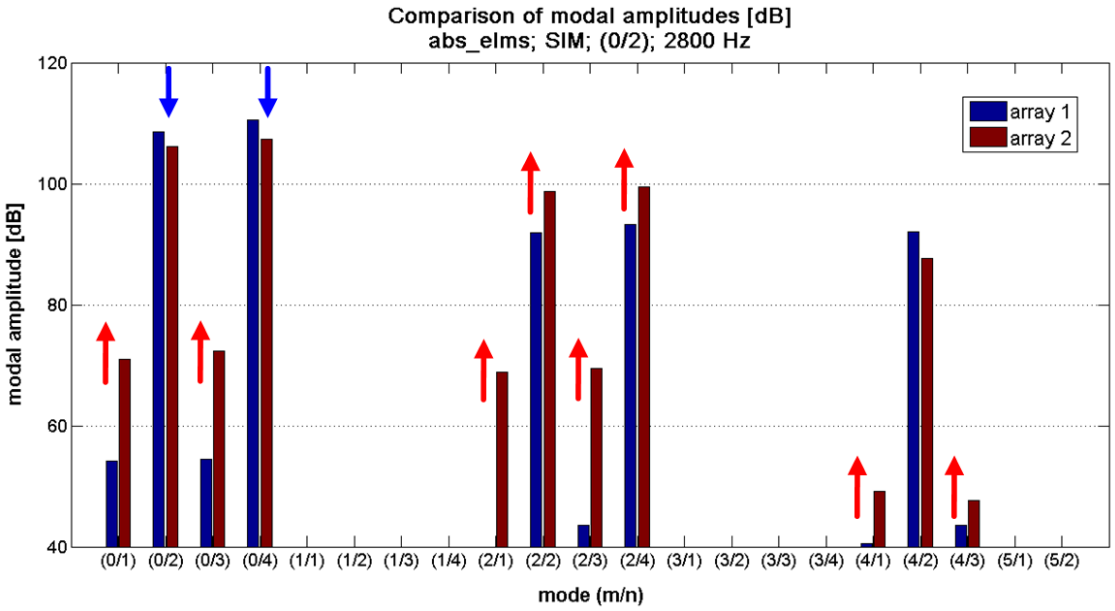

Figure 3.41: Comparison of modal amplitude spectra; array 1 ↔ 2; abs_elms; SIM; (0/2); 2800 Hz

The figure clearly shows the reduction of the primary modes and the increase in all other secondary and neighboring y-modes throughout the test section containing the MAL panels.

3.6 Summary of experimental and numerical study

Concluding the results of this validation, it can be said that both studies correlate quite well with respect to the overall power reduction as well as individual modal effects that emerged for the MAL panels and the area-equivalent liners. Figure 3.42 thus opposes the average modal amplitude reduction of the two MAL configurations (passive (*MAL_pass*) and active (*MAL_opt*)) and the two equivalent liner types (area-equivalent (*equiv_A*) and averaged impedance (*equiv_Z*)) as far as available.

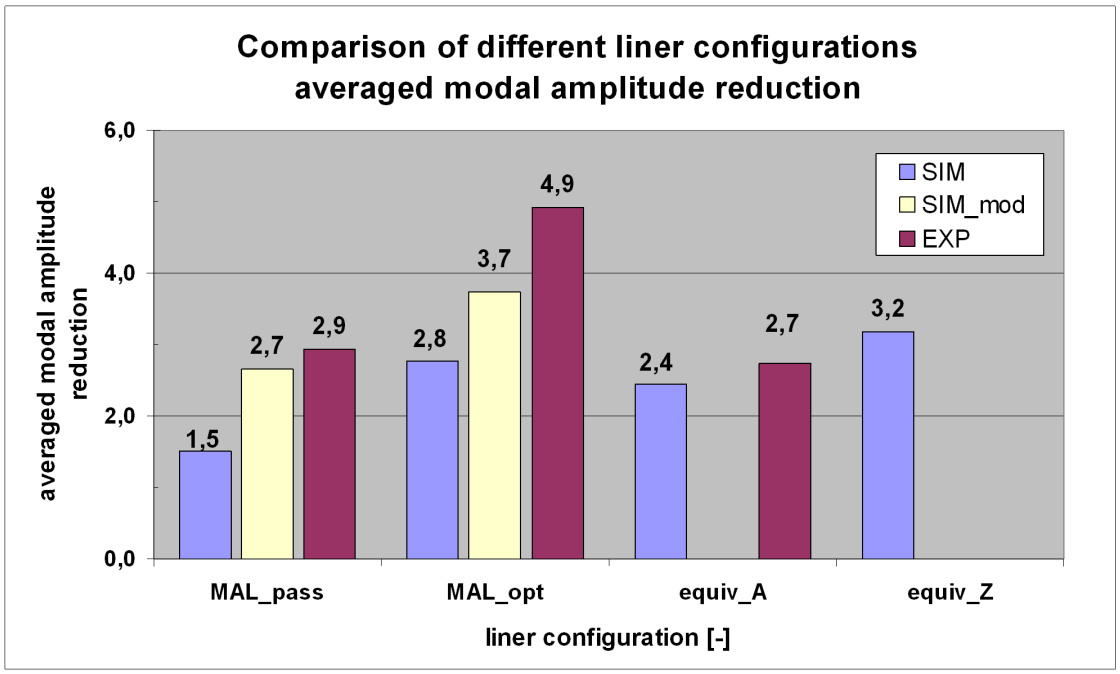

Figure 3.42: Comparison of average modal amplitude reduction; SIM ↔ EXP; 2000 Hz

At first, considering only the numerical results of the original (not the modified) BE model, the diagram points out that the MAL panels tuned to their optimum impedance, achieve a level of average reduction exactly between the averaged impedance liner (-0.4 dB) and the area-equivalent liner (+0.4 dB). This result indicates, on the one hand, the importance of the effective panel length on the modal sound field, and, on the other hand, the effect of scattering or modal redistribution effects on the overall performance of a liner.

With respect to the first point, and considering the individual modal performance, the averaged impedance liner (equiv_Z) having the same circumscribed area as the MAL panels, resembles their acoustic effect most suitably.[5] In contrast, a concentrated equivalent liner offering the same acoustically effective area, does not yield the same level of noise reduction. Additionally, due to its short length, it causes different effects related to a modal restructuring and associated reflections at the liner interfaces.

The MAL panels, combining discrete absorber elements being assigned an absorptive impedance with a hardwalled support, act in effect like an averaged impedance liner of the same circumscribed area. However, in contrast to the numerical simulation of the averaged

[5]This result differs from the findings of Myers and Cochrane [184] who studied the effect of a continuous impedance variation on the acoustic absorption and found differences between this type of liner and one with an averaged impedance for a general sound field. In contrast, Parrott and Jones [185] found a good correlation between the two models in plane wave impedance tube measurements. However, the liners investigated by these researchers differ fundamentally from the ones analyzed within this chapter consisting of discrete absorptive elements within a (nearly) hardwalled matrix.

impedance liner, scattering effects could be observed for the MAL panels, which slightly influence the overall performance, even if they range at a reduced power level compared to the main contributing modes. This low scattering level can be related to the relatively large ratio of the wavelength ($\lambda = 170$ mm) to the distance between two neighboring absorbers (50 mm). Moving to higher frequencies (and lower wavelengths), an increasing level of scattered modes should be expected.

With respect to the deviations observed between the experimental and numerical results for the MAL panels, it could be shown that the differences are related to simplifications used in the first BE model, neglecting geometric details of the MAL panels, as well as the finite impedance of the Rohacell foam. In contrast, for the area-equivalent liner, which has been modeled with adequate accuracy, quite a good correlation has been achieved between the numerical and the experimental model ($\Delta = 0.3$ dB).

For a closing remark, it should be stated that the local impedance measurement employed in the MAL configuration exposed strong weaknesses in this application involving distinct modal sound fields. It showed a strong sensitivity to small variations in the microphone locations, which have to be determined very accurately to correctly deduce the impedance of the MAL element. Additionally, problems arose in cases where the microphones were located close to zero points of the modal functions. Due to these deficiencies, the local impedance measurement method cannot be recommended for future applications involving similar types of modal sound fields.

Chapter 4

Concept and characteristics of the Virtual Scarf Inlet (VSI)

In this chapter, the basic concept of the Virtual Scarf Inlet will be presented. It aims at reducing or, more precisely, redirecting the forward radiation of an aircraft engine - especially the components directed towards the ground. With respect to the deficiencies of the alternative solutions presented in the chapter about the state of the art (chapter 2), the VSI proposes a novel method of influencing noise radiation.

At first, the physical principle of this concept will be explained in general. Subsequently, a parametric study comprising its geometric parameters will be presented, followed by a thorough analysis of the results and a deduction of guidelines, which will be considered in the assessment of a number of advanced VSI lining concepts in chapter 6. At the end of this chapter, the effect of the VSI on a propagating mode will be summarized and its main influencing factors will be derived.

4.1 Basic concept of the VSI

The basic idea of the VSI is to shield the lower sector of an aircraft engine inlet by suitably redirecting the directivity characteristic. This can be accomplished by an abrupt change of the acoustic impedance boundary condition at a favorable position inside the inlet instead of a modification of the inlet geometry (as done in the Negatively Scarfed Intake (NSI), a geometrically non-uniform concept which has been presented in chapter 2.3.3.2).

Thus, the VSI design implies the positive effects of the negative scarf but requires only little change to the inlet design avoiding a tradeoff with aerodynamic or weight considerations. In a practical implementation, the characteristic impedance discontinuity causing the deflection of the sound pattern may be achieved by a (relatively) small semi-circular strip of liner exhibiting an impedance considerably lower than the surrounding material at a specific position close to the exit plane of the inlet (as sketched schematically in figure 4.1).

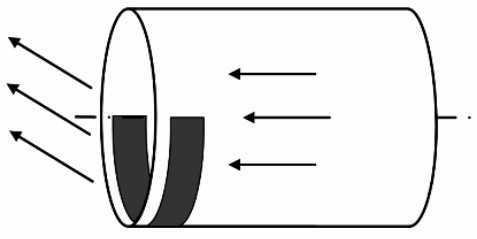

Figure 4.1: Conceptual sketch of the Virtual Scarf Inlet (VSI) effect

This liner strip will be denoted *'reflective'* in the scope of this thesis referring to its effect on the modal sound patterns as will be explained in the following. In its final application, the reflective liner is supposed to be integrated into a conventional uniform liner design, both of which might be adaptive to achieve a maximum noise reduction at all flight conditions.

The physical phenomenon causing the deflection of the sound pattern within the duct and the corresponding deflection of the radiation characteristic, is based on the special boundary condition imposed at the reflective liner location. An impedance close to zero (both the resistance and reactance values) represents a *softwall condition* (as presented in figure 2.15 in chapter 2.1.1.2). This corresponds to a zero value of the sound pressure and a maximum of the sound particle velocity at the duct wall. A wave traveling towards the wall is thus reflected at the same amplitude but opposite phase, which leads to a local cancellation of both sound waves, and may be denoted a 'passive anti-sound mechanism' (referring to the Active Noise Control (ANC) concepts presented in chapter 2.3.2.2).

By this effect, the radial distribution of pressure maxima and nodes within the duct cross section can be shifted relative to its undisturbed position, which is illustrated in figure 4.2 for the two cases of an axisymmetric mode ($m = 0$) and an azimuthal mode ($m > 0$).[1] On the left and right hand side, the radial characteristics of the 'zeroth' and first radial mode are sketched, respectively. They exhibit (local) maxima at the duct walls and $n - 1$ zero points between the duct center line and the outer wall. By postulation, they are perfectly symmetric (for $m = 0$) or antisymmetric (for $m > 0$) with respect to the center line. In between these two conventional radial mode orders, the case of a vanishing impedance BC at the lower duct wall is inserted. Accordingly, this adds an additional zero point (at the duct wall), which might suggest the notation of the mode to be n = '1 1/2', since a single zero point has been added in the radial direction.[2]

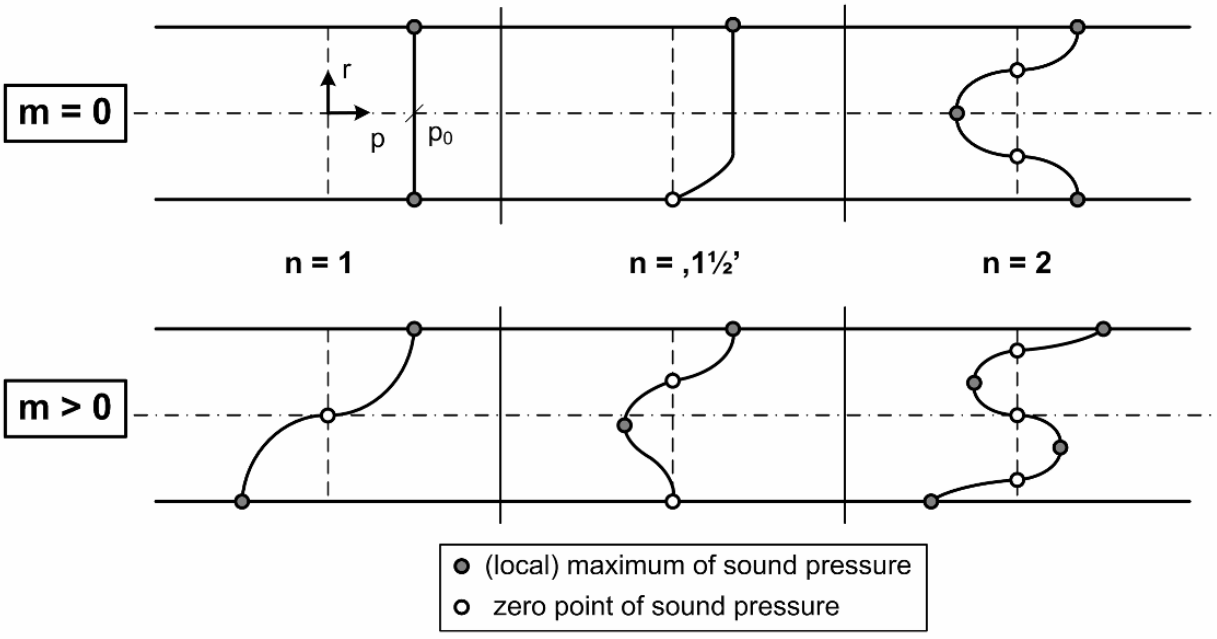

Figure 4.2: Sketch of the radial distribution of sound pressure within a cross-sectional plane for different modal numbers and BCs

[1] For an explanation of the modal notation refer to figure 2.4.

[2] However, the concept of the modal notation is, strictly speaking, not applicable in this case as the basic postulation of symmetry or periodicity in the modal concept is not fulfilled any more. This will be explained in more detail in chapter 5.5.

This resulting asymmetry of the propagating wave is transferred as well to the far field by the laws of diffraction and radiation, if the effect can be achieved at a location close to the exit. Preferably, in the application envisaged for the VSI, the radiation of an aircraft engine may be by these means influenced to contribute more to the upper angles and less to the ground, where residents in the vicinity of an airport are annoyed by the sound impact of passing aircraft.

To assess the potential of the reflective liner strip with respect to this objective, a parametric numerical BE study comprising its geometric characteristics (position inside the inlet, length, angular sector) has been performed, which will be presented in the next sections. After an evaluation of the results, the main influencing factors of the VSI effect will be derived at the end of this chapter.

4.2 Numerical modeling of engine inlet duct

For this parametric study, the geometry of the ROSTI (ROtor STator Interaction) test rig situated at EADS Innovation Works in Ottobrunn has been selected to enable a future experimental validation. Its main dimensions (a diameter $D = 0.5$ m which widens at the inlet to $D_e = 0.7$ m and an inlet length $l_i = 0.55$ m, yielding a diameter to inlet length ratio of $D/l_i \approx 0.91$) and the simplifications used in the BE model are given in figure 4.3.

As indicated, the duct has been terminated in the numerical implementation at the rotor plane by a so-called *modal surface* (compare explanation in chapter 2.4.3.4) enabling the excitation of single propagating modes. These modes then propagate into the positive axial direction (*z-axis*) and are reflected at the inlet depending on the geometry and their cut-off ratio. From the ratio of the amplitude coefficients at the modal surface, the reflection coefficients can be determined, which will be used later on in the analysis of the results.

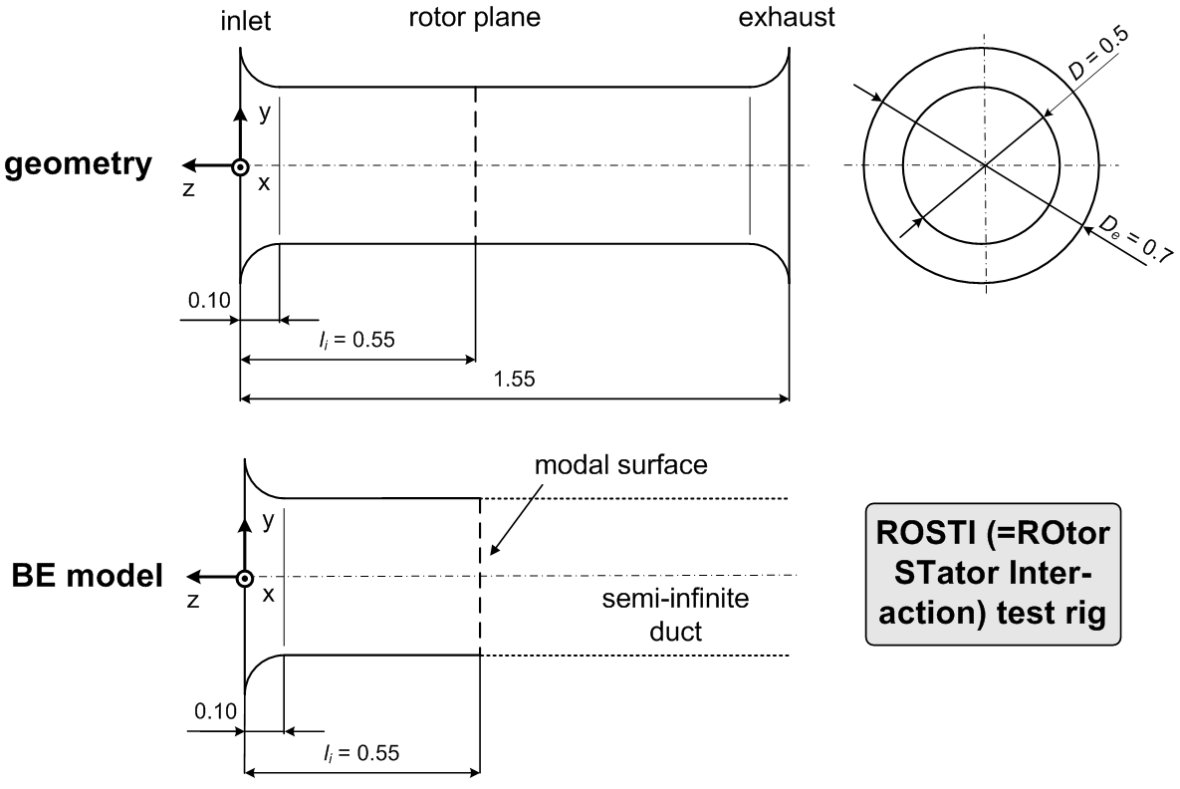

Figure 4.3: Sketch of ROSTI test rig and BE model geometry

Concerning the analysis of the results, several field point (FP) meshes have been created enabling the determination of the sound pressure level, the intensity, or the radiated power at selected locations of interest, among them a quarter sphere centered at the inlet plane (figure 4.4) to analyze the radiated power into the lower forward sector.

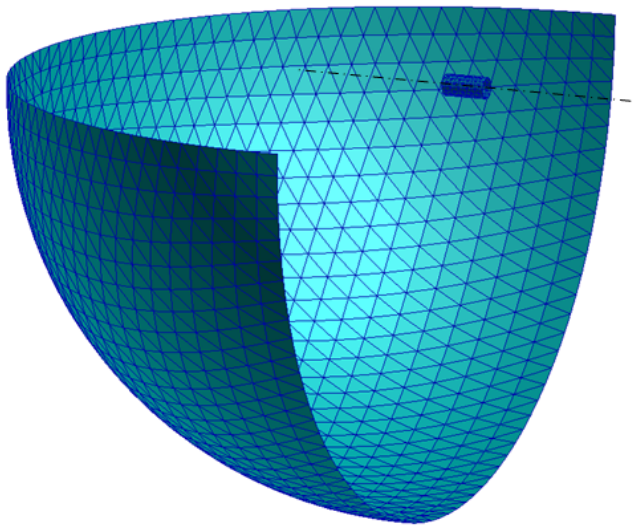

Figure 4.4: Quarter sphere field point mesh for radiated power determination

Figure 4.5 indicates the nomenclature used within the context of directivity plots: the direction vertically towards the ground is denoted -90°, the engine axis corresponds to the 0° direction, and +90° is directed towards the sky. To compare with the directivity plots, also the solution at a vertical FP plane located at the duct midplane has been computed for a graphical display of the radiation characteristics.

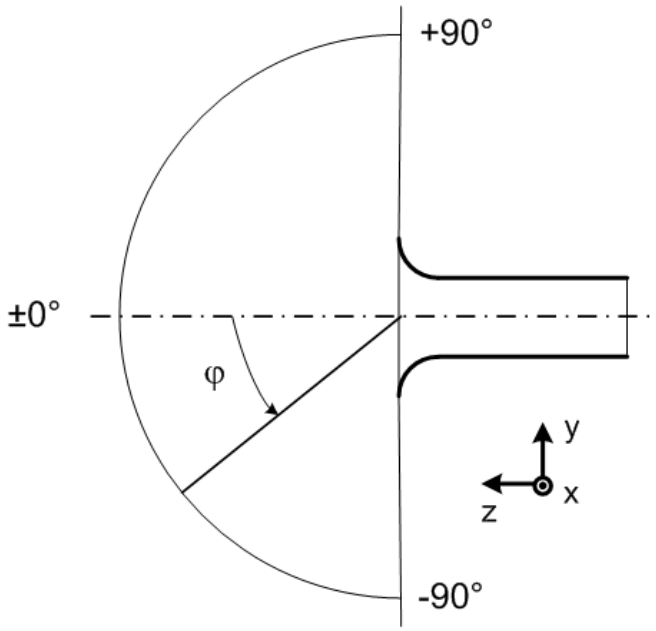

Figure 4.5: Definition of angles in vertical directivity plots

For this systematic parametric study, the simplified geometry described above has been converted into a numerical model as presented in figure 4.6.

The mesh consists of simple triangular elements of an average element length of 10 mm (i.e. $D/50$), yielding a valid frequency range up to 3000 Hz (equivalent to $k \cdot R \approx 14$).[3] It allows for a very flexible definition of acoustic BCs by predefined property groups in the front half of the inlet (indicated by differently colored elements in the figure). Altogether, the model contains 252 different groups at 7 axial (4 in the cylindrical part of the inlet and 3 in the lip area) and 36 circumferential positions (at 10° increments).

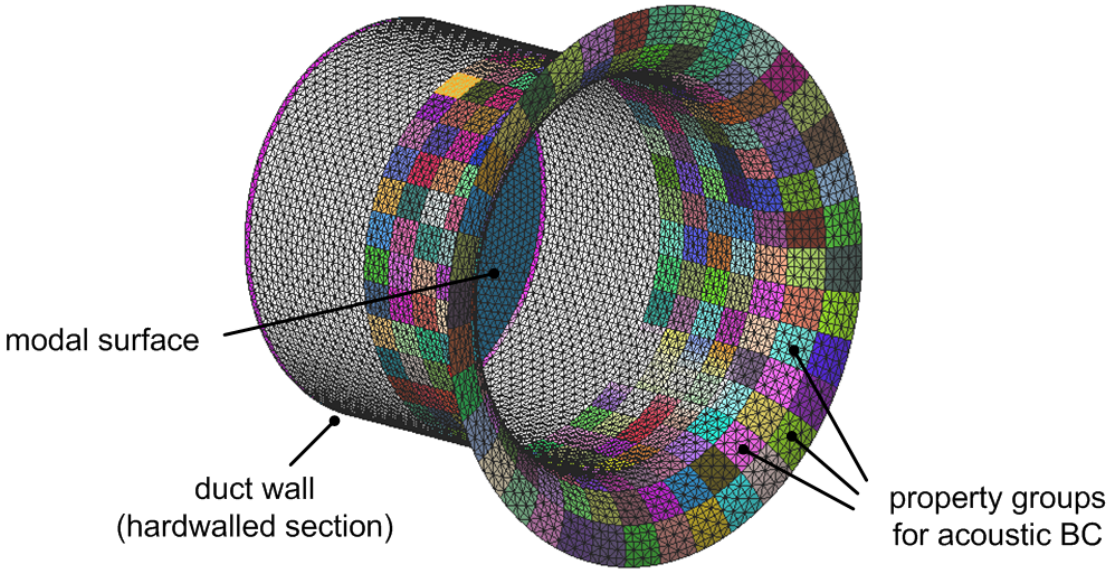

Figure 4.6: BE model of ROSTI test rig used for parametric study

Within the parametric study, these property groups will be combined to larger liner segments of varying axial and circumferential dimensions. The adjacent uniform section of the duct wall will be assumed hardwall within this study to separate the effect of the reflective liner strip from any other influences. At the rear end of the duct, the modal surface has been defined, a set of elements which is acoustically transparent but enables the definition of modal pressure patterns.

Within the scope of this chapter, only circumferentially standing wave patterns (the so-called 'non-spinning modes', resulting from the choice $A_3 = B_3$ in equation (2.29)) will be analyzed, since spinning modes involve additional effects in the lateral direction, as will be presented in the next chapter.

The reflective impedance[4] has been chosen to be $Z_r = (0.05 - i \cdot 0.05) \cdot \rho c$ to achieve a condition close to the theoretical softwall BC, which could not be used for practical reasons. All other elements feature by default hardwall BCs corresponding to an impedance $Z_{hw} = \infty$.

4.3 Parametric study of Virtual Scarf concept

4.3.1 Geometric parameters of reflective liner

The parameters evaluated comprise the geometric dimensions of the reflective liner segment as well as its position inside the duct inlet. Therefore, three sets of variations have been computed successively:

[3] Following the '10 elements per wavelength' rule proposed by the ACTIPOLE manual [169].
[4] This value has been chosen by estimation and not been optimized at this stage.

- an axial variation of the position of the reflective liner segment (at fixed axial and circumferential dimensions),
- a variation of the axial length of the liner (centered at a fixed location with constant circumferential length),
- a variation of the circumference angle (at a fixed axial position and length).

Due to the characteristics of the discretized geometry, and to limit the number of configurations, axial steps of 50 mm increments (i.e. $D/10$) have been selected. Their locations in the front inlet area and numbering may be inferred from figure 4.7. Likewise, these groups of elements may be combined to obtain larger liner patches.

In the circumferential direction, only symmetric configurations with respect to the vertical plane have been chosen starting from an enclosed angle of 100° (i.e. 50° to each side) with increments of 20° up to a semi-circle (180°). Beyond that, larger angular increments have been used to study a further increase in the circumferential dimension of the liner up to a closed segment of 360°.

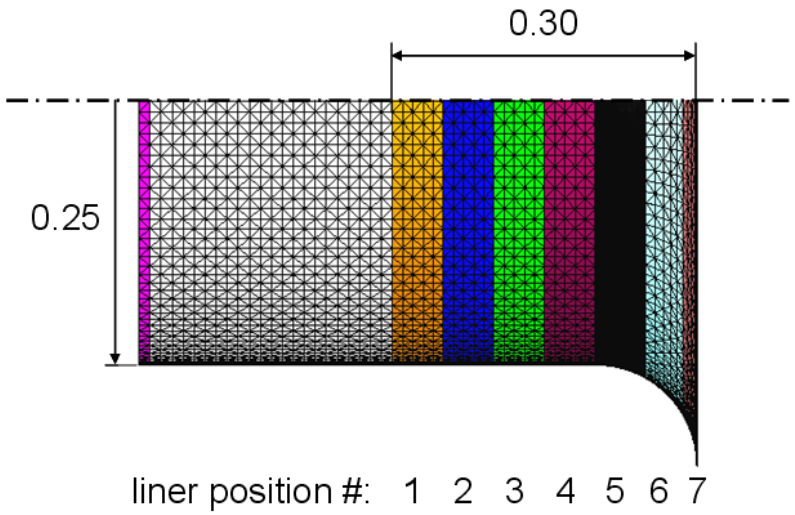

Figure 4.7: Numbering of axial liner locations in BE model [186]

Concerning the frequencies of excitation, three third octave band center frequencies[5] (1000, 1600, 2000 Hz $\equiv k{\cdot}R = 4.62, 7.39, 9.24$) have been selected to study the influence of frequency changes on the results. At each frequency, all propagating modes have been evaluated, which are summarized in table 4.1.

Therein, the colors indicate the additional propagating modes at the respective frequency: green ≡ 1000 Hz, blue ≡ 1600 Hz, and red ≡ 2000 Hz. To conclude, table 4.2 summarizes all parameters involved in the parametric study and their specific values.

In the table, squared brackets indicate that the respective value has not been applicable or available in all cases, e. g. only a reduced number of modes is propagating at 1000 Hz.

In the following, the results of the three variations described above will be presented and interpreted one after the other. Concluding, a summary will be given, and guidelines for the subsequent studies in the next chapter will be deduced.

[5] In acoustic analyses, third octave bands are conveniently used to limit the number of frequencies to compute. As an octave represents a certain ratio of its edge frequencies (2:1), the center frequency is chosen to represent the acoustic behavior within this frequency band. The center frequencies are, in turn, calculated by means of the concept of 'preferred numbers' (proposed by Charles Renard in the 1870s, adopted later on as the ISO 3 standard).

Table 4.1: Cut-off frequencies of first relevant modes (circular cylinder, $D = 0.5$ m)

n \ m	0	1	2	3	4	5	6	7	8
1	0	399	661	909	1151	1389	1625	1857	2088
2	829	1154	1452	1735	2009	2277	2540	2799	3055
3	1519	1848	2158	2456	2745	3028	3305	3578	3847
4	2202	2534	2851	3157	3455	3747	4034	4316	4595

Table 4.2: Parameters used in parametric VSI study [186]

circumference angle [°]	no. axial groups [-]	axial pos. [-]	frequency [Hz]	mode (m/n)
100	1	1	1000	(0/1), (0/2), [(0/3)]
120	2	2	1600	(1/1), [(1/2)], [(1/3)]
140	3	3	2000	(2/1), [/2/2)]
160		4		(3/1), [(3/2)]
180		5		[(4/1)]
220		[6]		[(5/1)]
260		[7]		[(6/1)]
300				[(7/1)]
360				

4.3.2 Variation of axial position

At first, the basis configuration with a fixed axial length ($l_{ax} = 50$ mm $\equiv$ one property group in the axial direction) and circumference angle ($\phi = 180°$) has been positioned at all 7 axial positions within the front inlet region (as described above). In figure 4.8, the resulting directivity curves in the vertical plane (at a radius of 10 m, i.e. $20 \cdot D$, centered at $x = 0$) are given at the example of mode (2/1) at $f = 1000$ Hz. For reference, the hardwall characteristic has been added indicated by the dashed black line. Corresponding to figure 4.7, 'pos. 1' refers to the liner position closest to the modal surface and 'pos. 7' to the one closest to the exit plane.

It can be seen that moving the reflective liner to the front causes a successive reduction in sound pressure level in the lower sector [-90°; 0°] and an increase in the upper sector [0°; +90°] up to position 6 (the center part of the inlet lip area). Beyond that, the pressure level rises again in the lower sector, wherefore position 6 seems to be the most favorable in this case. This is due to the fact that the liner segment located directly at the exit (position 7), and nearly perpendicular to the duct axis, is not able to effectively redirect the main lobes of radiation. Additionally, it may be observed that for the first position, the level in the lower sector is even above the hardwall solution (which is due to effects in the upper duct sector of the inlet which will be explained in the following).

The horizontal and the slightly tilted lines in the figure serve to clarify the effect of the reflective liner: it tilts the directivity curve by an angle α_1 compared to the (symmetric) hardwall configuration. This causes a decrease in sound pressure level in the lower sector and an increase in the upper sector.

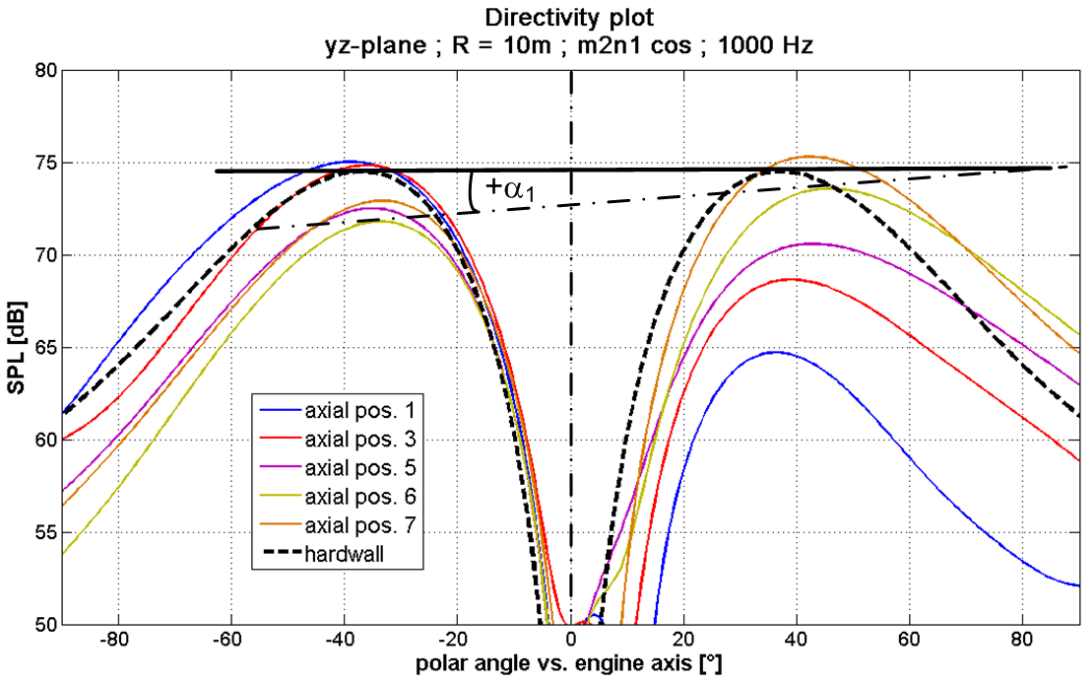

Figure 4.8: Comparison of vertical directivity plots at duct midplane; hardwall condition ↔ axial variation of reflective liner; (2/1); 1000 Hz; $R = 10$ m [187]

To verify these tendencies, the same mode has been analyzed at a higher frequency (2000 Hz) where its first radial mode (2/2) is propagating, as well (as can be deduced from the side lobes in figure 4.9).

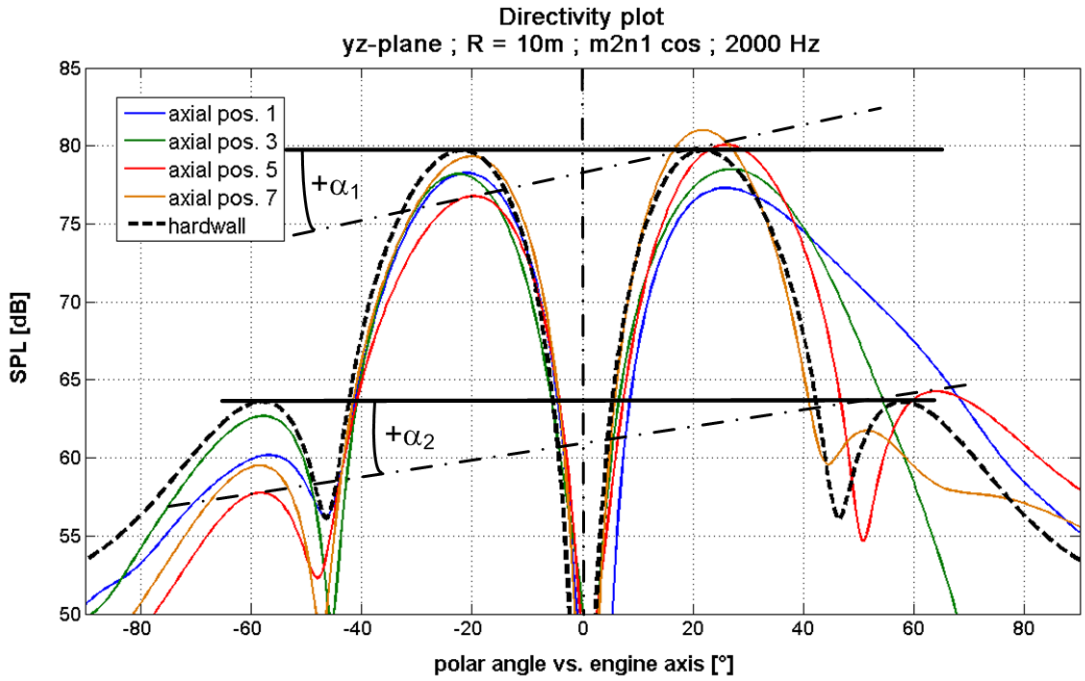

Figure 4.9: Comparison of vertical directivity plots at duct midplane; hardwall condition ↔ axial variation of reflective liner; (2/1); 2000 Hz; $R = 10$ m [187]

As before, the directivity pattern changes as the position of the reflective liner strip is varied within the front inlet. With respect to the lower main lobe (at $\approx -20°$), the level stays nearly constant for the first three positions (pos. 1-3) and then drops considerably at position 5.

Beyond that, the pressure level rises again and becomes less desirable. With respect to the side lobe (at $\approx -60°$), the tendency is slightly different, yielding an increase in sound pressure level (SPL) up to position 3 and minimum levels at position 5. Overall, at this higher frequency, position 5 seems to be the most promising one to achieve the desired effect of tilting the radiation characteristic and reducing the SPL in the lower sector. In this case, two angles (α_1 and α_2) can be defined representing the tilt angles of the main and side lobes, respectively (compare figure 4.9).

Concerning the power radiated into the lower sector ([-90°; 0°]) computed by an integration of the normal intensity over the FP mesh depicted in figure 4.4, the following tendencies have been observed: for modes close to the cut-off limit the radiated power into this sector increases at first with increasing axial position and then drops again to yield another minimum at position 5 or 6. Depending on mode and frequency, either the first minimum (at position 1) or the second one yield the global minimum with respect to radiated power. This tendency changes to only one minimum value (at position 5 or 6) with an increasing cut-off ratio. An example of both trends is given in figure 4.10 for mode (5/1) at 1600 and 2000 Hz, respectively ($f_c = 1389$ Hz).

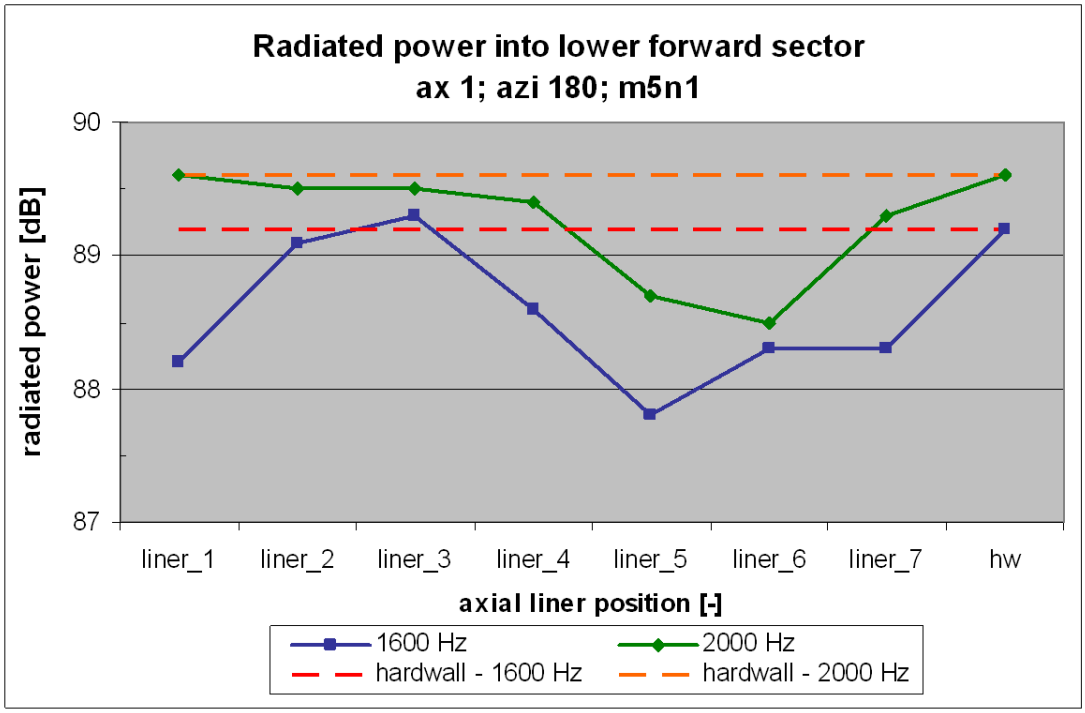

Figure 4.10: Radiated power into lower forward sector as function of axial reflective liner position; ax1; azi180; (5/1)

The figure plots the radiated power into the lower forward sector for the two frequencies as a function of the axial position of the reflective liner. As a reference, the levels of the hardwall solutions have been added as dashed lines. The curves reflect the tendencies described above exhibiting a global minimum at position 5 or 6, respectively.

The sound pressure amplitude distribution in the duct midplane ($x = 0$) for the more generally applicable case of one radiated power minimum (i.e. mode (5/1) at 2000 Hz) is depicted in figure 4.11 starting from position 1 in the upper left corner up to position 7 and the hardwall case in the lower right corner.

The low (or zero) sound pressure amplitude (appearing in these images in blue color) at the reflective liner position enforced by the corresponding BC, can clearly be observed. At this location, the modal energy traveling close to the duct wall is deflected to lower radial

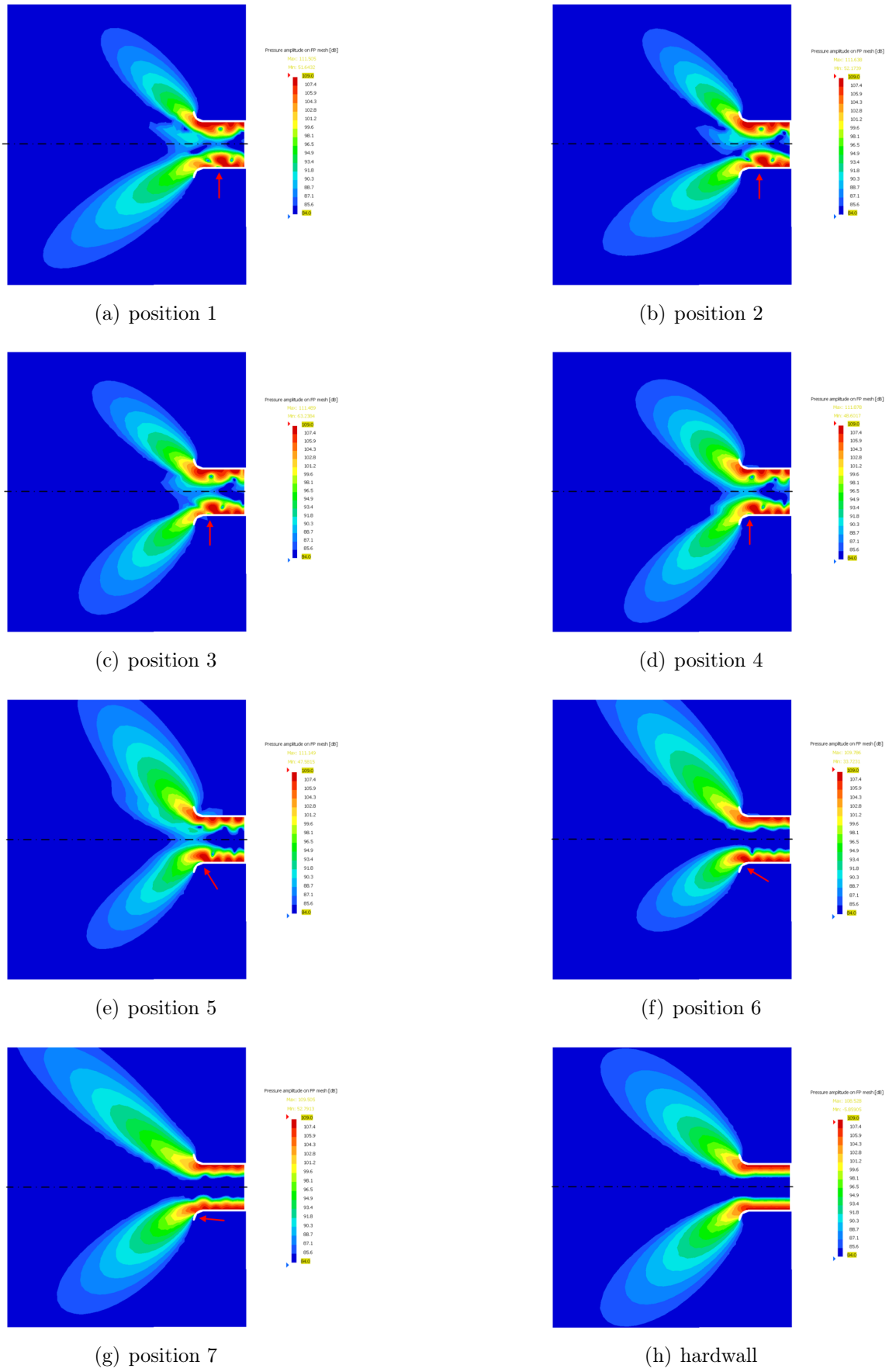

(a) position 1

(b) position 2

(c) position 3

(d) position 4

(e) position 5

(f) position 6

(g) position 7

(h) hardwall

Figure 4.11: Sound pressure amplitude distribution in duct midplane as function of axial reflective liner position; ax1; azi180; 2000 Hz; (5/1)

positions. When this softwall BC is removed behind the reflective liner segment (seen in the propagation direction towards the inlet), the energy tends to reattach to the wall as can be seen for the rearmost liner positions (figures 4.11(a) - 4.11(d)).

Starting from position 5 (beginning at the transition between the straight and the curved duct sections), this reattachment does not take place anymore. In contrast, the deflected pressure maximum is diffracted at the expansion of the duct and radiates to the far field at a corresponding angle. Compared to the hardwall configuration shown in the lower right corner, the direction of the main lobes of radiation, as well as their respective pressure amplitude, thus change with the varying position of the reflective liner segment. Additionally, superimposed standing wave patterns caused by increased levels of reflection at the reflective liner position are clearly visible in terms of changes in the pressure amplitude behind the reflective liner, especially if compared to the uniform levels in the hardwall case.

The global minimum of sound radiation into the lower sector at position 6 (according to figure 4.10) at this frequency can be confirmed from these images. In contrast, at the foremost liner position (pos. 7), at which the liner segment is located nearly vertical, the reflective liner loses effectiveness, and is thus not able to influence the radiation lobe. The result at this position resembles - to a large extent - the hardwall configuration.

For a mode closer to the cut-off limit (e. g. at a lower frequency), another effect emerges, which causes the interim increase in radiated power into the lower sector as observed at 1600 Hz (compare blue curve in figure 4.10). To study this effect, again the sound pressure distribution inside the duct is plotted for all available liner positions in figure 4.13 along with a directivity plot of a selection of characteristic liner locations (figure 4.12).

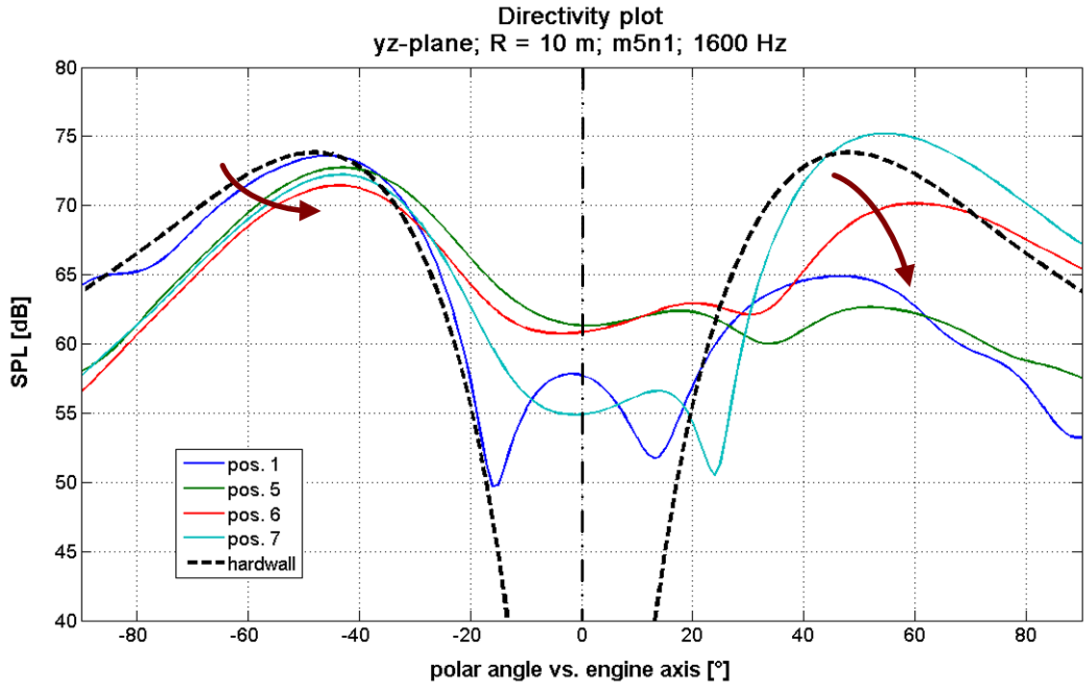

Figure 4.12: Comparison of vertical directivity plots at duct midplane; hardwall condition $\leftrightarrow$ axial variation of reflective liner; (5/1); 1600 Hz; $R = 10$ m

For the first (rearmost located) positions of the reflective liner, only very little acoustic power is radiated into the upper sector (up to -10 dB with respect to the hardwall peak level). This, in the following to be called 'cut-off effect', has to do with the deflection of the acoustic pressure pattern at the reflective liner location. As sketched in figure 4.2 in the introductory part of this chapter, this forces an additional quarter-wavelength into the cross section. If this modification of the mode shape occurs sufficiently far away from the

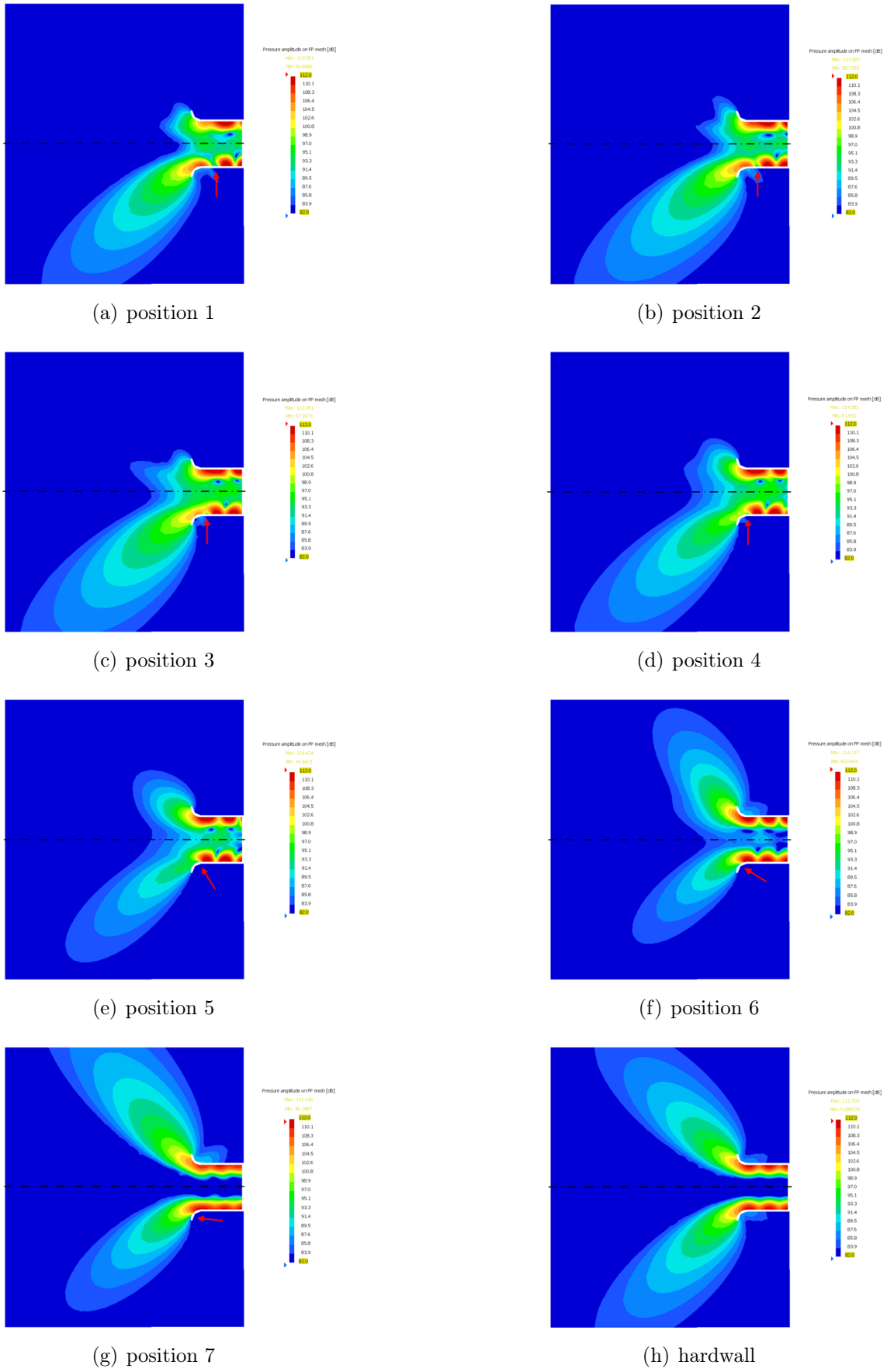

(a) position 1

(b) position 2

(c) position 3

(d) position 4

(e) position 5

(f) position 6

(g) position 7

(h) hardwall

Figure 4.13: Sound pressure amplitude distribution in duct midplane as function of axial reflective liner position; ax1; azi180; 1600 Hz; (5/1)

duct termination (as for positions 1-4), so that the effect cannot be transferred directly to the far field, the upper lobes of the mode (having a cut-off ratio of $\xi = 1.152$ at the current frequency, i.e. not too far from the cut-off limit) cannot propagate any more, but are strongly reflected back into the duct. On the other hand, the lower lobes, which have been shifted in the radial direction by the reflective liner, and hence are not any more attached to the duct wall, can still propagate and contribute to the far field radiation.

The effect of the reflective liner may alternatively be interpreted as a virtual constriction of the effective duct diameter representing a modification of the phenomenon analyzed by Ovenden, Eversman, and Rienstra in Refs. [188] and [189] extending the study of Nayfeh and Telionis [190]. They observed a distinct transition point in slowly varying flow ducts, at which the axial wave number changes from real to imaginary, and the mode becomes cut-off. As a consequence, the incident modal energy is split up into a cut-off transmitted mode (which does not transport any energy) and a cut-on reflected mode.

However, in the special case of the VSI, this (virtual) constriction of the duct diameter is an asymmetric one affecting only the lower part of the duct. By this, the shifted lower sound pressure maxima are able to propagate beyond the liner position, while the ones in the upper sector are switched to cut-off.

Starting from position 5, close enough to the expansion of the duct at the exit plane, an ever increasing sound radiation into the upper sector can be observed, yielding a minimum with respect to the radiation into the lower sector at this position. This tendency is clearly confirmed by the directivity plot showing strong reductions in the upper sector for the rear liner positions and a shift to more positive angles at a slightly reduced peak level in the lower sector.

In anticipation of chapter 5.5, in which the extent of modal scattering effects due to the non-uniform VSI liner design will be studied, figure 4.14 presents a comparison of the modal amplitude spectra (i.e. the amplitudes of the individual modes) of the hardwall configuration and a number of axial liner positions. These results have been obtained at an axial station $z = -0.40$ m, i.e. approximately midway between the source plane and the rearmost reflective liner position (pos. 1).

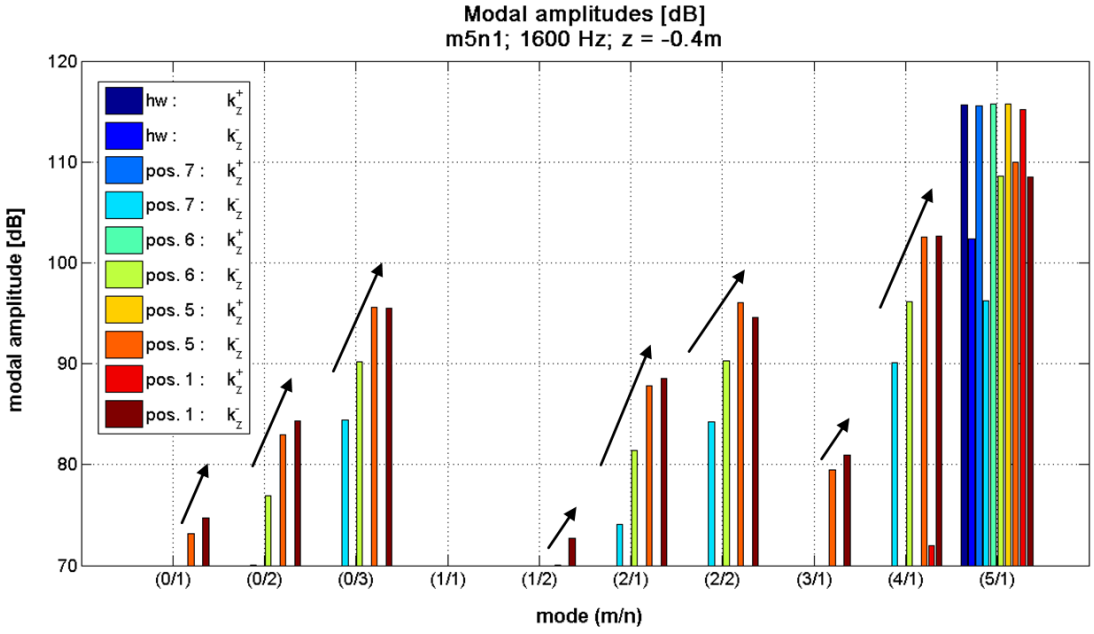

Figure 4.14: Comparison of modal amplitude results as function of axial reflective liner position; ax1; azi180; (5/1); 1600 Hz; $z = -0.40$ m

The figure contains the modal amplitudes of both the positively (k_z^+) and negatively (k_z^-) traveling waves for the same axial liner positions as in the directivity plot above. They show a dominant peak of 116 dB at the excited mode (5/1) and a varying level of reflections. As expected, in the hardwall configuration noteworthy reflection levels can only be observed for the mode itself (at -14 dB).

However, in the non-uniform VSI configurations, all propagating modes contribute to the reflected spectra, especially the even azimuthal mode numbers ($n = 0, 2, 4$). With respect to the axial liner position, their individual levels increase with a position farther inside the duct, i.e. a decreasing position number. At position 1, the pressure level of the highest scattered reflected wave $(4/1)^-$ reaches 103 dB, i.e. the level of the direct reflection (mode $(5/1)^-$) in the hardwall configuration. This tendency can also be confirmed from the pressure plots in figure 4.13, which show an increasing amount of standing wave components inside the duct.

Apart from these generally observed effects, mode (0/1) (the plane wave mode) shows a different tendency depicted in figure 4.15.

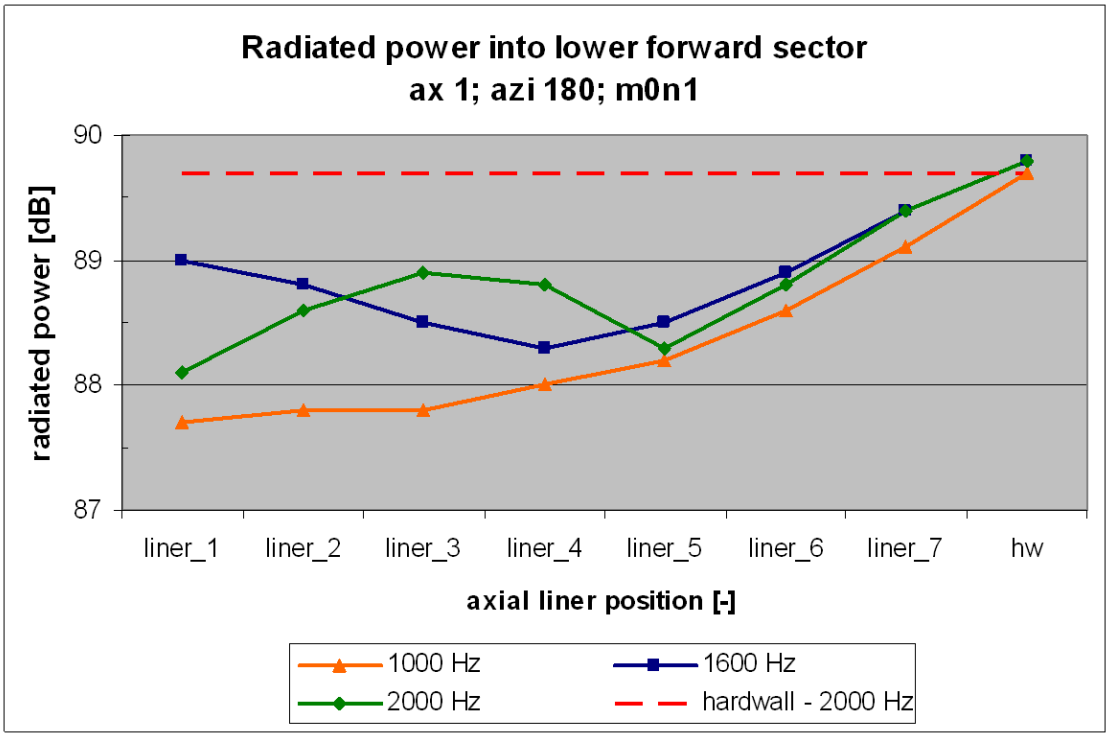

Figure 4.15: Radiated power into lower forward sector as function of axial reflective liner position; ax1; azi180; (0/1)

In this case, at the lowest frequency (1000 Hz) position 1 (located furthermost inside the duct) yields the lowest power value in the lower forward sector. The curve then increases continuously up to the hardwall solution with a decreasing distance to the inlet plane (increasing position number). To better understand these results, figures 4.16 and 4.17 present the corresponding pressure and directivity plots, respectively.

For the fundamental mode, where the pressure distribution is relatively uniform across the duct cross section in the hardwall configuration (compare figure 4.16(h), the small variations are due to reflections at the exit plane), the maximum radiated SPL is centered at the duct axis. However, already for the foremost reflective liner location (position 7), the directivity is shifted to positive angles, i.e. into the upper sector, by $\approx 3°$, though at a constant peak pressure level (compare the directivity plot in figure 4.17).

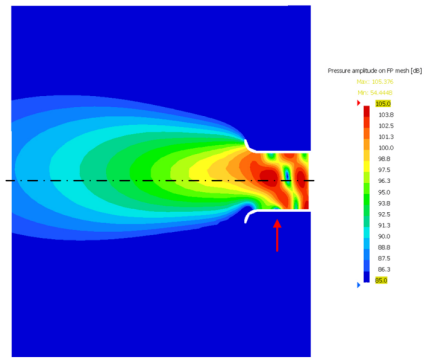

(a) position 1

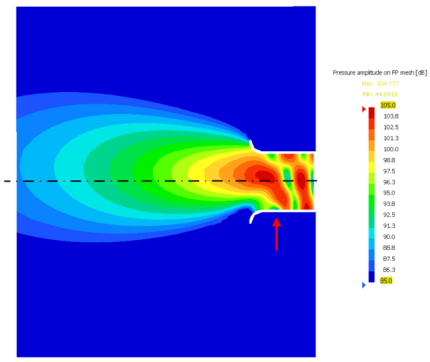

(b) position 2

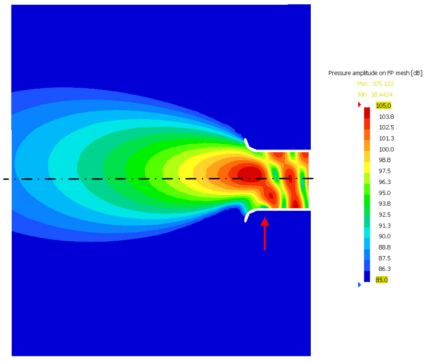

(c) position 3

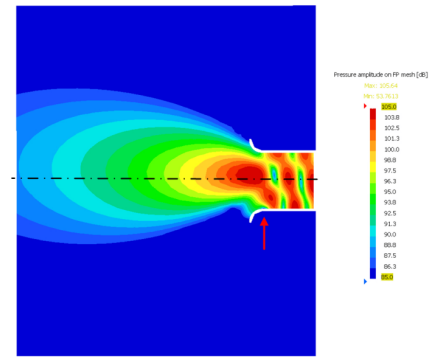

(d) position 4

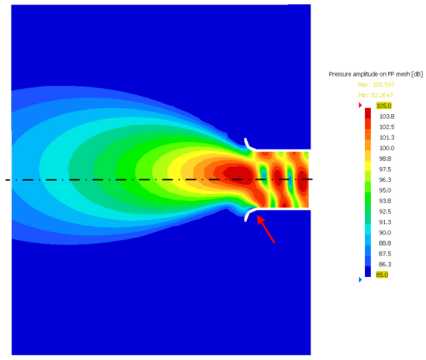

(e) position 5

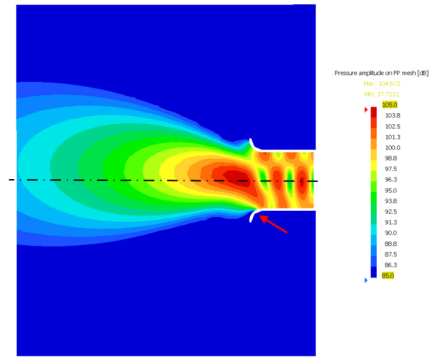

(f) position 6

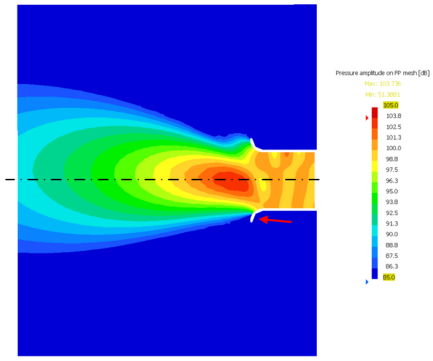

(g) position 7

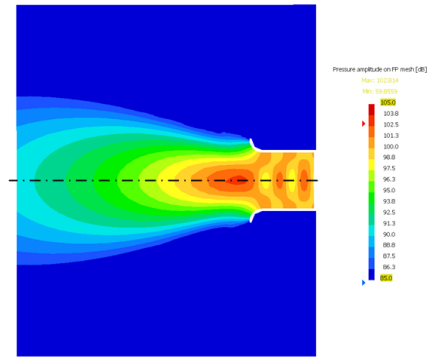

(h) hardwall

Figure 4.16: Sound pressure amplitude distribution in duct midplane as function of axial reflective liner position; ax1; azi180; 1000 Hz; (0/1)

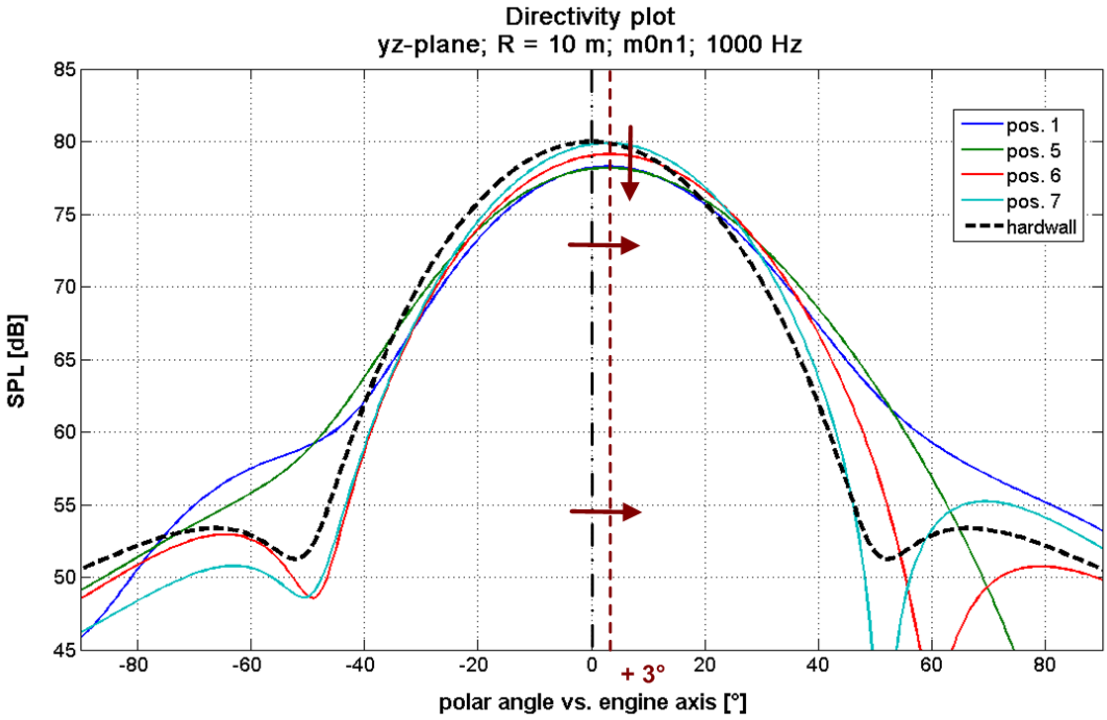

Figure 4.17: Comparison of vertical directivity plots at duct midplane; hardwall condition ↔ axial variation of reflective liner; (0/1); 1000 Hz; $R = 10$ m

At the next two (farther rear located) liner positions (i.e. positions 6/5), this maximum pressure value has been reduced by an additional 1 dB and 2 dB, respectively, at the same radiation angle. Beyond position 5, the peak level stays approximately constant (still at the same shifted radiation angle (+3°)) yielding a continuously increasing attenuation (compare figure 4.15) attributed to reductions in the sector [-50°; ± 0°].

This different phenomenon observed for the plane wave mode at the lowest frequency can be explained by the relatively long wavelength compared to the duct diameter ($D/\lambda_{|1000\ Hz} = 1.471$) and the corresponding diffraction effects at the duct termination. Also, no reattachment of the mode occurs in this special case of the plane wave mode in which the reflective liner (in contrast to the observations presented up to this point) is able to influence the directivity up to the foremost liner position (pos. 7) shifting the originally axially centered main lobe into the upper sector. This effect is similar to the one reported for the Negatively Scarfed Intake (NSI) [132], which consistently showed an angular shift equivalent to the negative scarf angle.

To investigate the level of reflections resulting from the reflective liner segment, figure 4.18 compares the modal amplitude spectra for the plane wave mode at 1000 Hz for the same configurations and axial position ($z = -0.40$ m) as in the previous example.

The results of the hardwall configuration show noteworthy reflection levels only for the mode itself and its first radial (0/2). As above, the scattered contributions of nearly all other propagating modes (in this case more prominent the odd azimuthal mode numbers ($n = 1, 3$)) increase with a decreasing position number (position farther inside the inlet) reaching a maximum level of 100 dB, i.e. only 3 dB below the peak pressure of the excited mode. The corresponding increasing amount of standing wave components can again be confirmed by the pressure plots (figure 4.16).

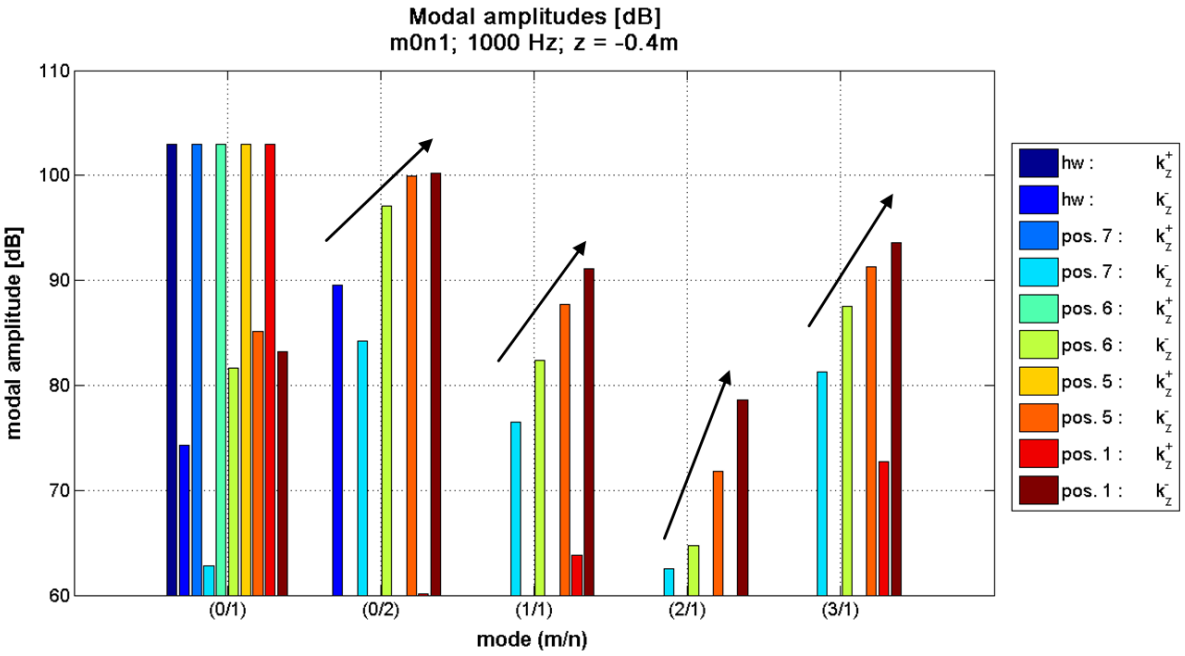

Figure 4.18: Comparison of modal amplitude results as function of axial reflective liner position; ax1; azi180; (0/1); 1000 Hz; $z = -0.40$ m

Summarizing the results of this first parametric variation, in the general case of a well cut-on mode (apart from the plane wave mode), it can be stated that the axial variation of the reflective liner segment tilts the directivity characteristic of a propagating mode in such a way that a liner position closer to the exit reduces the radiated power into the lower forward sector up to a certain point, beyond which it increases again. For nearly all combinations of mode number and frequency tested, the location at the transition between the straight duct wall and the curved inlet lip showed the best potential. This corresponds to positions 5/6 in the BE model, whereas the optimum position tends to move closer to the exit with a decreasing cut-off ratio (compare figure 4.10). This can be explained by the corresponding steeper propagation and radiation angles, for which the reflective liner causes the maximum effect closer to the exit plane.

Compared to the Negatively Scarfed Intake, for which a change in the scarf angle was directly correlated to a shift of the directivity curve (to higher angles), the effect of the Virtual Scarf Inlet exhibits a different characteristic. It can be best described by a tilt of the directivity yielding lower pressure levels in the lower sector and (possibly) increased ones in the upper sector.

4.3.3 Variation of axial length

The second parameter variation is related to the length of the reflective liner segment in the axial direction. Based on the results of the first part of the study, axial positions close to the respective optimum liner position have been analyzed. With respect to the circumferential extent of the liner under investigation, the standard angle of $\phi = 180°$ has been used.

An example of the influence of an extension of the axial length of the liner is presented in figure 4.19. It compares the directivity characteristics (in the vertical plane) of mode (2/1) at 1600 Hz for different liner positions and lengths.

At first, considering only the single-element (axial) liners, the reflective liner located at position 4 (blue curve) yields the most promising noise reduction potential in the lower forward sector ([-90°; 0°]) with respect to the hardwall reference configuration (dashed black

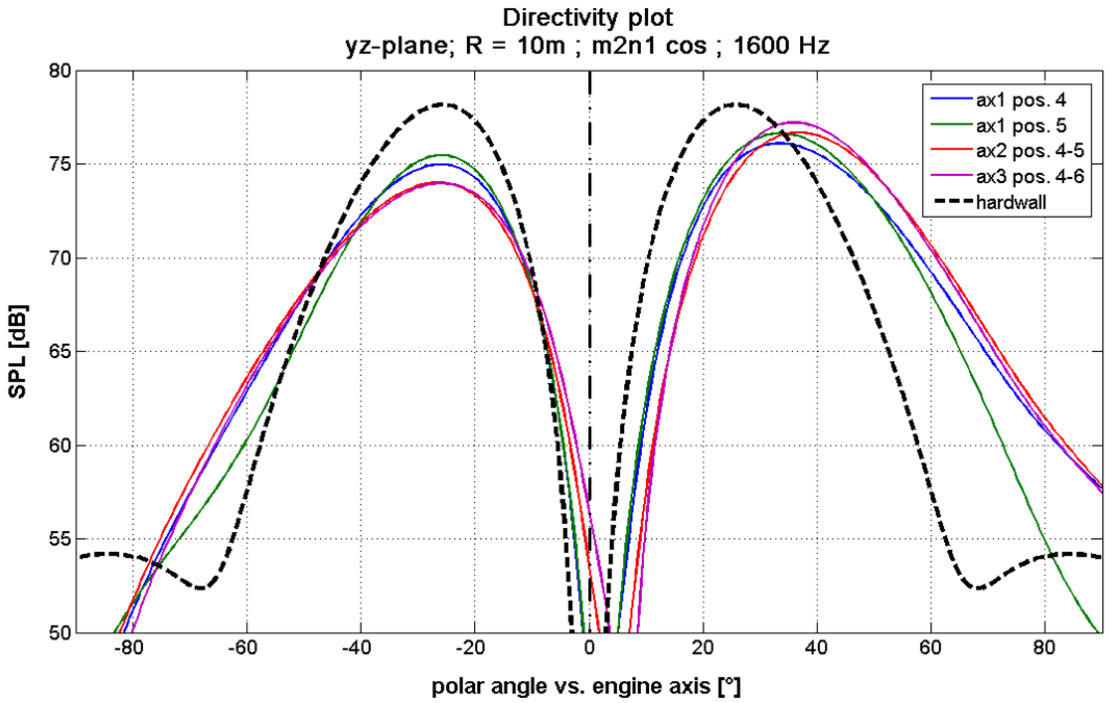

Figure 4.19: Comparison of vertical directivity plots at duct midplane; hardwall condition ↔ variation of axial length of reflective liner; (2/1); 1600 Hz; $R = 10$ m [187]

line). Its effect on the propagating mode can be observed also in the pressure amplitude plot at duct midplane in figure 4.20.

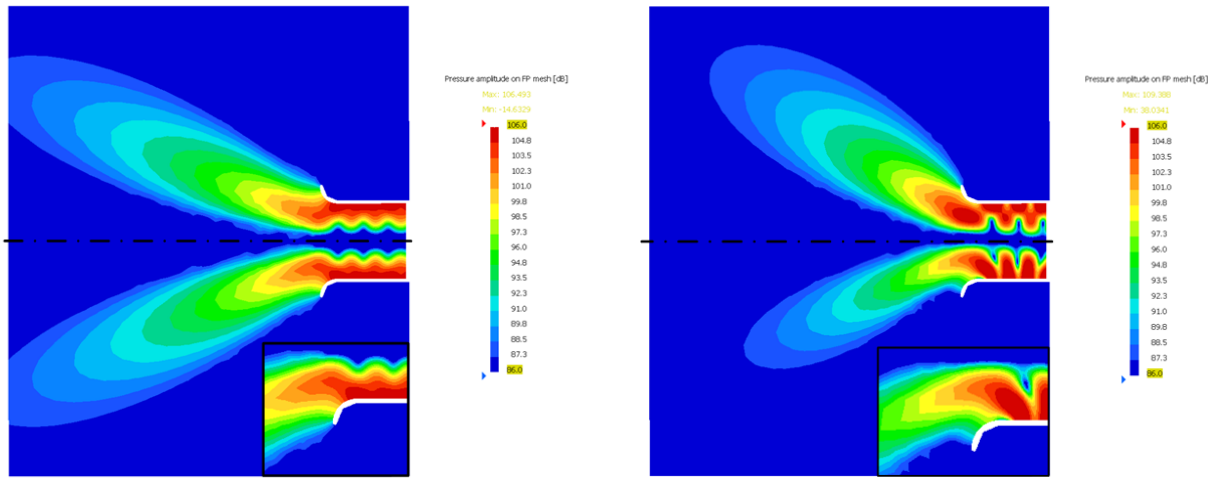

(a) hardwall

(b) position 4

Figure 4.20: Sound pressure amplitude distribution in duct midplane; hardwall ↔ liner 4; ax1; azi180; 1600 Hz; (2/1)

As found out in the first part of this parametric study, this location corresponds to the optimum position for this combination of mode and frequency. For reference, the result of the reflective liner at position 5 (green curve) is added in figure 4.19, showing a slightly higher SPL at the peak in the lower sector.

An extension of the axial length by one element group (positions 4+5 - red curve) reduces the maximum sound pressure value by an additional ≈ 1 dB, in this case without a considerable change in the angle of maximum sound radiation or the general shape of the directivity

curve. From the corresponding pressure plot at duct midplane depicted in figure 4.21(a), it becomes obvious that this is due to the prevention of a partly reattachment of the deflected sound pressure maximum (compare figure 4.20(b)).

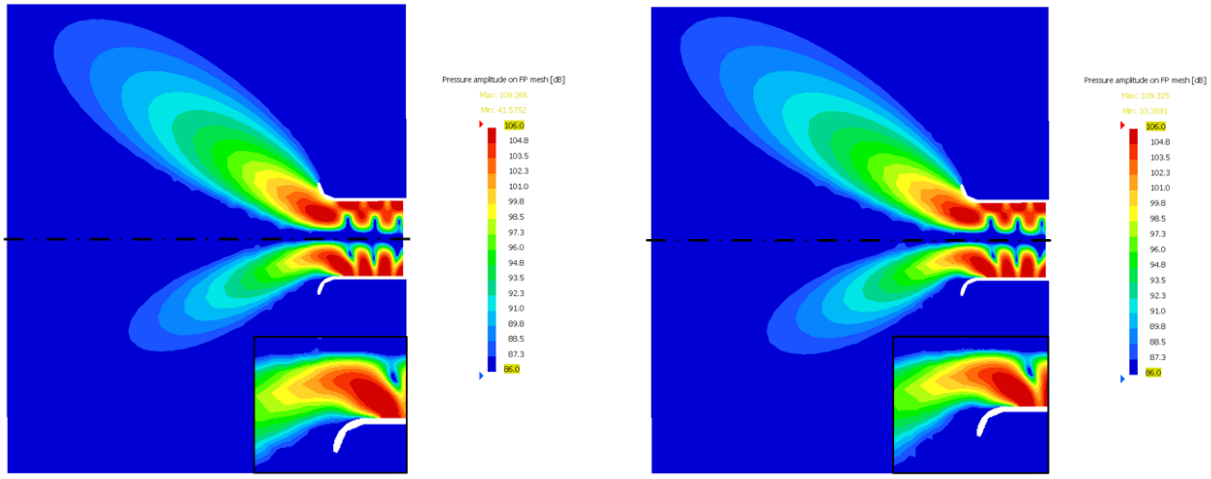

(a) positions 4+5 (b) positions 4+5+6

Figure 4.21: Sound pressure amplitude distribution in duct midplane; liner 4+5 ↔ liner 4+5+6; azi180; 1600 Hz; (2/1)

A further extension to a 3-element liner section (pink curve and figure 4.21(b)) barely changes the result in the lower sector. From this, it might be deduced that the axial length of the reflective liner influences the sound radiation only up to a certain point, and is not directly related to the overall performance. However, in the following, this phenomenon will be analyzed in greater detail by considering the overall radiated power into the lower forward sector. For this analysis again the FP mesh depicted in figure 4.4 has been used. The results are shown exemplarily at the frequency $f = 1600$ Hz in figure 4.22. In this figure, radiated power results for several combinations of axial liner positions and axial liner lengths are opposed to the hardwall solution (blue curve).

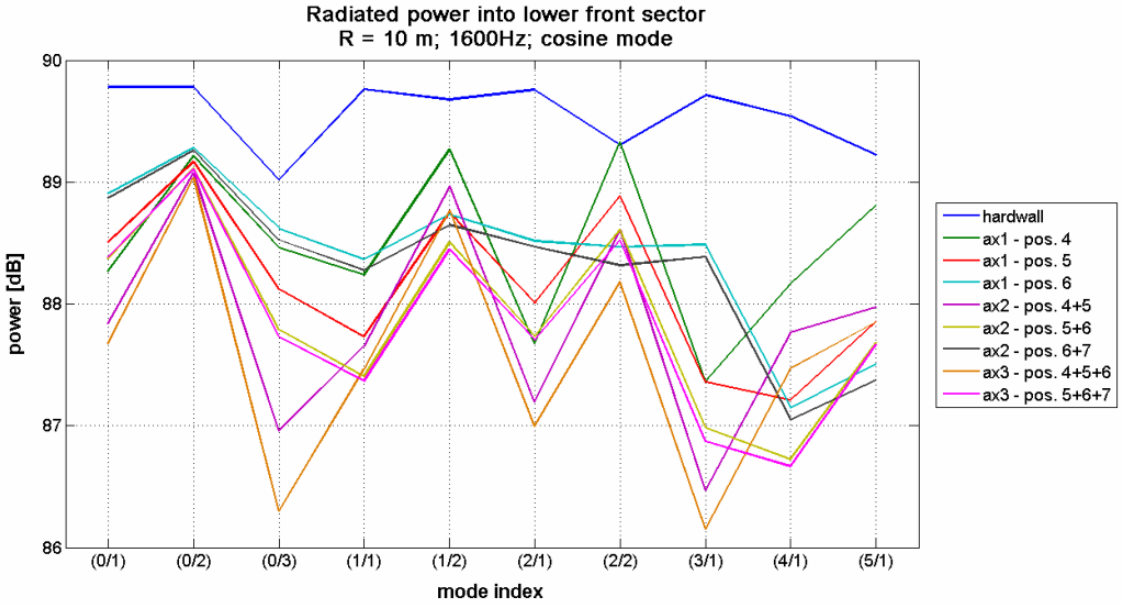

Figure 4.22: Radiated power into lower forward sector as function of axial liner length & position; azi180; 1600 Hz

It can be clearly seen that the performance of the various liner configurations is strongly influenced by the mode order. For example, for the single-element liners, as observed in the previous example, position 4 yields the best result at mode (2/1) but is inferior compared to position 5 for most other modes. Thus, the overall performance may be quantified by computing the *average attenuation* over all propagating modes defined by a signed rms-value

$$\Delta dB_{rms} = \sqrt{\frac{\sum_{mn} (\Delta dB_{mn}^2 \cdot sgn(\Delta dB_{mn}))}{N_{modes}}} \,, \tag{4.1}$$

which reflects the average performance of each configuration taking into account the sign (negative = attenuation, positive = amplification).[6] The corresponding results are presented in figure 4.23. The bar plot on top shows the individual modal attenuation values for all configurations similar to figure 4.22 and the plot in the lower right corner the corresponding average attenuation values (ΔdB_{rms}) as defined above.

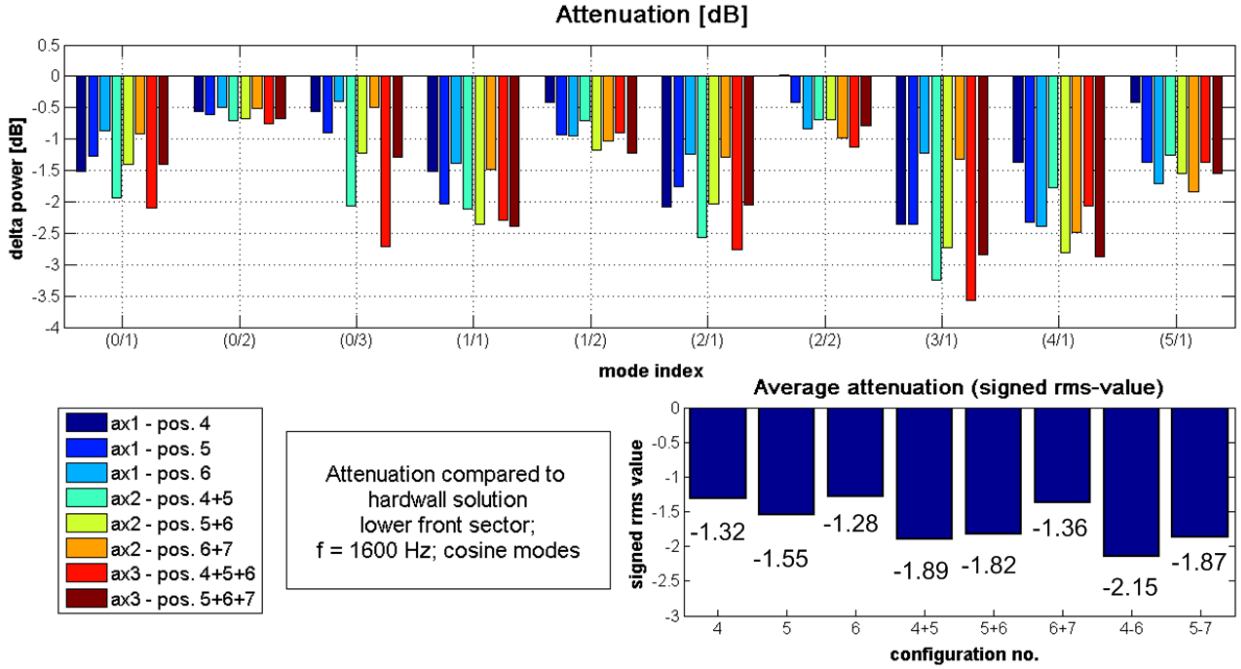

Figure 4.23: Attenuation in lower forward sector as function of axial liner length & position; azi180; 1600 Hz

As mentioned in the summary of the results of the first part of the study, for the single-element liners, position 5 yields the highest average attenuation (-1.55 dB). For the 2-element liners, configurations 4+5 and 5+6 perform on average nearly equally well (−1.89 dB/ −1.82 dB), although there are clear differences for single modes. The foremost possible combination (groups 6+7), however, shows nearly the same results as a single-element liner at position 6. This result could be expected regarding the weak performance of a single-element liner at position 7 (directly at the duct exit) observed in the previous section. Hence, this result provides another indication that not the overall axial length of the reflective liner might be of primary importance, but its placement at the optimum position.

For a 3-element liner (the longest configuration tested in this context), groups 4-6 yield again an increase in average attenuation by -0.26 dB compared to the optimum 2-element liner to a level of -2.15 dB. This performance increase is slightly lower than the step from a

[6] However, this averaging does not take into account the individual absolute PWLs of the respective modes, compare discussion in chapter 5.3.3.

single- to a 2-element liner (-0.34 dB) where the liner area has been doubled. As before, the 3-element liner located at positions 5-7 closely resembles the result of the 2-element liner 5-6 following the explanation given above.

Considering as well the results obtained at the two other frequencies analyzed (f = 1000 Hz/ 2000 Hz) - which are given in appendix B.1 - the general tendency may be subsumed as follows: an increase in the axial length of the reflective liner yields a (considerable) advantage only if the position added coincides with a favorable position for at least one of the contributing modes. As mentioned before, these favorable positions vary depending on the modal numbers and frequency, but are, in general, located relatively close to the duct exit. Additionally, an extension of the reflective liner length is advantageous in cases where the optimum single-element liner position is located relatively far from the exit plane such that a reattachment of the sound pressure maxima might occur for the single-element liner in some cases. This effect can be prevented by increasing the reflective liner length and leads to a considerable increase in achievable attenuation as is summarized in the chart in figure 4.24.

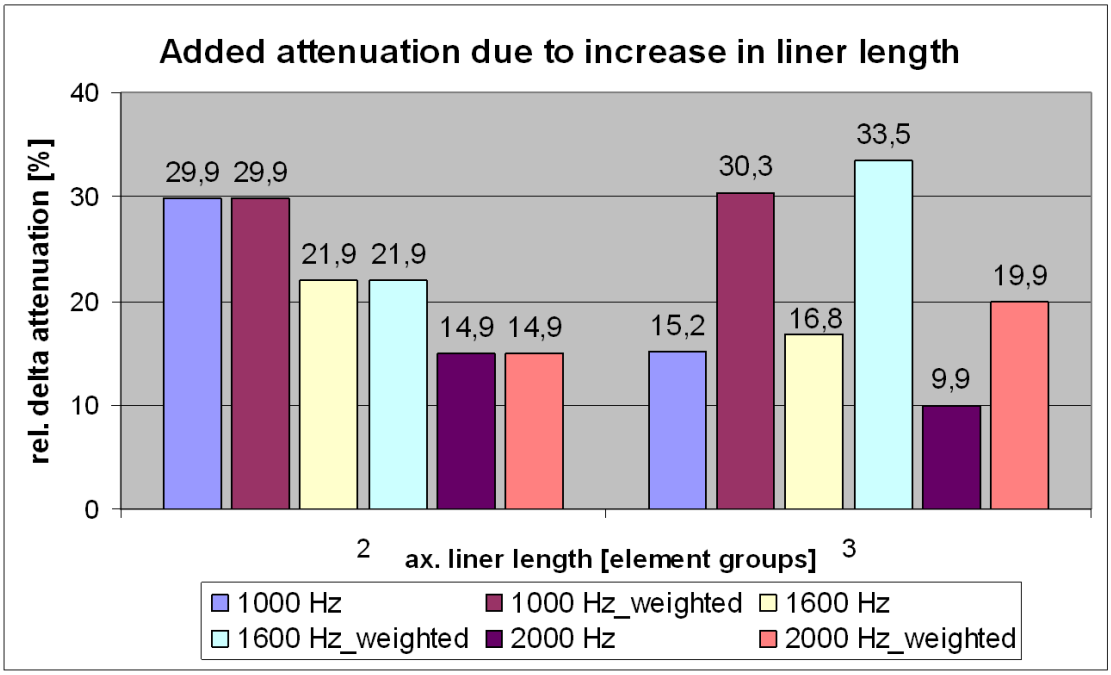

Figure 4.24: Added attenuation in lower forward sector due to increase in axial liner length

The first bar for each frequency reflects the relative increase in attenuation (in percent) due to the extension of the reflective liner by an additional segment (element group). For the 2-element liners, a decrease of additional attenuation with increasing frequency could be observed, which does not occur in the same way for the 3-element liners. Additionally, the effect of adding a liner segment to a 2-element liner seems to increase the achievable attenuation only by a reduced amount compared to the step from a single-element to a 2-element liner. However, if the additional attenuation is weighted by the area ratio of the original to the extended liner (plotted as the second bar for each frequency), the results change in a way that the relative increase stays at least constant (1000 Hz) or even increases (1600 Hz/ 2000 Hz).

On the other hand, as will be of more importance in the context of the comparison of the Virtual Scarf performance with a uniform absorptive liner, additional reflective liner area corresponds to a decrease in absorptive area, and has to be considered carefully. Particularly against this background, the axial extension of the reflective liner should be limited to the

favorable positions. Thus, in a practical application, an axial length of 2 element groups ($\equiv$ to an axial length of $l_{ax} = 100$ mm) should be used as a good compromise between average added attenuation and liner size.

4.3.4 Variation of circumference angle

At last, the effect of changes of the circumferential dimension of the reflective liner segment will be analyzed, again keeping the other two parameters fixed ($l_{ax} = 50$ mm, axial liner position 5). Figure 4.25 shows an example of the dependency of the directivity in the vertical plane on the angular dimension of the liner patch. In this context, the minimum enclosed angle has been set to $\phi = 100°$, which has been incremented symmetrically up to a full circular segment (red dashed line). As before, the hardwall solution yielding a symmetric radiation pattern has been added for reference (black dashed curve).

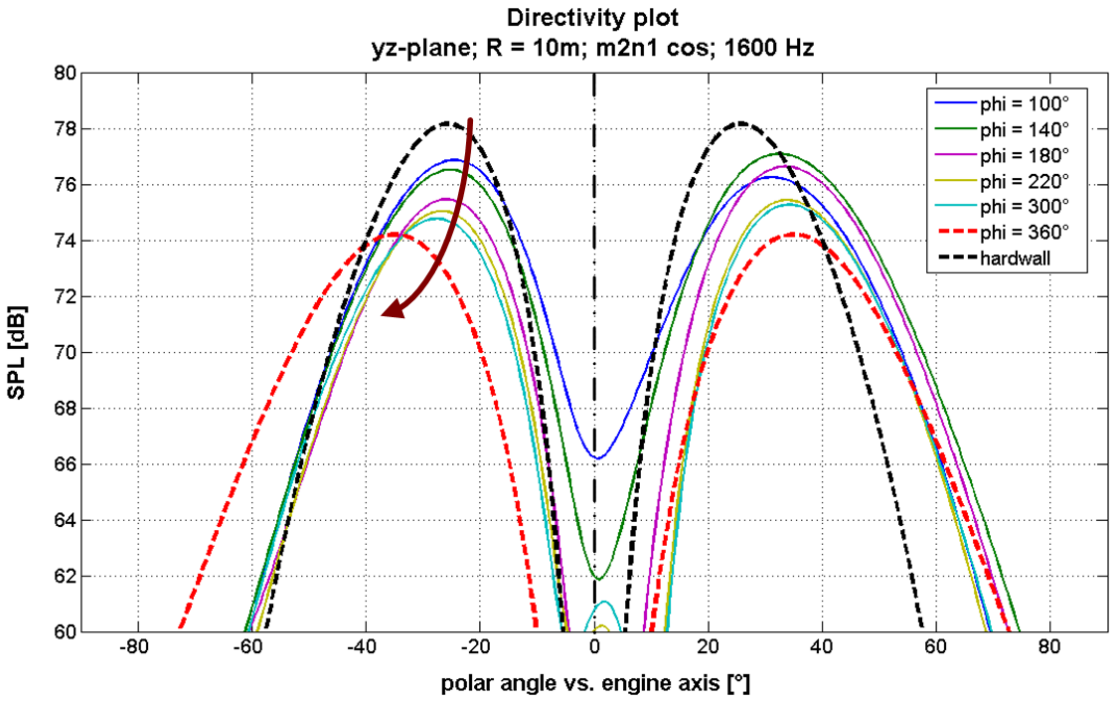

Figure 4.25: Comparison of vert. directivity plots at duct midplane; hardwall ↔ variation of circumference angle of reflect. liner; pos. 5; (2/1); 1600 Hz; $R = 10$ m

For the first configurations, an extension of the reflective liner in the angular dimension yields a reduction of the SPL in the lower sector at an approximately constant polar angle. This effect occurs up to a circumference angle of $\phi \approx 180° - 220°$. Beyond that, the relative reductions decrease, but the peaks are shifted to steeper radiation angles. This leads, in effect, to a net increase in sound pressure at the ground due to the reduced distance.

This distance effect has been sketched in general in figure 4.26, where the angles φ and φ' denote the undisturbed and the deflected radiation angle, respectively, of the main lobe due to the reflective liner effect. The distances R and R' stand for the corresponding distances from the duct exit to the point of impingement on the ground plane located at a distance Δy below the duct axis. Accordingly, the deflection of the main lobe of radiation due to the VSI effect causes an axial shift Δz of the impingement point. This increased distance to the impingement point causes, according to the free field variation of the sound pressure level of a monopole source (spherical wave source) given in equation 2.75, the observed reduction in maximum SPL on the ground plane.

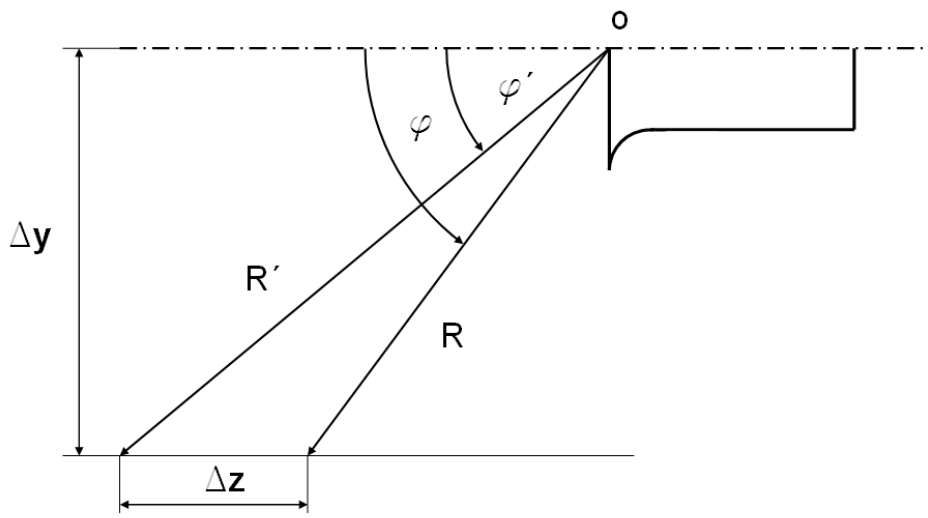

Figure 4.26: Sketch of effect of variation in radiation angle on horizontal distance

Additionally, it should be mentioned that the closed liner segment again yields a symmetric directivity curve, as expected. However, the sound pressure values range at a considerably reduced level due to increased reflections at the jump of impedance, as will be explained in the following.

For modes of a low cut-off ratio (i.e. close to the cut-off limit), the 'cut-off effect' already discussed in the first parametric variation (observable in figure 4.13) has again been observed. It is related to a virtual constriction of the duct causing a strong reduction of the lobes in the upper sector. However, in this case the intensity and azimuthal extent of this characteristic effect increase with an increasing circumferential dimension of the liner and affect, in the limit of a closed (360°) liner segment, the whole forward radiation, as can be seen in the directivity plot in figure 4.27.

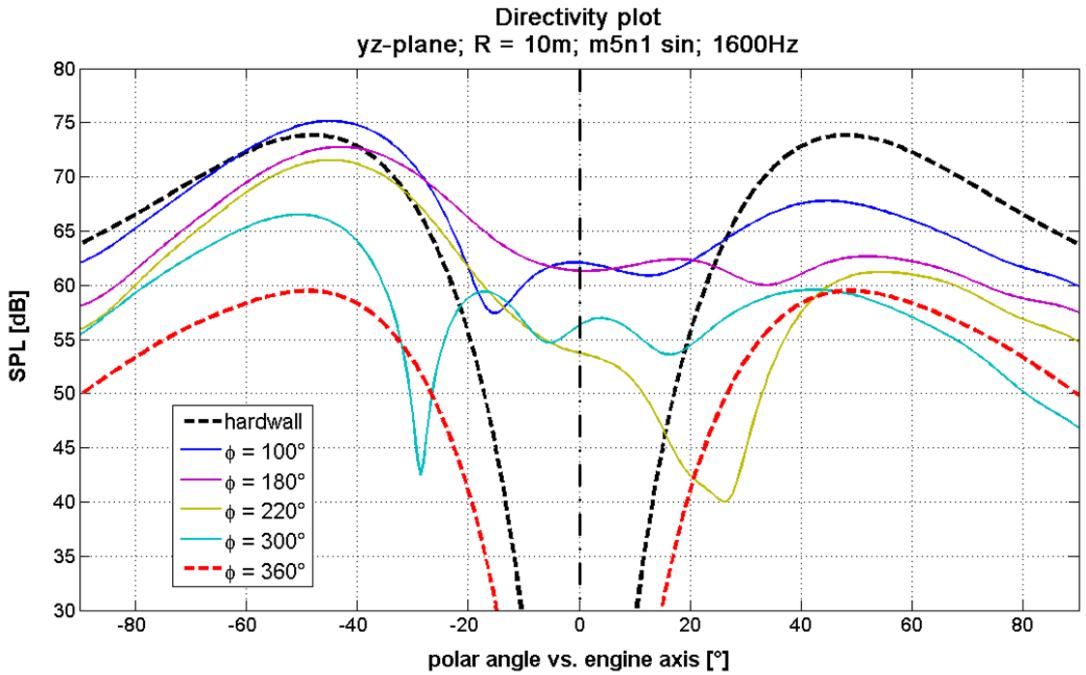

Figure 4.27: Comparison of vert. directivity plots at duct midplane; hardwall ↔ variation of circumference angle of reflect. liner; pos. 5; (5/1); 1600 Hz; $R = 10$ m

Accordingly, the difference between the peak pressure of the hardwall and the closed reflective liner configuration yields ≈ 14 dB for this example of a near cut-off mode ((5/1), $\xi = 1.152$), compared to only ≈ 4 dB for mode (2/1) ($\xi = 2.421$) presented in figure 4.25.

For an explanation of this phenomenon, the modal amplitude spectra within the duct (at $z = -0.40$ m, as in chapter 4.3.2) of the different liner circumference angles are compared to each other in figure 4.28.

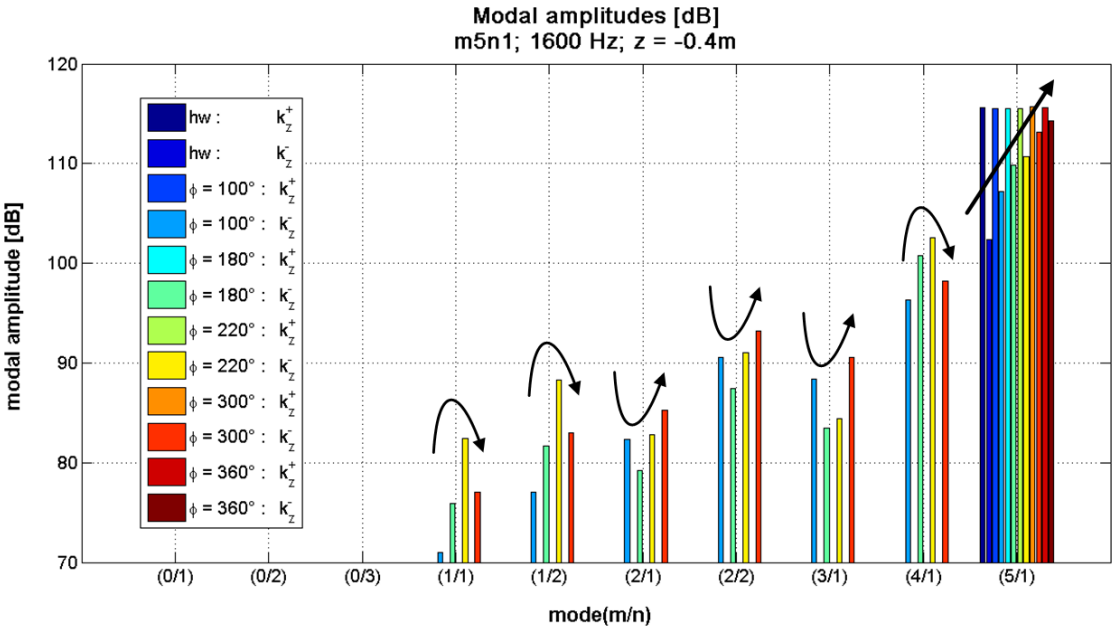

Figure 4.28: Comparison of modal amplitude results as function of circumference angle of reflective liner; ax1; pos. 5; (5/1); 1600 Hz; $z = -0.40$ m

As in the previous examples analyzing the modal composition of different lining configurations, the hardwall reference case shows only reflections into the propagating mode itself at a low overall level (in this case: -14 dB). In contrast, for all non-uniform VSI lining configurations of a varying circumferential extent, a coupling with all other propagating modes can be observed. For these reflected modes, the dependency of the amplitude upon the circumference angle is not as obvious as in the first parametric variation (where the amount of reflections consistently increased with a more rearward liner position) but depends also on the azimuthal mode number as indicated by the small arrows in the figure.

In parallel, the reflection level of the primary mode $(5/1)^-$ increases with a larger circumferential extent of the reflective liner and reaches its maximum (only 2 dB below the positively traveling excited mode $(5/1)^+$) for the closed segment. This explains the strongly reduced radiated pressure level observed in the corresponding directivity plot (figure 4.27) for this configuration. Due to its axisymmetry, the closed liner segment again yields a 'clean' modal spectrum containing only contributions from the primary mode.

Concluding it may be stated that, with respect to the circumferential dimension of the reflective liner, an angle of $\phi = 180° - 200°$ yields the best overall results, as it reduces the sound pressure in the lower sector at an approximately constant radiation angle. Beyond that, the main lobe is shifted to steeper radiation angles, which yield, in effect, a net negative effect on the ground, as described above. Additionally, strong (backwards) reflections occur for modes close to the cut-off limit which disturb the sound field within the duct and might cause detrimental effects concerning the turbomachinery or the rearward radiation. Hence, due to the results obtained here, and the reason of a convenient modeling, in forthcoming analyses, a semi-circular reflective liner segment will be used.

4.3.5 Summary of parametric study and conclusions

To conclude the parametric study, the main results obtained during the three parametric variations of the geometric characteristics of the reflective liner segment shall be recapitulated:

The most important influencing factor for the performance of the reflective liner seems to be its axial position relative to the inlet plane. In general, a location close to the duct exit seems favorable, whereas also the geometry of the inlet is involved (compare the results reported in chapter 4.3.2). As the exact optimum position varies with the modal numbers, these need to be involved in a general description, e. g. in terms of the cut-off ratio. Thus, in the following section the influence of this and other parameters on the Virtual Scarf effect will be analyzed and generalized as far as possible.

With respect to the relevance of finding the optimum position for the reflective liner segment, its extent in the axial direction seems to be of minor importance. This can be explained by the physical effect causing the redirection of the sound radiation: as has been explained in figure 4.2, the change in the acoustic BC at the reflective liner location causes a change in the radial distribution of the acoustic energy which can subsequently lead to a modified radiation pattern. This phenomenon takes place directly at the jump of impedance from the hardwalled duct to the reflective liner patch and does not require a certain minimum length to come into effect. Hence, it might be deduced that the axial extent of the liner segment could be reduced to a minimum. However, if the extension of the reflective liner leads to a configuration that includes an additional favorable location for at least one of the propagating modes, this increases the average attenuation. As well, a reattachment of the sound pressure maxima to the duct wall has to be prevented to achieve a maximum effect, wherefore a certain axial extent of the reflective liner segment might be advisable.

Finally, the circumferential dimension of the liner was found to influence the radiated power, as well. However, with respect to the radiated power reduction towards the ground, a semi-circular liner segment yielded the best net effect. Larger circumference angles were accompanied by a shift of the main lobe(s) towards steeper angles, which influenced the overall performance negatively, even if a further reduction of the absolute sound pressure level could be achieved.

4.4 Derivation of main influencing parameters

In this final section, the main influencing quantities of the Virtual Scarf effect will be summarized systematically. The prime motivation for this is to obtain a generally valid description of the dependencies of the reflective liner effect on a limited number of variables for future designs or performance predictions.

For a hardwalled or uniformly lined duct, the cut-off ratio has been determined to be the only parameter necessary to describe the modal propagation and radiation characteristics. It has been introduced by Rice in Ref. [4] in 1976 (as described in chapter 2.1.1.2) and is conveniently used in the pertinent literature. However, with respect to the VSI, it will emerge, and could have been expected from the analysis up to this point, that this still important parameter will not remain the only value of importance for this special type of a non-uniform liner.

At first, the radiated power into the lower forward sector shall be regarded for a representative configuration (axial length $l_{ax} = 1$, liner position = 5, circumference angle $\phi = 180°$, $f = 2000$ Hz). Figure 4.29 plots the radiated power as a function of the modal order in comparison to the hardwall configuration.

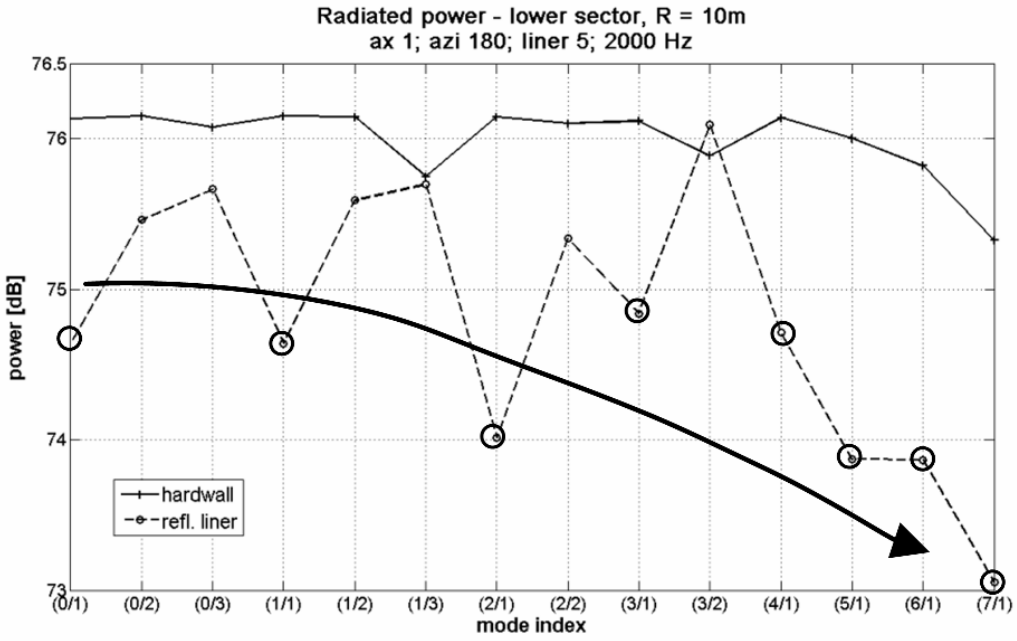

Figure 4.29: Tendency concerning radiated power into lower forward sector for azimuthal modes; 2000 Hz; ax1; azi180; liner 5

This figure shall serve to demonstrate that the radiated power reduction in the lower forward sector due to a reflective liner segment tends to increase with a decreasing cut-off ratio (from the left to the right) - at least for the azimuthal modes ($n = 1$) as indicated by the trend line. This effect related to the decreasing cut-off ratio can be explained by an increasing concentration of the acoustic energy at the duct wall, where the change in boundary condition is applied. However, for the radial mode orders ($n > 1$), the results vary strongly.

Regarding the corresponding directivity plots in a vertical plane located at the duct center line, the effect of the reflective liner may be described as a tilt of the directivity characteristic (as explained in chapter 4.3.2) by an angle $+\alpha$ such that the sound pressure values are reduced in the lower sector and increased in the upper sector (compare figure 4.30(a)). This effect dominates up to a certain limit of the cut-off ratio ξ.

Beyond that, the radiation pattern in the upward direction is more or less influenced by the effect that has been described in chapter 4.3.2 and is observable in figure 4.13, especially in figures 4.13(a) - 4.13(d). This 'cut-off-phenomenon' in the upper sector caused by the virtual constriction of the duct diameter (by the radial redistribution of the energy at the reflective liner position) reduces the sound pressure peak by up to 10 dB. Additionally, for the lower sector, a shift to more positive radiation angles at a slightly reduced peak level has been observed (compare figure 4.30(b)).

For the three frequencies observed in this parametric analysis, the cut-off ratio limit ξ_l, which separates the two effects described above, has been determined to be

$$\xi_l \approx 1.25 \; . \tag{4.2}$$

Concerning the influence of the radial mode order, the following effects have been observed: as reported above, for the zeroth radial mode (in the nomenclature used in this work: $n = 1$), the radiated lobes are shifted upwards by an angle $+\alpha$. Contrarily for the higher radial orders ($n > 1$): for these modes, the angle α becomes negative, which causes, in general, an increase in power radiated towards the ground.

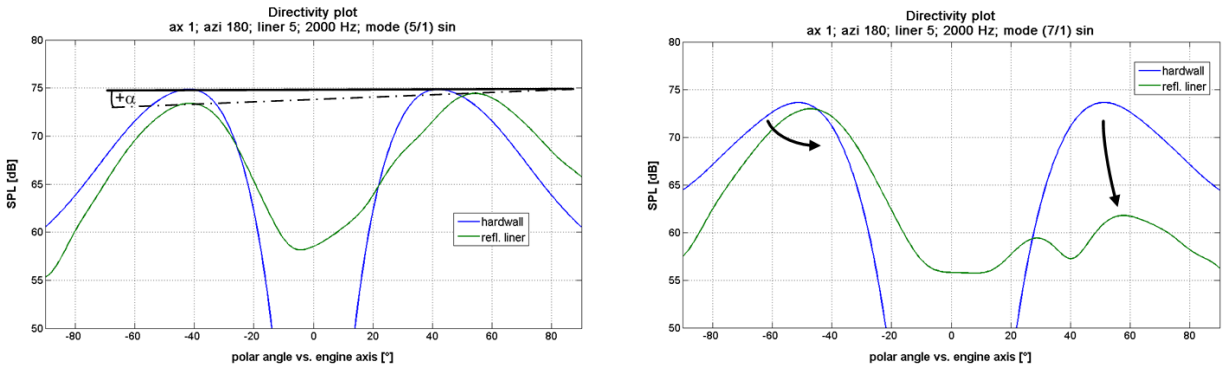

(a) mode (5/1), $\xi = 1.441$ (b) mode (7/1), $\xi = 1.078$

Figure 4.30: Comparison of vertical directivity plots at duct midplane; (5/1) ↔ (7/1); ax1; azi180; 2000 Hz

An example of a result showing this behavior, is presented in figure 4.31(a). The directivity plot seems to indicate a negative rotation angle due to the VSI effect. However, this characteristic results from the interaction of the radial distribution of the energy and the non-uniform liner, as will be analyzed in detail in the next chapter (section 5.4).

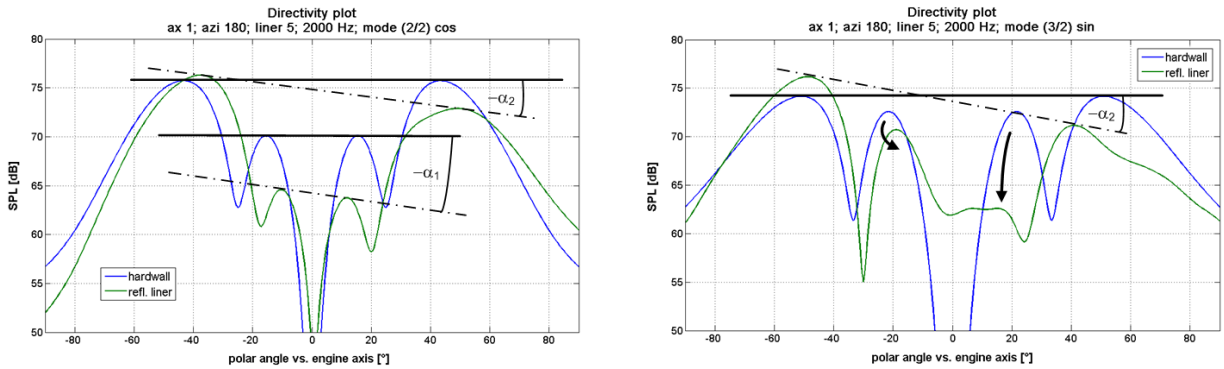

(a) mode (2/2), $\xi = 1.377$ (b) mode (3/2), $\xi = 1.153$

Figure 4.31: Comparison of vertical directivity plots at duct midplane; (2/2) ↔ (3/2); ax1; azi180; 2000 Hz

In this case, both radial lobes have been tilted by angles $-\alpha_1$ and $-\alpha_2$ with respect to the hardwall configuration. As for the azimuthal modes, starting from a certain value of the cut-off ratio ($\xi_l \approx 1.25$), one of the radial lobes (in all cases observed the innermost radial lobe) in the upper sector becomes strongly attenuated (by ≈ 10 dB) as can be seen in figure 4.31(b).

An additional effect that occurred only for the two lowest azimuthal mode orders ($m = 0, 1$) is shown in figure 4.32: for mode (0/3), the central maximum has been eliminated and the energy - as it seems - been distributed to the adjacent radial lobes (figure 4.32(a)). Contrarily for mode (1/2) plotted in figure 4.32(b): in this case, the two innermost radial lobes have been eliminated and a central maximum has been generated. However, even if these two examples seem to contradict each other, generally speaking, the total number of the radial lobes from the duct axis to the duct wall has been reduced by one. This might be related to the virtual increase of the radial mode order due to the VSI effect (compare figure 4.2).

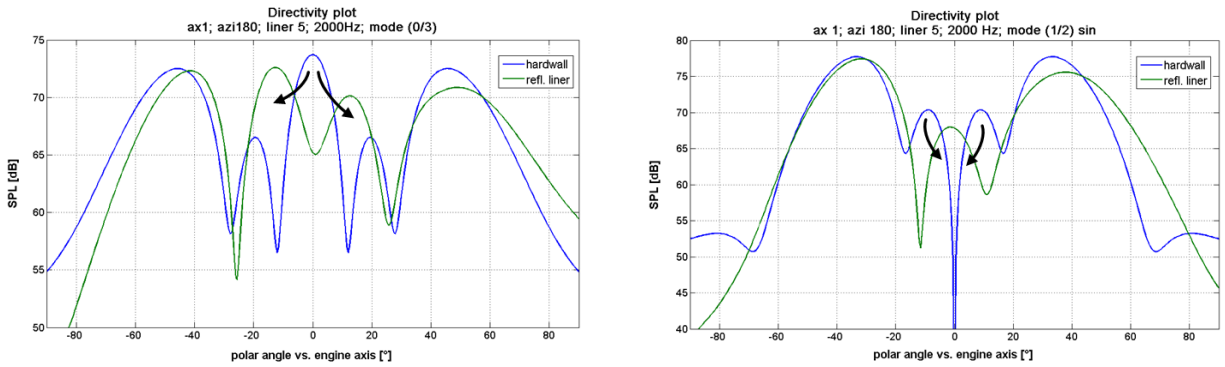

(a) mode (0/3), $\xi = 1.318$ (b) mode (1/2), $\xi = 1.733$

Figure 4.32: Comparison of vertical directivity plots at duct midplane; (0/3) $\leftrightarrow$ (1/2); ax1; azi180; 2000 Hz

To conclude these observations, the influencing parameters involved in the reflective liner effect, and derived within this section, will be summarized. These are, in descending order of importance, the following (in brackets the influencing factors observed only for certain conditions):

1. the cut-off ratio ξ:
   - $\xi > \xi_l$: tilt of directivity pattern (involving all radial lobes),
   - $1 < \xi < \xi_l$: 'cut-off effect' (strong reductions) in upper sector (at least for innermost radial lobe),
2. the radial mode order n
   - $n = 1 : +\alpha$ (positive tilt of directivity by angle $+\alpha$),
   - $n > 1 : -\alpha$ (negative tilt of directivity by angle $-\alpha$),
3. (the azimuthal mode order m)
   - $m = 0, 1$: reduction of (total) radial lobe number by 1,
4. (special case: the plane wave mode (0/1))
   - no tilt of directivity characteristic, rather an angular shift at a reduced peak level, similar to the NSI effect.

Thus, the VSI effect for fixed geometric parameters (size and position of the reflective liner segment) may be defined to be a function of the above named quantities:

$$\text{VSI effect} = f(\xi, n, (m)) \; . \tag{4.3}$$

This confirms the statement that for the non-uniform VSI liner configuration, the cut-off ratio does not remain the single relevant parameter (as for most other, especially the uniform lining designs), but additional parameters influence the effects on the directivity, foremost the radial mode number.

Chapter 5

Comparison of Virtual Scarf concept with uniform absorptive liner

In this chapter, the effect of the VSI on the radiation characteristic of a single propagating mode will be compared with the one of a uniform (absorptive) liner. Therefore, a cylindrical duct model of the same radius as the ROSTI duct ($R = 0.25$ m) has been created (as can be seen in figure 5.1). This simple geometry has been chosen to remove the influence of a more complicated inlet geometry and to make possible a comparison with analytical solutions. As for the previously used BE model of the ROSTI duct, a modal surface positioned at the far end of the duct (corresponding to the source plane) has been used for the modal excitation. Additionally, two semi-circular groups of elements of an axial length of 0.15 m equivalent to $0.3 \cdot D$ (the duct diameter) have been defined close to the inlet plane. To these, the varying impedance BCs of the different lining configurations will be assigned, which allows for the use of the same BE model for the whole numerical study.

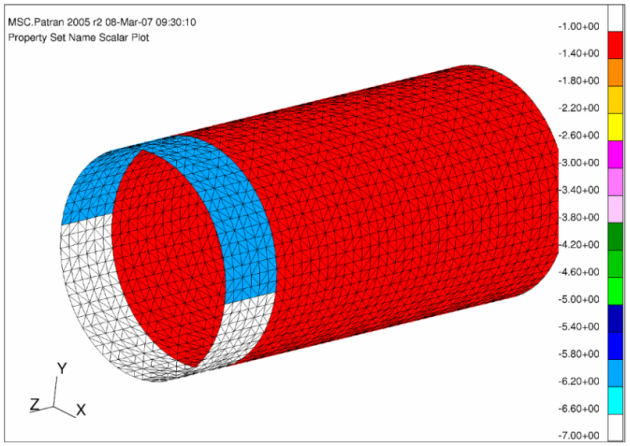

Figure 5.1: BE model of cylindrical duct model including liner property groups

Within this study, three inlet configurations have been compared against each other with respect to different quantities (the name of the respective configuration is inserted in the squared brackets):

- a hard walled duct (no impedance BCs assigned) [*hardwall*],
- a uniform (absorptive) impedance for both the lower and the upper property groups (marked blue and white in the figure) [*uniform*],
- an absorptive impedance for the upper part (blue group) and a low (reflective) impedance for the lower part (white group) [*VSI*].

Concerning the frequencies of excitation, the same three third-octave band center frequencies have been used as in the parametric study (compare table 4.2). As well, the reflective liner impedance has been set to the value of $Z_r = (0.05 - i \cdot 0.05) \cdot \rho c$. For the absorptive liner segment and the uniform liner, an impedance of $Z_a = (1.00 - i \cdot 0.50) \cdot \rho c$ has been chosen, which does not represent an optimized value, but on average yields quite a good performance.

In the first part of this chapter analyzing the VSI effect with respect to the directivity and the radiated power, at first the in this context called 'non-spinning' basic geometric modes (cos-/ sin- modes equivalent to standing waves in the circumferential direction) will be observed as they involve the least complexity (analogous to the procedure in the previous chapter). Later on, in each respective section, as well the results for spinning modes (exp±) will be given and compared to the former ones.

To summarize, the parameters involved in this study are recapitulated in table 5.1:

Table 5.1: Parameters used in comparison of VSI and uniform liner

configuration	frequency [Hz]	Helmholtz number	mode type	impedance
hardwall	1000	4.62	cos/sin	∞
uniform	1600	7.39	exp +/-	Z_a
VSI	2000	9.24		Z_r

However, to start, the cylindrical duct model shown in figure 5.1 will be compared to an analytical solution as well as to the ROSTI duct model presented in the previous chapter (figure 4.3) with respect to the reflection coefficients obtained at the modal surface. This may serve, on the one hand, to verify the validity of the BE model and, on the other hand, to estimate the amount of reflections from the inlet geometry for subsequent analyses.

Following, representative results of the computations for the two configurations under comparison will be presented and compared to each other with respect to the hardwall reference case. To give a first impression of the different effects of the liners, in the beginning, directivity plots in the vertical duct symmetry plane will be shown. As these do not contain all the information (only in a single plane), and the results cannot be easily quantified, the radiated power towards the ground will be computed subsequently.

Plots of the sound pressure distribution on the ground (to create a kind of 'footprint' of the duct radiation) and on the forward hemisphere serve to visualize and clarify individual results. As well, to analyze the phenomena caused e. g. by the reflective liner, plots of the sound pressure amplitude on the duct midplane will be added if applicable. Additionally, for selected cases, a modal analysis of the sound pattern inside the duct will be conducted at several axial stations.[1]

To further optimize the acoustic effect achievable by the VSI, a variation of the circumferential position of the reflective liner patch has been studied for spinning modes, for which an additional lateral deflection has been observed. Concerning the type of sound field, additional to the study of the single mode excitation generally used within this thesis, also broadband noise and a combination of both have been evaluated to improve the significance of the final results.

[1]However, the classical modal analysis is, in fact, not physically correct in application to the asymmetrical sound pattern resulting from the non-uniform VSI liner, as will be explained in more detail in the corresponding section (chapter 5.5), but may help to analyze its effect. Shortly speaking, this has to do with the basic assumption of a symmetry or periodicity of the modal patterns, which is not fulfilled anymore.

5.1 Influence of inlet geometry

At first, the two different BE models used up to now will be compared with respect to the influence of the inlet geometry on their directivity and the level of reflections. Figure 5.2 shows an example of the instantaneous sound pressure level (real part) of mode $(2/2)^+$ at the duct midplane, i.e. a snapshot of the propagating mode. In figure 5.2(a), the results for the cylindrical duct geometry are depicted, figure 5.2(b) shows the results for the ROSTI model. For both models, the pressure values on the (inner) duct surface are plotted, as well.

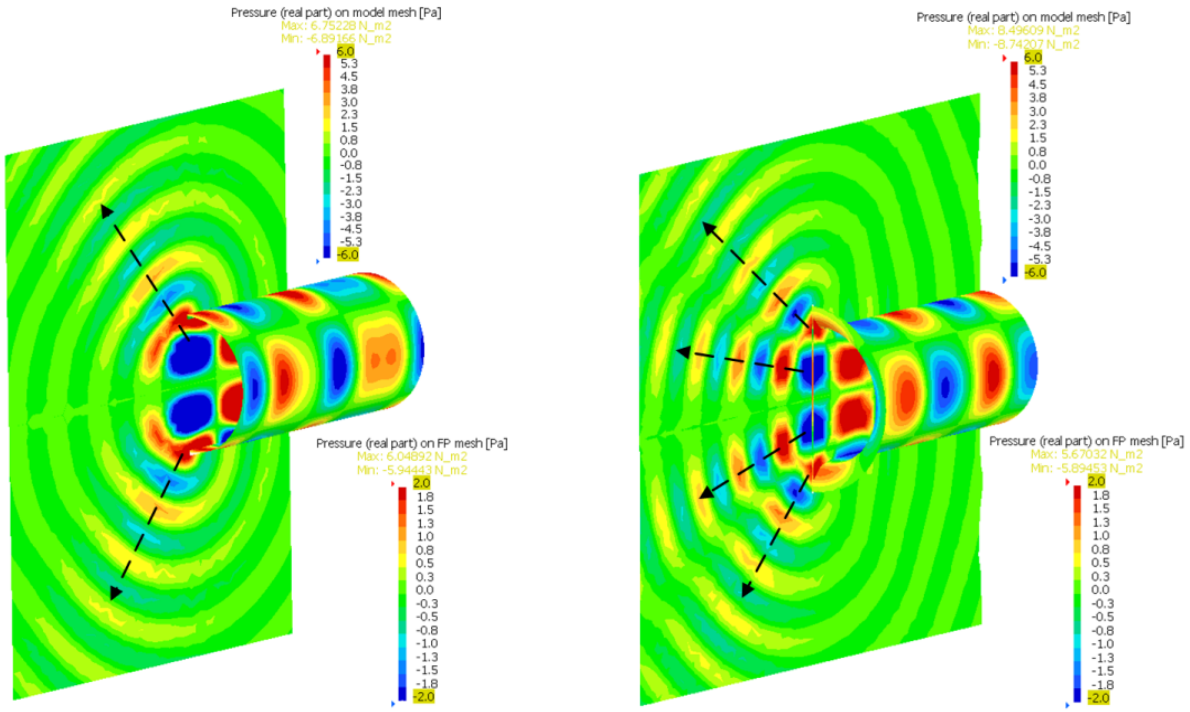

(a) cylindrical duct (b) ROSTI duct

Figure 5.2: Comparison of radiation characteristics on duct midplane; hardwall condition; cylindrical duct ↔ ROSTI duct; $(2/2)^+$; 1600 Hz; real part of sound pressure

For the ROSTI duct, the modal pattern (1st radial mode, 2 lobes in the radial direction) is diffracted at the opening due to the widening of the cross section, and then radiated to the far field at certain characteristic angles. Similarly for the cylindrical duct, however, the higher jump of impedance at the exit plane (from the impedance of air inside the duct to the free medium) causes a distortion of the modal pattern at the exit plane which nearly leads to an elimination of the inner radial lobes. This corresponding different directivities of the two models can be better observed in figure 5.3 (blue curve: cylindrical duct, green curve: ROSTI). This clearly shows the reduced pressure levels at the inner lobes for the cylindrical duct (≈ -20 dB) which are related to different levels of reflections.

Consequently, the reflection coefficients at the modal surface will be compared in the following. At first, for a verification of the results of the BE calculations, a comparison will be presented of the plane wave mode (0/1) total reflection coefficient (r_{mnt}) for the cylindrical duct (calculated numerically using the BE code) with an analytical solution given by Levine and Schwinger in Ref. [191] (by combination of both the low- and high-frequency approximations).

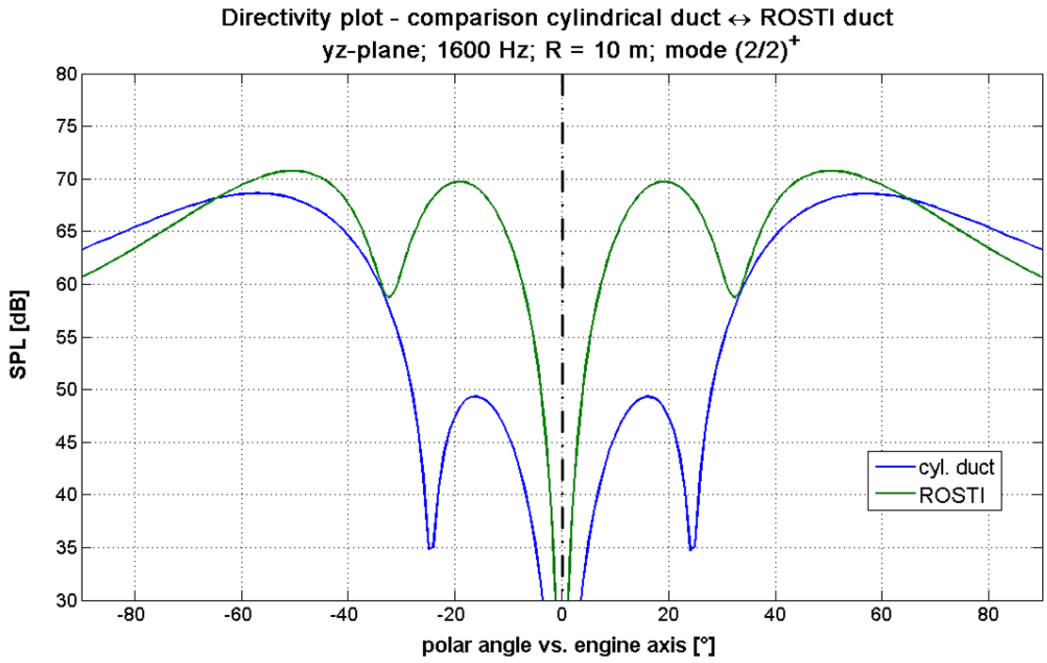

Figure 5.3: Comparison of directivity plots at vertical duct midplane; cylindrical duct ↔ ROSTI duct; $(2/2)^+$; 1600 Hz; $R = 10$ m

The result is depicted in figure 5.4 and shows a very good agreement up to the cut-off frequency of the first radial mode ($f_{c_{(0/2)}} \approx 830$ Hz), which is not included in the analytical solution. As well, the results for the ROSTI duct have been included in the figure in the green curve.

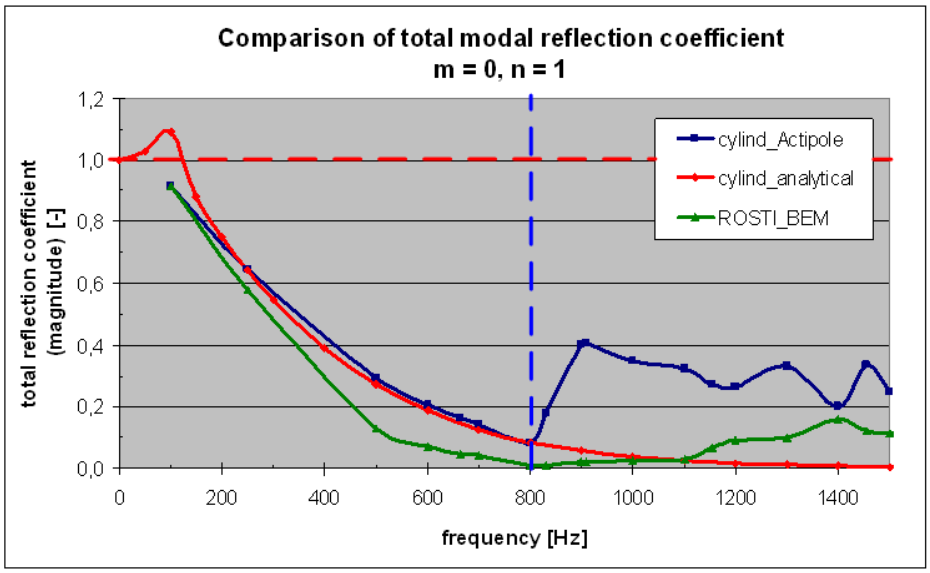

Figure 5.4: Comparison of plane wave reflection coefficient with analytical solution

They start at nearly exactly the same level at the lowest frequency computed ($f = 100$ Hz $\equiv He = 0.462$), but then fall off more sharply to a level close to zero at the cut-off frequency of mode $(0/2)$. This is in good correlation with the BE results of Selamet et al. [192] who studied the effect of different inlet geometries on the plane wave reflection coefficient. In their work, the ROSTI results correspond to an unflanged bellmouth inlet of curvature to radius ratio $r_{BM}/R = 0.4$.

Figure 5.5 then opposes the reflection coefficients of the two BE models compared above for the axisymmetric modes ($m = 0,\ n = 1, 2, 3$). The solid lines represent the amplitude of the direct reflection coefficients r_{mnn} (i.e. the reflection coefficient of the excited mode into itself), whereas the dashed lines represent the total reflection coefficients r_{mnt} (i. e. the sum of the direct reflection coefficients and all coupling coefficients).[2] The dashed vertical lines at 830 Hz and 1520 Hz indicate the cut-off frequencies of the first radial modes ($n = 2, 3$) and the horizontal red line at $r = 1.0$ the upper physical limit for the reflection coefficient.[3]

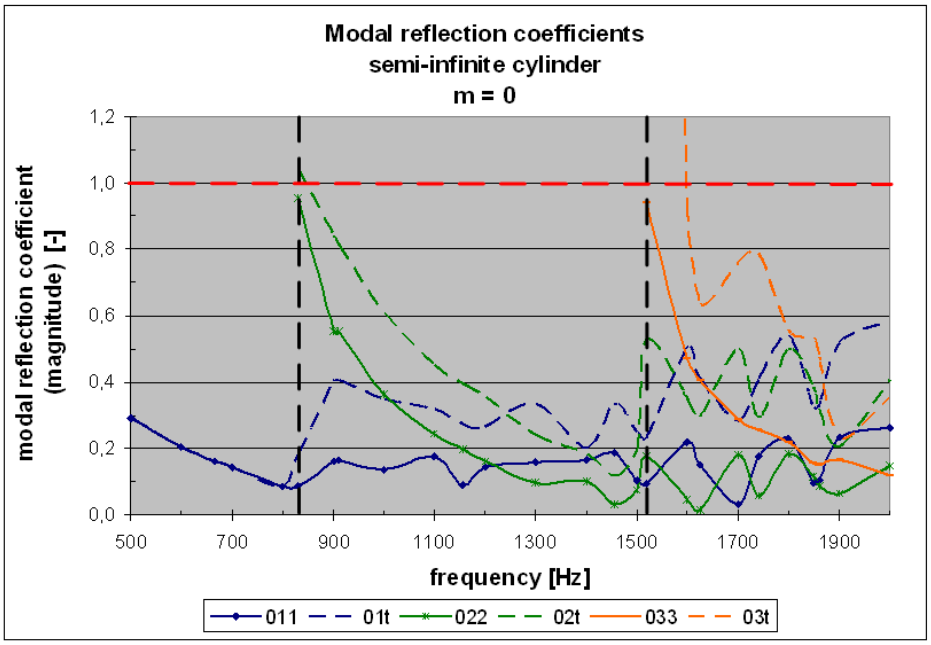

(a) cylindrical duct

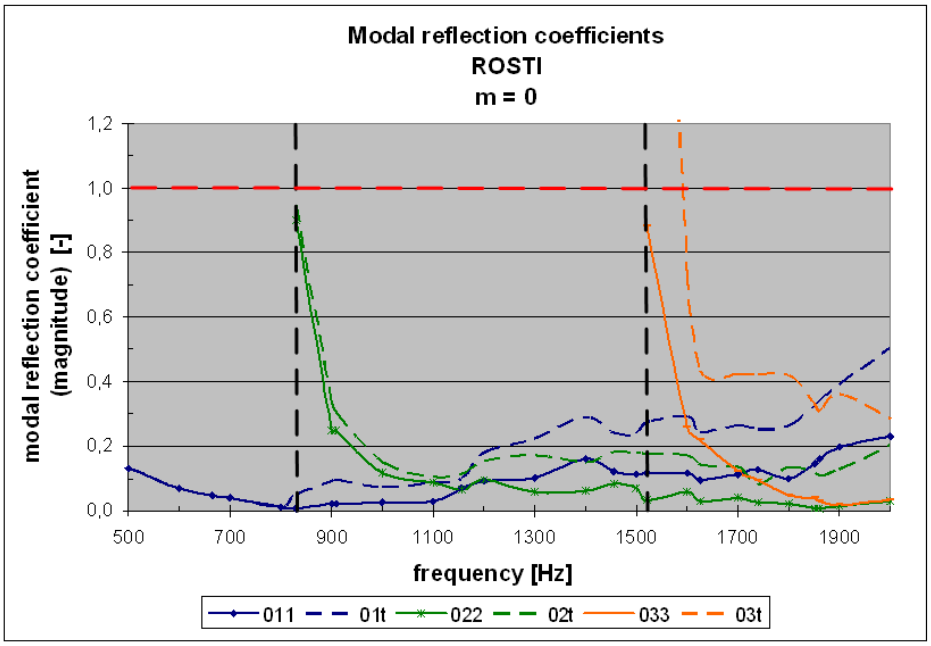

(b) ROSTI duct

Figure 5.5: Comparison of modal reflection coefficients; hardwall condition; $m = 0$

[2]For the definition of these coefficients refer to chapter 2.1.2 or Weinstein [9].

[3]The values larger than 1 for the total reflection coefficient r_{03t} of mode (0/3) may be explained by numerical inaccuracies close to the cut-off frequency of the mode.

As can be seen in figure 5.5, the individual reflection coefficients start at the cut-off frequency of the respective mode at a value of approximately unity and decrease continuously with increasing frequency and cut-off ratio. At the cut-off frequency of the next higher radial mode, the curves experience a kink in their characteristic and an increase in the reflection levels (more pronounced in the cylindrical duct case), but then tend to decrease again.

In comparison with the semi-infinite cylinder, the ROSTI geometry yields a considerably steeper slope of the individual coefficients and, in general, lower reflection levels which can be attributed to the better transition from the finite duct radius to the infinite domain, and hence, a lower impedance discontinuity causing lower reflection levels.

5.2 Effect on radiation directivity

In this section, a few examples of the results obtained from the BE calculations concerning the directivity of radiation will be presented to illustrate the effects of the non-uniform VSI liner in comparison with the uniform liner configuration. This will be done first for the basic geometric 'non-spinning' modes representing standing waves with respect to the circumferential direction, later on the characteristic differences for the exponentially recombined spinning modes will be mentioned and shown.

5.2.1 Circumferentially standing wave patterns

As a reference, in figure 5.6 the magnitude of the sound pressure of mode (0/1) at 1000 Hz ($k \cdot R = 4.62$) at the duct midplane ($x = 0$) is presented for the hardwall solution. To permit the visualization of the pressure distribution inside the duct, the geometric mesh has been removed.

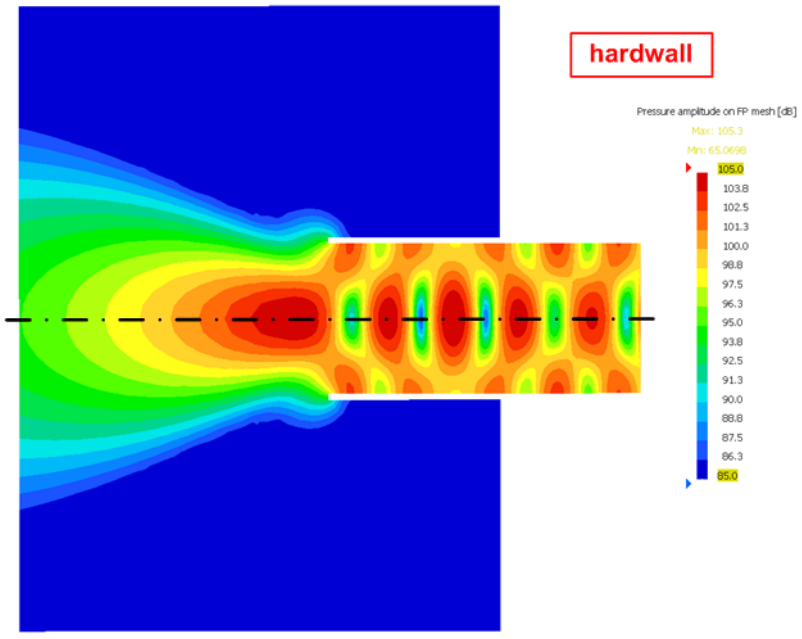

Figure 5.6: Radiation characteristic on vertical duct midplane; (0/1); 1000 Hz; pressure amplitude - hardwall configuration

The SPL amplitude shows axial and radial variations due to reflections (compare figure 5.4: $r_{mnt,1000\ Hz} \approx 0.349$). These cause standing wave components in the axial direction and contain also contributions from other radial modes of the same azimuthal mode number (at the frequency considered within this example only from the first radial mode (0/2)).

This contribution can also be inferred from figure 5.5(a). At the frequency considered here (1000 Hz), the coupling coefficient accounts for even 60% of the total reflection coefficient. The modal pattern is then diffracted at the duct exit and radiates predominantly axially.

Figure 5.7 then opposes the uniform (figure 5.7(a)) and the VSI (figure 5.7(b)) configurations.

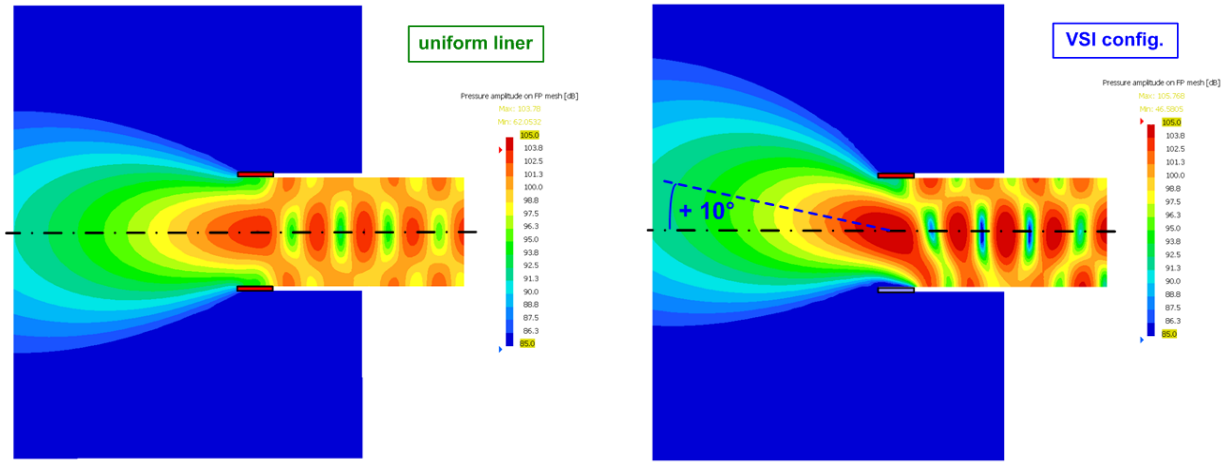

(a) uniform liner (b) VSI configuration

Figure 5.7: Comparison of radiation characteristics on vertical duct midplane; (0/1); 1000 Hz; pressure amplitude - lined duct configurations

In the uniform liner configuration (figure 5.7(a)), the modal energy propagating at the duct wall is being attenuated by the liner which focuses the radiation on the axis of rotation and reduces the radiation towards the ground.

From figure 5.7(b), it can be observed how the main lobe is shifted to positive angles by approximately $+10°$ in the non-uniform VSI configuration. This is directly coupled with a substantial noise reduction at the ground. Additionally, a change in the sound pressure distribution even behind the liner can be noticed corresponding to the increased level of reflections at the impedance discontinuity in both the axial and circumferential direction (this effect will be studied in detail in chapter 5.5).

These tendencies are also reflected in the directivity plot of the different configurations depicted in figure 5.8. The curve of the hardwall configuration shows a small radial contribution at the higher angles related to the first radial mode (0/2). In the uniform liner configuration, these side lobes are attenuated very efficiently and the main lobe is reduced by ≈ 3.3 dB. The curve of the non-uniform VSI configuration shows, as above, an upward shift of $\approx +10°$ and a slightly higher sound pressure level (+0.3 dB at the maximum) compared to the uniform liner case. This angular shift in case of the plane wave mode has already been observed in the parametric study concerning the VSI effect in chapter 4.3.2.

To visualize the positive effect of the reflective liner strip, the sector in which a noise reduction could be achieved is highlighted in the figure by hatching. For this mode, the non-uniform configuration yields an advantage compared to the uniform liner essentially in the whole lower forward sector $[-90°; 0°]$ (in anticipation of the next section, this corresponds to -2.0 dB concerning the radiated power onto a ground plane of predefined dimensions).

As a second example, the results for the azimuthal mode (2/1) at a higher frequency (2000 Hz $\equiv k \cdot R = 9.24$) is presented in figures 5.9 and 5.10.

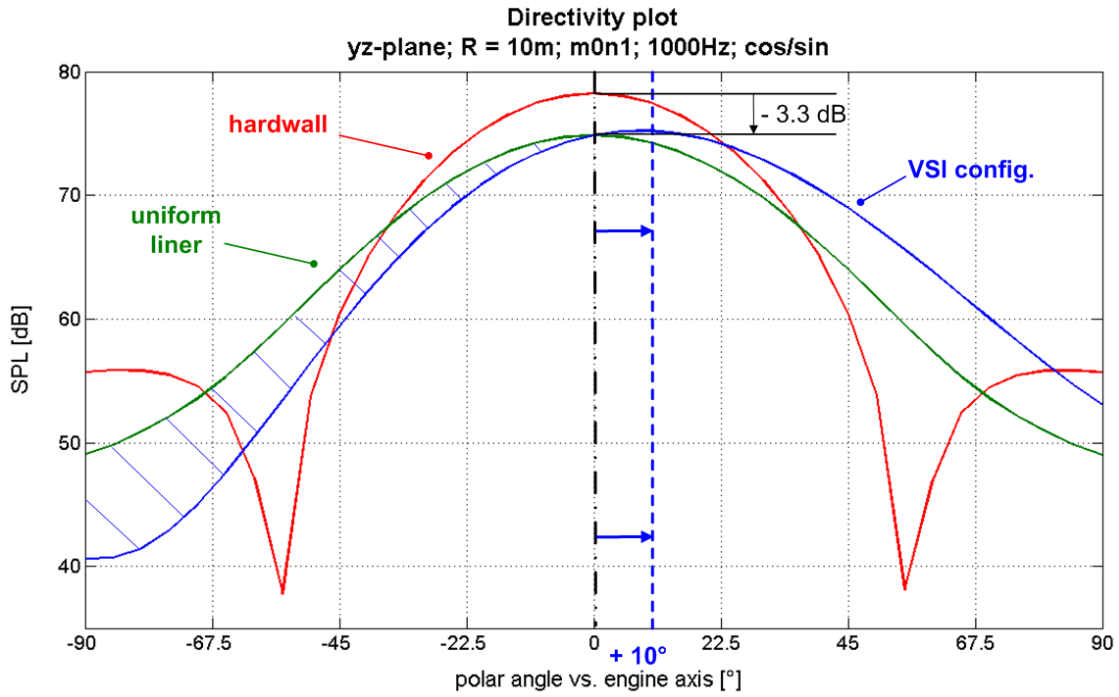

Figure 5.8: Vertical directivity plot at duct midplane; hardwall condition ↔ uniform liner ↔ VSI configuration; (0/1); 1000 Hz; $R = 10$ m

Clearly visible in the radiation pattern of the hardwall case in figure 5.9 are the two main lobes located in the duct midplane, as well as small radial contributions radiating at higher angles. These originate from the modal pattern within the duct and the diffraction effects at the duct exit (at this frequency, the first radial mode (2/2) is cut-on, as well).

In the uniform liner configuration (figure 5.10(a)), the radial components are completely eliminated, but the main lobes radiate at approximately the same angle as in the hardwall

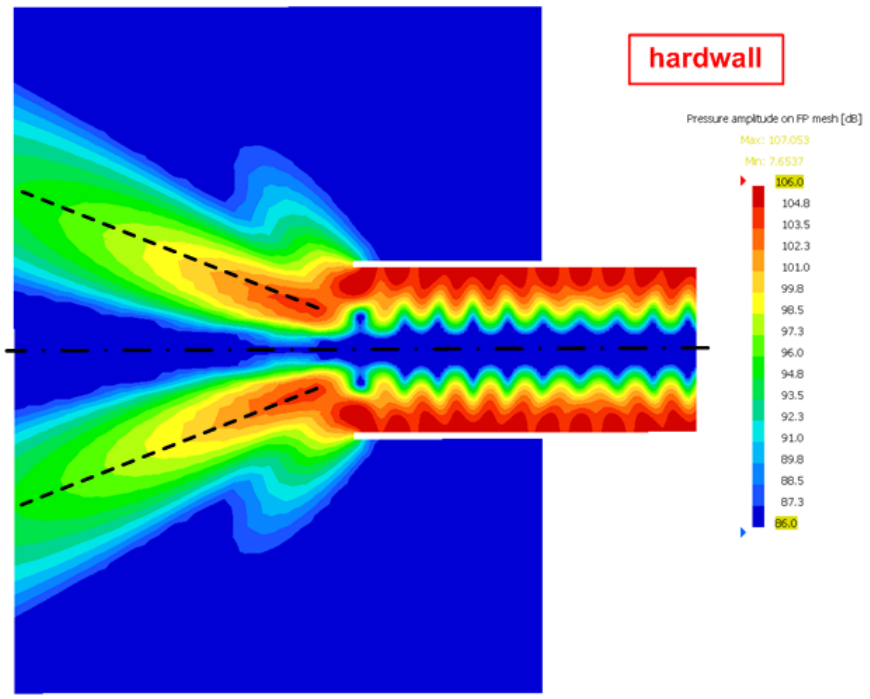

Figure 5.9: Radiation characteristic on vertical duct midplane; (2/1); 2000 Hz; pressure amplitude - hardwall configuration

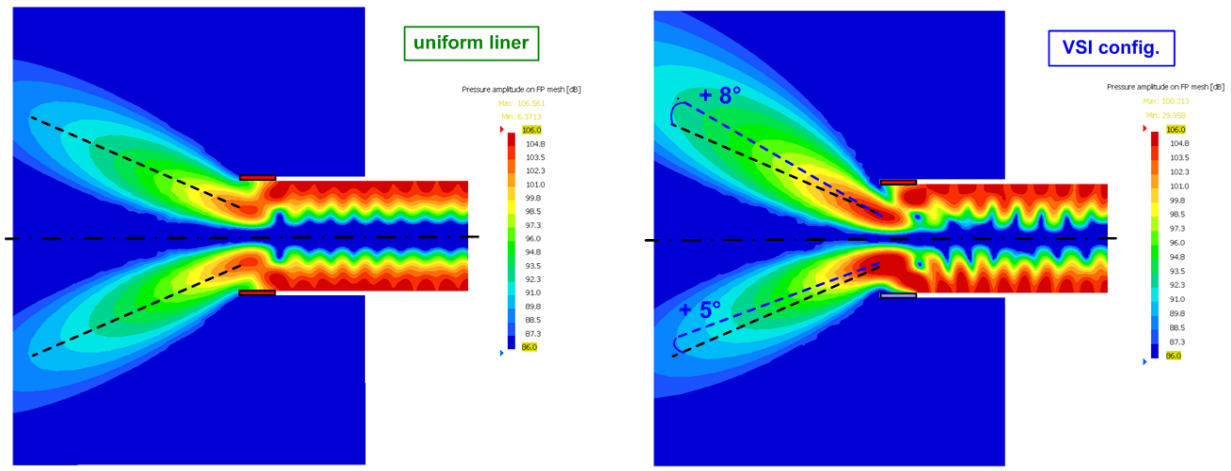

(a) uniform liner (b) VSI configuration

Figure 5.10: Comparison of radiation characteristics on vertical duct midplane; (2/1); 2000 Hz; pressure amplitude - lined duct configurations

configuration (as indicated by the dashed lines). Thus, on the ground, a substantial noise reduction can be expected due to the liner. The VSI liner configuration (figure 5.10(b)), on the other hand, tilts the main lobes by $\approx +5°/+8°$. This has a noticeable effect on the radiation pattern, but the effect on the ground might be expected to be weaker compared to the plane wave mode presented before.

A clearer view can be obtained from the corresponding directivity plot in figure 5.11: the hardwall result containing radial contributions is attenuated by 5.2 dB at the peak pressure (at $\pm 25°$), and the side lobes are removed in the uniform liner configuration.

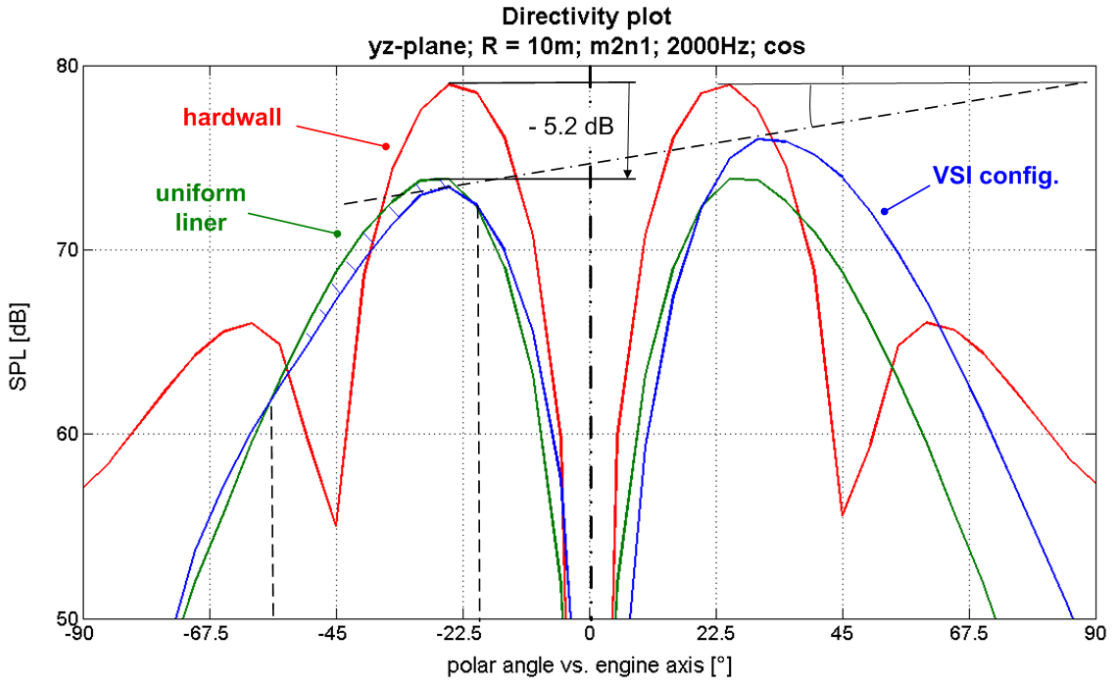

Figure 5.11: Vertical directivity plot at duct midplane; hardwall condition ↔ uniform liner ↔ VSI configuration; (2/1); 2000 Hz; $R = 10$ m

As marked, the non-uniform VSI configuration yields an advantage in the angular sector $[-55°; -20°]$ though not as impressive as for mode (0/1). In result, this configuration achieves

-0.3 dB with respect to power radiated onto the lower forward plane. Within this figure, the tilting effect on the directivity curve in the VSI configuration is again clearly visible. As mentioned in the previous chapter, this angular tilt describes the effect of this type of non-uniform liner more precisely, in contrast to Ref. [132], where the effect of the NSI has been described by a corresponding shift in angular position in the directivity plot.

In contrast to the examples presented above, where the tendencies derived from the directivity plots could be directly confirmed by the power calculations (presented in the next section), some other modes did not yield such a good correlation and required further investigations. For example, the comparison of the directivity curves of the different configurations for mode (0/3) at 1600 Hz ($k \cdot R = 7.39$), depicted in figure 5.12, gave reason to expect quite good power reductions on the ground for the VSI configuration. However, the radiated power into the forward plane, when evaluated on the ground, yielded only -0.4 dB compared to the uniform configuration.

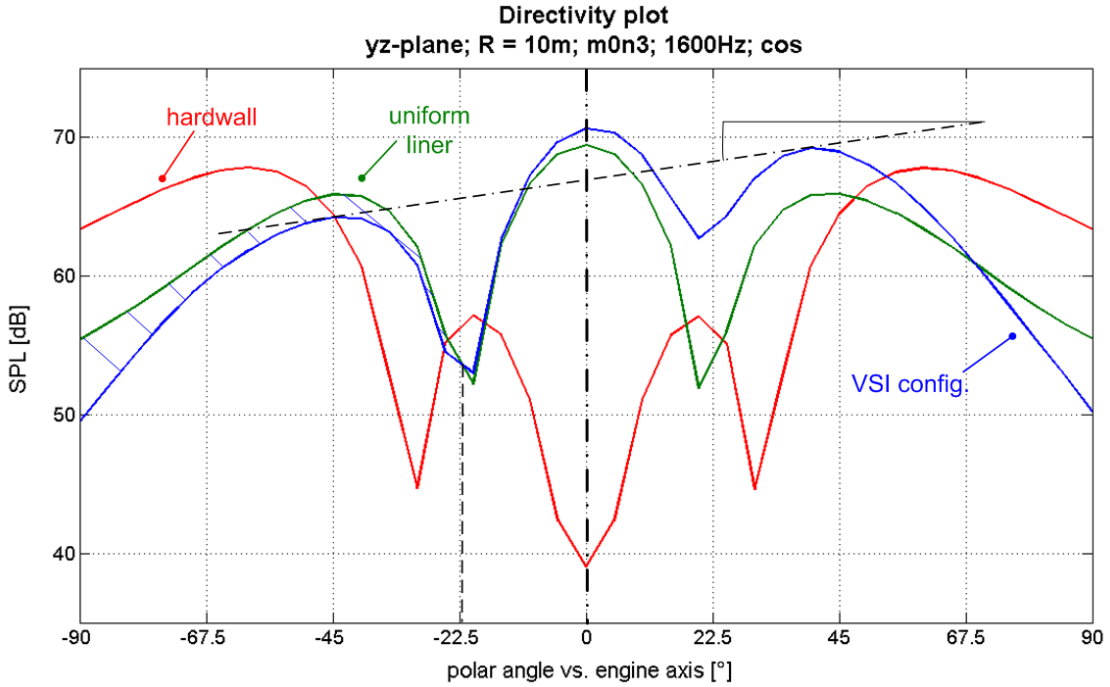

Figure 5.12: Vertical directivity plot at duct midplane; hardwall condition ↔ uniform liner ↔ VSI configuration; (0/3); 1600 Hz; $R = 10$ m

To study this effect in more detail, the pressure distribution on the forward hemisphere of radius $R = 5$ m centered at the origin of the coordinate system (the center of the inlet plane) has been calculated and is presented in figure 5.13 for both configurations along with a vertical duct midplane FP mesh to visualize the pressure patterns inside the duct. The suggested 'streamlines' indicate the directions of propagation of the respective main lobes.

These figures clarify the results: The circular pattern at an angle of $\approx 45°$ with respect to the duct axis indicating the maximum sound pressure level radiated by the first radial lobes (apart from the axially centered contribution) for the uniform configuration has been split up in the non-uniform liner results into three maxima: one on top and one symmetrically to each side in the lower half. Consequently, the directivity plot in the vertical plane shows low pressure levels for the lower sector and an increase in the upper half. However, the two maxima to the left and right still contribute to the pressure distribution (and hence the radiated power value) at the ground, and reduce the net effect of this configuration.

These observations underline the necessity of considering the whole picture for the non-uniform liner configurations analyzed here, as a confinement to certain evaluation points

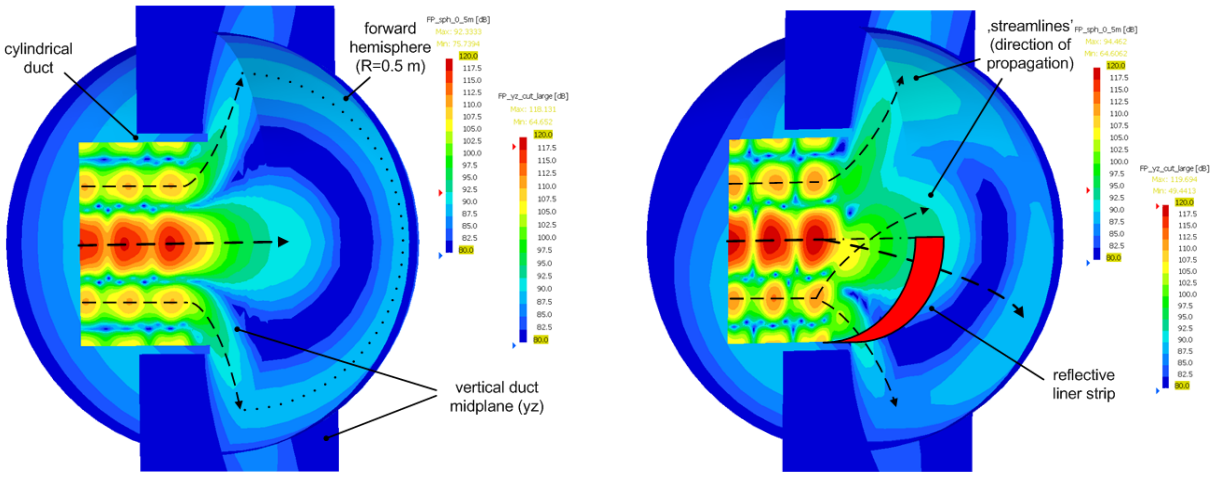

(a) uniform liner (b) VSI configuration

Figure 5.13: Comparison of sound pressure distributions (magnitude) on forward hemisphere (R = 5 m) and vertical duct midplane; (0/3); 1600 Hz

might disregard effects at other locations, and lead to a misinterpretation of the results. Thus, in the final analysis of the performance of the VSI configuration, only radiated power values into specific sectors will be regarded.

5.2.2 Spinning modes

As mentioned in chapter 2.1.1.2, spinning modes are an exponential recombination of the basic mode shapes (cos/sin) and do not represent an elementary difference to those modes.

In effect, for spinning modes, the radiation characteristics in the vertical plane (as presented in the three examples above) yield the identical results with respect to the deflection of the main lobes. This can be sen in a comparison of the directivity plots of these two types of modes in figure 5.14. It compares the results of the two lining configurations and the hardwall case for mode (1/1) at 1000 Hz.

As can be seen in the figure, there is a 3 dB separation (corresponding to the factor $1/\sqrt{2}$) between the exponential and the cos-/ sin- modes (spinning mode configurations are indicated by dashed lines, non-spinning ones by solid lines). This relates to the recombination of the two basic mode shapes (cos/sin) causing a different SPL for all modes $m > 0$, for which in all cases two solutions are found. Accordingly, the respective sound pressure levels can be obtained by the following relations:

$$\begin{aligned} p_{exp\pm} &= p_{cos} = p_{sin} \quad &: m = 0\ , \\ p_{exp\pm} &= \frac{1}{\sqrt{2}} \cdot p_{sin/cos} \quad &: m > 0\ . \end{aligned} \tag{5.1}$$

Apart from this shift of the absolute level, the characteristics of all configurations exactly agree. However, an analysis of the horizontal directivity plots (located in the plane $y = 0$) discloses a fundamental difference between the two types of modes: the non-uniform liner also affects the lateral radiation of the spinning modes, as shown exemplarily in figure 5.15. For purposes of clarity, in this figure only the non-spinning results have been plotted for the symmetric configurations (hardwall, uniform liner). As before, solid lines represent non-spinning modes and dashed (or dotted) lines spinning modes.

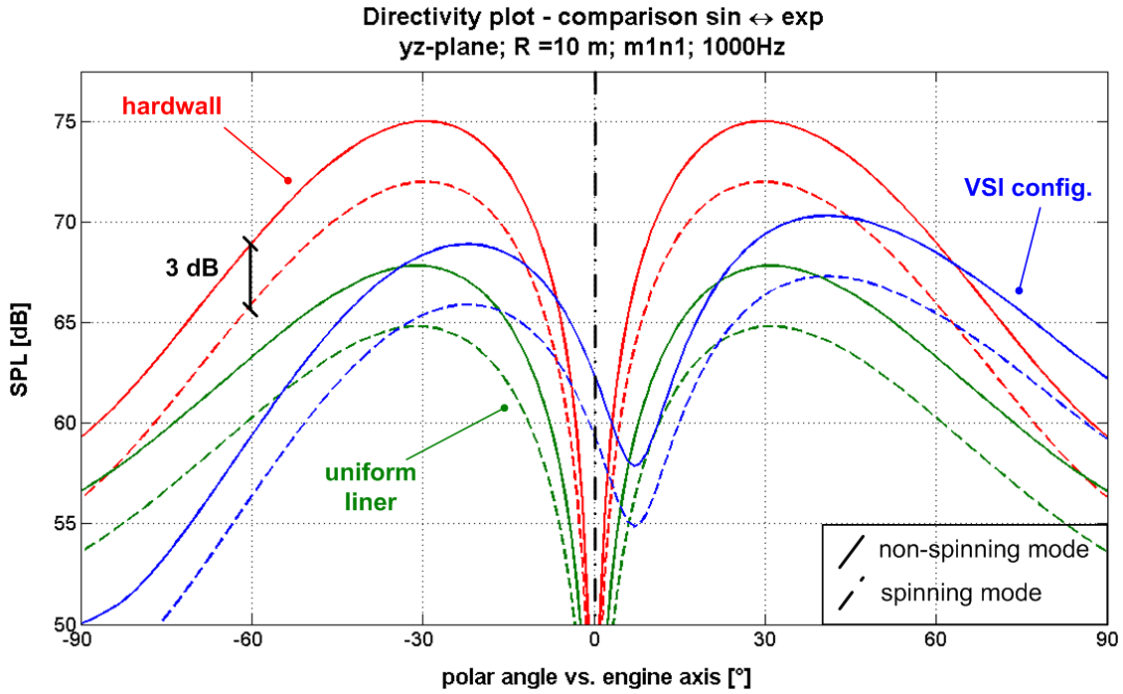

Figure 5.14: Vertical directivity plots at duct midplane; non-spinning ↔ spinning modes; (1/1) sin ↔ exp; 1000 Hz; $R = 10$ m

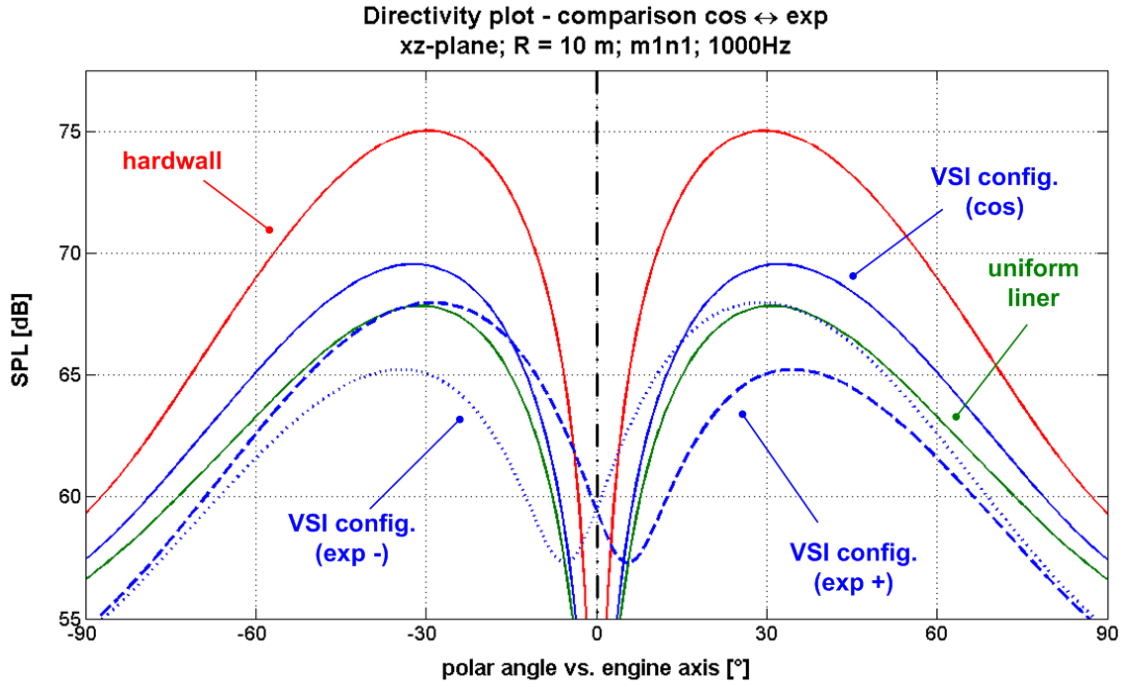

Figure 5.15: Horizontal direct. plots at duct midplane; non-spinning ↔ spinning modes; (1/1) cos ↔ exp$^{\pm}$; 1000 Hz; $R = 10$ m

For the hardwall and uniform liner configurations, the two curves are identical in shape but separated by the above mentioned 3 dB in SPL. In contrast, for the non-uniform configuration, two curves result for the two spinning directions, which are both different from the non-spinning directivity curve, but symmetric to each other with respect to the duct center line.

The lateral deflection in the VSI configuration is caused by the impedance discontinuity in the circumferential direction at the reflective liner segment. A similar effect has been

observed in computations and experiments involving scarfed intakes or, in general, three-dimensional inlets, published e. g. by Schönwald [193] and Lan [194]. Depending on the direction of rotation, the modal pattern is thus deflected sideways.

As mentioned above, to make sure no informations is disregarded, and to picture the effect of the non-uniform liner on both the non-spinning and the spinning mode propagation, figure 5.16 shows a comparison of the radiation characteristics on the forward hemisphere (seen from behind) for mode (1/1).

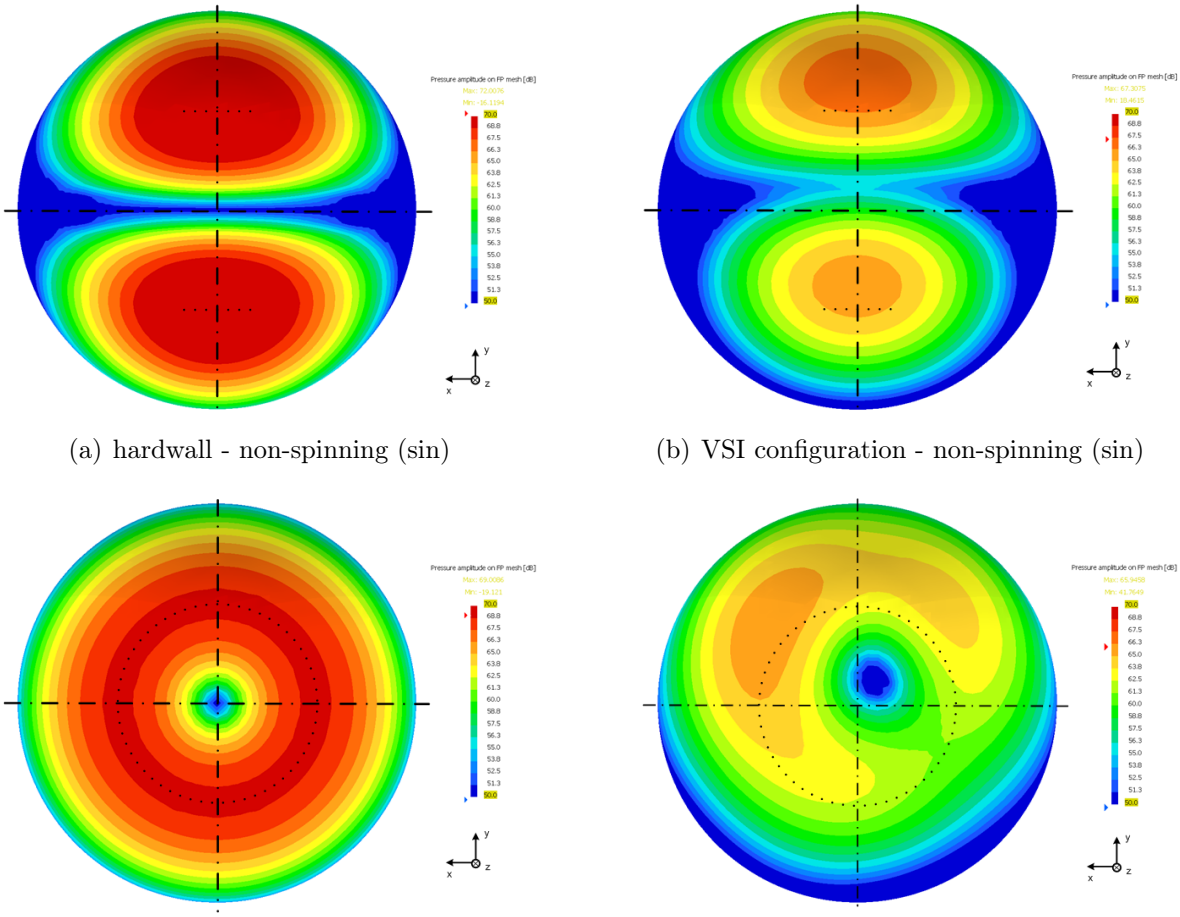

(a) hardwall - non-spinning (sin)

(b) VSI configuration - non-spinning (sin)

(c) hardwall - spinning

(d) VSI configuration - spinning

Figure 5.16: Comparison of sound pressure distributions (magnitude) on forward hemisphere (R = 10 m); non-spinning ↔ spinning modes; (1/1); 1000 Hz

Whereas for the pure sinus-mode (figure 5.16(b)), the VSI shows an upward shift of the two main lobes and reduced peak levels for the lower one, the location of maximum sound pressure levels of the spinning mode (figure 5.16(d)) - which for the hardwall and uniform liner configurations shows a concentric circular pattern - is asymmetric and tilted to the left hand side.

This figure also discloses a potential for improvement with respect to the VSI liner design: if it was achieved to locate the pressure maximum exactly above the duct axis, further noise reductions on the ground should be expected. This could be achieved e. g. by adjusting the circumferential position of the reflective liner patch for the respective mode. At the end of this chapter (in section 5.6), results of an optimization study making use of this effect will be presented. They will demonstrate the considerable potential of this modification and suggest an adaptive system to be used since the rotation angle depends on the modal numbers and the frequency.

5.3 Analysis of radiated power reduction

After these interpretations of the directivity patterns, the net effect on the ground will be analyzed in terms of the radiated power values. Therefore, at first, a rectangular FP mesh of the dimensions 500 m x 500 m at the vertical distance of 100 m below the duct has been defined, yielding an angular sector of [-90°; -11°] in the forward direction and [-90°; -22°] laterally with respect to the duct axis (compare figure 5.17). Accordingly, the power values have been obtained by integration of the normal intensity over this plane as described in chapter 2.1.3.

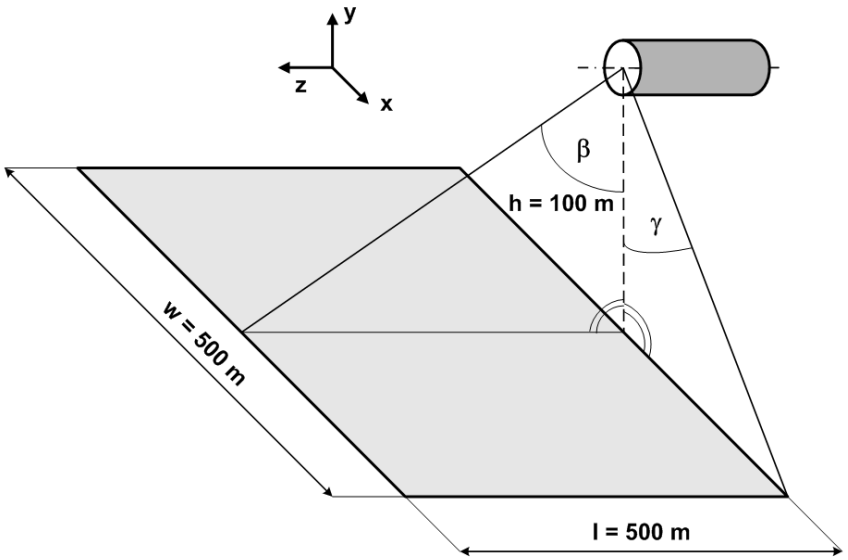

Figure 5.17: Sketch of the ground plane FP mesh used for radiated power calculations

5.3.1 Circumferentially standing wave patterns

As in the previous section, at first, the results of the circumferentially standing wave patterns will be presented before evaluating the differences for the spinning modes.

Figure 5.18 shows the results of this investigation in ΔPWL (PWL: sound power level) in decibel with respect to the uniform liner configuration. Using this referencing, negative values indicate a lower power value - and hence an advantage - of the VSI configuration and vice versa. For each mode, the results of the cos- and sin- solutions have been averaged to bring them into line with the spinning mode results.

From the graph, a positive effect (for the VSI configuration) can be observed for modes (0/1) and (1/1), and partly for modes (2/1) and (0/3), so mainly for the lower order zeroth radial modes. For the plane wave mode, which shows the largest effect, the additional noise reduction on the ground yields -2.0 dB at the lowest frequency considered (1000 Hz).

To better understand the reason for these advantages of the VSI configuration, two examples of a positive VSI effect have been plotted side by side in figure 5.19. From the top, the resulting sound pressure amplitude distributions on the ground are depicted for the hardwall, the uniform liner, and the VSI configuration for modes (0/1) at 1000 Hz (on the left) and (0/3) at 1600 Hz (on the right). The cylindrical duct containing the modal sound source is in each case located at the center right boundary where the coordinate system is indicated.

As can be seen when comparing the figures, for mode (0/1) in the VSI configuration, the location of the maximum sound pressure level has been shifted farther away from the origin and, as well, been reduced in its peak level (from 40.8 dB to 38.7 dB) compared to

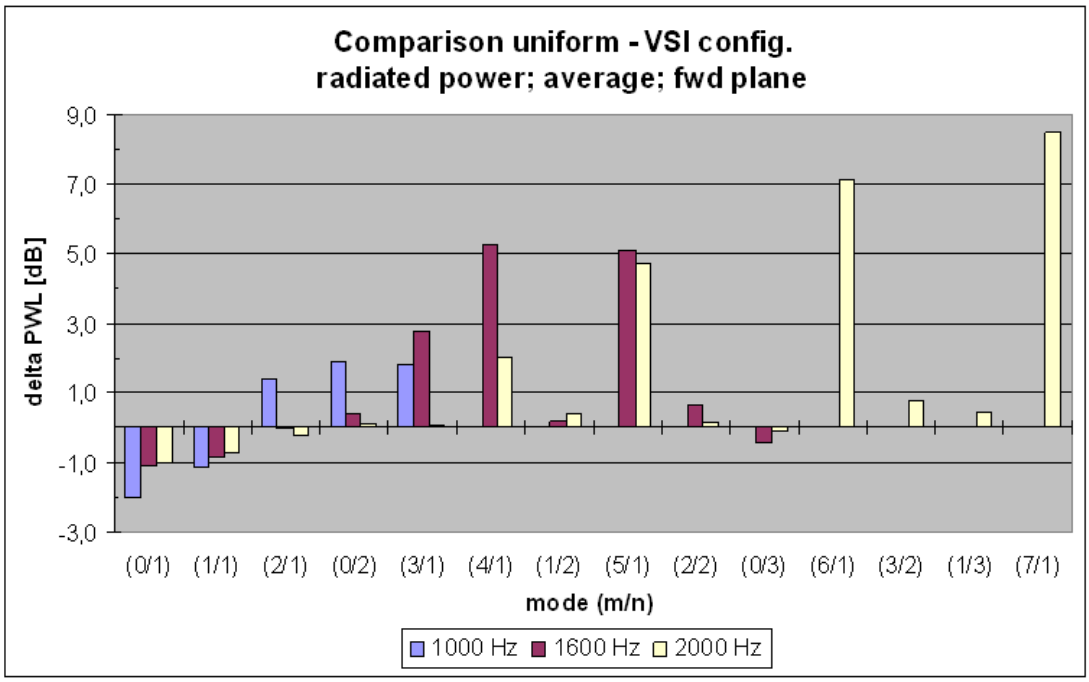

Figure 5.18: Power results on forward ground plane; average of cos/sin modes

the uniform liner configuration. This is due to the extended radiation distance towards the ground for the deflected main lobe (as has been explained in the previous chapter using geometric considerations in figure 4.26).

In the case of mode (0/3) at 1600 Hz, even the uniform liner configuration seems to show a horizontal shift of the location of the maximum sound pressure level. This is due to the relative redistribution of the modal energy in the radial direction by the liner. The outermost radial component propagating directly at the duct wall has been attenuated very effectively which causes the mode to radiate more axially (as could be seen in the corresponding directivity plot in figure 5.12 and the combined plot in figure 5.13(a)). In contrast, in the VSI configuration, the circular pattern of the outer radial component of mode (0/3) (figure 5.20(a)) has been split up into three maxima (compare figures 5.13 and 5.20(b)) which broadens the footprint on the ground at a reduced maximum SPL (38.5 dB compared to 40.1 dB for the uniform liner).

Coming back to the power results in figure 5.18, in contrast to the favorable results reported up to this point, in several cases, especially for the higher order azimuthal modes, considerably higher radiated power levels into the lower sector have been observed compared to the uniform liner.

However, these results need to be interpreted in the following way: the upward angular shift of the main lobes observed from the directivity plots causes a shift of the pressure peaks on the ground plane. As this is accompanied by an increase in distance from the source, the peak values will decrease proportionally to the $1/r$ dependency of the pressure (equation 2.75). Yet, for the barely cut-on higher order modes radiating at steep angles, this angular shift corresponds to only a small increase in distance, and hence, is less effective than for the more axially propagating lower order modes.

On the contrary, the uniform liner becomes more and more effective with lower cut-off ratios and higher propagation angles related to an increase in the effective liner length. This imbalance is reflected in the bar plot by an overall increase in the negative effect of the VSI configuration compared to the uniform liner with a decreasing cut-off ratio (from the left to the right in figure 5.18).

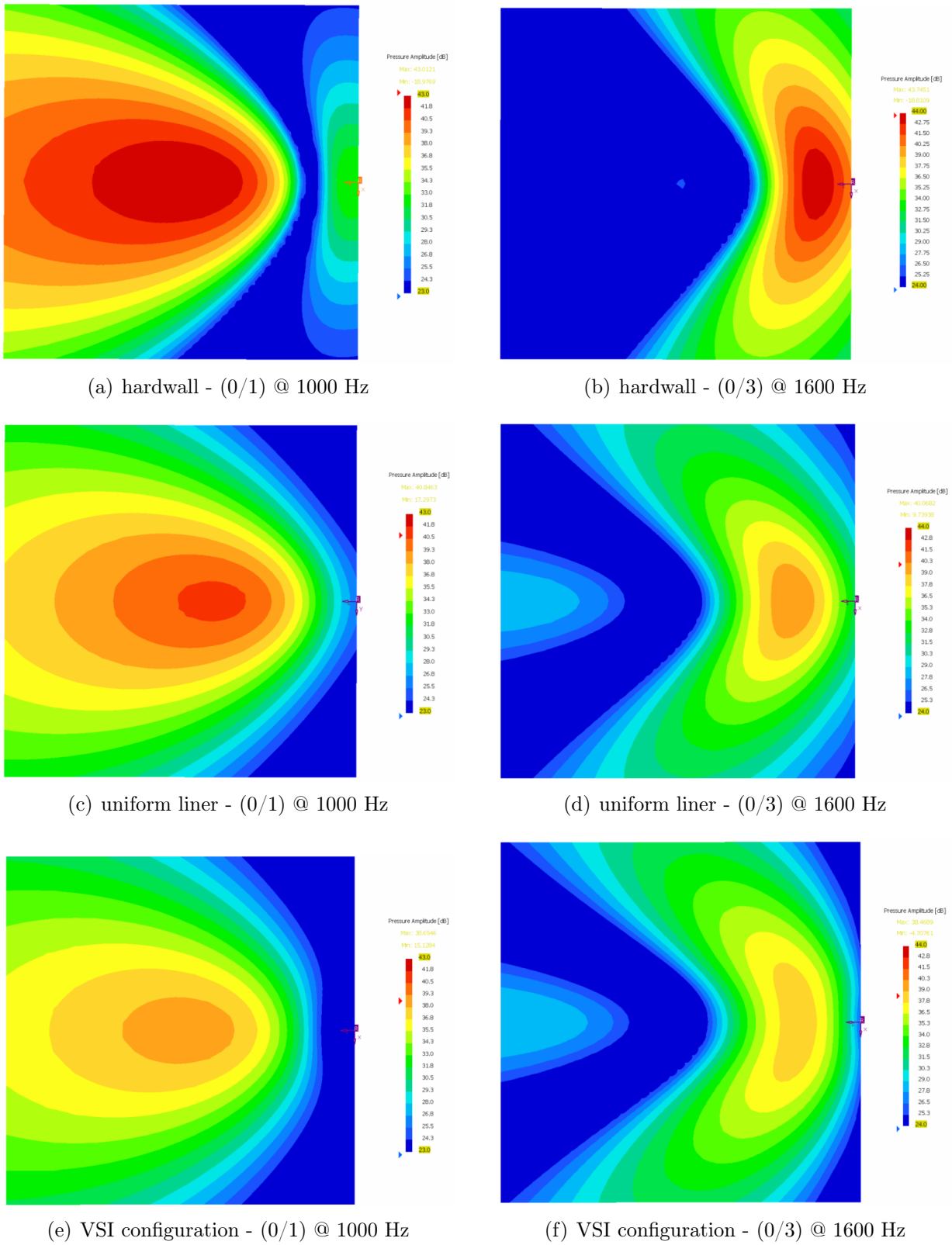

(a) hardwall - (0/1) @ 1000 Hz

(b) hardwall - (0/3) @ 1600 Hz

(c) uniform liner - (0/1) @ 1000 Hz

(d) uniform liner - (0/3) @ 1600 Hz

(e) VSI configuration - (0/1) @ 1000 Hz

(f) VSI configuration - (0/3) @ 1600 Hz

Figure 5.19: Comparison of sound pressure distributions (magnitude) on forward ground plane; (0/1) / (0/3); 1000 Hz / 1600 Hz

However, this tendency can only be consistently observed for the azimuthal mode orders, the radial modes show, in general, lower differences (which again confirms the dependency of the VSI effect on the radial mode order).

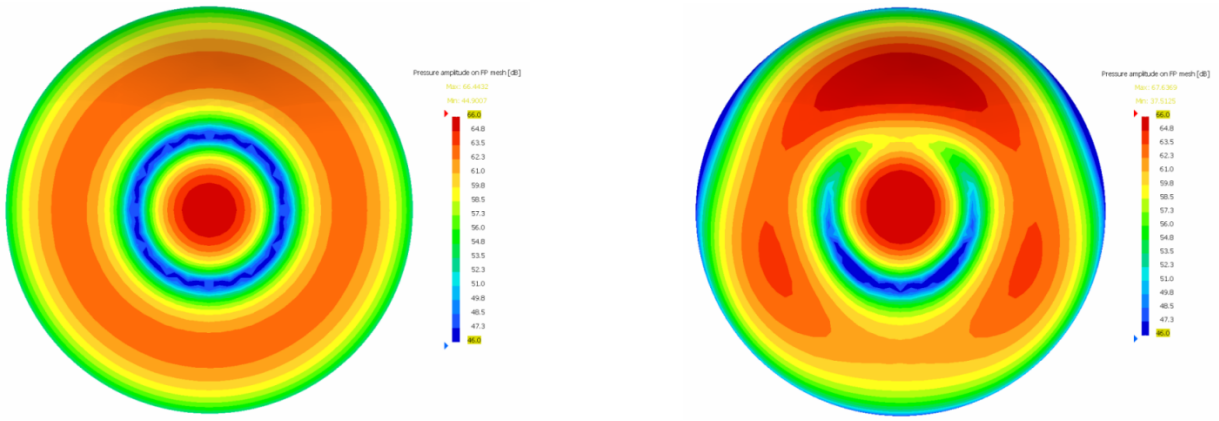

(a) uniform liner (b) VSI configuration

Figure 5.20: Comparison of sound pressure distributions (magnitude) on forward hemisphere (R = 10 m); (0/3); 1600 Hz

As an example of these higher order azimuthal modes, figure 5.21 plots the 'footprints' of the three configurations for mode (4/1) at 1600 Hz.

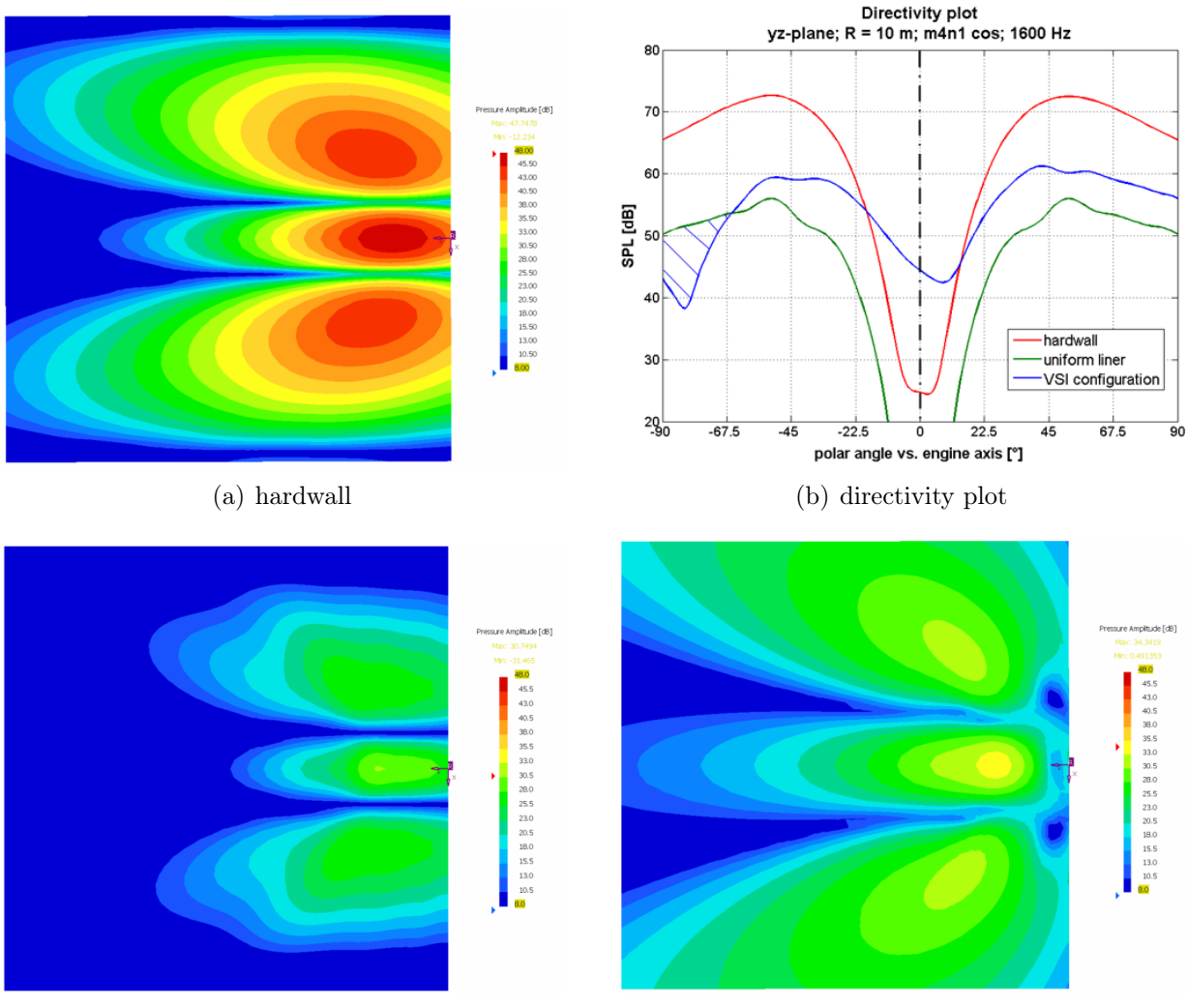

(a) hardwall (b) directivity plot

(c) uniform liner (d) VSI configuration

Figure 5.21: Comparison of sound pressure distributions (magnitude) on forward ground plane and directivity plot; (4/1); 1600 Hz

It can be seen that the radiation is strongly reduced by the uniform liner by ≈ 17 dB at the peak value. Even if a tilt in the directivity characteristic could be achieved in the VSI configuration, which yields in the extremely steep sector (between -90°and -65°) an advantage for this configuration, overall higher sound pressure levels are observed in the remaining part of the lower forward sector in parallel with an increase in the size of the footprint. This larger affected area as well counteracts the distance effect on the SPL in the power calculation.

Because of this, instead of comparing the radiated power through the ground plane, the maximum SPL on the ground will be regarded in the following. This quantity is of significant importance in the calculation of the effective perceived noise level (EPNL), a measure for the noise perceived by an observer on the ground (compare chapter 2.2.3). Figure 5.22, presents the corresponding results for the maximum SPL on the ground plane.

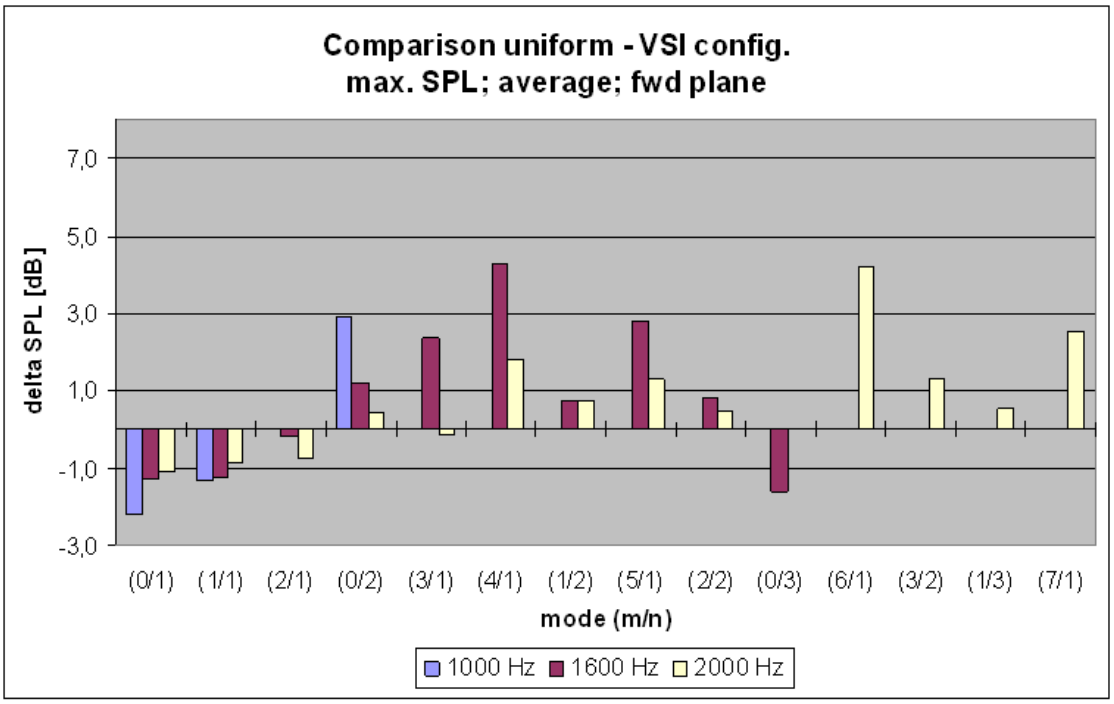

Figure 5.22: Maximum SPL results on forward ground plane; average of cos/sin modes

They show slightly better results for the VSI configuration, especially for mode (0/3) at 1600 Hz (-1.6 dB compared to only -0.4 dB in PWL) which can be attributed to the avoidance of the above observed effect of an increase in the footprint size for the tilted lobes.

Even if quite illustrative to picture the noise footprint of a certain mode and lining configuration, the ground plane defined in figure 5.17 covers quite a large angular sector (both laterally and to the front). Accordingly, apart from the distance effect mentioned above, no advantages of the VSI configuration could be expected. More precisely, none of the angular deflections by the non-uniform liner causes a lobe to be shifted completely (or at least partly) out of this reference plane, which would yield a considerable positive effect on the radiated power value.

Hence, in the following, the reference area will be confined to a certain sector of the forward hemisphere which is most relevant for community noise: from 40° below the duct axis to the vertical axis [-40°; -90°] (resulting from analyses within the SILENCER project and reported e. g. by Montétagaud [132]). This reference sector is depicted in figure 5.23 together with the cylindrical duct geometry at a distance of 10 m ($= 20 \cdot D$) to illustrate the proportions.

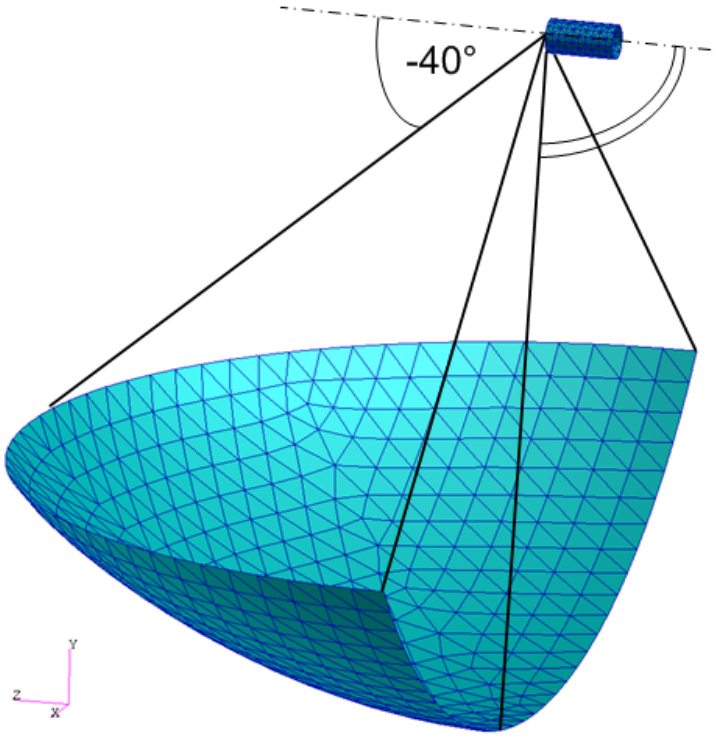

Figure 5.23: Reference sector of forward hemisphere [-40°; -90°]

In the following figures, the corresponding results for power radiated through this reference sector are presented - as before,in all cases with respect to the uniform liner configuration. In detail, figure 5.24 shows the individual results for the cos- and sin- modes, which differ from each other except for the axisymmetric modes ($m = 0$), and figure 5.25 represents the averaged results of both mode shapes, which will be used to compare with the spinning mode results later on.

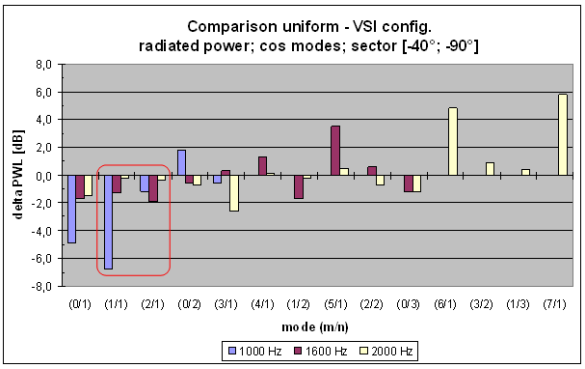

(a) cos modes

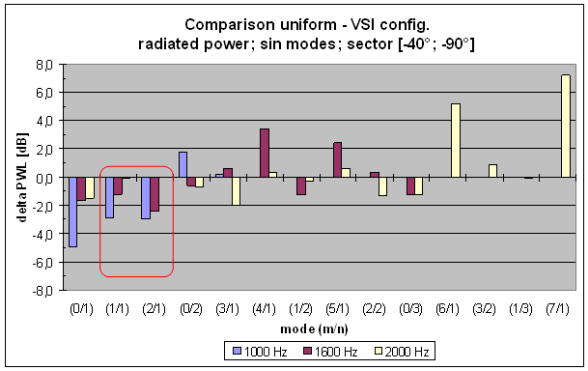

(b) sin modes

Figure 5.24: Power results in sector [-40°; -90°]; cos ↔ sin modes

The first observation concerning figure 5.24 is that the results of the two basic mode shapes differ noticeably, especially for modes (1/1) and (2/1). This is related to the effect of the non-uniform liner upon the individual modal maxima, and their overall impact on the radiated power. However, this characteristic will be removed automatically, when spinning modes will be regarded in the following.

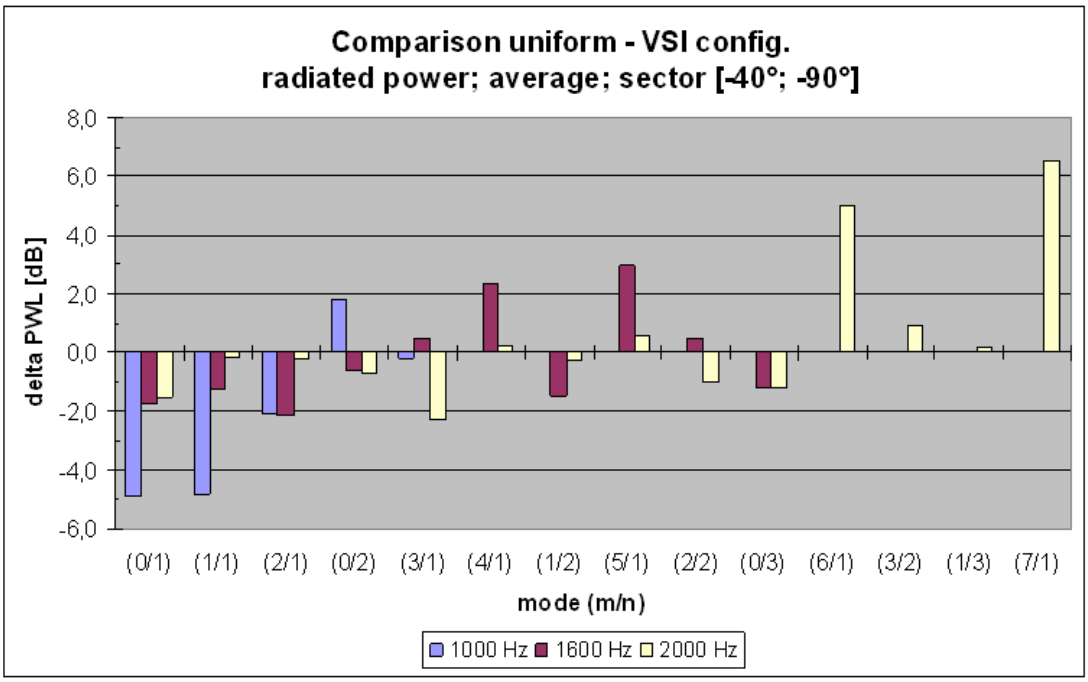

Figure 5.25: Power results in sector [-40°; -90°]; average of cos/sin modes

Comparing the averaged results in figure 5.25 to the ones for the forward ground plane (figure 5.18), the former ones look much more promising: the power reduction for the low order modes is enhanced (e. g. from -2.0 dB up to -4.9 dB for mode (0/1), and even from -1.2 dB to -4.9 dB for mode (1/1)), additionally several other modes yield reductions of between 1 dB and 2 dB compared to the uniform liner. Only for the higher order azimuthal modes, the VSI configuration loses performance due to the increasing effectiveness of the absorptive liner (as explained above).

This overall improvement might be explained by the fact that for the smaller reference sector, the non-uniform liner causes several lobes of radiation to be shifted (at least partly) out of it. An example of this effect is given in figure 5.26, which illustrates the advantage of the VSI configuration with respect to sound radiation towards the ground by plotting the two modal solutions of order (2/1) at 1600 Hz side by side for the uniform and VSI liner configurations (the remaining area of the forward hemisphere has been grayed out in the figure).

From this figure, it becomes comprehensible why for this mode the sin- shape yields the higher power reduction (-2.4 dB compared to -1.9 dB for the cos- shape): by the VSI effect, both radiation lobes directed towards the ground have been shifted upwards, and thus farther away from the reference sector, even if the peak levels at the maxima are slightly higher than for the uniform liner. This explains the differences between both mode shapes observed in figure 5.24.

In summary, the reduction of the reference area concerning the power calculation to the sector most relevant for community noise ([-40°; -90°]) disclosed the potential of the VSI liner configuration: Compared to a conventional uniform absorptive liner, the VSI liner becomes more efficient especially for the lower order (well cut-on) azimuthal modes and a number of radial modes, but loses performance for the higher order (barely cut-on) azimuthal modes.

These tendencies will be studied for the case of spinning modes as well as additional types of sound fields in the following.

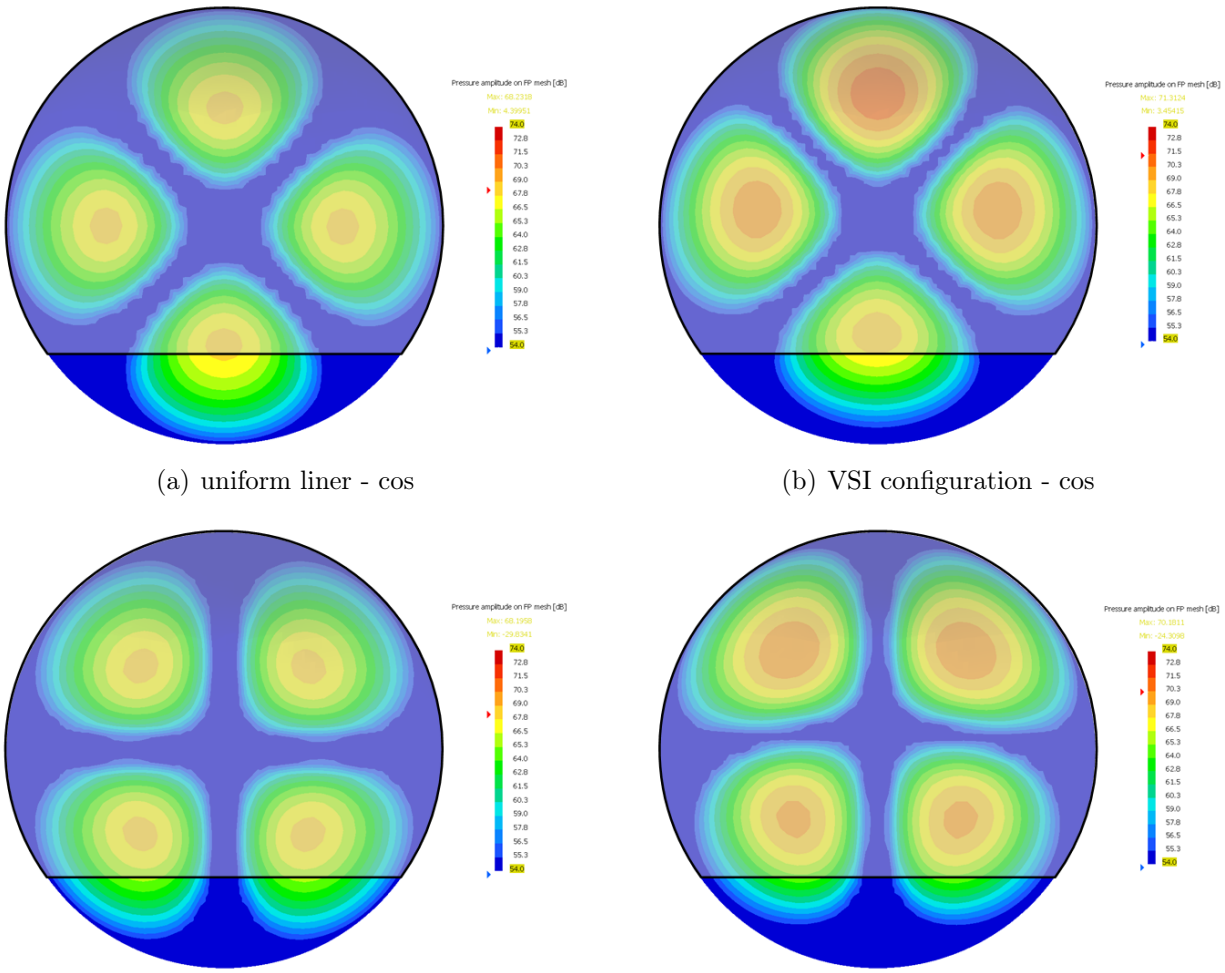

(a) uniform liner - cos

(b) VSI configuration - cos

(c) uniform liner - sin

(d) VSI configuration - sin

Figure 5.26: Comparison of sound pressure distributions (magnitude) on forward hemisphere (R = 10 m); (2/1) cos ↔ sin; 1600 Hz

5.3.2 Spinning modes

In general, apart from small variations, the power results for the spinning modes are very similar to the results for the non-spinning (cos/sin) modes, if the average of these two basic mode shapes is regarded (compare figure 5.27). This outcome could have been expected bearing in mind the results of the directivity comparison in the previous section (where at least the vertical directivity of the spinning modes turned out to be exactly equal to the one of the non-spinning modes).

With respect to the forward ground plane, only for mode (1/1) at 1000 Hz, a larger deviation between both results can be observed, where the spinning mode yields only an advantage of the VSI configuration of -0.8 dB compared to -1.2 dB of the averaged cos-/ sin- modes. This has been observed similarly but with a slightly increased variation for the smaller reference sector.

This deviation can be explained considering figure 5.16, which plots the corresponding radiation pattern on the forward hemisphere for both types of modes. Due to the lateral deflection of the spinning mode, part of the positive effect of the VSI configuration is lost. This is more pronounced at the low frequencies (implying a larger propagation angle) and affects the lowest order azimuthal mode (1/1) the most. Accordingly, the differences between the two types of modes remain below 0.1 dB at 2000 Hz.

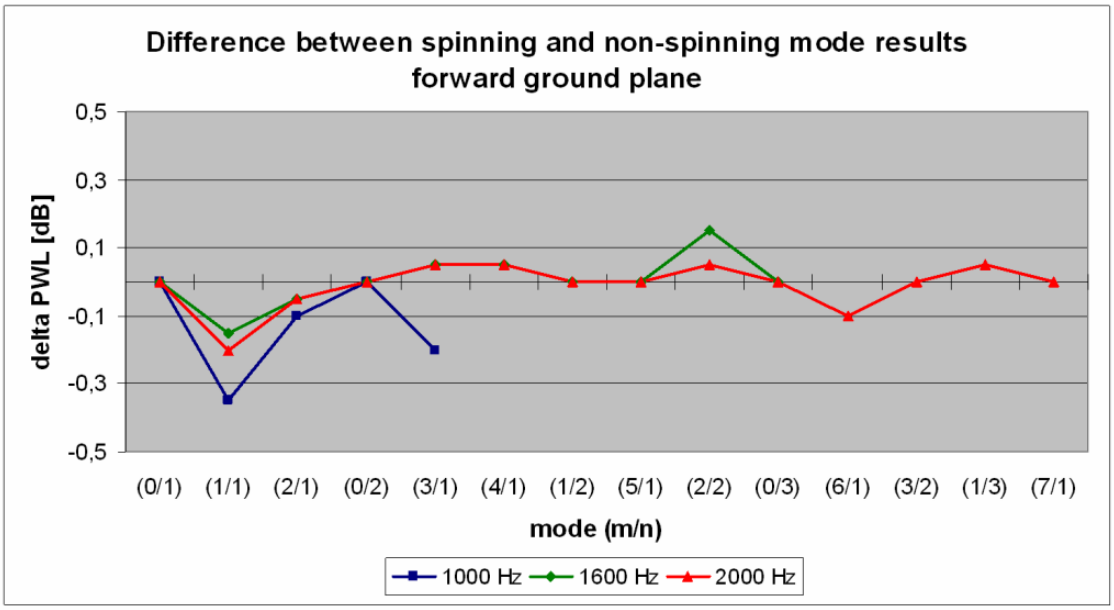

Figure 5.27: Comparison of power results on forward ground plane; spinning ↔ non-spinning modes

Altogether, the overall results show a good correlation of both types of modes, which justify the procedure starting with the next section of considering only the spinning modes.

5.3.3 Broadband noise field

In addition to the single mode excitation considered up to this point, a modal mix of all propagating modes (at the respective frequency) will be evaluated in the following. This is equivalent to a broadband noise source, a commonly used assumption in case the BPF tones are cut-off (as achieved e. g. by a 1BPF cut-off design, compare chapter 2.2.2). Furthermore, it simplifies the comparison of the different liner configurations by regarding only one characteristic value instead of a list of single mode attenuations. Additionally, it overcomes the deficiency of the average attenuation value presented in chapter 4.3.3 of not taking into account the individual power level of each mode. The latter results in a reference value which does not reflect the relative efficiency of the liners dependent on the modal order (or, for the uniform liner, the conveniently used cut-off ratio). Thus, barely cut-on (low cut-off ratio) azimuthal modes which are very efficiently attenuated by the liner, strongly influence the average attenuation and might lead to a misinterpretation of the results.

In contrast, if the overall or average power over all modes is computed, which includes the relative weighting of the modes by their power level, these modes do not have a large contribution in the lined duct cases. Thus, misleading results will be avoided, and a comparison of the effectiveness of the different liner types is made possible.

Therefore, the computed data will be recombined in two different ways to yield average or overall radiated power values for each configuration:

- a broadband noise field (achieved by computing the rms-value over all propagating modes excited with equal modal energy) [figure 5.28(a)],
- a combination of a broadband noise field and a single protruding mode (the single mode being the highest propagating azimuthal mode separated by 20 dB from the broadband component) [figure 5.28(b)].

The first recombination corresponds to the above mentioned reference value taking into account the individual modal power level, and will be used in the following to evaluate the overall performance of a liner configuration. The second one is modified by adding a single dominant mode of high azimuthal order to the broadband noise field. It reflects the application case of e. g. the rotor alone tone at takeoff which clearly sticks out of the background broadband noise field (as described in chapter 2.2).

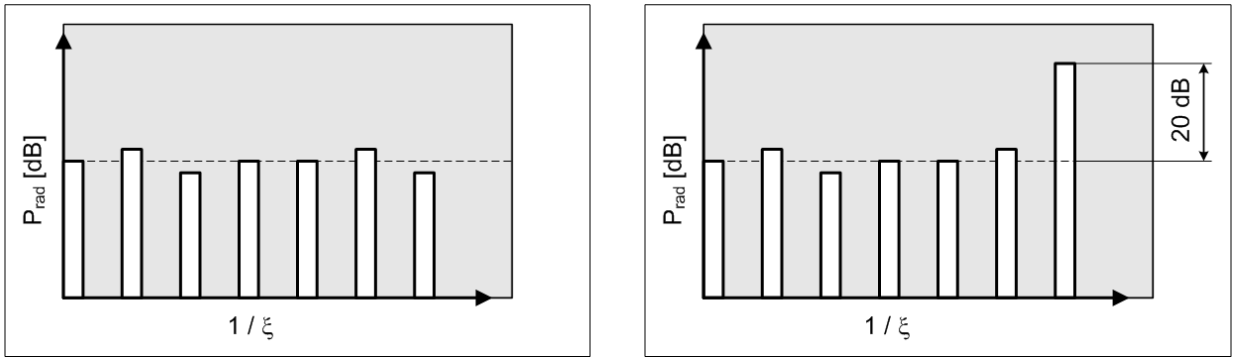

(a) broadband noise field (b) broadband noise field + single mode

Figure 5.28: Sketch of broadband modal noise fields

As the figure indicates, the individual modes contributing to the broadband noise field may slightly vary in terms of radiated power values (even if all excited at the same PWL) as they imply varying reflection coefficients at the duct exit - even in the hardwall case (for the definition of these coefficients refer to chapter 2.1.1.2). However, the average power level is quite uniform and clearly separated from the single protruding mode in the second excitation case.

5.3.3.1 Average power level / broadband noise field

To obtain the average power level of the broadband modal field, the rms-value of all propagating modes has been computed as follows (similar to the signed rms-value in the previous chapter (equation 4.1))[4]

$$P_{rms} = \sqrt{\frac{\sum_{m,n} {P_{mn}}^2}{N_{modes}}} \; . \tag{5.2}$$

At first, to demonstrate the difference between the average attenuation value and the average (rms-) power level, figure 5.29 shows the results for the radiated power through the forward ground plane at 2000 Hz for the three configurations *hardwall*, *uniform liner*, and *VSI liner*.

On the top left, the 'raw data', i.e. the radiated power onto the ground plane for each mode has been plotted for the three configurations. From this, it becomes obvious that, apart from small variations for the lower order azimuthal and radial modes, the power level drops considerably for the higher order azimuthal modes for both lined duct cases. Additionally, the superior performance of the uniform liner for these modes becomes apparent. This is also reflected in the attenuation (left) and average attenuation (right) plots in the lower part of the figure. Accordingly, the VSI liner achieves only -7.7 dB of average attenuation compared to -10.9 dB for the uniform liner.

[4]This calculation has to be performed on a linear scale, only the final results have been translated into the dB scale.

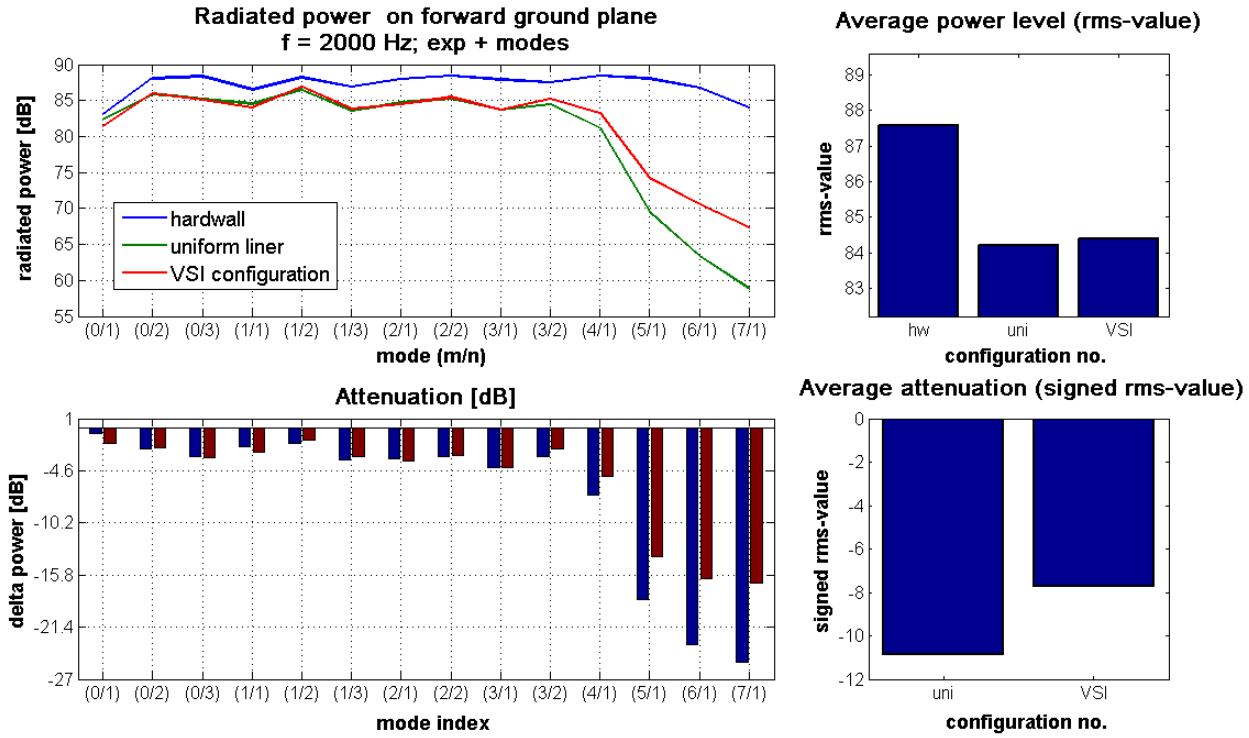

Figure 5.29: Comparison of radiated power results on forward ground plane; 2000 Hz

However, in terms of the average power computed by the procedure described above (equation (5.2)), and plotted in the top right corner of the figure, the uniform liner is superior by only 0.2 dB ($P_{rms,uni}$ = 84.2 dB compared to $P_{rms,VSI}$ = 84.4 dB). This demonstrates the meaningful effect of the power level weighting. In result, the VSI configuration yields nearly the same effect on the broadband sound field at this frequency as the uniform liner, which seemed to be clearly superior considering the results depicted in figure 5.18 (comparing only the single mode results).

In the following, all results (on the ground plane and in the reference sector) will be summarized in terms of the rms-value of the radiated power. To start, the corresponding results on the ground plane are plotted in figure 5.30, which compares the values of the three configurations at all three frequencies.

As can be seen, the results of the uniform liner and the VSI configuration reside at nearly exactly the same level. In detail, the uniform liner yields a slightly lower average power level at 1000 Hz and 2000 Hz (in both cases -0.2 dB), at 1600 Hz both configurations perform equally well. Compared to the hardwall reference case, both lined configurations achieve between 3.5 dB and 4.0 dB attenuation.

With respect to the reference sector chosen to be most important concerning the radiation towards the ground ([-40°; -90°]), figure 5.31 summarizes the corresponding results. For this sector, the results show a slight advantage of the uniform liner at 1000 Hz (-0.3 dB), but lower power levels for the VSI configuration at the other two frequencies (-0.6 dB at 1600 Hz and -0.2 dB at 2000 Hz). Overall, the lined configurations yield between 6.0 dB and 7.0 dB attenuation with respect to the hardwall case.

In summary, it can be stated that the weaker performance of the VSI configuration for the higher order azimuthal modes, which has been observed in the previous section of this chapter, does not cause a considerable negative effect on the average radiated power or an equipartitioned (in terms of energy) modal mix. If the (relatively large) ground plane is used as a reference, the levels of the uniform and the VSI liner nearly match. Considering

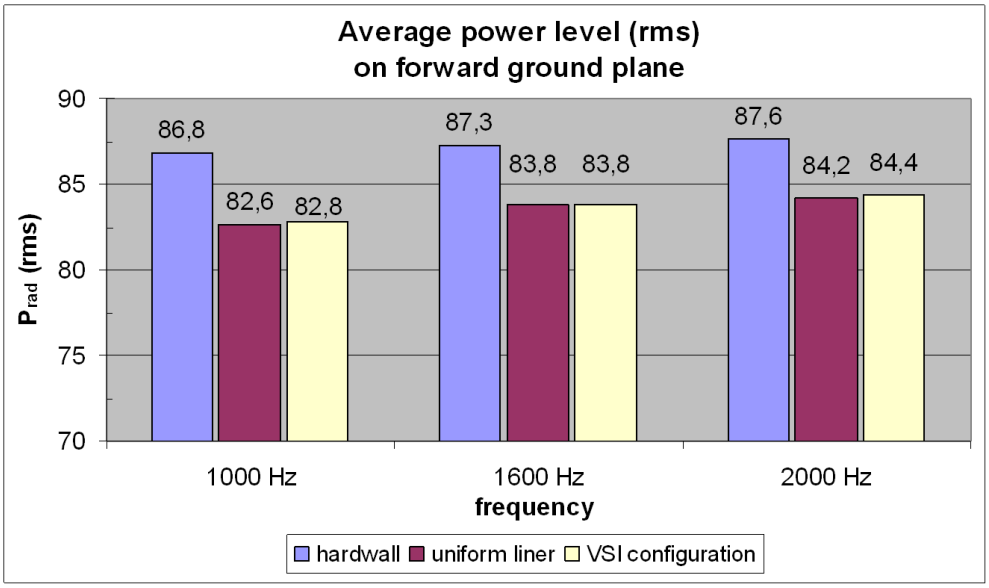

Figure 5.30: Comparison of average radiated power on forward ground plane

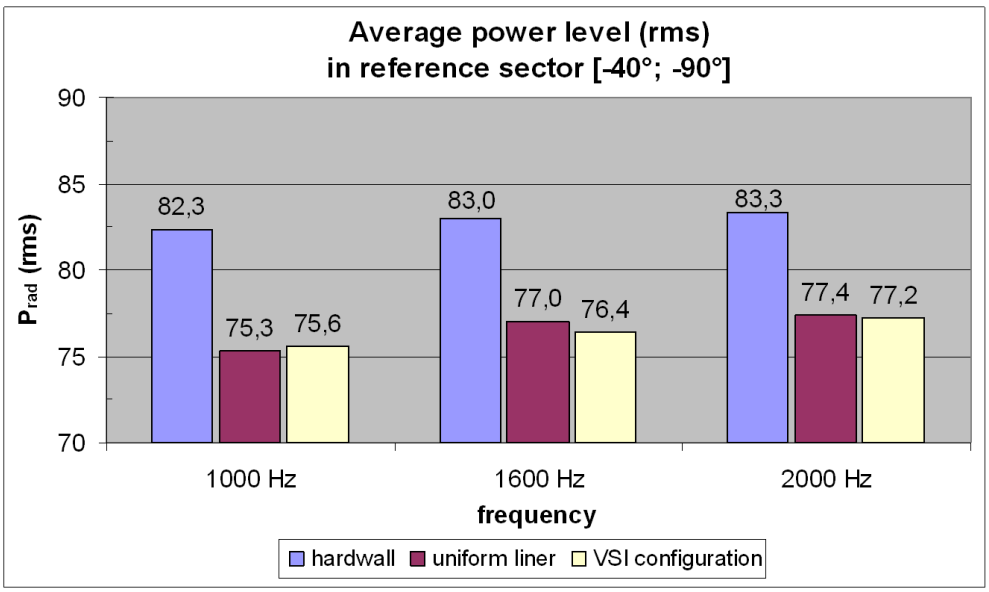

Figure 5.31: Comparison of average radiated power in reference sector [-40°; -90°]

only the radiation sector directed towards the ground, the VSI configuration even yields an advantage compared to the uniform liner in two out of three frequencies.

5.3.3.2 Single protruding mode + broadband component

For this case, the hardwall power values of all modes - except for the highest propagating azimuthal mode - have been reduced by 20 dB (corresponding to the optimization of the liner for a single dominant mode). Finally, the individual values have been summed up, and the result of the protruding mode affected by the corresponding liner has been added

$$P_{BB+mode} = \left(\sum_{\substack{n=1 \\ m=0}}^{\substack{m=m_{max}-1 \\ n=n_{max}}} P_{m,n\,|\,hw} - 20\ \mathrm{dB} \right) + P_{m_{max},1\,|\,lined}\ . \tag{5.3}$$

In table 5.2, the cut-off ratios of the three chosen protruding modes are listed to point out that these are all quite close to the cut-off limit (as is the rotor alone tone at takeoff). This ensures steep propagation and radiation angles and, hence, an efficient absorptive liner performance.

Table 5.2: Cut-off ratios of the protruding modes

frequency [Hz]	mode (m/n)	cut-off ratio (ξ)
1000	(3/1)	1.0996
1600	(5/1)	1.1522
2000	(7/1)	1.0772

In the following figures (figures 5.32 and 5.33), the results of the two liner configurations (and the hardwall reference case) are compared to each other for this kind of input sound field. To estimate the level of protrusion of the single mode from the broadband component, the total power of the broadband component has been added for reference.

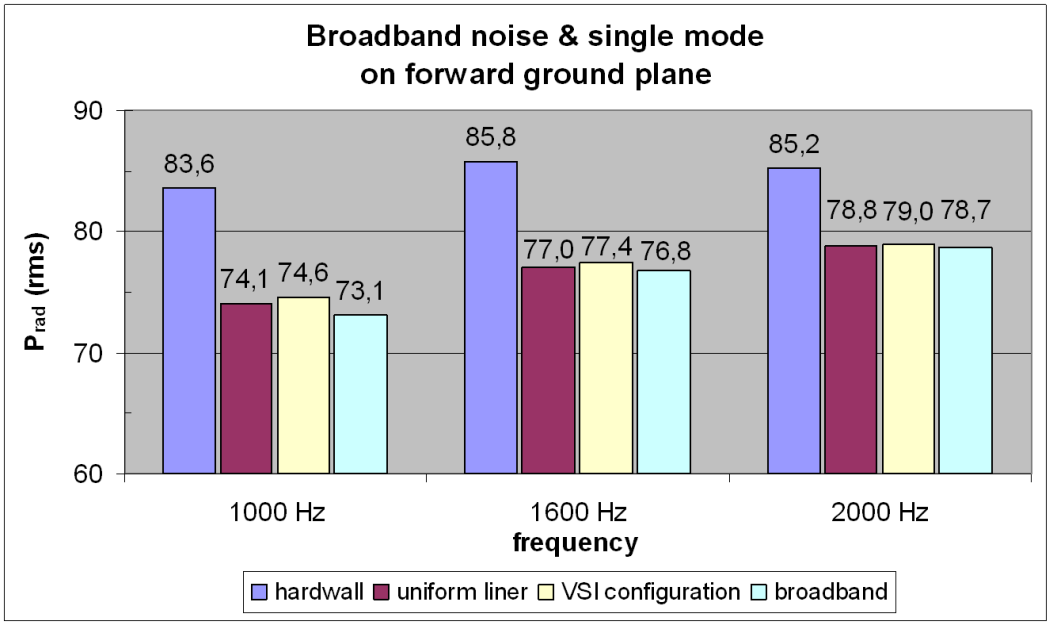

Figure 5.32: Comparison of overall radiated power (broadband + single mode) on forward ground plane

With respect to the forward ground plane, it can be seen in the hardwall case how the single mode clearly raises the radiated power level from the broadband reference (by up to 10 dB at 1000 Hz). Compared to that, the lined duct configurations do not clearly protrude from the overall power of the broadband component (for the uniform liner by 1 dB at 1000 Hz), but are nearly at the same level at the higher frequencies.[5] Relative to each other, the VSI configuration yields slightly higher power levels, however, with a decreasing difference towards the higher frequencies (+0.5 dB at 1000 Hz, but only +0.2 dB at 2000 Hz).

[5]However, note that in this case the radiated power of a single mode (the highest propagating azimuthal mode) has been compared to the summation of power of all other modes contributing to the broadband component.

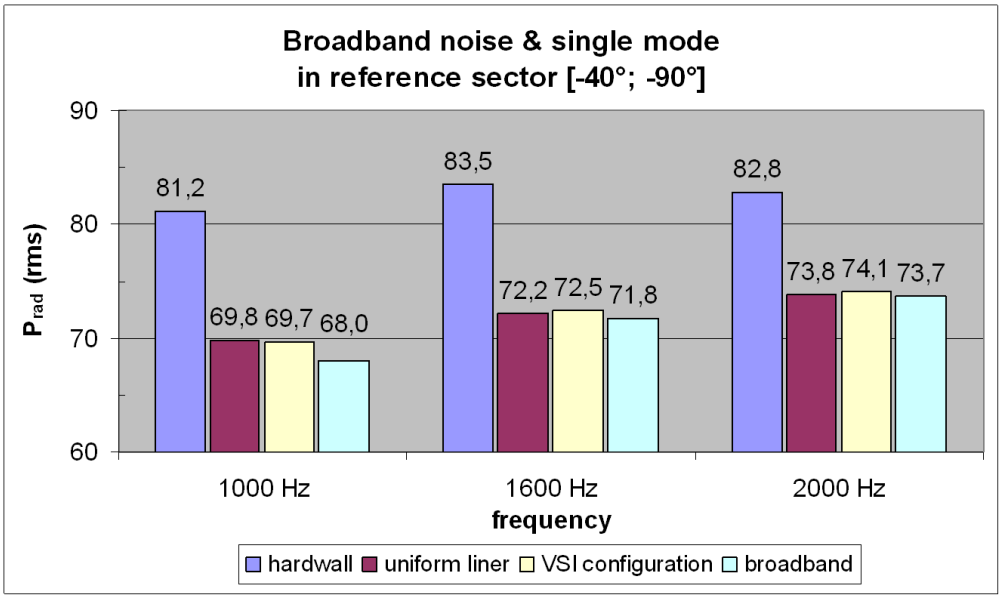

Figure 5.33: Comparison of overall radiated power (broadband + single mode) in reference sector [-40°; -90°]

For the reference sector ([-40°; -90°]), similar tendencies can be observed. As well, the protrusion of the single mode diminishes with an increasing frequency (and in parallel increasing number of modes) for the lined configurations. Concerning the performance of the two liner types, the VSI configuration even yields a slightly lower power level at 1000 Hz (-0.1 dB), and slightly higher results at the other two frequencies (in both case +0.3 dB).

To conclude, the results show a slightly raised radiated power level for the VSI configuration in most cases observed (in the range of 0.3 dB on the overall power). However, it has to be noted that this kind of sound field represents the *worst case scenario* for the VSI configuration, and quite a favorable application case for the uniform liner. Due to the high azimuthal mode order of the single protruding mode, and the corresponding steep propagation angle, the uniform liner performs very efficiently. On the other hand, the VSI liner is most efficient for the lower order azimuthal modes and the higher order radial modes, and falls behind the uniform liner for the modes chosen to be the dominant ones in this type of sound field, where the maximization of absorptive area dominates over the redirection effect.

5.4 Detailed investigation of VSI effect

In this section, the physical effect of the non-uniform liner segment inside the duct inlet on different radial mode orders will be pictured and described in greater detail. This should serve to clarify the influence upon the individual radial components, and to explain the large differences in the performance observed in the previous chapter and sections for different radial mode orders. Up to now, the odd radial mode orders ($n = 1, 3$) showed quite a promising potential for the VSI configuration, but the even radial orders ($n = 2$) revealed negative effects in several cases.

To understand these phenomena, the first three radial mode orders of the axisymmetric mode $m = 0$ have been analyzed at a frequency of 2000 Hz using a very fine FP mesh located at the vertical duct midplane to resolve the modal patterns. At first, mode (0/1) (the plane wave mode) will be analyzed. The resulting pressure fields are opposed to each other in figure 5.34 (the insets show the radiation patterns on the forward hemisphere) together with the corresponding directivity plot.

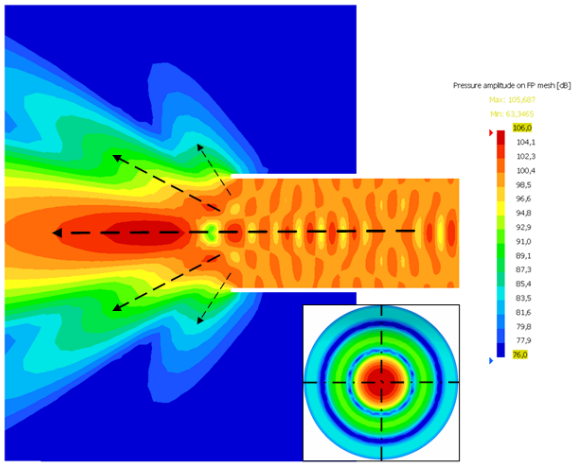

(a) hardwall

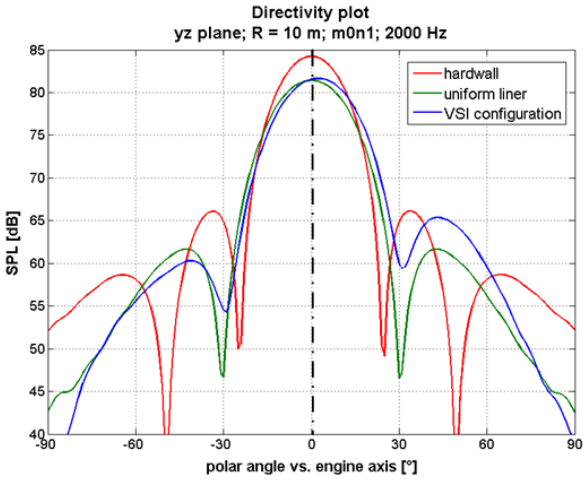

(b) directivity plot

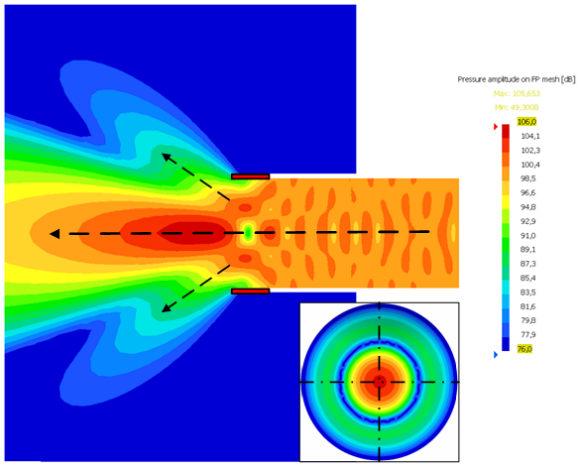

(c) uniform liner

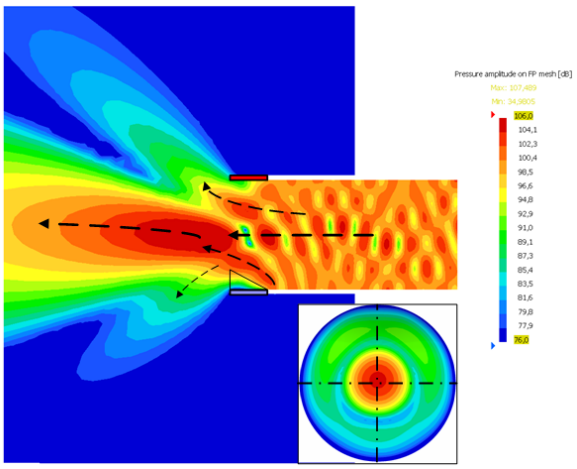

(d) VSI configuration

Figure 5.34: Comparison of radiation characteristics on vertical duct midplane and directivity plot; (0/1); 2000 Hz; pressure amplitude

In the hardwall case (figure 5.34(a)), the pressure field inside the duct is not perfectly uniform (as should be expected for the plane wave in idealized conditions), but slightly disturbed by reflections from the inlet inducing standing wave components and the participation of higher radial mode orders, as already explained in chapter 5.2. The resulting radiation characteristic consists of the main lobe radiated axially and two radial side lobes at reduced peak levels (as two higher radials are cut-on at this frequency).

For a uniform absorptive liner - as indicated in figure 5.34(c) - the pressure pattern inside the duct and the corresponding radiation pattern show the typical behavior for this type of liner: the modal energy propagating at the duct wall is effectively attenuated by the liner and, hence, only one side lobe can be observed radiating at an angle of $\approx \pm 40°$ to the duct axis (compare also the directivity plot in figure 5.34(b)). Additionally, the peak level of the main lobe has been reduced by 2.8 dB. Thus, in summary, the uniform liner is most effective for modes or modal components propagating at (or close to) the duct wall and, in result, tends to focus the radiation on the duct axis. Overall, the noise reduction compared to the hardwall configuration amounts to -0.6 dB on the ground plane and -1.4 dB in the reference sector [-40°; -90°].

In the VSI configuration involving the non-uniform liner, quite a different propagation and radiation characteristic can be observed in figure 5.34(d). Again, the position of the liner

segments is indicated in the picture (red: absorptive; blue: reflective liner segment). The reflective liner strip seems to act like a wedge or ramp (as suggested in the figure) deflecting the energy propagating close to the lower wall. This deflection influences the whole radial energy distribution and results in an articulately modified radiation pattern: the main lobe is shifted into the upper sector at a slightly higher peak level, and the side lobes are affected asymmetrically yielding the characteristic 'tilt' of the directivity curve. Due to the deflection at the lower duct wall, only a reduced part of the energy is radiated towards the ground (-1.4 dB with respect to the uniform liner at the peak of the lower side lobe). In results, this configuration yields an attenuation of -1.7 dB at the ground and -2.9 dB in the reference sector compared to the hardwall case, which is 1.1 dB and 1.5 dB, respectively, higher than for the uniform liner.

Interesting are, as well, the changes in the modal structure behind the liner compared to the hardwall and the uniform liner case. They are due to an increased level of reflections at the impedance discontinuity and a resulting different modal composition, which will be studied in the following section.

Observing the second example, the first radial mode (0/2), the radiation patterns presented in figure 5.35 result for the three different configurations.

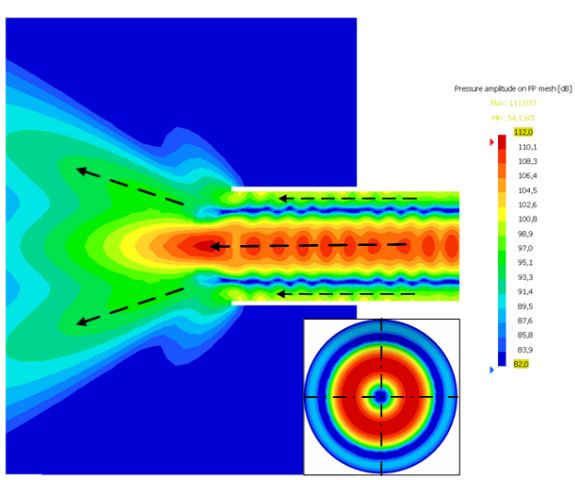

(a) hardwall

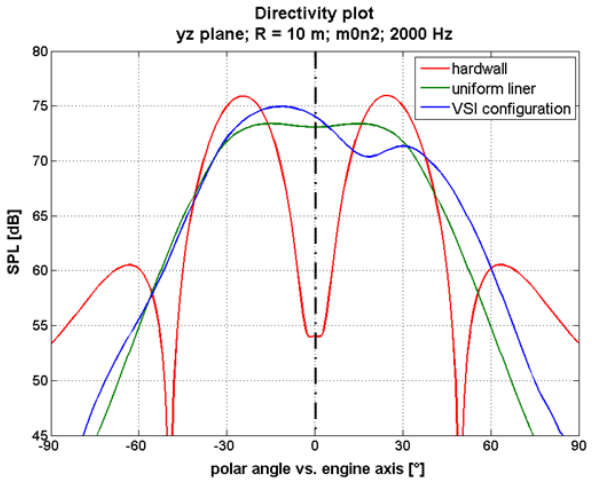

(b) directivity plot

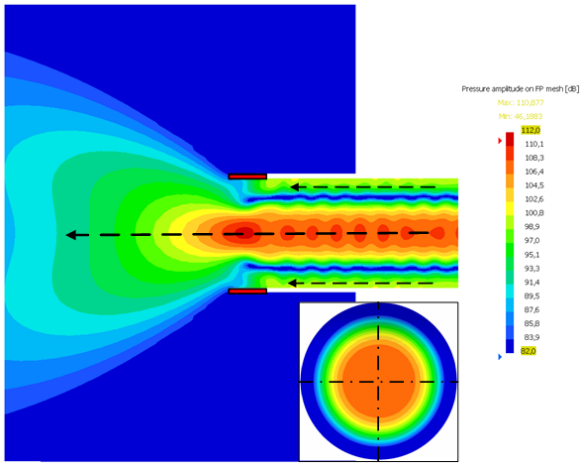

(c) uniform liner

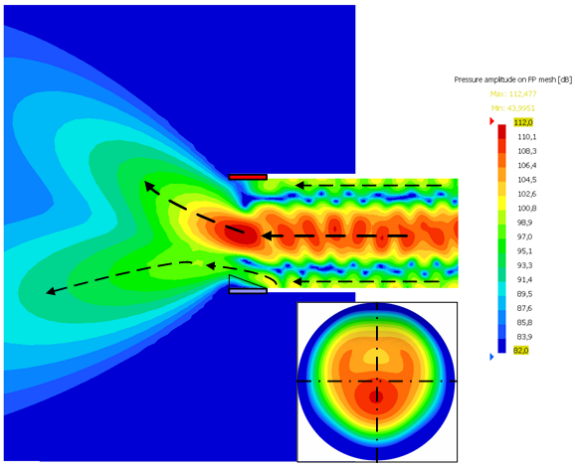

(d) VSI configuration

Figure 5.35: Comparison of radiation characteristics on vertical duct midplane and directivity plot; (0/2); 2000 Hz; pressure amplitude

On the top left, the hardwall case with the typical radial energy distribution inside the duct shows a concentric circular main lobe at an angle of $\approx \pm 25°$, which results from diffraction effects at the duct exit. By means of the uniform liner (figure 5.35(c)), the outer radial components are strongly attenuated. The axially centered component, rather unaffected by the liner, thus represents the main contribution radiating to the far field with a broad central maximum 2.5 dB below the peak level of the hardwall solution. The corresponding noise reductions both on the ground and in the reference sector ([-40°; -90°]) with respect to the hardwall configuration yield -2.2 dB.

The VSI configuration (figure 5.35(d)) shows, as for the plane wave mode, a deflection of the energy propagating close to the wall, which influences as well the main component centered at the axis. The upper part of the outer radial component has been attenuated by the absorptive liner patch in the upper duct half. Thus, at the duct exit, both the deflected lower radial component and the central lobe are diffracted yielding two asymmetrical maxima in the vertical direction: one with the peak at $\approx -10°$ and one at $\approx +30°$ at a lower pressure level. However, even if this lower maximum has been shifted to a higher angle compared to the hardwall (and uniform liner) case, the higher peak level produces a weaker noise reduction on the ground than in the uniform liner configuration (-2.1 dB, i.e. a 0.1 dB lower attenuation). On the contrary, considering the reference sector ([-40°; -90°]), the VSI configuration outperforms the uniform liner with respect to attenuation by 0.6 dB.

At last, the second radial mode (0/3) will be analyzed. The hardwall case shows a main lobe at $\approx \pm 50°$ and a weak inner side lobe at $\approx \pm 15°$ (compare figure 5.36(a) and 5.36(b)). As in the previous examples,the uniform liner tends to focus the radiation on the axis (figure 5.36(c)). The outer radial (main) lobe is shifted closer to the center line (by $\approx 12°$) and the two inner radial lobes have been combined to a single central maximum (with an even 3 dB higher peak level than the outer one). This leads to power reductions of -3.1 dB at the ground and -5.7 dB in the reference sector.

In the VSI configuration, again, all lobes are deflected at the reflective liner location (compare figure 5.36(d)). In result, the lower part of the first radial component leaves the duct nearly axially, whereas in the uniform liner configuration, it radiates at an angle of $\approx$ -30°. The main contribution to the radiation towards the ground originates from the second radial component (considerably weaker in terms of sound pressure level) at an angle approximately equal to the angle of the first radial component in the uniform liner case (compare figure 5.36(c)). This results in a slightly enhanced noise reduction on the ground (-0.1 dB) and in the reference sector (-1.2 dB) compared to the uniform liner configuration, in which the second radial component has been almost eliminated, but the first radial one remained nearly unaffected.

In summary, the performance of the VSI configuration, involving a combination of both a semi-circular absorptive and reflective liner segment, depends strongly upon the radial mode order or radial energy distribution inside the duct. In contrast to the uniform absorptive liner which attenuates, by default, mainly the energy propagating at the duct wall and tends to focus the radiation on the axis, all radial components are affected. This is induced by the change in the boundary condition at the reflective liner location, where the conditions with respect to sound pressure level and particle velocity are (in the idealized case of an impedance equal to zero) exactly reversed with respect to the hardwall case (compare figure 2.15 in the theory section).

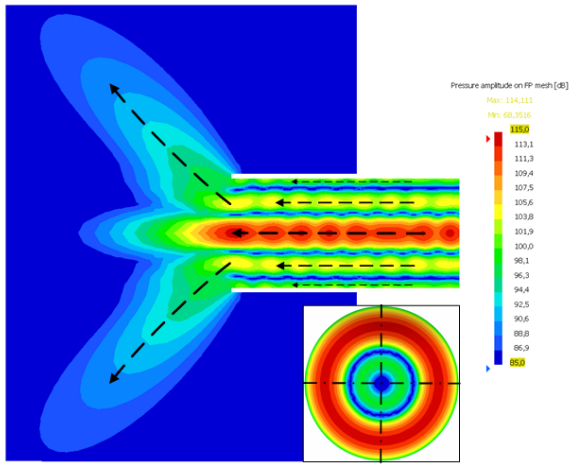

(a) hardwall

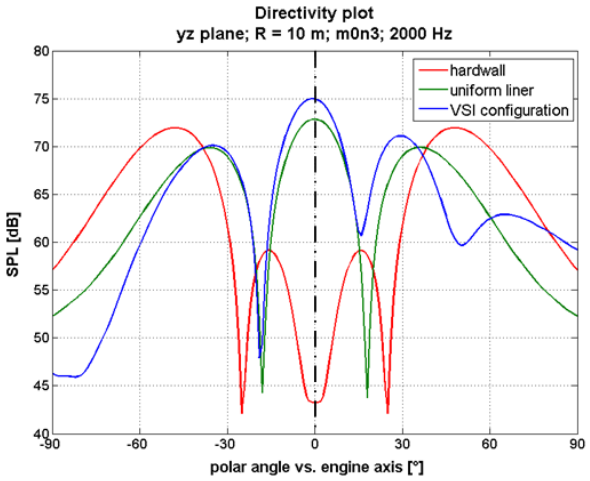

(b) directivity plot

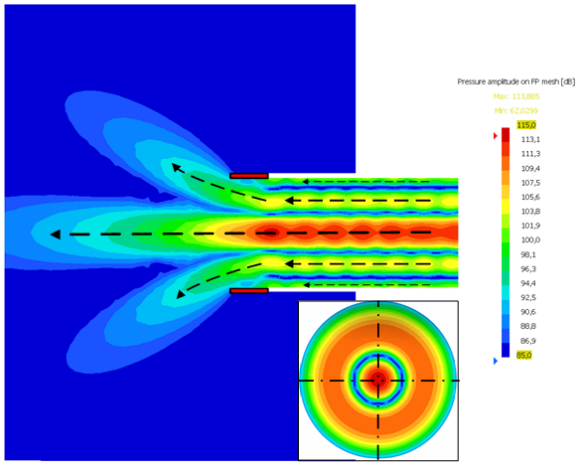

(c) uniform liner

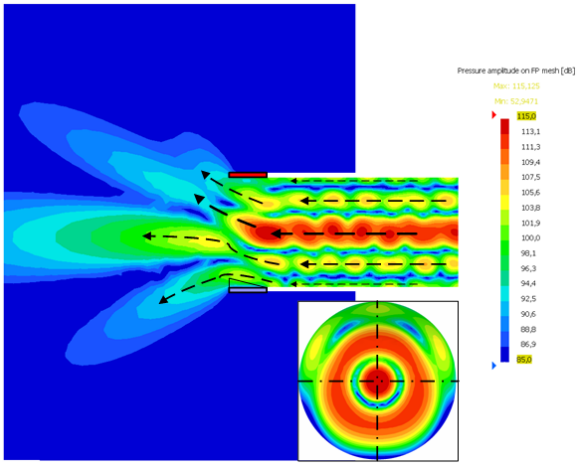

(d) VSI configuration

Figure 5.36: Comparison of radiation characteristics on vertical duct midplane and directivity plot; (0/3); 2000 Hz; pressure amplitude

Generally speaking, the VSI effect may be described as a change in the propagation and the resulting radiation angle at the same energy level. This yields a considerable noise reduction in a corresponding reference sector (e. g. directed towards the ground). However, whether its performance is superior to the one of a uniform absorptive liner, depends upon several other factors as e. g. the cut-off ratio and the radial mode order.

In addition, the resulting radiation patterns reveal a possibility for improvement in cases where the resulting global maximum has been shifted into the lower sector (compare figures 5.35(d) and 5.36(d)), or in the case of spinning modes, where the pressure maximum has been shifted laterally (as observed and mentioned e. g. in the description of figure 5.16(d)). By a suitable positioning of the reflective liner segment on the circumference of the inner duct wall, additional noise reductions in the reference sector should be expected. This expectation justifies a corresponding optimization study to be presented in section 5.6.

5.5 Modal scattering effects

The concept of a modal analysis of the propagating or radiated pressure field, which has been already used in chapter 3, will be applied to the different lining configurations in the following.

However, as has been noted before, the decomposition into orthogonal modes is not physically correct for this specific type of a non-uniform lining. This is related to the asymmetry of the pressure field behind the VSI liner which contradicts the basic assumption of an axisymmetry or at least a periodicity of the modal pattern. In contrast, due to the shifting of the boundary condition at the reflective liner location, the modal pattern is shifted within the cross section yielding an asymmetric pressure distribution. Even if a modal decomposition of this type of sound field yields a mathematical result (a corresponding modal amplitude spectrum), it does not reflect the actual input sound field. This can be verified by performing the inverse operation, which does not yield the original pressure distribution.

Yet, as the modal analysis is commonly used in duct acoustic problems, especially in non-uniform lining configurations with respect to the analysis of modal scattering effects, it will be applied as well to the VSI liner cases. Bearing in mind that its results have to be interpreted with caution, it may serve to get an idea of the effects of the VSI configuration on the modal composition.

In contrast to the experimental results analyzed in chapter 3, in this numerical study, virtual microphones (i.e. field points at which the SPL can be 'measured') can be positioned at any desired location in the duct cross section, not only at the duct wall. This simplifies the determination of the mode shapes compared to the configuration generally used in experimental studies involving several axially shifted arrays of wall mounted microphones to separate the radial mode orders (compare figure 5.37).

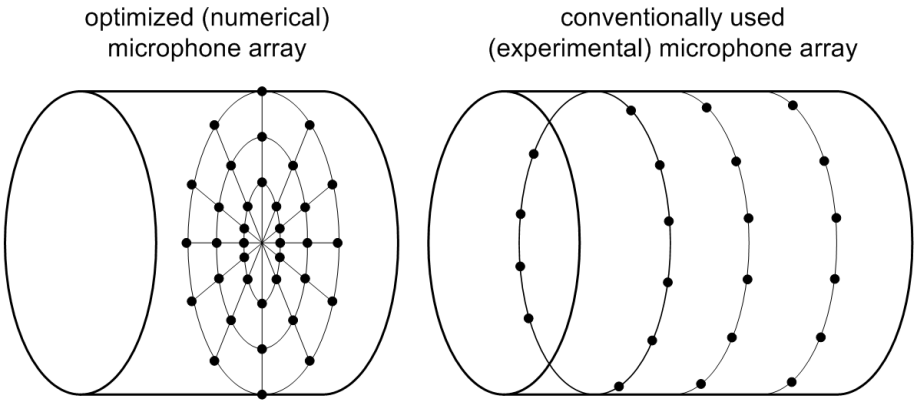

Figure 5.37: Schematic sketch of microphone arrays for modal analysis

Concerning the necessary number of sensors, similar rules to the ones mentioned in the context of designing the MAL test rig have to be accounted for. In detail, the number of circumferential measurement points has to be greater than twice the highest propagating circumferential mode number (compare equation (3.1))

$$N_{mic_{\,\mathrm{circumf}}} \geq 2 \cdot m_{max} + 1 \; . \tag{5.4}$$

Correspondingly, the number of radial measurement positions has to be equal to the maximum radial mode order (in the notation used in this thesis)

$$N_{mic_{\,\mathrm{radial}}} = n_{max} \; . \tag{5.5}$$

Both conditions correspond to the postulation of using a number of sensors at least equal to the number of zero points defined by the nodal lines and circles, respectively, incremented by one. However, for a separation of the axially positively and negatively traveling waves, again, two axial arrays have to be evaluated.

As described in the corresponding section of the MAL chapter (chapter 3.3), at first the transformation matrix T (equation (2.37)) has to be assembled including the axial, radial, and circumferential modal variations of the sound pressure p for all propagating modes. This matrix has then to be inverted by an SVD (Singular Value Decomposition) and multiplied by the vector of 'measured' complex sound pressure values to obtain the vector of modal amplitudes A (as in equation (2.36))

$$[T]^{-1} \cdot \{p\} = \{A\} \, . \tag{5.6}$$

The above described modal analysis has been carried out at a number of axial positions to investigate the effects of the lining configurations on the sound field. An example of the results is depicted in figure 5.38 for mode (0/1) at 1000 Hz and an axial position of $z = -0.50$ m (i.e. midway between the source and exit planes).

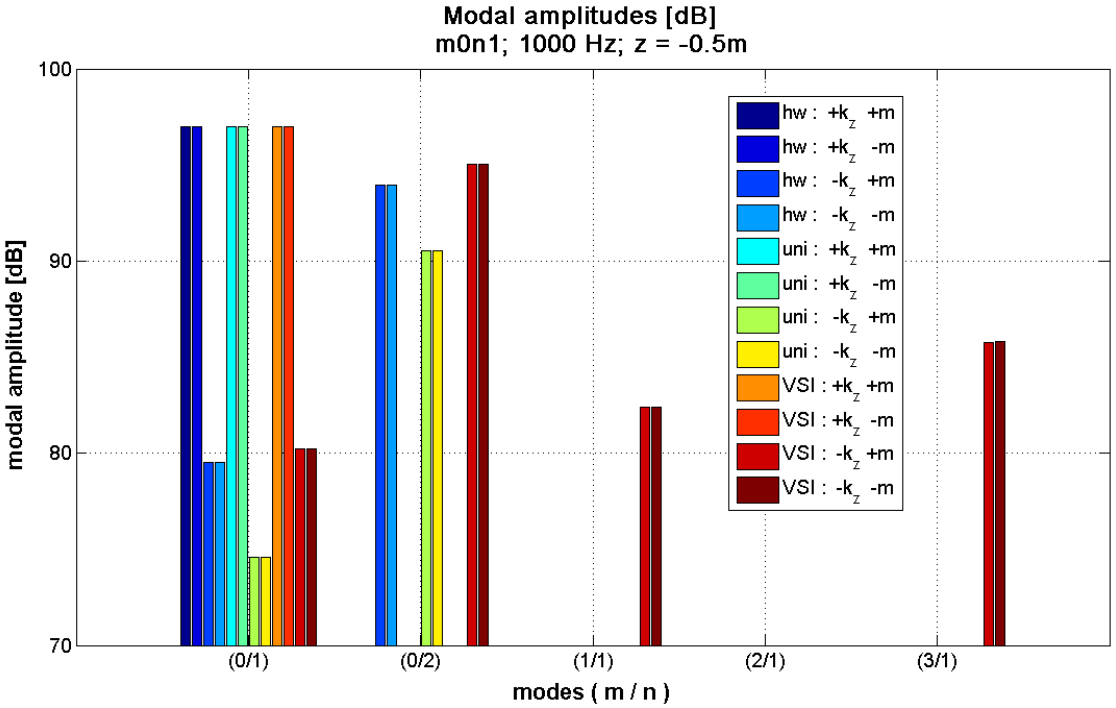

Figure 5.38: Comparison of modal amplitude results; hardwall ↔ uniform ↔ VSI liner; (0/1); 1000 Hz; $z = -0.50$ m

The figure compares the modal amplitude spectra of the three configurations (hardwall, uniform liner, VSI liner), at which for each mode the result consists of four values, i.e. the positive and negative axial and azimuthal directions. However, for the axisymmetric modes ($m = 0$), the amplitudes of the $+m$ and $-m$ modes yield the identical results.

In the hardwall configuration, the excited mode (0/1) shows reflections in terms of the mode itself and the first radial mode (0/2). As has been shown both in the theory section (figure 2.16) and the analysis of the effect of reflections in the first part of this chapter (figure 5.5(a)), a coupling between radial modes of the same azimuthal order may occur even in hardwalled ducts due to the influence of the duct termination. Moreover, as reported by Zorumski [10], lower order radial modes are more likely to be converted into higher order ones. This could explain the higher reflection level of mode (0/2) compared to the primary one.

However, the reason for these different levels might also be the axial variations in the sound pressure distribution due to these reflections and the resulting standing wave components, as clearly visible in figure 5.6. In addition to this, no other modal components are observed in the amplitude spectra, as should be expected. Similarly for the uniform liner configuration: only the primary (excited) mode and reflections of both radial orders are visible, however the latter ones at reduced levels (-5 dB/ -3 dB) compared to the hardwall configuration due to the attenuation by the liner.

In contrast, the VSI liner configuration shows some more contributions in the reflected spectra: additional to the primary modal amplitudes, which range at approximately the same levels as in the hardwall case, the level of the first radial mode is even slightly higher than without any liner (+1 dB). As well, contributions from the modes (1/1) and (3/1) are observed in the reflected spectra. This confirms the higher level of reflections for this non-uniform liner configuration containing as well different azimuthal components, primarily of an odd azimuthal order ($m = 1, 3$).

After passage of the liner section, the modified modal spectra shown in figure 5.39 result from the analysis process at the axial position $z = \pm 0.00$ m.

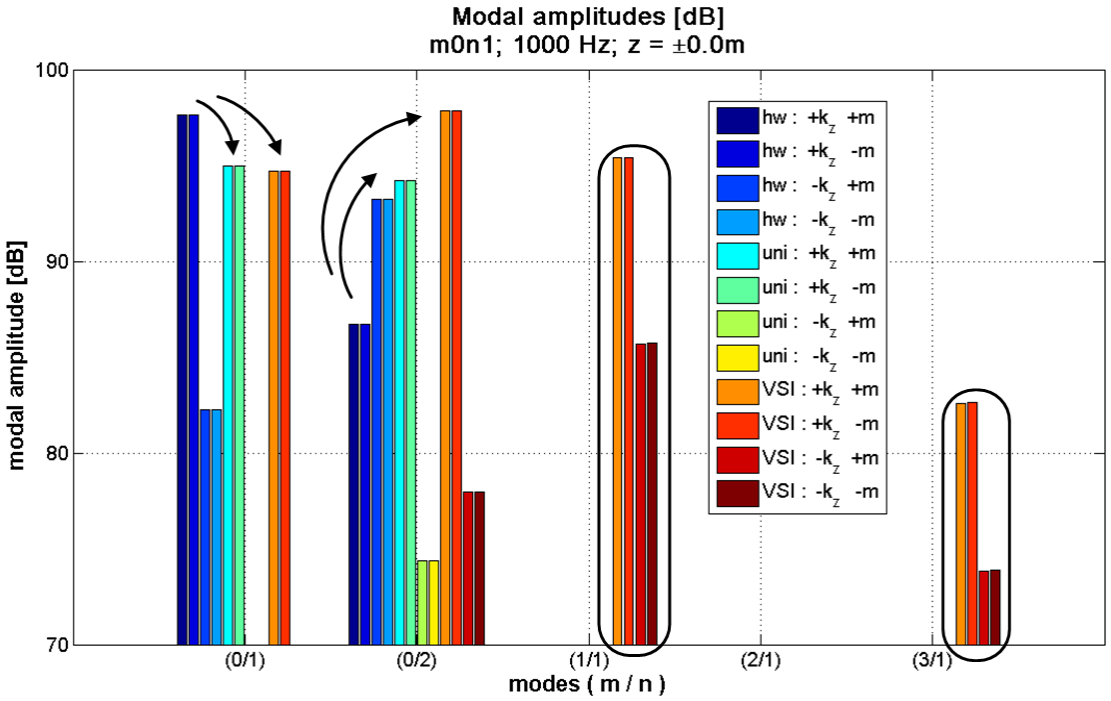

Figure 5.39: Comparison of modal amplitude results; hardwall ↔ uniform ↔ VSI liner; (0/1); 1000 Hz; $z = \pm 0.00$ m

Compared to the previous figure obtained at the rear axial position, it can be seen that also a small first radial contribution is radiated to the far field in the hardwall case (at -11 dB compared to the primary modal amplitude). The uniform liner consistently shows reduced levels for the radiated and reflected primary waves, which result from the absorptive effect of the liner. On the other hand, the increased levels at the first radial originate from the modified pressure distribution in the duct cross section more equivalent to a mode (0/2) (compare figures 5.7(a) and 5.35(c)).

Additional to the approximately equal primary amplitude ($\approx$ 95 dB), the VSI liner configuration contains even stronger contributions from the first radial mode (+3 dB) and the azimuthal modes (1/1) and (3/1), which partially even exceed the level of the fundamental mode. These components are the mathematical results of the asymmetric liner distribution

in this configuration and the resulting directivity exhibiting one maximum shifted into the upper sector. However, as mentioned in the introduction of this section, they do not actually represent the resulting pressure field, and may serve mainly to illustrate the disturbed modal structure.

The second example will be the azimuthal mode (2/1) at 2000 Hz, which also has been studied concerning the directivity in chapter 5.2, however of the spinning mode type in this case. In figure 5.40, the corresponding modal amplitude spectra of the three lining configurations (hardwall, uniform, VSI) are plotted for the excitation of a positive spinning direction (exp+) analyzed at $z = -0.50$ m.

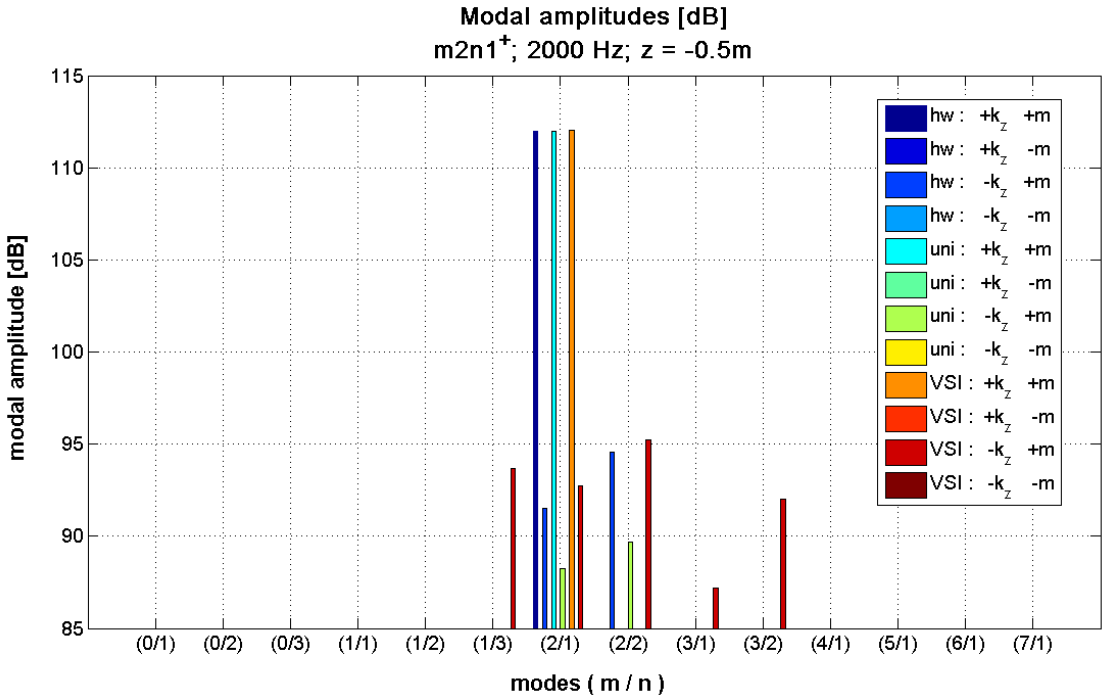

Figure 5.40: Comparison of modal amplitude results; hardwall ↔ uniform ↔ VSI liner; (2/1); 2000 Hz; $z = -0.50$ m

As in the previous example, at the rear axial position ahead of the respective lining sections, the spectra contain only the primary (excited) mode propagating into the positive axial direction. All configurations also contain reflections from the duct inlet (and/or the jump of impedance at the beginning of the liner). These are quite low (-20 dB in the hardwall case) as the mode is well cut-on ($\xi = 3.026$) at this frequency.

In the uniform liner configuration, the reflected contributions are reduced by 4 dB due to the absorptive effect of the liner. However, the VSI configuration shows an even slightly increased level of reflections of the primary mode, as well as contributions from modes (1/3), (3/1), and (3/2) (within the range of ≈ -30 dB from the primary peak). As expected, these modal components are all of the same spinning mode direction (exp +) as the primary mode.

Directly at the duct exit ($z = \pm 0.00$ m), and thus influenced by the different lining configurations, the modal spectra depicted in figure 5.41 have been obtained. These show a strong reduction of the primary peak in the uniform liner configuration (-24 dB) and a slight increase in the level of the first radial component (+3 dB). With respect to the VSI results, they exhibit a dominant peak of the first radial mode (+7 dB compared to the primary mode) and contributions from several other modes of an odd azimuthal mode number ((3/1), (3/2), (5/1), and (1/3)). These demonstrate, again, the non-uniformness of the resulting pressure field for this special type of a circumferentially non-uniform liner.

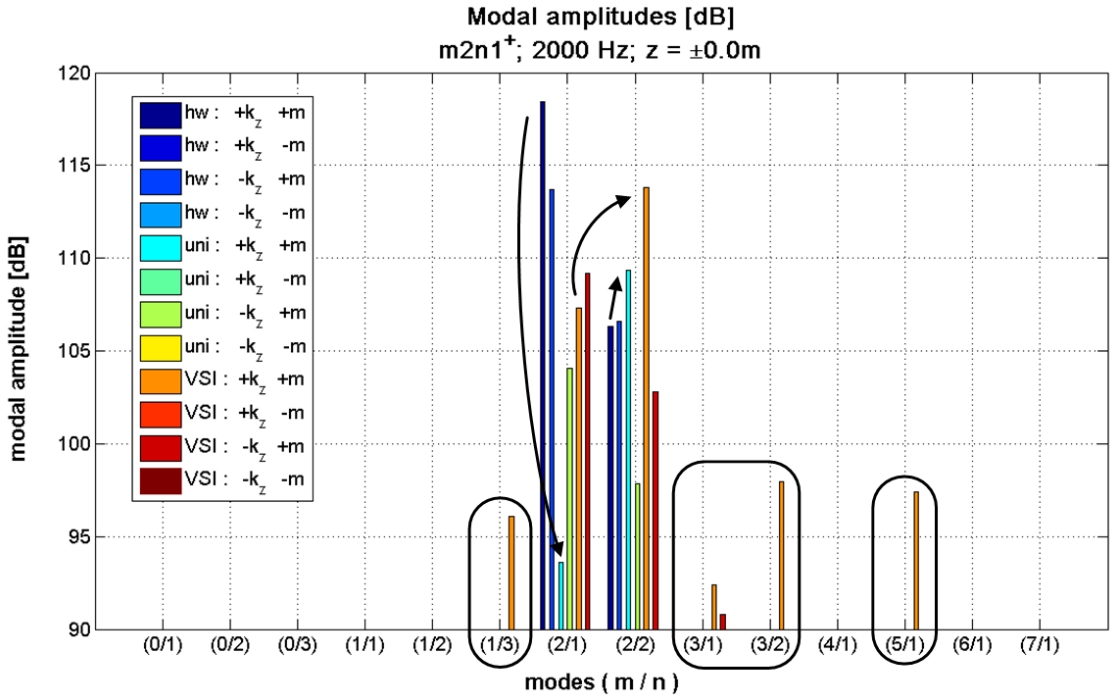

Figure 5.41: Comparison of modal amplitude results; hardwall ↔ uniform ↔ VSI liner; (2/1); 2000 Hz; $z = \pm 0.00$ m

To conclude this inspection of the modal spectra, it can be summarized that the modal decomposition of a measured or simulated noise field is a useful method to analyze its structure. If applied at two different duct stations, e. g. ahead of and behind an acoustic liner segment, it can be used to describe and understand the observed physical phenomena. However, care has to be taken in case of finite length ducts without anechoic terminations which introduce reflections influencing the pressure distribution by superimposed standing wave components. These correspond to axial variations in the sound pressure level and the resulting pressure pattern, and have to be considered within the analysis.

With respect to the non-uniform VSI liner inlet configuration, the modal analysis may be used to get an idea of the effects introduced by the liner patches. Yet, as mentioned at several points within this thesis, due to the asymmetric influence of the reflective liner at the lower duct wall shifting the complete cross-sectional pressure pattern, this decomposition into orthogonal modes is - strictly speaking - physically not correct. Contrarily, as reported before, the VSI liner shifts (or tilts) the directivity of a propagating mode to yield an asymmetric characteristic which cannot be described by the classical concept of symmetric and periodic mode shapes (compare figure 4.2 in the introductory part of chapter 4 visualizing the physical effect of the VSI liner).

5.6 Optimization for spinning modes

As has been identified during the analysis of the directivity plots and the radiated power reductions, the VSI effect exhibits some potential for improvement, especially in the case of spinning modes. This is, on the one hand, related to the lateral deflection of the radiated lobes by the non-uniform VSI liner and, on the other hand, to the occasionally detrimental resulting pressure distributions, e. g. for higher radial modes.

5.6.1 Modified BE model

Thus, to assess the full potential of the VSI configuration, an optimization study has been conducted involving a circumferential variation of the reflective liner position, which constitutes an additional DOF of the liner design and will be described in the following. For this optimization study, a modified BE model (depicted in figure 5.42(a)) which allows for the variable definition of a circumferentially shifted reflective liner segment has been created.

Accordingly, the front inlet part has been divided into 16 property groups yielding increments of 22.5° between two adjacent groups. Concerning the notation, the configuration number (V_0 - V_{15}) refers to the starting position of the reflective liner segment (using a positive rotation direction around the duct axis) as sketched in figure 5.42(b). The symmetric VSI liner configuration used up to this point will thus be denoted 'V_0'. To limit the number of parameters, only semi-circular liner segments have been analyzed in this study.[6]

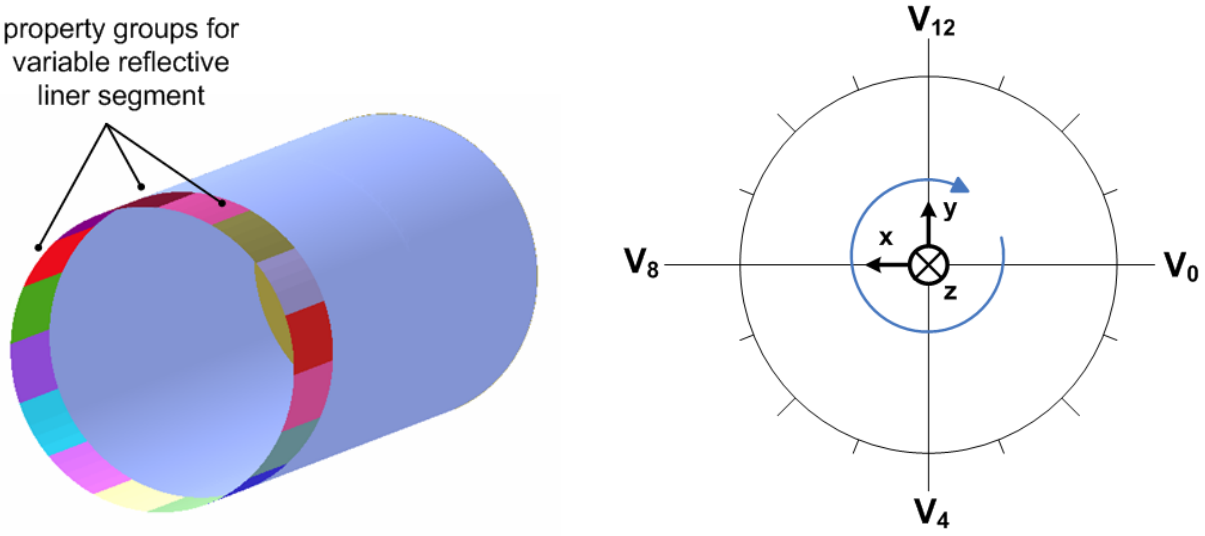

(a) BE model for variable (asymmetric) VSI study

(b) notation of configurations

Figure 5.42: BE model and notation used in variable (asymmetric) VSI study

This discretization (in the circumferential direction) was estimated to be fine enough for a first optimization study analyzing the general dependencies of the liner rotation angle and the far field radiation directivity. The BEM solution has been computed for all configurations, applying the low (reflective) impedance Z_r to the respective reflective liner patch and the absorptive impedance Z_a (both as in the previous sections of this chapter) to the resulting (identically rotated) absorptive liner segment. This yielded a complete dataset for all possible rotation angles of the VSI liner configuration (with the chosen step width of $\Delta\vartheta = 22.5°$).

[6] To recall, these also yielded the best net results in the parametric study in chapter 4.3.5.

The results have been evaluated, on the one hand, in terms of the far field radiation pattern on the forward hemisphere (graphically) and, on the other hand, by evaluation of the maximum SPL on the ground plane and the total radiated power values with respect to the ground plane and the angular reference sector [-40°; -90°] (as in the previous analyses).

5.6.2 Effect on far field radiation

For a first estimation of the effect of the liner rotation, figure 5.43 gives a representative example of the resulting plots for mode (1/1) at 1000 Hz, in which on the left hand side, the radiation is plotted on the forward hemisphere of radius $R = 10$ m.

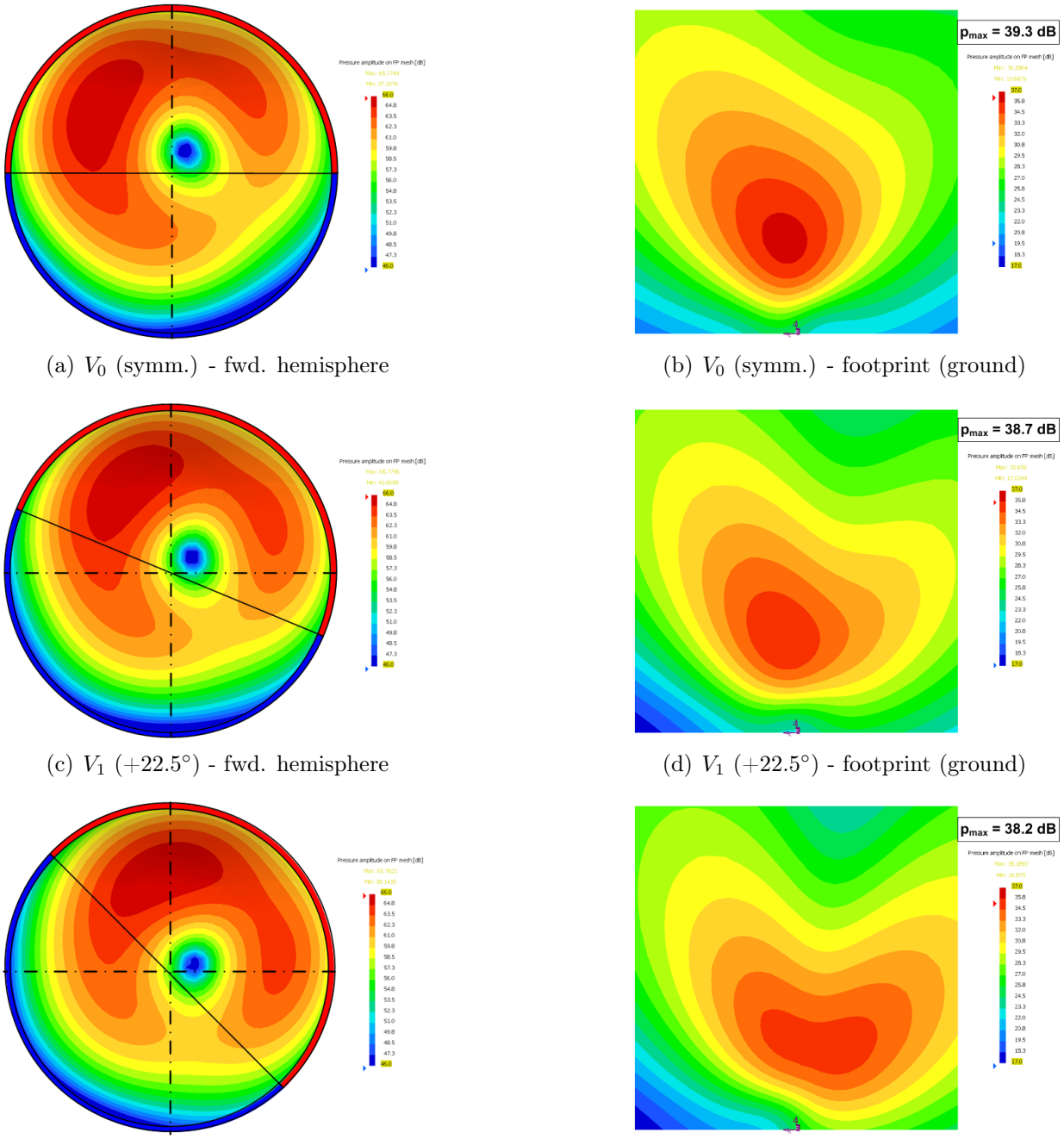

(a) V_0 (symm.) - fwd. hemisphere

(b) V_0 (symm.) - footprint (ground)

(c) V_1 (+22.5°) - fwd. hemisphere

(d) V_1 (+22.5°) - footprint (ground)

(e) V_2 (+45°) - fwd. hemisphere

(f) V_2 (+45°) - footprint (ground)

Figure 5.43: Comparison of sound pressure distributions (magnitude) on forward hemisphere and ground plane (footprint) for different rotation angles of VSI liner; (1/1); exp+; 1000 Hz

The represented variable is the sound pressure amplitude in dB for three rotation angles of the VSI configuration: the symmetric condition (V_0) and the two rotation angles $\vartheta_1 = 22.5$ (V_1) and $\vartheta_2 = 45°$ (V_2). For a better visualization, the particular location of the two liner segments has been indicated by colored arcs (red = absorptive liner, blue = reflective liner). On the right hand side, the corresponding pressure amplitude plots on the forward ground plane (as specified in figure 5.17) are added including the respective maximum sound pressure levels in dB.

The first distinctive feature is the fact that the rotation of the VSI liner configuration directly correlates with the rotation of the far field radiation pattern. This means that for a rotation of the reflective liner of one property group ($\equiv 22.5°$), the far field pattern rotates by the same amount, and analogously for the second configuration V_2 (and all others). Accordingly, the footprint on the ground (to be interpreted as an intersection of the three-dimensional radiation characteristic and the ground plane) varies consistently in level and shape. From these figures, favorable rotation angles may be determined by considering one of the two relevant quantities: the resulting max. SPL on the ground or the overall radiated power.

In this particular example, by rotating the VSI liner configuration by one angular increment ($V_0 \rightarrow V_1$), the maximum SPL could be reduced by 0.6 dB, as can be clearly seen in the figure. An additional incremental rotation ($V_1 \rightarrow V_2$) adds another 0.5 dB to the overall attenuation of the maximum SPL ($\Delta p_{max,t}$ = -1.1 dB). Thus, with respect to the maximum SPL on the ground, configuration V_2 yields the best result which can be confirmed from the superposition of all 16 VSI configurations together with the hardwall and the uniform liner reference cases as a function of the modal numbers in figure 5.44. Even though not easily readable due to the large number of data series, the plot shall serve to demonstrate the deviation of the results for the different configurations.

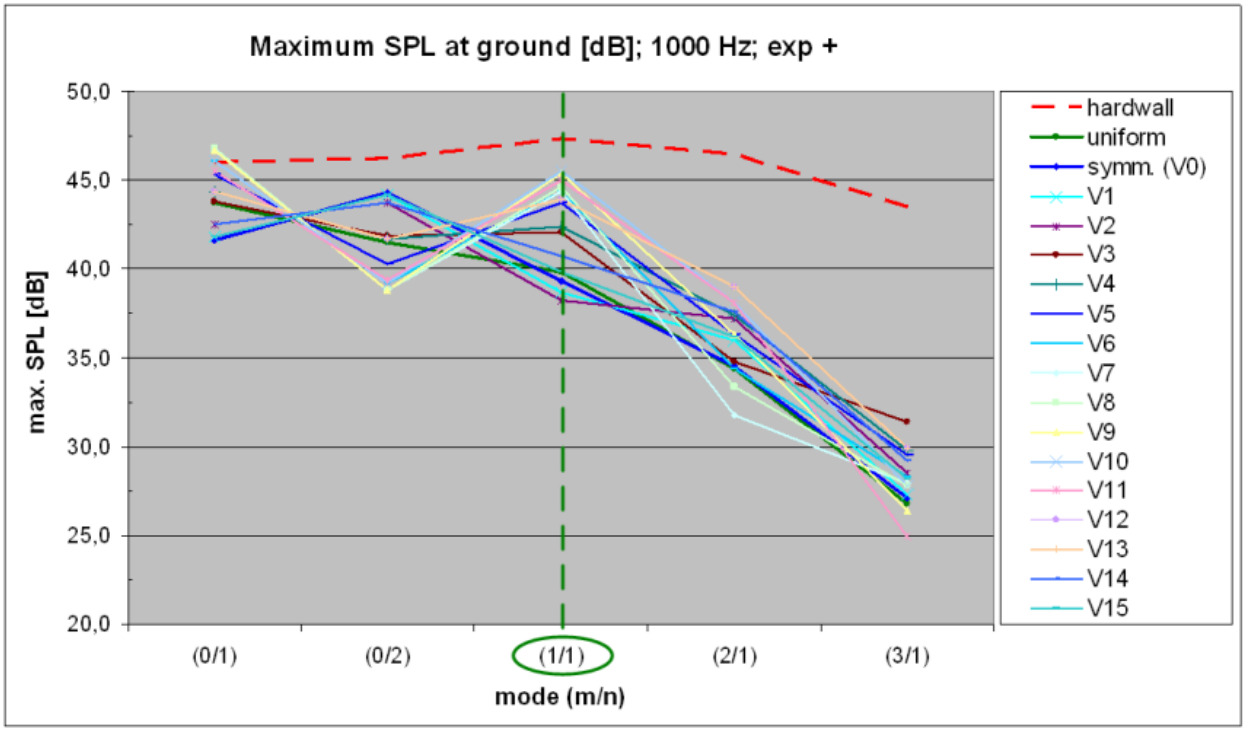

Figure 5.44: Comparison of maximum SPL on forward ground plane for different rotation angles of VSI liner; 1000 Hz; exp+ modes

However, if the radiated power is regarded, a different optimum configuration has been found, as can be deduced from figure 5.45. Similar to the previous figure, it contains the graphs of the radiated power at 1000 Hz for all 16 VSI configurations as well as the reference cases.

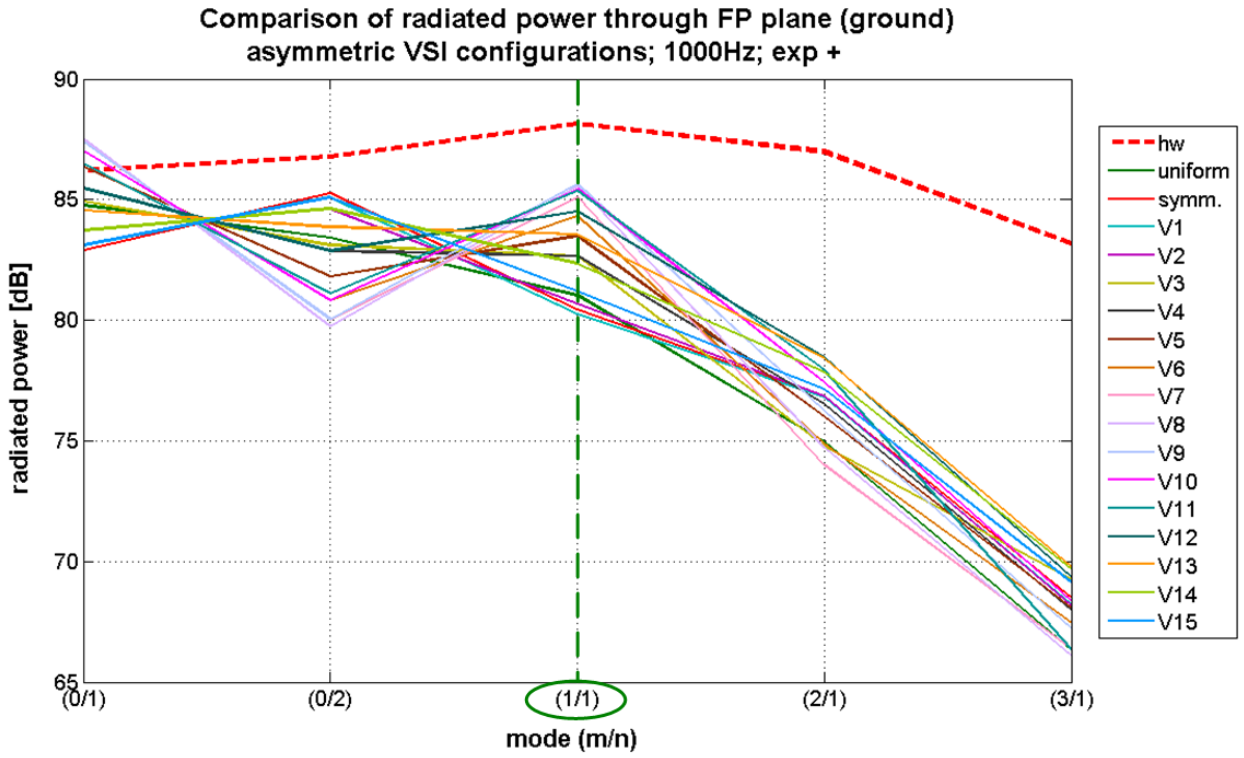

Figure 5.45: Comparison of power results on forward ground plane for different rotation angles of VSI liner; 1000 Hz; exp+ modes

It is quite obvious that the results for the various VSI configurations differ substantially from mode to mode. Thus, one rotational angle may yield the best result for a certain mode but perform inferior to others for the next one. This fact points out the sensitivity of the VSI performance upon the modal input. However, for each propagating mode an optimum configuration could be determined by means of taking the envelope below the curves in figure 5.45, e. g. for the mode currently under investigation configuration V_1.

Furthermore, it seems noteworthy that (at least at the frequency considered here) for each respective mode, at least one configuration with a lower radiated power value could be found than the uniform liner configuration (this feature is not ensured anymore at higher frequencies where at the highest propagating azimuthal modes the uniform liner still yields the best results).

5.6.3 Evaluation of results

As for the power results of the symmetric VSI liner configuration in chapter 5.3, at first a single mode excitation will be examined. Subsequently, the two broadband sound fields introduced in chapter 5.3.3 will be computed and evaluated for all rotated configurations (V_1 - V_{15}). Additionally, the optimum configurations at each respective mode will be combined to obtain a maximum achievable attenuation value. However, this requires an adaptive or active system to achieve the optimum condition at all times, as will be discussed in the next chapter.

5.6.3.1 Single mode excitation

After evaluation of the results for a single mode excitation with respect to the above mentioned quantities, the following plots have been obtained: Figure 5.46(a) presents a comparison of the radiated power values through the ground plane of the symmetric VSI configuration and the optimum VSI configuration determined within this study (as before, with respect to the uniform liner performance). In the lower plot (figure 5.46(b)), the difference between the two datasets, i.e. the additional attenuation due to the liner optimization, has been plotted.

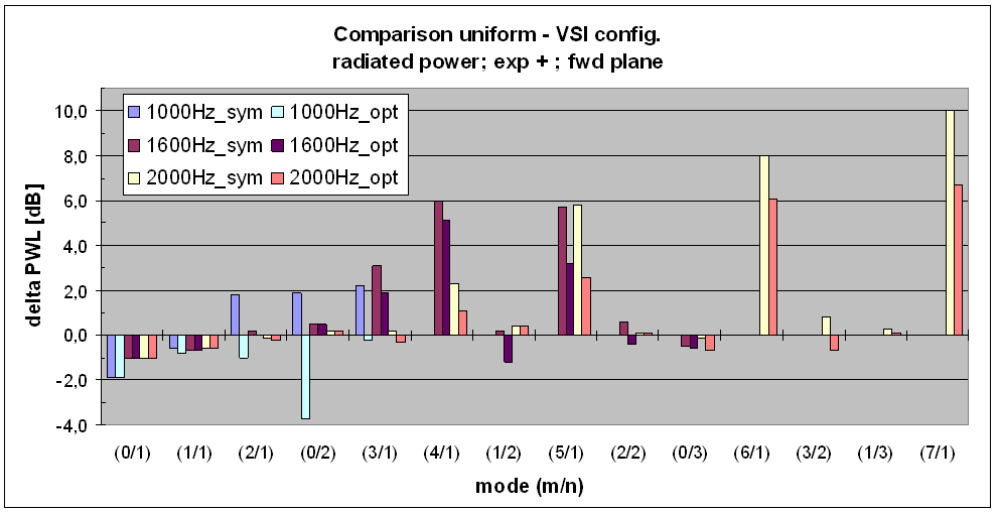

(a) comparison of radiated power; symmetric ↔ optimum

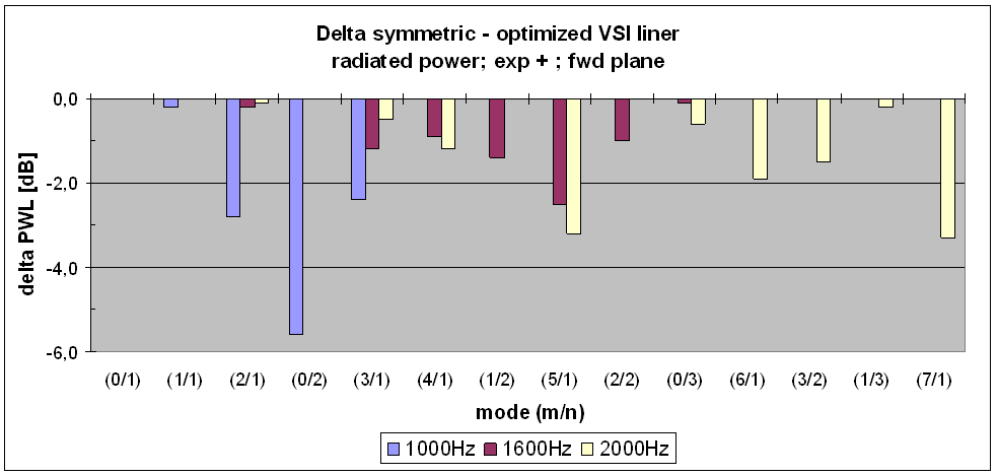

(b) additional power reduction

Figure 5.46: Comparison of power results on forward ground plane; symmetric ↔ optimized VSI liner

From both figures, the advantages of the optimization procedure (by rotation of the VSI liner configuration for each individual mode) become quite obvious: nearly all modes experienced a substantial noise reduction by this measure, only for the plane wave mode no improvement could be found (remember that this mode yielded the overall best results for the symmetric VSI configuration compared to all other modes). Especially modes exhibiting a weaker VSI effect or a negative performance compared to the uniform liner, have been attenuated considerably.

These are in particular the higher order propagating azimuthal modes (e. g. (2/1), (3/1) at 1000 Hz, (4/1), (5/1) at 1600 Hz, and (6/1), (7/1) at 2000 Hz) and the first radial modes ($n = 2$).

The largest improvement due to a rotation of the VSI liner has been observed for mode (0/2) at 1000 Hz, which yielded a 1.9 dB higher radiated power than the uniform liner in the original (symmetric) configuration. For this mode, a VSI liner rotated by 180° (corresponding to configuration V_8, an exactly reversed liner setup), achieved a resulting noise reduction of -3.7 dB, which adds up to a 5.6 dB improvement. Additionally, for several other modes power reductions of between 2.0 dB and 3.0 dB have been obtained. In result, it can be stated that by this optimization of the circumferential position of the reflective liner, the positive effects of the VSI could be enhanced, as well as negative effects for certain modes could be reduced or even turned into positive ones.

With respect to the maximum SPL on the ground, as analyzed in chapter 5.3, quite similar results have been obtained, depicted in figure 5.47.

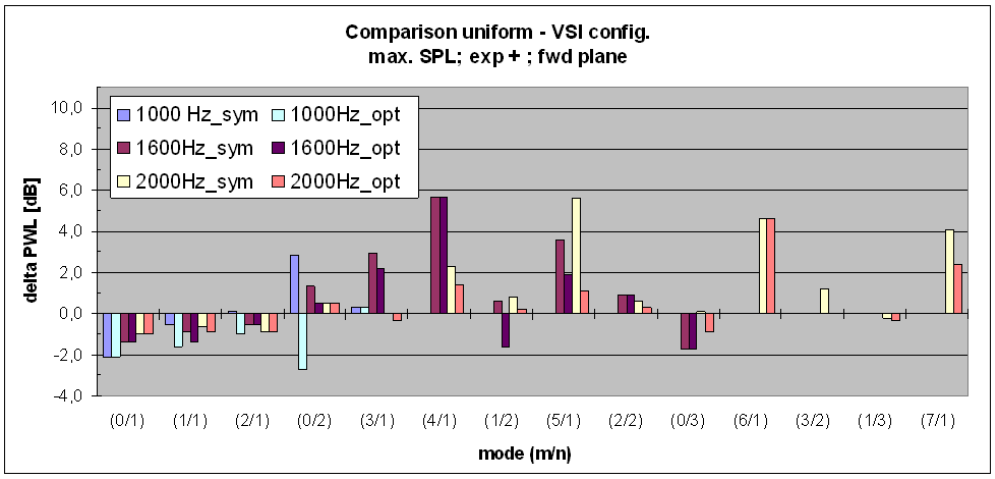

(a) comparison of radiated power; symmetric ↔ optimum

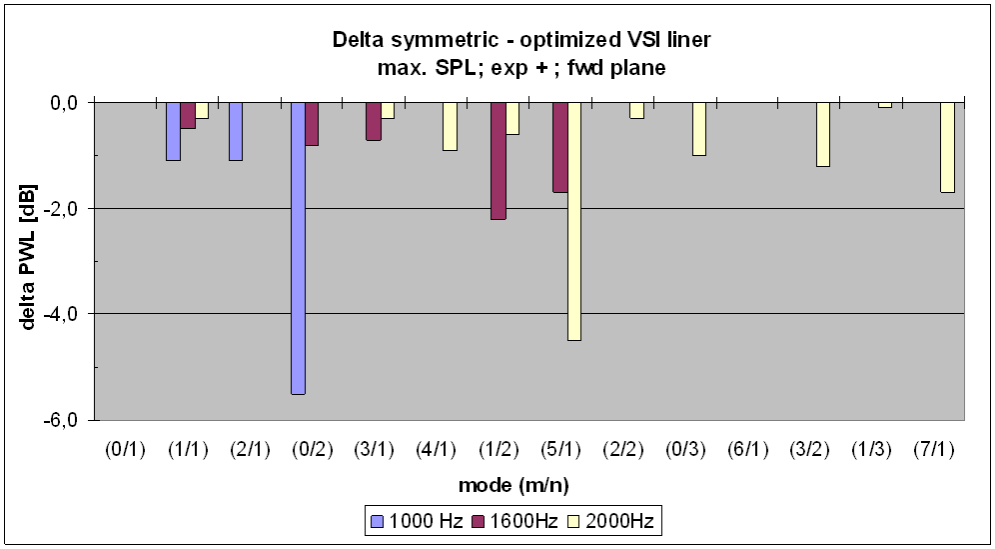

(b) additional power reduction

Figure 5.47: Comparison of max. SPL results on forward ground plane; symmetric ↔ optimized VSI liner

In general, the same tendencies and orders of magnitude concerning the reduction by the optimized VSI liner configuration have been observed. However, for some modes, different levels of reduction are found compared to the radiated power treated above: for instance, no additional benefit could be achieved for mode (3/1) at 1000 Hz in terms of the maximum SPL on the ground, whereas, with respect to radiated power, a 2.4 dB reduction could be

observed.[7] Additionally, for the higher order modes, in general, a reduced advantage of the optimization of the circumferential VSI liner position has been determined compared to the radiated power values. On the other hand, the optimized VSI configuration performed very well for mode (5/1) at 2000 Hz (-4.5 dB in max. SPL), even better than the radiated power reduction (-3.2 dB). These variations are difficult to interpret in general terms. However, both with respect to the maximum SPL and the radiated power, a promising potential has been observed.

To complete the analysis of the VSI liner rotation, the radiated power results in the reference sector ([-40°; -90°]) are given in figure 5.48 (as before, a comparison of the symmetric VSI liner results and the optimized (rotated) ones in figure 5.48(a) and the advantage due to the optimization in figure 5.48(b)).

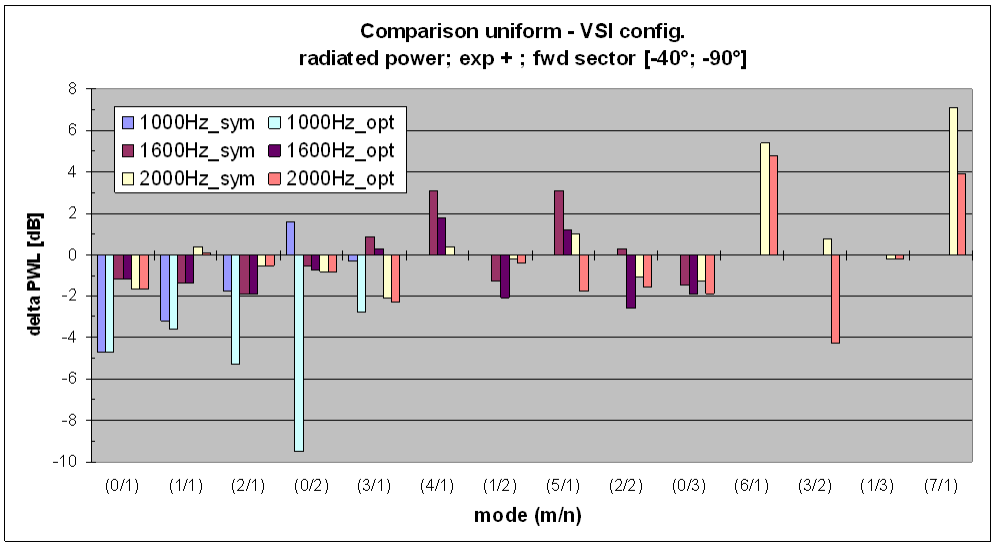

(a) comparison of radiated power; symmetric ↔ optimum

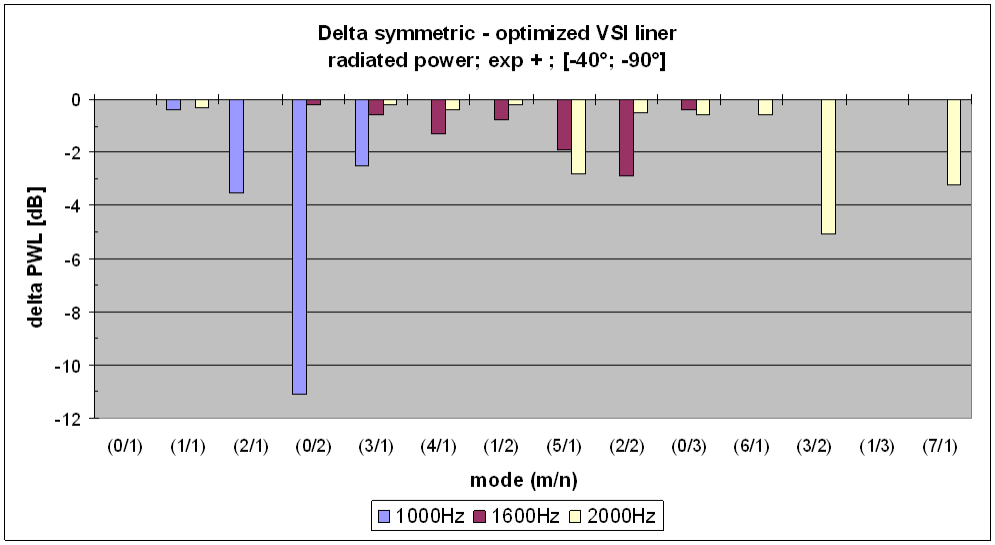

(b) additional power reduction

Figure 5.48: Comparison of power results in reference sector [-40°; -90°]; symmetric ↔ optimized VSI liner

[7] It remains to note that the maximum SPL of mode (3/1) for the symmetric VSI configuration was only 0.3 dB higher than the one for the uniform liner, in contrast to the radiated power value, which was 2.2 dB above the respective uniform one.

To recall, as analyzed in chapter 5.3, already the results of the symmetric VSI liner configuration in this reference sector seemed quite favorable (compare figure 5.25). With the circumferential liner position optimization, even better results could be attained, as can be seen in the current figure: up to -11.1 dB of improvement result for mode (0/2) at 1000 Hz, and between 2 dB and 4 dB have been achieved for several other modes. This yields an advantage compared to the uniform liner configuration for nearly all modes considered, only for the one or two highest order azimuthal modes (at each frequency) the uniform liner still remains more efficient. However, if not only single modes but a broadband noise field or a modal mix are considered, these modes should not have a large influence on the overall radiated power as will be seen in the next section.

5.6.3.2 Broadband noise field

After the evaluation of the single mode performance of the circumferentially rotated VSI configurations, the average (or rms-) values of the radiated power have been computed to obtain a single number characterizing the effect of the respective configuration (according to equation 5.2). It also serves to estimate the liner performance with respect to a broadband noise field.[8]

A representative result is shown in figure 5.49 for the frequency $f = 1000$ Hz with respect to the forward ground plane. In the upper half of the figure, the average radiated power levels of the hardwall reference case, the uniform liner configuration, the symmetric VSI configuration, and all 15 rotated VSI liner configurations are plotted next to each other. In the lower half, the average attenuation is added for comparison (recall the discussion about the characteristic differences between these two quantities in chapter 5.3.3).

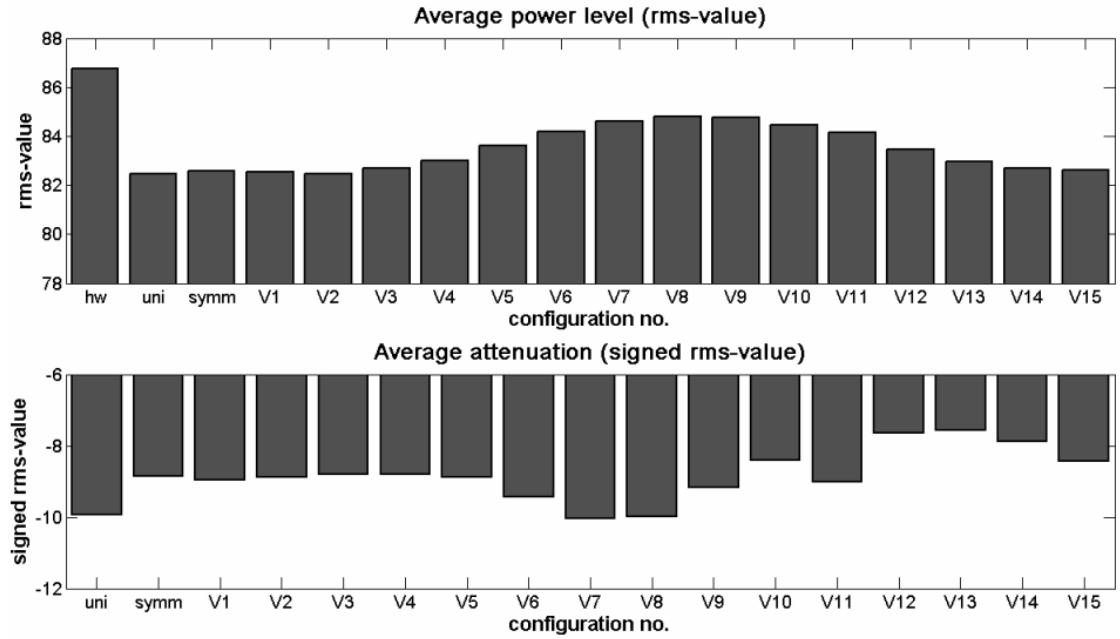

Figure 5.49: Comparison of average radiated power and attenuation on forward ground plane for different rotation angles of VSI liner; 1000 Hz

The average power level shows a clear variation with the circumferential liner position exhibiting a global minimum centered at the symmetric VSI configuration. In both directions ($\rightarrow V_1, V_2$) and ($\rightarrow V_{15}, V_{14}$), the levels stay approximately constant and then rise to yield a maximum at configuration V_8.

[8] Recall the explanations given in chapter 5.3.3.

Thus, for this frequency and reference area (the ground plane), the symmetric VSI liner represents the most favorable configuration attaining nearly exactly the level of the uniform liner. Contrarily for the average attenuation values: here, the uniform liner achieves -9.9 dB while the symmetric VSI liner reaches only -8.9 dB; the overall highest average attenuation of -10.0 dB is observed for configurations V_6 and V_7. This again underlines the statement that the maximum average attenuation does not correspond to the minimum average radiated power because of the negligence of the varying power levels of the individual modes.

As mentioned in the introduction of this section, additional to the rms-value reflecting the average liner performance, the optimum achievable VSI liner performance will be computed as well. This is accomplished by a combination of all single mode optima into one rms-value. In realization, this requires an adaptive or active system combined with a suitable sensor array to detect and adapt to any propagating mode.

To start, the average radiated power results of the optimization process will be presented and compared for the two consistently used reference areas: the forward ground plane and the lower forward reference sector [-40°; -90°].

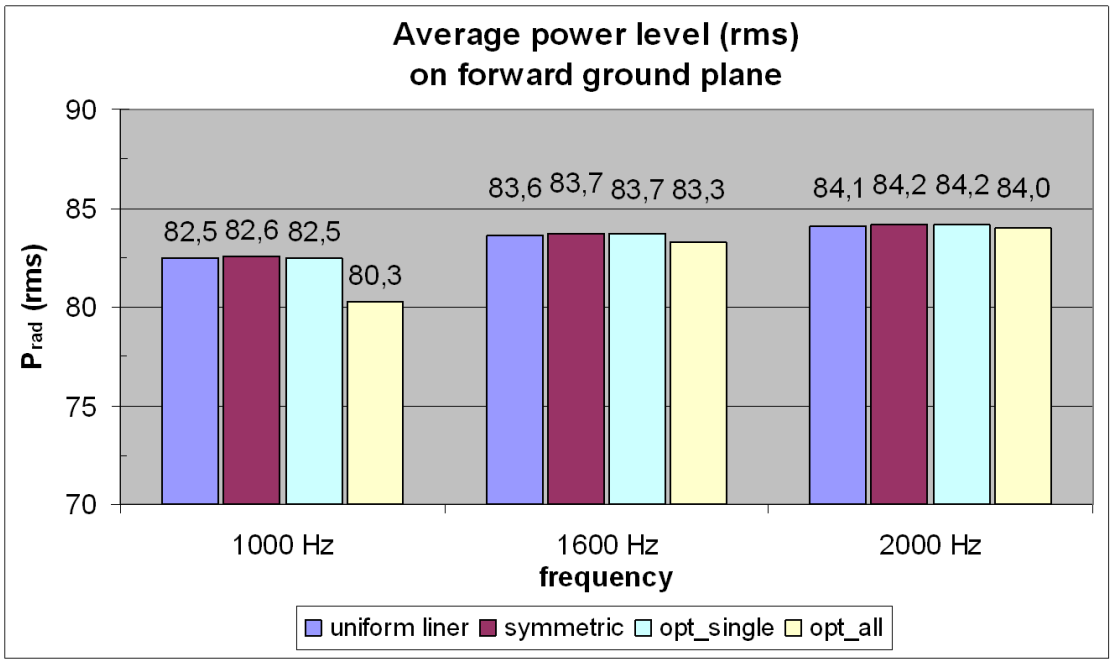

Figure 5.50: Comparison of average radiated power on forward ground plane; optimized

Figure 5.50 compares for the three frequencies considered within this study the average power values of the uniform and the symmetric VSI liner configurations with the optimum rotated VSI configuration (*opt_single*) and the minimum achievable power level (*opt_all*). The former one represents the single asymmetric configuration (V_0 - V_{15}) with the lowest average power level at the respective frequency. Accordingly, the configuration number yielding the best result with respect to this quantity (average radiated power) might change from frequency to frequency (as will be the case). In contrast, the *opt_all* configuration is a superposition of the individual best performances for each respective mode. Thus, it does not represent a single configuration but a theoretically achievable optimum, and will be used to estimate the maximum VSI liner effect given the geometric and parametric constraints of the model used in this chapter.

As reported in the evaluation of the symmetric VSI liner results (chapter 5.3.3.1), the first observation from figure 5.50 might be that the symmetric VSI configuration yields nearly the same performance as the uniform liner (only a 0.1 dB higher power level).[9] Similarly for the single optimum configuration, which indicates that this might coincide with the symmetric VSI configuration. In effect, this is true at 1600 Hz and 2000 Hz, at which configurations V_0 as well as V_1 (and V_2 at 1600 Hz) yield the lowest average power levels. At the lowest frequency (1000 Hz), configurations V_1 and V_2 achieve the best results equal to the uniform liner level.

Combining the optimum results at all modes in the *opt_all* configuration, the radiated power level can be reduced by another 2.2 dB at 1000 Hz. Yet, at 1600 Hz the difference amounts to only 0.3 dB, and at 2000 Hz, only 0.1 dB can be added to the overall attenuation. However, as has been observed in the previous parts of the analysis, the ground reference plane shows a considerably lower potential of the VSI configuration (commented in more detail in chapter 5.3.1) than the reference sector [-40°; -90°] accounting merely for the radiation directed towards the ground being most relevant for the assessment of community noise.

Accordingly, figure 5.51 presents the corresponding results concerning the average power radiated into this reference sector.

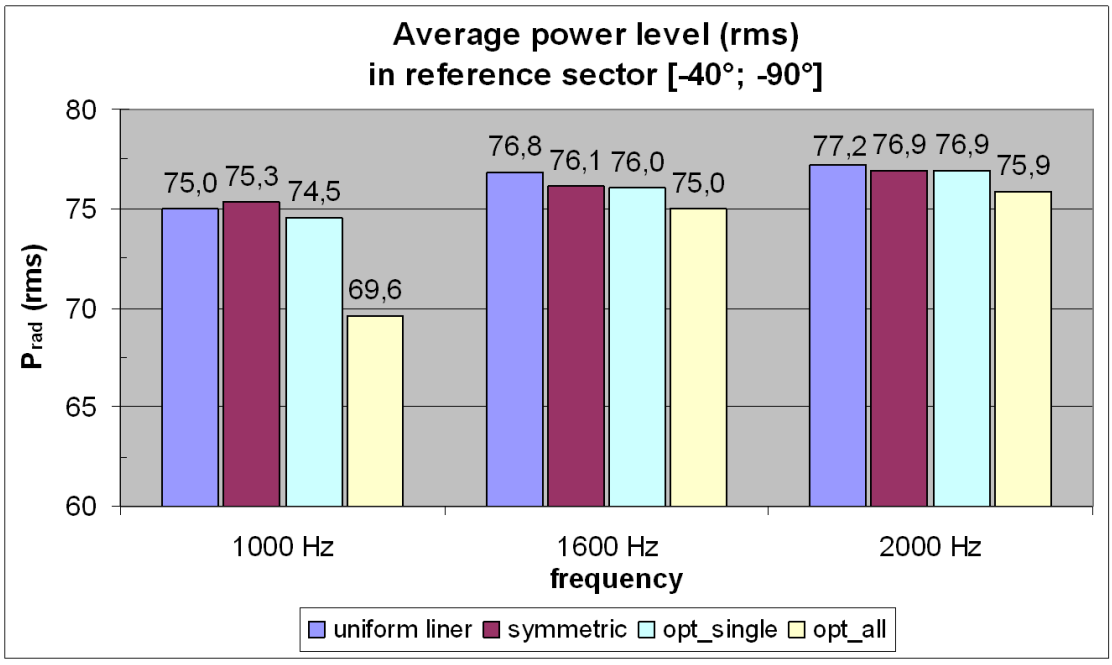

Figure 5.51: Comparison of average radiated power in reference sector [-40°; -90°]; optimized

At the lowest frequency (1000 Hz), configuration V_2 shows the best result being 0.5 dB lower than the uniform liner value and 0.8 dB lower than the symmetric VSI result. Differently at the higher frequencies, where the symmetric VSI configuration again coincides with the single optimum configuration, and achieves a power reduction of 0.8 dB and 0.3 dB at 1600 Hz and 2000 Hz, respectively, compared to the uniform liner. This attenuation is even more pronounced for the *opt_all* configuration, which yields 5.4 dB, 1.8 dB, and 1.3 dB of additional power reduction, respectively at the three frequencies.

[9] The small differences to the results e. g. in figure 5.30 originate from the use of two different BE models, however, the results qualitatively and quantitatively agree very well.

These values confirm again the quite promising potential of the VSI configuration even for an equally distributed modal mix. By the optimization of the circumferential liner position, the radiated power value in the reference sector could be reduced by 0.8 dB at the lowest frequency. For the other two frequencies, the symmetric VSI liner configuration already represents the best average solution. However, if for each single mode the optimum condition could be attained, a considerable potential would be observed, especially for the lower frequencies.

Analogously to the procedure in the section dealing with the radiated power considerations in the main part of this chapter (chapter 5.3.3.2 involving the symmetric VSI configuration), additional to the average power level, the combination of a broadband background noise field and a single dominating mode will be analyzed for the rotated VSI configurations. As before, the single mode is chosen to be the highest propagating azimuthal mode at each frequency (compare table 5.2 for the corresponding mode numbers and cut-off ratios).

The resulting radiated power values for all configurations and frequencies with respect to the ground plane are summarized in figure 5.52. Compared to the average power level results presented above, only the single optimum VSI configuration has been considered here, which corresponds to the optimum configuration for the single protruding mode. An optimization as done for the *opt_all* configuration above, trying to achieve a maximum noise reduction for all contributing modes, makes no sense for this kind of input sound field. Instead, the accumulated power level of the broadband component has been included in the figure to estimate the grade of protrusion of the single dominant mode.

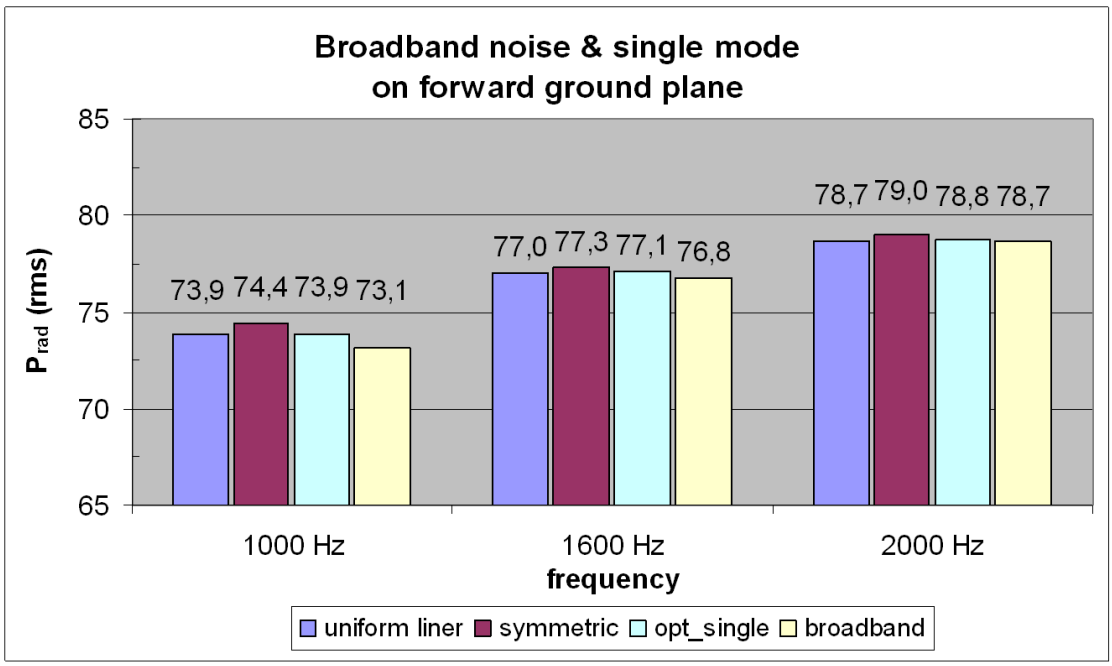

Figure 5.52: Comparison of overall radiated power (broadband + single mode) on forward ground plane; optimized

The results show a slightly increased power level of the symmetric VSI configuration compared to the uniform liner case (between 0.3 dB at 1600 Hz and 2000 Hz and 0.5 dB at 1000 Hz). This can be explained with the efficiency of the uniform absorptive liner especially for the low cut-off ratio modes (as described in section 5.3.3.2). As well, the protrusion of the dominating mode decreases with an increasing frequency.

Contrarily, the power values of the optimum VSI configuration nearly exactly match the results of the uniform liner, which ensures that the VSI liner configuration does not cause a negative effect for this type of sound field representing the worst case scenario for the VSI liner application. In particular, for the two higher frequencies, configuration V_2 corresponding to a rotation angle of +45° (in the positive axis direction) yields the best results. Contrarily at 1000 Hz, where configuration V_8 achieves the lowest radiated power value. This configuration corresponds to an exactly reversed VSI liner setup (compare figure 5.42(b)) and is caused mainly by the superior performance of this configuration for the first radial mode (0/2) as reported in the previous section (compare also figure 5.46).

For the second reference area, the lower forward sector ([-40°; -90°]), the results are compared in the same representation in figure 5.53.

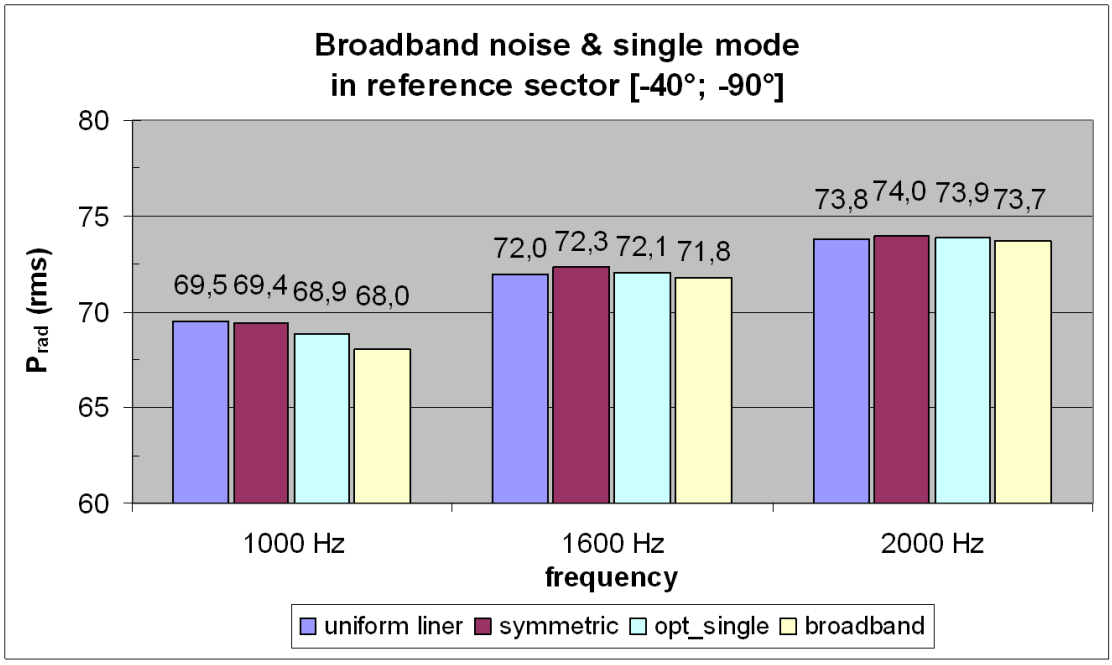

Figure 5.53: Comparison of overall radiated power (broadband + single mode) in reference sector [-40°; -90°]; optimized

As before, the results slightly improve for this reference sector, especially for the lowest frequency (1000 Hz), at which even the symmetric VSI configuration reaches the level of the uniform liner, and the optimized configuration achieves 0.6 dB of additional attenuation. Explicitly, the optimum configurations are V_{11} at 1000 Hz, and V_1/ V_2 at 1600 Hz and 2000 Hz.

In summary, the optimization of the circumferential VSI liner position yields - for the case of a broadband noise field - an improvement basically at the lowest frequency observed (1000 Hz). For the higher frequencies, the symmetric configuration already represents the best solution. However, if the optimum condition at each contributing mode could be achieved, e. g. by an active or adaptive system, the VSI liner offers an even more interesting potential as well for this type of sound field (up to an additional 5.4 dB attenuation). With respect to the worst case scenario (for the application of a VSI liner) of a single dominant azimuthal mode of low cut-off ratio (occurring e. g. for the rotor-alone tone at takeoff), the circumferential VSI liner optimization achieves power levels equivalent to the uniform liner (and in one case even a 0.6 dB lower result). This is especially interesting in context of the question whether the VSI liner application may cause negative effects under certain conditions.

Concluding the section about the circumferential VSI liner optimization, it can be summarized that the individual rotation of the reflective liner segment improves its performance drastically. This implies additional noise reduction in the reference areas compared to the uniform liner and, even more important, the reduction of negative effects for certain modes, which might be even turned into positive ones. These tendencies have been consistently observed for a single mode excitation, but also offer some potential for a broadband excitation.

Additionally, they ensure the prevention of negative effects for unfavorable scenarios (for the VSI configuration) as e. g. the combination of a single dominant mode of high azimuthal order with a broadband noise field. Especially, of course, the combination of all single mode optima into the minimum achievable power level by means of this specific type of VSI liner shows a very interesting potential. Yet, this requires an adaptive or active system implicating a considerably increased complexity and additional weight and cost.

5.7 Summary of VSI potential and possible applications

Within this chapter, the VSI liner concept has been compared to a conventional uniform absorptive liner. The detailed analyses disclosed the fundamentally different effect of the non-uniform lining configuration on the directivity characteristic and, correspondingly, power radiated into the reference sector. In this respect, the VSI liner yields an advantage especially for the well cut-on lower order azimuthal modes and several radial modes.

Contrarily, for the highest propagating (barely cut-on) azimuthal mode orders the maximization of absorptive area dominates over the redirection effect and the uniform absorptive liner becomes more efficient. However, as could be expected, in case of a broadband noise source composed of an equipartitioned modal mix, the reduced performance for these modes does not have a large influence on the overall results due to their strongly reduced power levels behind the liner in both configurations.

Additionally, the optimization of the VSI liner circumferential position showed very positive results in terms of a maximization of the positive effects for spinning modes and a prevention of negative results especially for radial modes. This also guaranteed comparable power levels to the uniform liner in a special type of noise field representative e. g. for the takeoff condition: the combination of a broadband background noise and a single dominant mode of low cut-off ratio, which constitutes a favorable condition for the absorptive liner but represents the worst case scenario for the VSI liner.

With respect to modal scattering effects widely discussed in the context of non-uniform lining configurations, it has been observed that the VSI liner noticeably influences the modal composition both in the radiated field and within the duct (by reflections). However, as pointed out in the respective section, the classical modal analysis should only be used to get an idea of the VSI effect, but is strictly speaking physically not correct for the resulting asymmetric sound field.

As a consequence of these results, a favorable application of the VSI liner would be the approach condition due to the low engine power setting and the well cut-on dominant modes. Especially with respect to the limited performance of conventional and alternative novel concepts for these modes propagating at a small angle relative to the duct axis, the VSI effect may serve as a complement to existing designs.

Accordingly, in the next chapter, a number of advanced lining concepts including different possible implementations of a VSI liner will be presented and discussed on a conceptual basis.

Chapter 6

Discussion of advanced VSI lining concepts

In this final chapter, possible realizations concerning the implementation of a Virtual Scarf Inlet (VSI) into a commercial aircraft engine inlet will be presented and discussed. This outlook closes the analysis of this novel technology and creates a link to chapter 3 dealing with the Mechanically Adaptive Liner (MAL) concept by integrating it into an adaptive engine inlet liner system. To ensure a generality of the concluding statements, different kinds of concepts ranging from fixed designs optimized for a single condition over adaptive solutions to account for different flight conditions to a fully adaptive/ active system including an array of inlet sensors will be evaluated with respect to their individual potential and technological complexity. This may serve to facilitate the assessment of the expectable capability of these advanced engine inlet liner concepts. Moreover, a few comments will be given concerning the feasibility and technological challenges of the various designs.

In detail, the proposed concepts include the following (several of which are sketched schematically in figure 6.1):

1. a VSI liner configuration embedded in a conventional uniform liner (static, optimized for a fixed design point) *[C1]*,
2. a configuration as in (1), but frequency-adaptive (adaptation of the reactance) *[C2]*,
3. (a) a rotatable VSI liner segment (similar to the rotatable scarf inlet in Ref. [130]) *[C3a]*,
   (b) a circular segment of adaptive elements (w.r.t. both resistance & reactance) for an optimized azimuthal position & dimension *[C3b]*,
4. a fully-adaptive/ active system for both the VSI and the absorptive liner *[C4]*.

With respect to the proposed lining concepts C1 - C3a, it should be mentioned that, as a result of the parametric analysis in chapter 4, the limitation to a fixed axial position and extent is justified by the relatively small dependency of the VSI effect on these parameters (if properly optimized for the application case).

To start, the first and least complex configuration *[C1]* will be described. It consists of an axial combination of a conventional uniform liner and a reflective liner segment. From the results of the previous chapters, it might be deduced that this series connection of a uniform liner and a VSI liner segment can be expected to yield fairly good results. This estimation should be illustrated by means of a conceptual sketch in figure 6.2.

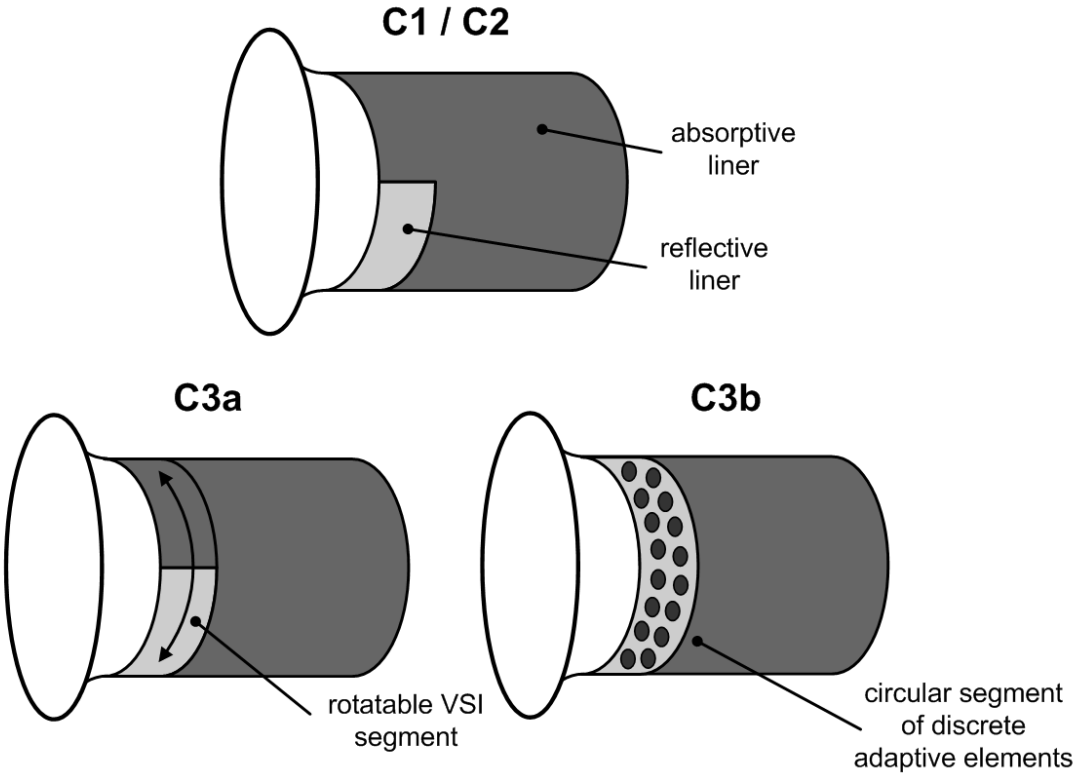

Figure 6.1: Schematic sketch of possible advanced VSI lining concepts

As observed within the preceding analyses, the uniform first part of this liner concept tends to focus the modal energy on the duct axis. This effect is related to the high effectiveness of the absorptive liner for modes propagating at steep angles, i.e. of a low cut-off ratio and a concentration of the acoustic energy at the duct wall. Accordingly, the remaining maxima of the modal pattern are located at the lower radial positions. However, the second non-uniform section of the VSI type is most effective for these low propagation angles shifting the corresponding lobes of radiation to more positive radiation angles, i.e. in direction to the sky (as has been described in the corresponding chapters).

While, on the one hand, the technical complexity of this first and simplest combined liner concept is quite low (i.e. accomplished by a simple replacement of an absorptive liner patch by a reflective one), on the other hand, its off-design performance might be low, or yield even negative effects in unfavorable conditions (compare analysis of noise field resembling takeoff conditions in chapter 5.3.3).

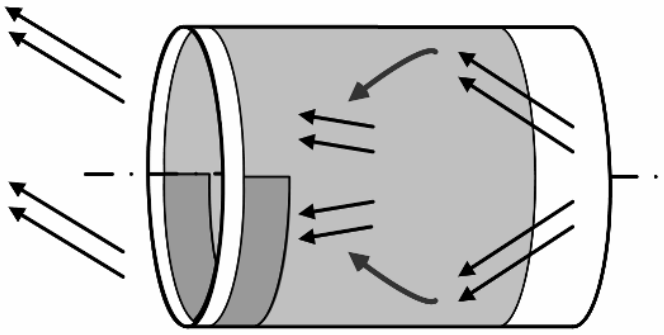

Figure 6.2: Schematic sketch of acoustic effect of combined uniform - VSI liner

However, using an elaborate optimization procedure, probably a good compromise can be found yielding a certain potential at the design condition and avoiding unwanted increases in noise level in adverse conditions. Yet, this design should be restricted to application cases involving a relatively constant sound field of well-known modal content.

Slightly more complex in terms of the technology, *concept 2 [C2]* allows for an adaptation of the reactance, e. g. mechanically or by a bias flow through the liner cavities (compare chapter 2.3.2.1). This possibility of changing the tuning frequency seems sufficient to achieve the desired (near) softwall conditions, a variation of the resistance is expected to have only a limited impact on the performance compared to the added complexity. To a certain extent, concept 2 could also permit the change from the softwall condition (impedance close to zero) at approach to an absorptive design (yielding an approximately uniform lining) at takeoff. This combines the individual advantages of the corresponding liner design methodologies at these two flight conditions most relevant for community noise. With respect to this objective, an additional numerical study should be conducted investigating the impedance limit to achieve the VSI effect and the degradations due to variations from the optimum (the softwall condition).

However, the range of adaptation also depends on the selected mechanism and is limited also by the available installation space. Accordingly, these factors have to be included into a performance estimation. Additionally, a system of sensors determining the frequency of the dominant tonal components, as well as the actual impedance of the adaptive liner, has to be developed and integrated into the liner concept. From the experiences during the experimental validation of the Mechanically Adaptive Liner (MAL) concept in chapter 3, a global impedance determination is recommended, since the local impedance measurement showed strong weaknesses in case of distinct modal sound fields.

Whereas the first two concepts considered a fixed circumferential dimension and position of the reflective liner segment, *concept 3 [C3]* aims at an increased flexibility, which could be useful in case of changes in the modal content with changing flight conditions or an insufficient knowledge of the input sound field. Accordingly, [C3a] provides a means of rotating the non-uniform liner section, a concept equivalent to the invention of Sankrithi proposing a 'rotatable scarf inlet' [130]. As for this design, a combination with a frequency adaptation seems to be rather complicated, and the complexity and risk of a rotatable inlet part quite high, an alternative design proposed as concept [C3b] seems advisable.

It extends the adaptive liner part to a full circular segment, so that both an adaptation of the circumferential position and its extent become feasible. Compared to [C2], it involves no fundamental increase in complexity with respect to the actuator, but a considerable advantage in terms of flexibility and performance in case of changing or unknown sound fields, which has been assessed promising in chapter 5.6, in combination with the avoidance of negative effects by the VSI configuration in unfavorable application cases. However, with respect to the sensoring equipment, both concepts [C3] necessitate a means of determining the incident modal components. This could be implemented by a microphone array integrated into the liner barrel and connected to a DSP performing the transformations to obtain the modal amplitudes (as described in chapter 2.1.1.2).

The most challenging, but obviously also most effective liner design *[C4]*, would incorporate also an adaptability of the uniform (absorptive) section. Due to its dimension, an adaptation of the complete barrel does not seem practicable. In contrast, the concept of changing the effective (area-weighted) impedance by discrete adaptive elements (as presented in chapter 3) rather seems advisable. By this, the effective impedance of the absorptive liner section could be adjusted to meet optimum conditions. However, of course, scattering effects possibly introduced at the jumps of impedance in-between the discrete adaptive elements, have to be estimated within the design process.

All 'rotatable' concepts (i. e. [C3] and [C4]) imply also the possibility to improve the in-flight interior noise levels in the forward cabin by a corresponding deflection of the directivity away from this sector. In contrast to a Negatively Scarfed Intake (NSI), this can be achieved without sacrificing the aerodynamic performance by simply rotating the VSI liner.

Figure 6.3 summarizes the individual performance expectations and corresponding technological risks of these five concepts in a graphical representation.

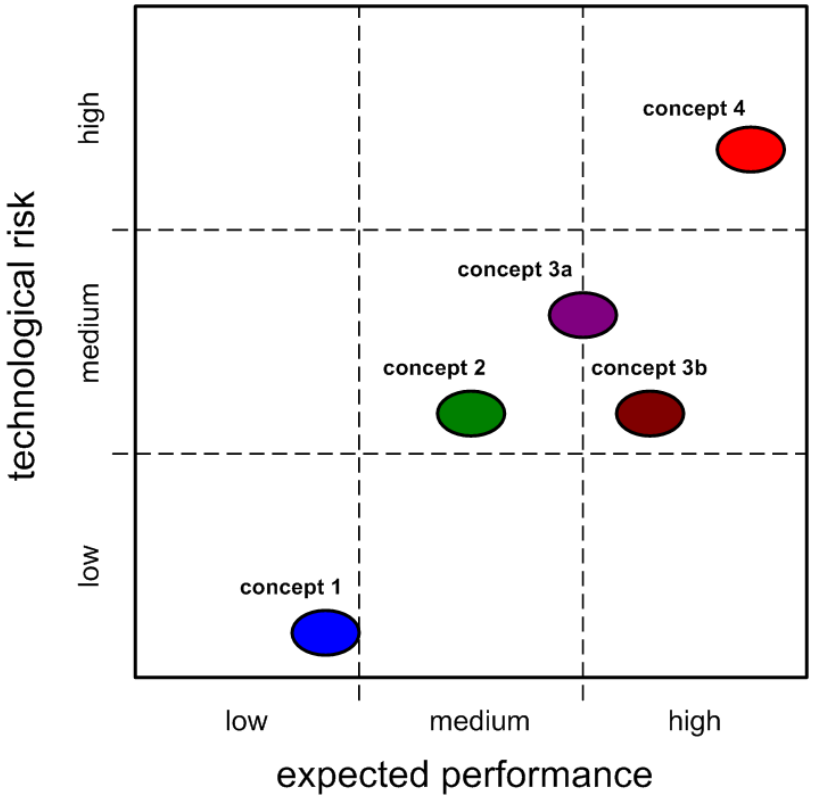

Figure 6.3: Risk-performance diagram of advanced VSI lining concepts

The figure illustrates the expected increase in performance with a more advanced design (from [C1] to [C4]), but also emphasizes the increasing complexity, or technological risk. Accordingly, the individual concepts exhibit different ratios of these two criteria corresponding to more or less favorable designs with the theoretical optimum in the lower right corner, combining the highest performance with the lowest risk/ complexity.

The final decision in favor of one of the above described concepts will obviously depend upon the knowledge and consistency of the input sound field. For fairly predictable, consistent conditions, and if possible negative effects in other flight conditions can be excluded or limited, concept 1 might be adequate yielding a satisfying increase in attenuation within the reference sector at the design point. However, for a more complex, changing sound field, or if an adaptation from the VSI configuration (at approach) to a (nearly) uniform absorptive liner (at takeoff) seems desirable - and possibly a third configuration in the cruise configuration -, concepts [C2], or rather [C3b], might be preferable. They include an adaptability of the tuning frequency of the reflective segment, as well as a variability of its circumferential position ([C3b]). A considerably more complex fully adaptive system (concept 4, including also an adaptability of the impedance of the absorptive liner section), in general does not seem advisable, especially with respect to its limited additional potential (as discussed in chapter 2.3.2.1).

Chapter 7

Conclusion and outlook

As has been shown in the previous chapters, the Virtual Scarf Inlet (VSI) represents a novel concept to overcome the deficiencies of current and previously studied duct lining concepts. In contrast to the most commonly used designs, the VSI does not attempt to maximize the absorptive effect of the lining material, but influences the radiation directivity by a non-uniformity in the lining impedance. Whereas most non-uniform concepts try to make use of scattering effects and the redistribution of modal energy, the main distinctive feature of the VSI is the deflection of the radiation pattern to reduce the impact upon certain sectors. This is made possible by an abrupt change in the wall boundary condition at a specific location within the front engine inlet changing the radial pressure distribution within the cross section, and accordingly, the radiation directivity.

After a recapitulation of the relevant theory, the state of the art of duct acoustics, and a short summary of available analytical and numerical tools for these kinds of problems in chapter 2, an adaptive liner concept has been analyzed experimentally and numerically in chapter 3. This served, on the one hand, to validate the Boundary Element Method (BEM) for duct acoustic problems involving non-uniform impedance distributions, and, on the other hand, to verify the means of an impedance adaption by discrete adaptive elements, which could be used in an advanced lining system (as presented in chapter 6).

In chapter 4, the basic concept of the VSI and the corresponding physical phenomenon have been presented. Subsequently, the VSI effect has been studied in detail by a systematic parametric variation of its geometric characteristics. Finally, the main influencing quantities, being the cut-off ratio as well as the radial mode number, have been extracted.

In the second main part of this thesis, in chapter 5, a VSI liner configuration has been compared to a conventional uniform absorptive liner. In this context, the individual advantages and disadvantages have been highlighted, resulting in different preferred fields of application.

Concluding, several advanced VSI lining concepts for an engine inlet have been discussed and assessed with respect to their individual technological complexity and expected performance (chapter 6). This analysis proposed integrated lining concepts of differing complexity and capability depending on the knowledge and consistency of the input sound field and the objective of the system.

Accordingly, after analysis of all data, a VSI liner seems to offer a promising potential in the application to an aircraft engine inlet duct as a complement to the existing absorptive liner design. It requires, in its simplest embodiment, only minor changes to the conventional design, avoiding weight or aerodynamic penalties resulting from competing approaches.

In contrast to all other lining concepts affecting mainly the modes propagating close to the duct wall (low cut-off ratio), the VSI design influences the overall modal pressure distribution within the duct, and is most effective for the more axially propagating well cut-on modes

(high cut-off ratio). This fact motivates its application to the approach condition involving a low engine power setting and (relatively) low propagation angles of the contributing modes. Especially with respect to the continuing importance of fan tones with increasing fan diameters and the limited potential of conventional as well as alternative novel methods, the VSI concept becomes attractive as a complement to existing technology (as mentioned e. g. by McAlpine et al. in Refs. [102] and [103]).

As described in detail in the previous chapter, in a realistic application case, the VSI liner should be integrated into the conventional liner design combining the individual advantages of these two liner types in a favorable way to yield a considerably enhanced noise reduction. Depending on the specific characteristics of the input sound field and the desired balance between performance and technological risk, the resulting advanced liner concept may exhibit different levels of complexity ranging from a static design to more and more complex and capable adaptive systems.

A second possible field of application might be the rearward radiation of the fan through the bypass duct of the engine. In this case, due to the annular geometry, the lining design is extended by an additional degree of freedom. However, in a first step, the reflective liner segments causing the effect on the directivity might be positioned as sketched in figure 7.1. In imitation of the naming of the inlet liner design, this application might be called the *Virtual Scarf Exhaust (VSE)*.

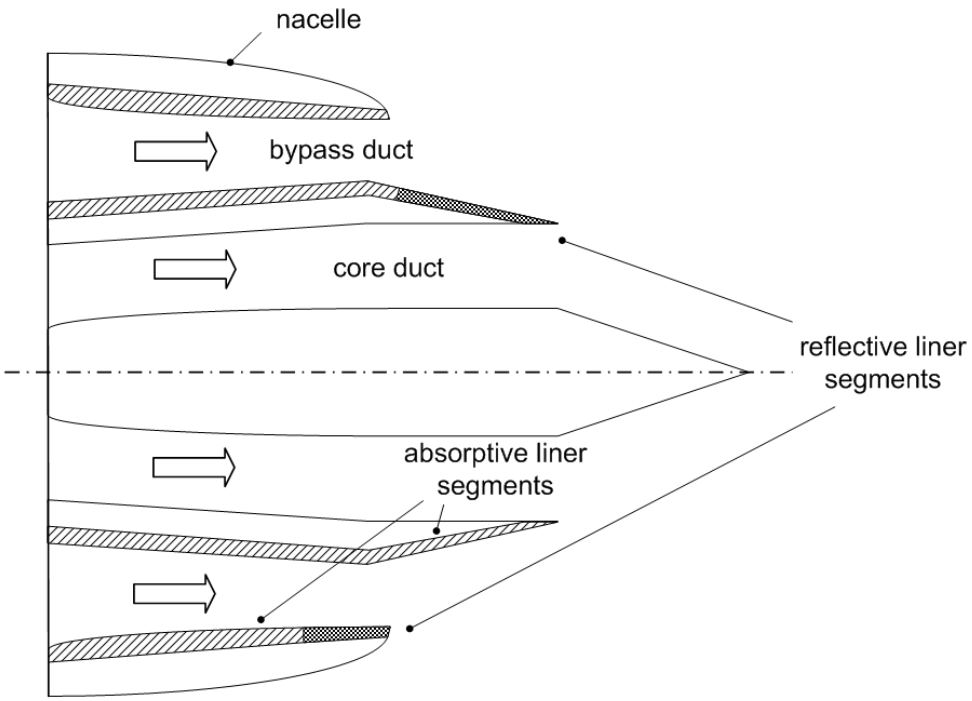

Figure 7.1: Sketch of non-uniform liner in bypass duct application (VSE)

The figure indicates the reflective liner segments on the respective lower wall sections of the bypass duct, i. e. the lower outer wall of the bypass duct in the lower half and the upper inner wall in the upper half. It might be expected that these liner strips of the same low impedance value as the one used in the lower front inlet are able to achieve a similar effect on the rearward radiation. However, of course, the more complex geometry, and especially the interaction of the sound radiation with the core stream, will strongly influence the overall effect. Accordingly, these parameters have to be included into the design and the numerical simulations to obtain reliable performance predictions.

Concerning the next logical steps in the development process of the VSI concept, at first, an experimental verification of the physical effect causing the redirection of radiation should be performed. This could be achieved with a relatively low effort on a laboratory acoustic test rig using an exchangeable non-uniform inlet liner segment according to the VSI design. From an arc of far field microphones, the directivity could be derived and compared to the numerical predictions.

Future work on the subject of the VSI (and the VSE) should include a detailed investigation of the influences of flow, which have not been studied within this thesis. These could be limited at first to uniform flow fields (as possible within the limitations of the BEM), but should be extended later on to non-uniform inflow conditions, for which e. g. an FEM code could be employed. By these studies, a clearer picture of the VSI effect in realistic application conditions could be derived. A subsequent experimental validation should be conducted in an aeroacoustic wind tunnel combining the advantages of a realistic flow field with adequate acoustic measurement conditions.

In addition, a parametric variation of the reflective liner impedance should be performed to investigate the dependency of the VSI effect on the accuracy of the softwall condition (impedance close to zero) and the degradation due to variations from this theoretical optimum.

With respect to the overall lining concept, an optimization should not only be aimed at the individual components (i. e. the VSI liner and the conventional absorptive liner), but also address at the performance of the complete system. This approach would make necessary several iterations involving the mutual dependencies of the two components, but should ensure an overall optimized design.

Bibliography

[1] Harvey H. Hubbard. *Aeoracoustics of Flight Vehicles - Theory and Practice*, volume 2: Noise Control. Acoustical Society of America, 1995.

[2] Klaus Ehrenfried. Skript zur Vorlesung Strömungsakustik II, Technische Universität Berlin, 2003.

[3] P. M. Morse and K. U. Ingard. *Theoretical Acoustics*. Princeton University Press, 1968.

[4] E. J. Rice. Acoustic liner optimum impedance for spinning modes with mode cut-off ratio as the design criterion. AIAA-76-516, 1976.

[5] E. J. Rice and M. F. Heidmann. Modal propagation angles in a cylindrical duct with flow and their relation to sound radiation. AIAA-79-0183, 1979.

[6] S. W. Rienstra and A. Hirschberg. *An Introduction to Acoustics*. Eindhoven Institute of Technology, 2004.

[7] T. L. Parrott, M. G. Jones, and W. R. Watson. Status of duct liner technology for application to aircraft engine nacelles. In *NOISE-CON 2005*.

[8] Ivar Veit. *Technische Akustik*. Vogel Buchverlag, Würzburg, 1988.

[9] L.A. Weinstein. *The Theory of Diffraction and the Factorization Method (Generalized Wiener-Hopf Technique)*. The Golem Press, Boulder, Colorado, 1969.

[10] W. E. Zorumski. Generalized radiation impedances and reflection coefficients of circular and annular ducts. *J. Acoust. Soc. America*, 54(6):1667–1673, 1973.

[11] L. B. Felsen and H. Y. Yee. Ray method for sound-wave reflection in an open-ended circular pipe. *J. Acoust. Soc. America*, 44(2):1028–1039, 1968.

[12] R. T. Muehleisen. *Reflection, radiation, and coupling of higher order modes at discontinuities in finite length rigid walled rectangular ducts*. PhD thesis, Pennsylvania State University, 1996.

[13] J. W. S. Rayleigh. *The Theory of Sound*, volume 2. reprinted by Dover, New York, 1945.

[14] H. Batard. Aircraft noise reduction: Airbus industrial needs in terms of new materials for nacelle liners. In *Journées scientifiques de l'ONERA*, 2003.

[15] R. Pongratz. Adaptive Liner zur Minderung von Triebwerkslärm - Konzept und Windkanalergebnisse. In *DGLR Symposium Nachbar Flughafen*, 2004.

[16] J. M. Tyler and T. G. Sofrin. Axial flow compressor noise studies. *SAE Journal.*, 70, 1962.

[17] A. McAlpine, M. J. Fisher, and B. J. Tester. 'Buzz saw' noise in acoustically lined ducts: Comparison of measurement with prediction. AIAA-2002-2448, 2002.

[18] Environmental technical manual on the use of procedures in the noise certification of aircraft. Technical Report Doc. 9501, ICAO, 2004.

[19] N. E. Antoine and I. M. Kroo. Optimizing aircraft and operations for minimum noise. AIAA-2002-5868, 2002.

[20] Handbook for acoustic ecology, 1999. `http://www.sfu.ca/~truax/handbook.html`.

[21] K. D. Kryter. The meaning and measurement of Perceived Noise Level. *Noise Control*, volume 6(5):12–17, 1960.

[22] A. H. Nayfeh, J. E. Kaiser, and D. P. Telionis. The acoustics of aircraft engine duct systems. AIAA-73-1153, 1973.

[23] P. G. Vaidya and P. D. Dean. State of the art of duct acoustics. AIAA-77-1279, 1977.

[24] R. A. Mangiarotty. Acoustic-lining concepts and materials for engine ducts. In *Aircraft Noise Symposium: Acoustical Duct Treatments for Aircraft*, 1970.

[25] U. Ingard. *Sound Absorption Technology.* Noise Control Foundation, Poughkeepsie, NY, 1994.

[26] H. A. Watson, Jr. Structural and environmental studies of acoustical duct-lining materials. In *Aircraft Noise Symposium: Acoustical Duct Treatments for Aircraft*, 1970.

[27] L. J. Sivian. Acoustic impedance of small orifices. *J. Acoust. Soc. America*, 7(2):94–101, 1935.

[28] P. D. Dean. An in situ method of wall acoustic impedance measurement in flow ducts. *J. Sound and Vibration*, 34(1):97–130, 1974.

[29] J. Atvars and R. A. Mangiarotty. Parametric studies of the acoustic behavior of duct-lining materials. In *Aircraft Noise Symposium: Acoustical Duct Treatments for Aircraft*, 1970.

[30] L. S. Wirt. Analysis, testing, and design of lined ducts. *J. Acoust. Soc. America*, 51(5):1448–1463, 1971.

[31] R. E. Kraft, R. E. Motsinger, W. H. Gauden, and J. F. Link. Analysis, design, and test of acoustic treatment in a laboratory inlet duct. CR 3161, NASA, 1979.

[32] M. G. Jones, M. B. Tracy, W. R. Watson, and T. L. Parrott. Effects of liner geometry on acoustic impedance. AIAA-2002-2446, 2002.

[33] L. Cremer. Theorie der Luftschall-Dämpfung im Rechteckkanal mit schluckender Wand und das sich dabei ergebende höchste Dämpfungsmass. *Acustica*, 3:249–263, 1953.

[34] P. M. Morse. *Vibration and Sound.* McGraw-Hill Book Company Inc., 1948.

[35] B. J. Tester. The optimization of modal sound attenuation in ducts, in the absence of mean flow. *J. Sound and Vibration*, 27(4):477–513, 1973.

[36] B. J. Tester. Ray models for sound propagation and attenuation in ducts, in the absence of mean flow. *J. Sound and Vibration*, 27(4):515–531, 1973.

[37] W. E. Zorumski and J. P. Mason. Multiple eigenvalues of sound-absorbing circular and annular ducts. *J. Acoust. Soc. America*, 55(6):1158–1165, 1974.

[38] E. J. Rice. Attenuation of sound in soft walled circular ducts. TM X-52442, NASA, 1968.

[39] E. J. Rice. Spinning mode sound propagation in ducts with acoustic treatment. TN D-7913, NASA, 1975.

[40] E. J. Rice. Spinning mode sound propagation in ducts with acoustic treatment and sheared flow. AIAA-75-519, 1975.

[41] J. P. D. Wilkinson. The calculation of optimal linings for jet engine inlet ducts - Part II. CR 1832, NASA, 1971.

[42] H. K. Liu and A. J. Martenson. Optimum lining configurations. In *Basic Aerodynamic Noise Research (NASA SP-207)*, pages 425–434, 1969.

[43] R. E. Kraft. Sound attenuation in a lined circular duct in the presence of spinning modes. TM 68-662, General Electric, 1968.

[44] H. E. Plumblee, P. D. Dean, et al. Sound propagation in and radiation from acoustically lined flow ducts: A comparison of experiment and theory. CR 2306, NASA, 1973.

[45] G. A. Wynne and H. E. Plumblee. Calculation of eigenvalues of the finite difference equations describing sound propagation in a duct carrying sheared flow. In *79th Meeting of the Acoustical Society of America, Atlantic City*, 1970.

[46] M. H. Dunn, J. Tweed, and F. Farassat. The prediction of ducted fan engine noise via a Boundary Integral Equation Method. AIAA-96-1770, 1996.

[47] M. H. Dunn and F. Farassat. Liner optimization studies using the ducted fan noise prediction code TBIEM3D. AIAA-98-2310, 1998.

[48] D. L. Lansing and W. E. Zorumski. Effects of wall admittance changes on duct transmission and radiation of sound. *J. Sound and Vibration*, 27(1):85–100, 1973.

[49] W. E. Zorumski. Acoustic theory of axisymmetric multisectioned ducts. TR R-419, NASA, 1974.

[50] F. Montétagaud and H. Batard. About the complexity of propagation and radiation of ducted modes. AIAA-2000-1955, 2000.

[51] F. Montétagaud, H. Batard, P. Lempereur, and C. Legros. Modal conversion from untreated to treated cylindrical ducts. AIAA-98-2309, 1998.

[52] W. Eversman. Computation of axial and transverse wave numbers for uniform two-dimensional ducts with flow using a numerical integration scheme. *J. Sound and Vibration*, 41(2):252–255, 1975.

[53] R. J. Astley, J. A. Hamilton, N. Baker, and E. H. Kitchen. Modelling tone propagation from turbofan inlets - The effect of extended lip liners. AIAA-2002-2449, 2002.

[54] D. Reed, W. Herkes, and B. Shivashankara. The Boeing Quiet Technology Demonstrator Program. In *25th ICAS Congress*, 2006.

[55] A. S. Hersh, B. E. Walker, and J. W. Celano. Effect of grazing flow and SPL on impedance of 2DOF resonators. AIAA-2002-2443, 2002.

[56] K. K. Ahuja, P. Cataldi, and R. J. Gaeta, Jr. Sound absorption of a 2DOF resonant liner with negative bias flow. CR 2000-210637, NASA, 2000.

[57] J. Julliard, H. Antoine, G. Riou, and S. Pillut-Lesavre. Development of a three degree of freedom liner. AIAA-2001-2203, 2001.

[58] P. Sijtsma and H. M. M. van der Wal. Modelling a spiralling type of non-locally reacting liner. AIAA-2003-3308, 2003.

[59] J. F. W. Herschel. On the absorption of light by coloured media, viewed in connexion with the undulatory theory. *Philosophical Mag. and J. of Science*, 3:401–412, 1833.

[60] G. Quincke. Über Interferenzapparate für Schallwellen. *Annalen der Physik und Chemie*, 128:177–192, 1866.

[61] L. A. Brady, R. A. Burdisso, and J. P. Smith. Investigation of the Herschel-Quincke tube concept for the suppression of higher-order modes in a duct. In *Proceedings of Internoise 99*, pages 545–550, 1999.

[62] R. A. Burdisso and J. P. Smith. Control of inlet noise from turbofan engines using Herschel-Quincke waveguides. AIAA-2000-1994, 2000.

[63] R. A. Burdisso and Wing. F. Ng. Fan noise control using Herschel-Quincke resonators. CR 2003-212097, NASA, 2003.

[64] Georgia Institute of Technology. New acoustic liner material uses tiny spheres to absorb noise and withstand high temperatures, August 1997.

[65] 01dB - Metravib. `http://www.01db-metravib.com`.

[66] P. Ladner, T. Mazoyer, and J. Périsse. Acoustic splitter development based on hollow spheres materials for aircraft engine application. In *Euronoise Naples 2003*, number 431, 2003.

[67] J. M. De Bedout and M. A. Franchek. Adaptive-passive noise control with self-tuning Helmholtz resonators. *J. Sound and Vibration*, 202(1):109–123, 1997.

[68] T. A. Laak, Jr. and D. W. Kapsos, Jr. US Patent 6,295,363: Adaptive passive acoustic attenuation system, 2001.

[69] K. K. Ahuja and R. J. Gaeta, Jr. Active control of liner impedance by varying orifice geometry. CR 2000-210633, NASA, 2000.

[70] U. Ingard and H. Ising. Acoustic nonlinearity of an orifice. *J. Acoust. Soc. America*, 42(1), 1967.

[71] P. D. Dean and B. J. Tester. Duct wall impedance control as an advanced concept for acoustic suppression. CR 134998, NASA, 1975.

[72] C. Heuwinkel, L. Enghardt, and I. Roehle. Experimental investigation of the acoustic damping of perforated liners with bias flow. AIAA-2007-3525, 2007.

[73] C. J. Radcliffe and C. Birdsong. An electronically tuneable resonator for noise control. *SAE Journal.*, 2001-01-1615, 2001.

[74] S. Horowitz, T. Nishida, L. N. Cattafesta, and M. Sheplak. Compliant-backplate Helmholtz resonators for active noise control applications. AIAA-2001-0817, 2001.

[75] S. Horowitz, T. Nishida, L. N. Cattafesta, and M. Sheplak. Characterization of compliant-backplate Helmholtz resonators for an electromechanically acoustic liner. AIAA-2002-0666, 2002.

[76] F. Liu, S. Horowitz, T. Nishida, L. N. Cattafesta, and M. Sheplak. A tunable electromechanical Helmholtz resonator. AIAA-2003-3145, 2003.

[77] M. Furstoss, D. Thenail, and M.-A. Galland. Surface impedance control for sound absorption: Direct and hybrid passive/ active strategies. *J. Sound and Vibration*, 203(2):219–236, 1997.

[78] D. Thenail, M.-A. Galland, M. Sunyach, and M. Sunhack. Active enhancement of the absorbent properties of a porous material. *Smart Mater. Struct.*, 3:18–25, 1994.

[79] O. Hilbrunner, M.-A. Galland, N. Sellen, and J. Périsse. Optimisation of a hybrid acoustic liner for noise reduction of engine aircraft nacelles. In *Active 2002*.

[80] M. Cuesta, P. Cobo, A. Férnandez, and J. Pfretzschner. Using a thin actuator as secondary source for hybrid passive/ active absorption in an impedance tube. *Applied Acoustics*, 67, 2005.

[81] S. Beyene and R. A. Burdisso. A new hybrid passive/ active noise absorption system. *J. Acoust. Soc. America*, 101(3), 1997.

[82] J. P. Smith, B. D. Johnson, and R. A. Burdisso. A broadband passive-active sound absorption system. *J. Acoust. Soc. America*, 106(5):2646–2652, 1999.

[83] P. A. Nelson. Active techniques and their potential application in aeroacoustics. In *6th AIAA/CEAS Aeroacoustics Conference*, volume AIAA-2000-31165, 2000.

[84] J. W. S. Rayleigh. *The Theory of Sound*, volume 1. reprinted by Dover, New York, 1945.

[85] P. Lueg. US Patent 2,043,416: Process of silencing sound oscillations, 1936.

[86] W. B. Conover. Fighting noise with noise. *Noise Control*, volume 2, 1956.

[87] K. Kido and S. Onoda. Automatic control of acoustic noise emitted from power transformers by synthesizing directivity. Science report of the research institutes, Tohoku University, 1972.

[88] R. E. Kraft and K. B. Kontos. Theoretical implications of active noise control for turbofan engines. AIAA-93-4355, 1993.

[89] R. E. Kraft and K. B. Kontos. US Patent 5,498,127: Active acoustic liner, 2006.

[90] R. H. Thomas, R. A. Burdisso, C. R. Fuller, and W. F. O'Brien. Active control of fan noise from a turbofan engine. AIAA-93-0597, 1993.

[91] J. D. Risi, R. A. Burdisso, and C. R. Fuller. Analytical investigation of active control of radiated inlet fan noise. *J. Acoust. Soc. America*, 99(1), 1996.

[92] P. Joseph, P. A. Nelson, and M. J. Fisher. Active control of fan tones radiated from turbofan engines - I. External error sensors. *J. Acoust. Soc. America*, 106(2), 1999.

[93] P. Joseph, P. A. Nelson, and M. J. Fisher. Active control of fan tones radiated from turbofan engines - II. In-duct error sensors. *J. Acoust. Soc. America*, 106(2), 1999.

[94] P. Joseph, E. F. Fruteau, and P. A. Nelson. Design rules and sensing strategies for the active control of turbofan engine noise. AIAA-2001-2222, 2001.

[95] R. Maier, J. Zillmann, A. Roure, M. Winninger, L. Enghardt, U. Tapken, W. Neise, H. Antoine, and E. Bouty. Active control of fan tone noise from aircraft engines. AIAA-2001-2220, 2001.

[96] D. Berge, E. Bouty, and J. M. Cailleau. Active noise control of a jet engine at low frequencies: BEM for predicting far-field noise reduction. AIAA-93-4354, 1993.

[97] G. W. Bielak, J. W. Premo, and A. S. Hersh. Advanced turbofan duct liner concepts. CR 1999-209002, NASA, 1999.

[98] D. W. Quinn. Attenuation of the sound associated with a plane wave in a multisectional duct. AIAA-75-496, 1975.

[99] D. T. Sawdy, R. J. Beckemeyer, and J. D. Patterson. Analytical and experimental studies of an optimum multisegment phased liner noise suppression concept. CR 134960, NASA, 1976.

[100] K. J. Baumeister. Optimized multisectioned acoustic liners. AIAA-79-0182, 1979.

[101] C. A. Reimann, A. F. Tinetti, and M. H. Dunn. Engine liner optimization using the fast scattering code. AIAA-2007-3494, 2007.

[102] A. McAlpine, R. J. Astley, V. J. T. Hii, N. J. Baker, and A. J. Kempton. Acoustic scattering by an axially-segmented turbofan inlet duct liner at supersonic fan speeds. *J. Sound and Vibration*, 294:780–806, 2006.

[103] A. J. Kempton, N. J. Baker, A. McAlpine, and J. Astley. EP Patent 1411225: Acoustic liner for gas turbine, 2003.

[104] E. J. Rice, A. S. Hersh, and B. E. Walker. EP Patent 1085196: Hybrid mode-scattering/ sound-absorbing segmented liner system and method, 2001.

[105] W. P. Patrick. EP Patent 1701016: Acoustic liner with nonuniform impedance, 2006.

[106] N. J. Lipstein. US Patent 3,890,060: Acoustic duct with asymmetric acoustical treatment, 1975.

[107] Ramani Mani. US Patent 3,937,590: Acoustic duct with peripherally segmented acoustic treatment, 1976.

[108] R. J. Astley, N. J. Walkington, and W. Eversman. Transmission in flow ducts with peripherally varying liners. AIAA-80-1015, 1980.

[109] R. J. Astley and W. Eversman. A finite element formulation of the eigenvalue problem in lined ducts with flow. *J. Sound and Vibration*, 65(1), 1979.

[110] Willie R. Watson. An evaluation of circumferentially segmented duct liners. AIAA-83-0732, 1983.

[111] P. Malbéqui and H. Gounet. Numerical optimization of liners for an aeroengine intake. In *ICSV12; Lisbon, Portugal*, 2005.

[112] W. R. Watson, M. G. Jones, T. L. Parrott, and J. Sobieski. A method for optimizing non-axisymmetric liners for multimodal sound sources. AIAA-2002-2516, 2002.

[113] M. S. Howe. The attenuation of sound in a randomly lined duct. *J. Sound and Vibration*, 87(1):83–103, 1982.

[114] W. R. Watson, J. H. Robinson, M. G. Jones, and T. L. Parrott. Design and attenuation properties of periodic checkerboard liners. AIAA-2003-3309, 2003.

[115] E. R. Rademaker, S. L. Sarin, and C. A. Parente. Experimental investigation on the influence of liner non-uniformities on prevailing modes. AIAA-96-1682, 1996.

[116] B. Regan and J. Eaton. Finite element investigation of the influence of liner splices on duct modes. AIAA-98-2313, 1998.

[117] T. Elnady and H. Bodén. Hard strips in lined ducts. AIAA-2002-2444, 2002.

[118] A. McAlpine, M. C. M. Wright, H. Batard, and S. Thezelais. Finite/ Boundary Element assessment of a turbofan spliced intake liner at supersonic fan operating conditions. AIAA-2003-3305, 2003.

[119] A. McAlpine and M. C. M. Wright. Acoustic scattering by a spliced turbofan inlet duct liner at supersonic fan speeds. *J. Sound and Vibration*, 292:911–934, 2006.

[120] W. P. Bi, V. Pagneux, D. Lafarge, and Y. Aurégan. Characteristics of penalty mode scattering by rigid splices in lined ducts. AIAA-2005-2897, 2005.

[121] W. P. Bi, V. Pagneux, D. Lafarge, and Y. Aurégan. Modelling of sound propagation in a non-uniform lined duct using a multi-modal propagation method. *J. Sound and Vibration*, 289:1091–1111, 2006.

[122] B. J. Tester, N. J. Baker, A. J. Kempton, and M. C. Wright. Validation of an analytical model for scattering by intake liner splices. AIAA-2004-2906, 2004.

[123] M. C. M. Wright. Hybrid analytical/ numerical method for mode scattering in azimuthally non-uniform ducts. *J. Sound and Vibration*, 292:583–594, 2006.

[124] M. C. M. Wright and A. McAlpine. Calculation of modes in azimuthally non-uniform lined ducts with uniform flow. *J. Sound and Vibration*, 302:403–407, 2007.

[125] H. Batard. The Zero Splice Engine Intake Liner: An efficient way of reducing aircraft noise without any weight or aerodynamic penalty. In *24th ICAS Congress*, 2004.

[126] F. Gantie, H. Batard, N.J. Baker, and P.J.G. Schwaller. Zero Splice Intake technology and acoustic benefit. AIAA-2006-2455, 2006.

[127] J. Yu et al. Quiet Technology Demonstrator 2 intake liner design and validation. AIAA-2006-2458, 2006.

[128] D. M. Brown. US Patent 3,545,464: Air intake duct for a gas turbine engine, 1970.

[129] G. Neumann. US Patent 3,964,569: Gas turbine engine noise shield, 1976.

[130] M. M. K. V. Sankrithi and P. E. Nelson. US Patent 6,764,043: Rotatable scarf inlet for an aircraft engine and method of using the same, 2004.

[131] L.R. Clark, R.H. Thomas, R.P. Dougherty, F. Farassat, and C.H. Gerhold. Inlet shape effects on the far-field sound of a model fan. AIAA-97-1589, 1997.

[132] F. Montétagaud and S. Montoux. Negatively Scarfed Intake: Design and acoustic performance. AIAA-2005-2944, 2005.

[133] A. R. Smith, R. Thorne, C. Gouttenoire, T. Surply, and P. Chanez. Aerodynamic aspects of application of negative scarf intake to high bypass ratio civil turbofans. AIAA-2005-4205, 2005.

[134] J. T. Kutney and R. B. Mishler. US Patent 3,946,830: Inlet noise deflector, 1976.

[135] M. M. Curtin, R. P. Dougherty, J. M. McConachie, and M. L. Sangwin. WO Patent 99/61316: Biplanar scarfed nacelle inlet, 1999.

[136] J.M. Abbott and J.W. Slater. Computational study of the aerodynamic performance of three-dimensional subsonic inlets. AIAA-2001-3886, 2001.

[137] J.M. Abbott. Aerodynamic performance of scarf inlets. AIAA-79-0380, 1979.

[138] C. H. Gerhold, L. R. Clark, and R. T. Biedron. Control of inflow distortion in a scarf inlet. AIAA-2002-2432, 2002.

[139] L. J. Sivian. Sound propagation in ducts lined with absorbing materials. *J. Acoust. Soc. America*, 9(1):135–140, 1937.

[140] P. M. Morse. Some aspects of the theory of room acoustics. *J. Acoust. Soc. America*, 11(1):56–66, 1939.

[141] P. M. Morse. The transmission of sound inside pipes. *J. Acoust. Soc. America*, 11(2):205–210, 1939.

[142] C. T. Molloy and E. Honigman. Attenuation of sound in lined circular ducts. *J. Acoust. Soc. America*, 16(4):267–272, 1945.

[143] E. Fisher. Attenuation of sound in circular ducts. *J. Acoust. Soc. America*, 17(2):121–122, 1945.

[144] E. J. Rice. Propagation of waves in an acoustically lined duct with a mean flow. *Basic Aerodynamic Noise Research*, 207:345–355, 1969.

[145] E. J. Rice. Attenuation of sound in ducts with acoustic treatment - A generalized approximate equation. TM X-71830, NASA, 1975.

[146] D. R. A. Christie. Theoretical attenuation of sound in a lined duct: Some computer calculations. *J. Sound and Vibration*, 17(2):283–286, 1971.

[147] S.-H. Ko. Sound attenuation in lined rectangular ducts with flow and its application to the reduction of aircraft engine noise. *J. Acoust. Soc. America*, 50(6):1418–1432, 1971.

[148] S.-H. Ko. Sound attenuation in acoustically lined circular ducts in the presence of uniform flow and shear flow. *J. Sound and Vibration*, 32(2):193–210, 1972.

[149] W. Eversman. The effect of Mach number on the tuning of an acoustic lining in a flow duct. *J. Acoust. Soc. America*, 48(2):425–428, 1970.

[150] W. Eversman. Initial values for the integration scheme to compute the eigenvalues for propagation in ducts. *J. Sound and Vibration*, 50(1):159–162, 1977.

[151] O. v. Estorff. Computational methods in acoustics. Skript zur Vorlesung, Technische Universität Hamburg-Harburg, 2001.

[152] W. K. Boyd, A. J. Kempton, and C. L. Morfey. Ray-theory predictions of the noise radiated from aeroengine ducts. AIAA-84-2332, 1984.

[153] R. P. Dougherty. Nacelle acoustic design by ray tracing in three dimensions. AIAA-96-1773, 1996.

[154] P. Malbequi. In duct propagation and radiation using a ray model. In *17th International Congress on Acoustics, Rome 2001*. ONERA, 2001.

[155] R. H. Lyon and R. D. DeJong. *Theory and Application of Statistical Energy Analysis*. Butterworth-Heinemann, 1995.

[156] G.D. Mey. A simplified integral equation method for the calculation of the eigenvalues of the Helmholtz equation. *Internat. J. Meth. Eng.*, 11:1340–1342, 1977.

[157] Y. Niwa, S. Kobayashi, and M. Kitahara. Determination of eigenvalues by Boundary Element Methods. In *Banerjee and Shaw, Developments in Boundary Element Methods*, chapter 6, pages 143–176. 2. Applied Science Publishers, 1982.

[158] L. H. Chen and D. G. Schweikert. Sound radiation from an arbitrary body. *J. Acoust. Soc. America*, 35(10), 1963.

[159] G. Chertock. Sound radiation from vibrating surfaces. *J. Acoust. Soc. America*, 36(7), 1964.

[160] M. Moosrainer. Fluid-Struktur-Kopplung. Fortschritt-Bericht 289, VDI, 2000.

[161] A. Sommerfeld. *Partial Differential Equations in Physics*. Academic Press, New York, 1949.

[162] H. A. Schenck. Improved integral formulation for acoustic radiation problems. *J. Acoust. Soc. America*, 44(1):41–58, 1968.

[163] G. Engeln-Muellges and F. Reutter. *Numerik-Algorithmen*. VDI Verlag, Düsseldorf, 1996.

[164] G. W. Benthien and H. A. Schenck. Structural-acoustic coupling. In *Ciskowski and Brebbia, Boundary Element Methods in Acoustics*, chapter 6, pages 109–129. Computational Mechanics Publications, 1991.

[165] LMS International. *LMS SYSNOISE Rev 5.6 On-line help.*

[166] M. A. Hamdi. *Formulation variationelle par equations intégrales pour le calcul de champs acoustiques linéaires proches et lointains.* PhD thesis, Université de Compiègne, 1982.

[167] L. Gaul, M. Kögl, and M. Wagner. *Boundary Element Methods for Engineers and Scientists.* Springer-Verlag, Berlin, 2003.

[168] R. Duraiswami. *An Introduction to Fast Multipole Methods.* `http://www.umiacs.umd.edu/~ramani/`.

[169] F. Darbas. *ASERIS - Actipole Users Manual V1.8.0.* EADS Innovation Works, Toulouse, France, 2007.

[170] L. Greengard and Rokhlin. V. A fast algorithm for particle simulations. *Journal of Computational Physics*, 73:325–348, 1987.

[171] Y. Yasuda and T. Sakuma. An effective setting of hierarchical cell structure for the Fast Multipole Boundary Element Method. *Journal of Computational Acoustics*, 13(1):47–70, 2005.

[172] R. Coifman, V. Rokhlin, and S. Wandzura. The Fast Multipole Method for the wave equation: A pedestrian prescription. *IEEE Antennas and Propagation Magazine*, 35(3), 1993.

[173] L. Gaul. Randelementmethoden für gekoppelte Feldprobleme. In *DAGA 2007, Stuttgart*, 2007.

[174] G. Alleon, S. Champagneux, G. Chevalier, L. Giraud, and G. Sylvand. Parallel distributed numerical simulations in aeronautic applications. Technical Report TR/CFD-PA/05/44, CERFACS, Toulouse, France, 2005.

[175] *LMS Virtual.Lab.* `http://www.lmsintl.com/simulation/lmsvirtuallab`.

[176] S. Lidoine, H. Batard, S. Troyes, A. Delnevo, and M. Roger. Acoustic radiation modelling of aeroengine intake - Comparison between analytical and numerical methods. AIAA-2001-2140, 2001.

[177] J. M. Song and W. C. Chew. Fast Multipole Method solution of combined field integral equation. In *ACES Conference Digest*, 1995.

[178] E. Kors. SILENCER - Halfway towards success. In *AIAA Aeroacoustics Conference 2004*, 2004.

[179] R. Pongratz. Actuator improvement for the Mechanical Adaptive Liner. Technical Report SILENCER D1.2-5.2-11, EADS CRC, 2001.

[180] R. Pongratz. Preliminary design of the phase 2 prototype. Technical Report SILENCER D1.2-5.2-12, EADS CRC, 2002.

[181] S. Pérennès. Acoustic requirements of adaptive liners. Technical Report SILENCER D1.2-5.0-11-1, SNECMA, 2001.

[182] C.H. Gerhold, R.H. Cabell, and D.E. Brown. Generation of higher order modes in a rectangular duct. In *ACTIVE 04*, 2004.

[183] D. Broszat and R. Pongratz. Acoustical behaviour and performance prediction of mechanically adaptive liner. Technical Report SILENCER D2.3-3.6-07, EADS CRC, 2006.

[184] M. K. Myers and A. T. Cochrane. Acoustics of nonuniform locally reacting absorbers. AIAA-99-1824, 1999.

[185] T. L. Parrott and M. G. Jones. Parallel-element liner impedances for improved absorption of broadband sound in ducts. *Noise Control Eng. J.*, 43(6):183–195, 1995.

[186] Kai-Michael Lochte. Analyse neuartiger Triebwerksauskleidungen zur Lärmreduzierung. Master's thesis, RWTH Aachen University, 2007.

[187] D. Broszat, R. Maier, and R. Pongratz. The Virtual Scarf Inlet. AIAA-2007-3553, 2007.

[188] N. C. Ovenden. Near cut-on/ cut-off transition in lined ducts with flow. AIAA-2002-2445, 2002.

[189] N. C. Ovenden, W. Eversman, and S. W. Rienstra. Cut-on/ cut-off transition in flow ducts: Comparing Multiple-Scales and Finite-Element solutions. AIAA-2004-2945, 2004.

[190] A. H. Nayfeh and D. P. Telionis. Acoustic propagation in ducts with varying cross sections. *J. Acoust. Soc. America*, 54(6):1654–1661, 1973.

[191] H. Levine and J. Schwinger. On the radiation of sound from an unflanged circular pipe. *Physical Review, Vol. 73 No. 4*, 1948.

[192] A. Selamet, Z. L. Ji, and R. A. Kach. Wave reflections from duct terminations. *J. Acoust. Soc. America*, 109(4):1304–1311, 2000.

[193] N. Schoenwald, L. Panek, C. Richter, and F. Thiele. Investigation of sound radiation from a scarfed intake by CAA-FWH simulations using overset grids. AIAA-2007-3524, 2007.

[194] J. Lan, J. Premo, et al. Phased array measurements of full-scale engine inlet noise. AIAA-2007-3434, 2007.

List of Figures

List of Tables

Appendix A

Specifications

A.1 Loudspeakers used in acoustic test rig

BMS

H 4540 ND Compression Driver

1" NEODYMIUM HIGH FREQUENCY COMPRESSION DRIVER

4540 ND is the ultimate BMS driver in its class - for now

- the smallest and lightest in its class
- the loudest in its class
- the most impressive of all is the superior sound
- Unique patented design
- Neodymium magnet assembly
- 114 dB sensitivity 1W / 1m
- Extended high frequency response up to 30 kHz
- Very small size and low weight
- 38 mm voice coil 1" 3/8 - 18 N screwor 1" flange adapter

BMS 4540 ND is a powerful 1" professional compression driver that delivers superb sonic quality in a very small package. The unique BMS annular diaphragm together with the high energy neodymium magnet achieve very high sensitivity and linear frequency response up to 30 kHz. The sound of 4540 ND is extremely transparent and detailed, it has an exceptional dynamic range and produces even the most complex music signals with depth and definition.

4540 ND - 1" compression driver is designed for a wide variety of applications including high level professional reinforcement systems, studio monitors and high-end audio.

Durability and reliability are key in heavy-use professional applications. Therefore each driver is systematically tested to strict standards to ensure highest possible quality.

Specifications	4540 ND
Throat diameter	1" (25,4 mm)
Nominal impedance	8 or 16 Ohm
Power capacity (AES)	60 W
Peak power	300 W
Sensitivity in:	
CD Horn 90°x75°, 1W / 1m	114 dB
Plane wave tube, 1mW	118 dB
Maximal SPL (cont.)	132 dB @ 60 W
Frequency range	1.200 - 30.000 Hz
Recommended crossover	1.900 Hz
Voice coil diameter	1,5" (38 mm)
Magnet material	Neodymium
Flux density	2,2 T
Voice coil material	Cooper Clad Aluminium
Voice coil former	Kapton
Diaphragm material	Polyester

Mounting information

Overall Diameter	72 mm (+/- 0,1mm)
Depth	45 mm
Net weight	0,530 kg
Mounting	1" 3/8 - 18N screw or 1" flange adapter

Figure A.1: Specification sheet of BMS loudspeakers H 4540 ND - page 1

BMS

H 4540 ND Compression Driver

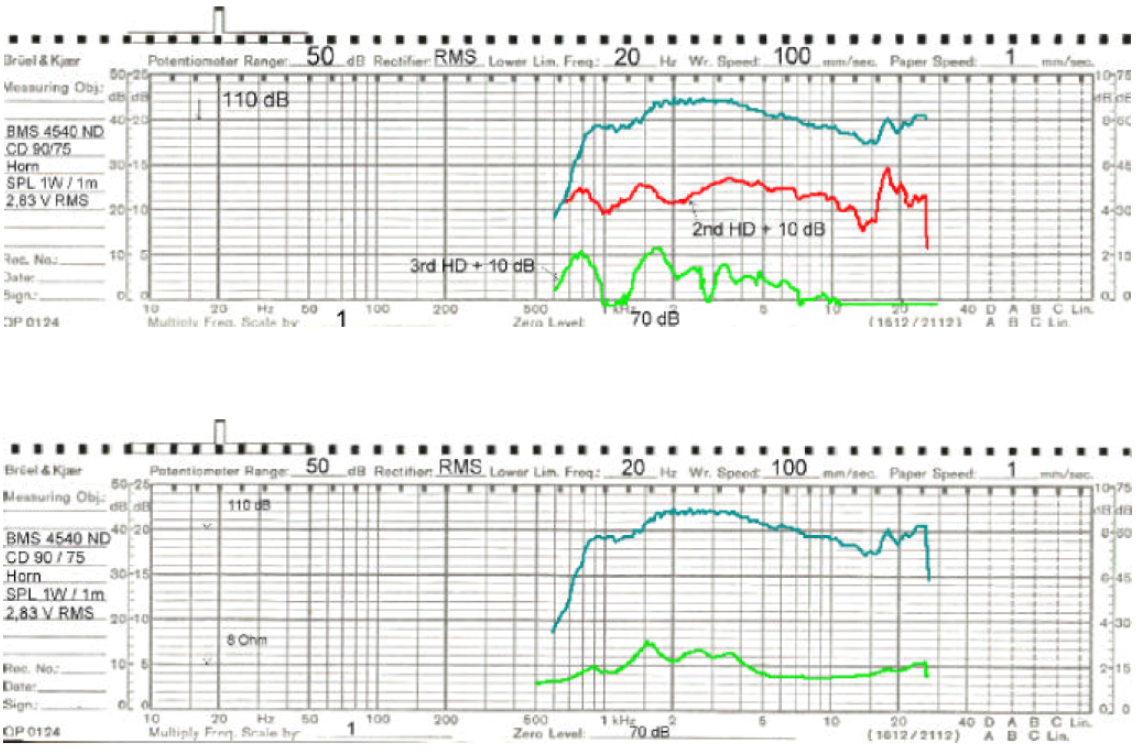

BMS Elektronik GmbH - Germany
Boulevard der EU 6, D-30539 Hannover
Phone +49(0)511-8 79 38 98 - Fax +49(0)511-8 79 3901
e-mail: info@bmselektronik.de

Figure A.2: Specification sheet of BMS loudspeakers H 4540 ND - page 2

A.2 Microphones used as sensors

Product Data

Microphone — Type 4196

USES:

- Simultaneous recording of time signals in medium to large microphone arrays for the analysis of non-stationary noise
- Spatial Transformation of Sound Fields (STSF) measurements
- Type 2 acoustical measurements

FEATURES:

- 7 mm (~1/4") prepolarized microphone with built-in preamplifier
- Free-field frequency response (re 1 kHz): 100 to 3000 Hz: ±1 dB and 3 kHz to 5 kHz: ±2 dB Dynamic range typically 43 dB to 140 dB
- Sensitivity 4,2 mV/Pa ±3 dB
- Microphone housing clips into Microphone Array System Type 9694
- Easy calibration via multitube adaptor for Pistonphone Type 4228
- Detachable cable
- Multi-cable support

Microphone Type 4196 is a 7 mm (~1/4") prepolarized microphone with built in preamplifier. The preamplifier terminates in a 3-pin LEMO® socket.

When used for simultaneous measurement of a large number of signals, for example for the measurement of STSF, the microphones can be clipped into a strong yet simple grid network to form a complete array.

Fig. 1 Microphone Type 4196

Microphone Type 4196 is intended for use in systems requiring a large number of microphones, for example for measurements of the Spatial Transformation of Sound Fields (STSF).

The microphone is prepolarized, which gives two advantages over externally polarized microphones:

- space is saved as no power supply is needed
- the preamplifier is more reliable in humid and polluted atmospheres

The microphone is back-vented for pressure equalization.

Type 4196 provides, at low cost, good amplitude linearity and phase matching over the limited frequency range relevant to array applications.

Arrays

When used for STSF measurements or other measurements requiring a large number of measurement points, it may be convenient to arrange the microphones in an array. This is possible using Microphone Array System Type 9694, available separately. The microphone housing clips directly into the grid.

Calibration

The microphones can be calibrated using any one of Brüel & Kjær's Calibrators (see Ordering Information). For ease of calibration, we recommend, however, Pistonphone Type 4228, for which a multitube adaptor is available (Brüel & Kjær order number WA 0728). This adaptor allows 6 microphones to be connected to the pistonphone at the same time, while they are still positioned in the array.

Cables

Two types of cable are available for use with Microphone Type 4196:

- a single cable terminated with a 7-pin LEMO plug (AO 0433)
- a 6-channel cable terminated with a 37-pole D-connector for connection to a 6-channel input module Type 3026 (AO 0432) used in Intelligent Data Acquisition System Type 3561

The 6-channel cables are both colour-coded and numbered for easy identification.

Brüel & Kjær

Figure A.3: Specification sheet of Brüel & Kjær microphones type 4196 - page 1

Specifications 4196

SENSITIVITY: 4.2 mV/Pa ±3 dB
POLARIZATION VOLTAGE (external): 0 V
FREQUENCY RESPONSE:
0° incidence free-field response (re 1 kHz):
+1 dB, 100 Hz to 3 kHz
+2 dB, 3 kHz to 5 kHz
INHERENT NOISE (A weighted):
43 dB (−10 to +40°C, 14 to 104°F)
51 dB (−10 to +55°C, 14 to 131°F)
DYNAMIC RANGE:
43 to 140 dB (A weighted, THD <3%)
SAFETY LIMIT: 150 dB (peak)
OUTPUT IMPEDANCE: 120 Ω
CURRENT CONSUMPTION:
3 mA with 15 V supply
MAX. LOAD: 5 kHz, 140 dB: 10 nF
PHASE MATCH: See Fig. 3
OUTPUT SOCKET: 3-pin LEMO®

Environmental

TEMPERATURE COEFFICIENT:
+0.01 dB/°C at 250 Hz
RELATIVE HUMIDITY INFLUENCE: <0.4 dB
MAGNETIC FIELD SENSITIVITY:
40 dB SPL for 80 A/m, 50 Hz field
VIBRATION SENSITIVITY (10 to 55 Hz)
Approx. 60 dB equivalent SPL for 1 m/s^2 axial acceleration

Dimensions and Weight

Diameter: 7 mm (~1/4")
Length: 183.5 mm (7.2")
Weight: 20.5 g (0.72 oz.)

Note: All values are typical at 25°C (77°F), unless measurement uncertainty or tolerance field is specified. All uncertainty values are specified at 2σ (i.e. expanded uncertainty using a coverage factor of 2)

COMPLIANCE WITH STANDARDS:

CE	CE-mark indicates compliance with: EMC Directive.
Safety	EN 61010–1 and IEC 1010–1: Safety requirements for electrical equipment for measurement, control and laboratory use.
EMC Emission	EN 50081–1: Generic emission standard. Part 1: Residential, commercial and light industry. EN 50081–2: Generic emission standard. Part 2: Industrial environment. CISPR 22: Radio disturbance characteristics of information technology equipment. Class B Limits. FCC Rules, Part 15: Class B limits.
EMC Immunity	EN 50082–1: Generic immunity standard. Part 1: Residential, commercial and light industry. EN 50082–2: Generic immunity standard. Part 2: Industrial environment. **Note 1:** The above is guaranteed using accessories listed in this Product Data sheet only. **Note 2:** HF-field 80 to 100 MHz: Inherent Noise (A-weighted) <30 µV (51 dB)
Temperature	IEC 68–2–1 & IEC 68–2–2: Environmental Testing. Cold and Dry Heat. Operating Temperature: −10 to +55°C (+14 to +131°F) Storage Temperature: −25 to +70°C (−13 to +158°F)
Humidity	IEC 68–2–3: Damp Heat: 90% RH (non-condensing at 40°C (104°F))
Mechanical	Non-operating: IEC 68–2–6: Vibration: 0.3 mm, 20 m/s^2, 10–500 Hz IEC 68–2–27: Shock: 1000 m/s^2 IEC 68–2–29: Bump: 1000 bumps at 250 m/s^2
Enclosure	IEC 529: Protection Provided by Enclosures: IP 20
Reliability	MIL-HDBK 217 F, GB (Part-stress): MTBF >500000 hours (max. 0.2% errors/1000 h)

Specifications are valid for Type 4196 from serial number: 1858818 (excluding 1909732 to 1909806)

Ordering Information

Optional Accessories

Cables for use with Intelligent Data Acquisition System Type 3561:

AO 0432 - AC 0221-x:
6-channel Cable terminated with 37-pole D-connector. Specify length x in metres when ordering (5 < x < 40 m)

AO 0433 - AC 0220-x:
Cable terminated with 7-pin LEMO plug. Specify length x in metres when ordering (5 < x < 40 m).

Note: For correct phase-match cables must be multiple of 5 m and the length of cables in a microphone array must not vary more than ±5 m.

Array:
Type 9694: Microphone Array System
KE 0351: Suitcase for 52 microphones Type 4196
Calibration:
Type 4228: Pistonphone
Type 4231: Sound Level Calibrator (includes 1/4" Adaptor DP 0775)
WA 0728: Multitube Adaptor for Pistonphone Type 4228

Brüel&Kjær reserves the right to change specifications and accessories without notice

Figure A.4: Specification sheet of Brüel & Kjær microphones type 4196 - page 2

A.3 Resistance sheet used for equivalent liner

Metallfiltergewebe Robusta - Technische Daten

Absolute Filterfeinheit µm	Nominale Filterfeinheit µm	Gewebe-bezeichnung Mesh	Streckgrenze Kette/Schuss Rp N/cm	Porenanzahl N Poren/cm²	AsK mm²/cm	AsS mm²/cm	Porosität %	A_{0rel} %	Gewicht kg / m2	Gewebe-dicke mm
14 - 17	10	850 x 155	80 / 160	40.800	0,25	0,48	53	11	0,58	0,16
18 - 21	15	720 x 150	95 / 205	33.500	0,27	0,58	52	14	0,69	0,18
23 - 26	20	600 x 125	100 / 220	23.300	0,34	0,60	53	17	0,75	0,20
35 - 38	25	600 x 100	100 / 220	18.600	0,33	0,61	57	30	0,75	0,22
54 - 60	40	280 x 70	210 / 330	6.100	0,71	0,95	56	23	1,34	0,39
56 - 62	50	*400 x 125	160 / 135	3.900	0,55	0,39	58	16	0,75	0,23
65 - 72	60	175 x 50	400 / 480	2.700	1,23	1,39	55	15	2,11	0,60
95 - 105	80	130 x 35	520 / 600	1.400	1,63	1,73	57	17	2,70	0,80
110 - 125	100	140 x 40	600 / 550	1.700	1,55	1,79	55	32	2,80	0,76

* Robusta Köper

A_0rel: theoretische freie Durchflussfläche, durch die das Filtrat hindurchfließen kann - bezogen auf die angeströmte Fläche.
A_s, A_sK, A_sS: wirksamer Querschnitt an den Schnittkanten, die senkrecht zu den Drähten verlaufen, um Zugkräfte aufzunehmen. AsK: Kettrichtung, As: Schussrichtung.
Gewebedicke: Näherungsangabe.
Gewicht: Näherungsangabe.
Porosität: Näherungswerte
Rp: maximal zulässige Belastung der Gewebe in Kett- (RpK) oder Schussrichtung (RpS), ohne bleibende signifikante Verformung.

Die Angaben sind typische Werte. Daraus lassen sich keine zugesicherten Eigenschaften ableiten. Technische Änderungen vorbehalten.

Figure A.5: Specification sheet of Spörl KG Robusta filter web

Appendix B

Data

B.1 Radiated power and attenuation in parametric study

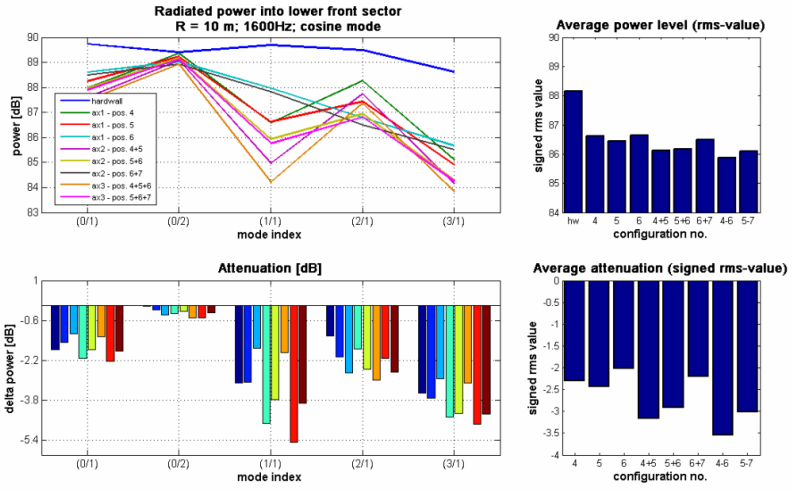

Figure B.1: Radiated power and attenuation in lower front sector as function of axial liner length and position; azi180; 1000 Hz

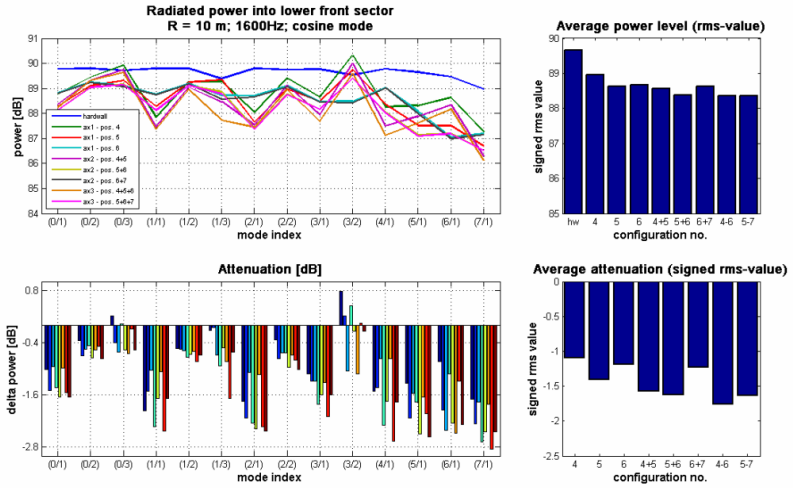

Figure B.2: Radiated power and attenuation in lower front sector as function of axial liner length and position; azi180; 2000 Hz